Raman spectroscopy for KATRIN: monitoring of continuous tritium gas flows and tritium-graphene interactions

Zur Erlangung des akademischen Grades eines

Doktors der Naturwissenschaften (Dr. rer. nat.)

von der KIT-Fakultät für Physik
des Karlsruher Instituts für Technologie (KIT)

angenommene

Dissertation

von

M. Sc. Genrich Zeller
aus Peterfeld

Referentin: Prof. Dr. Kathrin Valerius
Insitut für Astroteilchenphysik
Karlsruher Institut für Technologie

Korreferent: Prof. Dr. Helmut Telle
Departmento de Química Física Aplicada
Universidad Autónoma de Madrid

Tag der mündlichen Prüfung: 09.02.2024

ii

Declaration of Authorship

Herewith I affirm that I wrote the current thesis on my own and without the usage of any other sources or tools than the cited ones and that this thesis has not been handed neither in this nor in equal form at any other official commission.

Erklärung der Selbstständigkeit

Hiermit versichere ich, die vorliegende Arbeit selbstständig angefertigt zu haben und keine Hilfsmittel jenseits der kenntlich gemachten verwendet zu haben. Weiterhin habe ich weder diese noch eine äquivalente Version dieser Arbeit bei einer anderen Prüfungskommission vorgelegt.

Karlsruhe, den 8. Januar 2024

Genrich Zeller

Contents

List of Figures

List of Tables

1. Introduction

Neutrinos are elementary particles in the STANDARD MODEL OF PARTICLE PHYSICS (SM). The SM describes three flavors of neutrinos: electron, muon, and tau, corresponding to the three generations of charged leptons. In contrast, the neutrinos are neutral and thus only interact with other particles via the weak force, and are thus difficult to detect. In the SM neutrinos are massless. However, the discovery of neutrino oscillations demonstrated that neutrinos must have a non-zero rest mass. There are several experiments attempting to measure the neutrino mass, often using different and complementary approaches.

One of these approaches is the study of the kinematics of β-decay. In many past and current neutrino mass experiments, the hydrogen isotope tritium, ^{3}H, in this work denoted as T, is used as the β-emitter. Previous neutrino mass experiments with tritium have returned upper limits on the neutrino mass, *e.g.* the Troitsk [Ase11] and Mainz [Kra05] experiments. Since the first such experiments in 1947 [Kon47], substantial improvements have been made with regard to tritium sources and electrostatic spectrometers of the MAGNETIC ADIABATIC COLLIMATION WITH ELECTROSTATIC (MAC-E) type. The most recent of this type of experiment is the KARLSRUHE TRITIUM NEUTRINO (KATRIN) experiment.

The KATRIN collaboration recently published the results from their second neutrino mass measurement campaign, which returned the current best limit for the neutrino mass of [Ake22b]

$$m_\nu^2 = (0.26 \pm 0.34)\,\mathrm{eV}^2 \Rightarrow m_\nu < 0.9\,\mathrm{eV}\ (90\,\%\ \mathrm{C.L.}). \tag{1.1}$$

Combined with the result from the first neutrino mass measurement campaign in 2019 [Ake19], this yields

$$m_\nu < 0.8\,\mathrm{eV}\ (90\,\%\ \mathrm{C.L.}) \tag{1.2}$$

which is the first sub-eV sensitivity reached in a direct, kinematic neutrino mass measurement.

In order for the KATRIN experiment to reach its ultimate goal, all sources of systematic uncertainties need to be understood and quantified. One of these contributions stems from the source gas compositions in the WINDOWLESS GASEOUS TRITIUM SOURCE (WGTS). An ideal source would contain only pure tritium, T_2 [KAT05]. While in general T_2 is the majority molecular component (mole fraction $c_{T_2} > 0.9$), the other tritiated hydrogen isotopologues, HT and DT, are encountered as well (with $c_{HT} + c_{DT} < 0.1$) [Ake20b]. Note that minimal traces of the non-tritiated hydrogen isotopologues (D_2, HD, H_2) are also observed.

For the purpose of monitoring the tritium gas composition, a Laser Raman (LARA) system is employed at the KATRIN experiment. The suitability of the KATRIN LARA system for the accurate gas composition measurement has been demonstrated in several studies for over more than a decade [Stu10a; Sch14; Fis14; Zel17; Nie21a]. However, the final demonstration that the LARA system can achieve the metrological performance (trueness, precision, and accuracy) continuously and reliably over KATRIN's full operation time of several years, can only truly be demonstrated with the passing of operation time. One particular aspect of the LARA system, with respect to which the stability of several years was yet to be demonstrated, is the intensity calibration using a Standard Reference Material (SRM) supplied by National Institute of Standards and Technology (NIST).

The use of molecular tritium, T_2, is perceived as one of the limiting factors for the sensitivity of measurements of the neutrino mass via the β-decay of tritium, due to the exitation of rotational and vibrational states of the daughter molecule after the β-decay in a molecule. The distribution of these energy states is the so-called Final States Distribution (FSD), and can be calculated *a priori* [Sae00]. The ground-state manifold has a standard deviation of about $\sigma_{FSD} \approx 0.4 \, eV$ [Sae00; Bod15] and limits the neutrino mass sensitivity. Thus, it is envisaged to use atomic tritium sources in future experiments, and for this the use of solid-state tritiated targets rather than gaseous sources has been proposed.

In this context, graphene is well known for its hydrogen storage capabilities [Whi18], and was suggested as a possible solid-state (quasi) atomic tritium source / target [Bet13; Bet19a] that might overcome the limitations on neutrino mass measurement posed by the use of molecular tritium. From both aspects, theory and experiment, the hydrogenation of graphene is reasonably well understood. However, until this work, the tritiation of graphene was only investigated in a few theoretical studies [App22; Wu22], with no experimental measurements at all.

In order to avoid designing and building complex experimental systems to demonstrate that indeed graphene can be tritiated and results in stable samples, for this proof-of-principle work it was proposed to exploit self-radiolysis of tritium to provide the atomic tritium for the loading of graphene. However, since the properties of the self-radiolysis 'cold' plasma cannot be controlled directly, it is crucial to have available at least one method of *in-situ* monitoring of changes to the graphene sample during and after the exposure to tritium. Raman spectroscopic monitoring and spatially-resolved chemometric target mapping was identified as one of the key methodologies.

Raman spectroscopy and imaging have been demonstrated to be powerful analytical tools for the study and characterization of graphene [Fer13]. Establishing a Raman system that is suitable for the characterization of tritium-graphene interactions, and that is also flexible enough to allow for integration into a glove box system, is an important step towards the understanding of tritiated graphene, which could be the starting point for future neutrino mass measurement at KATRIN.

In summary, the work described in this thesis advances the use and understanding of Raman spectroscopy for the KATRIN experiment by (i) demonstrating the successful long-term operation of the tritium gas composition monitoring of the molecular KATRIN source; and (ii) establishing a new Raman system, a confocal imaging Raman microscope, to enable the studies of radioactive / tritiated solid-state tritium sources / targets, initially using graphene as the carrier material.

Specifically, the following questions have been addressed in this work.

1. The long-term performance of the LARA system needed to be demonstrated. In particular, it needed to be shown that the trueness requirement can be achieved over

extended periods of time, up to years, even when the certification of the intensity calibration standard is expired.

2. In the scope of this work, a CONFOCAL RAMAN MICROSCOPE (CRM) was set up at TRITIUM LABORATORY KARLSRUHE (TLK) in collaboration with UNIVERSIDAD AUTÓNOMA DE MADRID (UAM). This CRM is designed to allow the measurement of radioactively contaminated samples without the contamination of the entire system, and expensive components like the spectrometer. Since the CRM is constructed from 'off-the-shelf' components, and the assembly and alignment is performed manually, typical microscope parameters are not known *a priori*. Although several of these parameters can be partially calculated, all parameters need to be determined and demonstrated experimentally as well.

3. It needed to be shown that the CRM is suitable for the characterization of tritium-exposed graphene samples. For this purpose, graphene was tritiated for the first time, allowing for preliminary qualitative insights into tritium-graphene interactions.

This thesis is structured as follows. In the first part of Chapter 2, a brief introduction to neutrino physics is given; covering the discovery of the neutrino, the mechanism of neutrino oscillations, and a brief theoretical description of the postulated massive neutrinos. In the second part of Chapter 2, the KATRIN experiment is introduced, briefly covering the overall experimental setup. The main focus, however, is the description of the source composition monitoring, and the limitations arising from the use of molecular tritium.

In Chapter 3, the theory of Raman spectroscopy is introduced in both gaseous and solid samples, using the hydrogen isotopologues and graphene as examples, respectively.

In Chapter 4 the experimental setup, data analysis routines, and software of the KATRIN LARA and the CRM are described.

The results of and methods for the long-term operation of the LARA system are presented in Chapter 5.

In Chapter 6 the commissioning, characterization studies and measurements of the CRM are described.

In Chapter 7 the first tritium exposure of graphene is outlined, and results from the analysis of tritiated graphene samples using the CRM are presented. These provide first qualitative insights into the nature of the tritium-graphene interactions.

Finally, Chapter 8 provides a brief summary of the work and gives a concise outlook on future extensions of research efforts.

2. Measurement of the neutrino mass

In Section 2.1, the theory of neutrinos, the discovery of neutrino masses, and the fundamentals of tritium β-spectroscopy are outlined. Following, in Section 2.2 a brief introduction to the KARLSRUHE TRITIUM NEUTRINO (KATRIN) experiment is given. In the last two sections, namely Sections 2.3 and 2.4, the key elements that are crucial for the motivation of this work are highlighted, for neutrino physics in general and the KATRIN experiment in particular. First, the importance of source composition monitoring in the KATRIN experiment is summarized in Section 2.3. Second, in Section 2.4, an introduction to neutrino mass experiments beyond KATRIN is presented. This includes in Section 2.4.1 a discussion of the limitations that molecular tritium imposes on the neutrino mass measurement, and in Section 2.4.2 an outline of proposed (quasi) atomic tritium sources.

2.1. Neutrino physics

Neutrinos are elementary particles in the STANDARD MODEL OF PARTICLE PHYSICS (SM). The SM describes three flavors of neutrinos: electron, muon, and tau; corresponding to the three generations of electrically charged leptons. In contrast, the neutrinos are electrically neutral and thus only interact with other particles via the weak force, see Figure 2.1. Neutrinos are difficult to detect, and a brief history of their discovery is given in Section 2.1.1. Then, in Section 2.1.2, an overview of neutrino oscillation experiments and the theoretical mechanisms of neutrino mass generation is given. Finally, in Section 2.1.3, neutrino mass experiments are presented with the specific focus on experiments using tritium β-electron spectroscopy in Section 2.1.4. In general, and unless stated otherwise, the descriptions in this section follow Refs. [Pov15; Zub20].

2.1.1. History of the neutrino discovery

It was originally hypothesized that the β-decay is a two-body decay, in which the decaying neutron in the nucleus emits a proton p and an electron e^-. The theoretical expectation was that the energy of the electron would be a discrete energy spectrum. However, a continuous electron energy spectrum was observed experimentally. Confronted with this finding, W. Pauli postulated the existence of the neutrino ν in his now famous letter in 1930 [Pau30; Pau85]. With his postulation, the two-body decay turned into a three-body decay:

$$M(A, Z) \to D(A, Z+1) + e^- + \bar{\nu}_e, \tag{2.1}$$

where $M(A, Z)$ is the mother nucleus and $D(A, Z + 1)$ is the daughter nucleus with the atomic number Z and mass number A. In 1934, a theory for the shape of the β-electron spectrum was derived by E. Fermi [Fer34]. Already at that time, the estimate was that the mass of the then undiscovered neutrino must be considerably smaller than that of the electron, or even equal to zero. For more than 25 years after its postulation, the small interaction cross-section of the neutrino prevented its discovery. Eventually, the neutrino was directly detected in a nuclear fission reactor, which was at that time the strongest terrestrial source of (anti-)neutrinos available. C. L. Reines, F. Cowan and co-workers exploited the inverse β-decay reaction

$$\bar{\nu}_e + p \rightarrow e^+ + n \tag{2.2}$$

to detect the neutrino [Cow56]. In 1962, the AGS neutrino experiment discovered the muon neutrino [Dan62]. These neutrinos were produced by decaying pions in a proton accelerator at Brookhaven National Laboratory. Finally, the tau neutrino was discovered by the DONUT collaboration in 2000 [DON01].

Standard Model of Elementary Particles
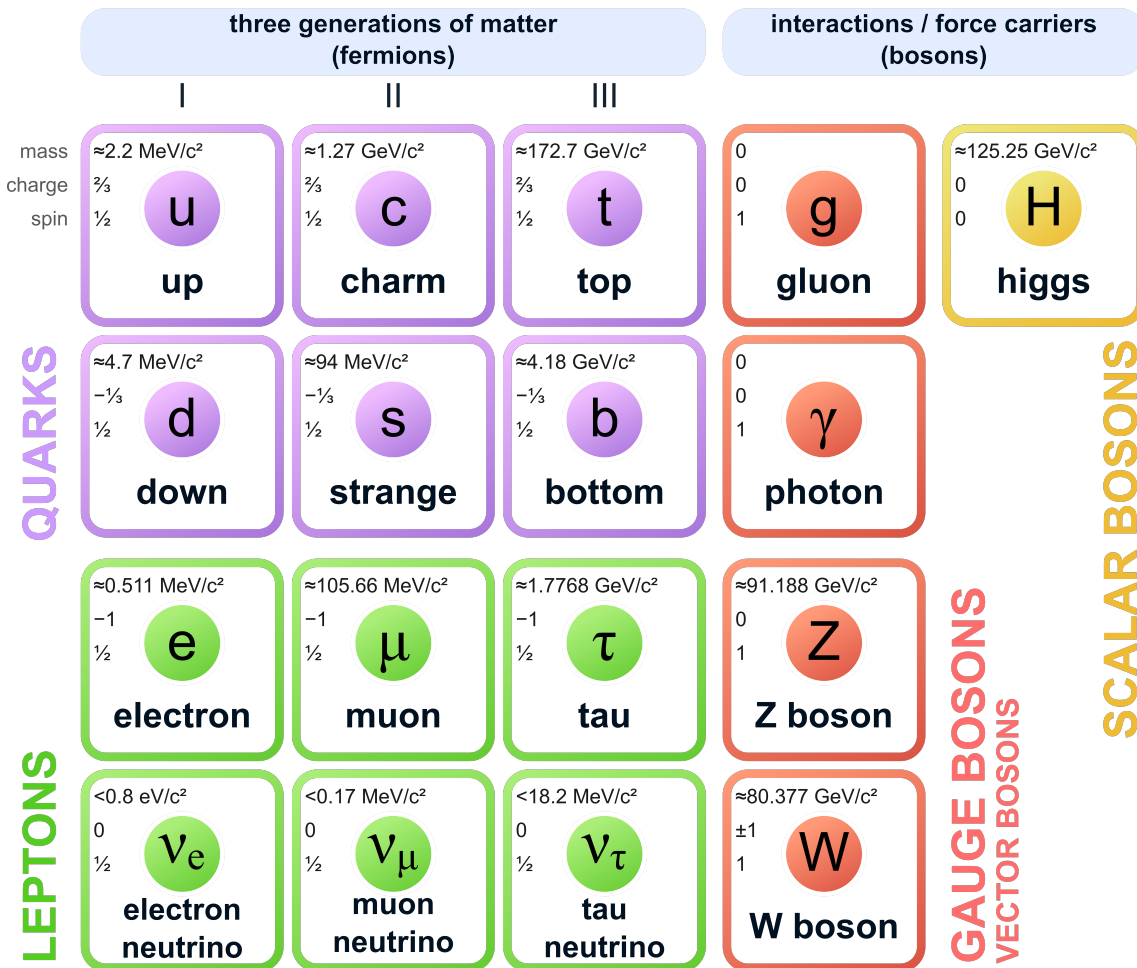
Figure 2.1.: Elementary particles and their properties in the STANDARD MODEL OF PARTICLE PHYSICS (SM). *Left:* The fermions are grouped according to the three generations of matter: quarks (purple) on the top and leptons (green) at the bottom. *Right:* The vector (or gauge) bosons (red) mediating the strong (g), electromagnetic (γ) and the weak (Z^0, $W^\pm$) force. The scalar Higgs boson (yellow) corresponds to the Higgs field. All the properties are taken from the latest version of the *Review of Particle Physics* [PDG22].

During precision measurements at the e^--e^+-collider LEP, no fourth neutrino flavor state with $m(\nu) \leq 104\,\text{GeV}$ was found; the measured width of the Z_0-resonance was found to be consistent with the predicted lifetime, assuming only $N_\nu = 3$ generations of light active neutrinos [ALE06].

According to V-A theory [Fey58; Sud58], parity is violated maximally. Therefore, only left-handed neutrinos and right-handed antineutrinos participate in the weak interaction, as was experimentally confirmed in the Goldhaber experiment [Gol58]. But in order to generate neutrino masses by the same mechanism as for all other particles in the SM, i.e., via Yukawa couplings, right-handed neutrinos and left-handed antineutrinos would be required as well. In the SM neutrinos are therefore massless. However, the discovery of neutrino oscillations demonstrated that neutrinos must have a non-zero rest mass (this paradigm is summarized concisely, e.g., in [Kin14]).

2.1.2. Neutrino oscillation and mass generation

The leptons can be written in three generation-doublets (see Figure 2.1):

$$\begin{pmatrix} \nu_e \\ e^- \end{pmatrix} \quad \begin{pmatrix} \nu_\mu \\ \mu^- \end{pmatrix} \quad \begin{pmatrix} \nu_\tau \\ \tau^- \end{pmatrix}. \tag{2.3}$$

In the description of neutrino oscillations, the flavor states $|\nu_e\rangle, |\nu_\mu\rangle, |\nu_\tau\rangle$ are not necessarily identical to the mass states $|\nu_1\rangle, |\nu_2\rangle, |\nu_3\rangle$. The flavor states can be written as an orthogonal linear combination of the mass states, namely:

$$\begin{pmatrix} |\nu_e\rangle \\ |\nu_\mu\rangle \\ |\nu_\tau\rangle \end{pmatrix} = \underbrace{\begin{pmatrix} U_{e1} U_{e2} U_{e3} \\ U_{\mu1} U_{\mu2} U_{\mu3} \\ U_{\tau1} U_{\tau2} U_{\tau3} \end{pmatrix}}_{U} \cdot \begin{pmatrix} |\nu_1\rangle \\ |\nu_2\rangle \\ |\nu_3\rangle \end{pmatrix}. \tag{2.4}$$

The possibility of neutrino mixing was first considered by Pontecorvo [Pon57] for neutrino-antineutrino oscillations and later by Maki, Nakagawa and Sakata [Mak62] for flavor mixing of two neutrinos. Therefore, the matrix U is commonly known as the PMNS matrix. Often, this PMNS matrix is parameterized as (see *e.g.* Ref. [PDG22])

$$U = \begin{pmatrix} 1 & 0 & 0 \\ 0 & \cos\theta_{23} & \sin\theta_{23} \\ 0 & -\sin\theta_{23} & \cos\theta_{23} \end{pmatrix} \begin{pmatrix} \cos\theta_{13} & 0 & \sin\theta_{13}e^{-i\delta} \\ 0 & 1 & 0 \\ -\sin\theta_{13}e^{-i\delta} & 0 & \cos\theta_{13} \end{pmatrix} \begin{pmatrix} \cos\theta_{12} & \sin\theta_{12} & 0 \\ -\sin\theta_{12} & \cos\theta_{12} & 0 \\ 0 & 0 & 1 \end{pmatrix} \tag{2.5}$$

with the mixing angles θ_{ij} and the CP-violating phase δ. The current best experimental values are summarized in Table 2.1. If neutrinos are Majorana particles, the PMNS matrix needs to be extended by

$$U_{\text{Majorana}} = \begin{pmatrix} 1 & 0 & 0 \\ 0 & e^{i\alpha_1/2} & 0 \\ 0 & 0 & e^{i\alpha_2/2} \end{pmatrix} \tag{2.6}$$

with the Majorana phases $\alpha_{1,2}$. In the following, the concept of neutrino oscillations is discussed in more detail for the simplified case of two generations of neutrinos, $|\nu_e\rangle, |\nu_\mu\rangle$. For this particular case, the system is described by one mass difference (*e.g.* $\Delta m_{12}^2 = m_2^2 - m_1^2$) and one mixing angle θ. The unitary transformation is then given by

$$\begin{pmatrix} |\nu_e\rangle \\ |\nu_\mu\rangle \end{pmatrix} = \begin{pmatrix} \cos\theta & \sin\theta \\ -\sin\theta & \cos\theta \end{pmatrix} \cdot \begin{pmatrix} |\nu_1\rangle \\ |\nu_2\rangle \end{pmatrix}. \tag{2.7}$$

Table 2.1.: Best fit values of the neutrino oscillation parameters for the case of three neutrinos. Values are derived by the Particle Data Group (PDG) from a combination of the results of different experiments [PDG22].

Parameter	Normal hierarchy	Inverted hierarchy
Δm_{12}^2	$(7.53 \pm 0.18) \times 10^{-5}\,\mathrm{eV}^2$	-
$\sin^2 \theta_{12}$	0.307 ± 0.013	-
Δm_{32}^2	$(2.437 \pm 0.033) \times 10^{-3}\,\mathrm{eV}^2$	$(-2.519 \pm 0.033) \times 10^{-3}\,\mathrm{eV}^2$
$\sin^2 \theta_{23}$	$0.547^{+0.018}_{-0.024}$	$0.534^{+0.021}_{-0.024}$
$\sin^2 \theta_{13}$	$(2.20 \pm 0.07) \times 10^{-2}$	-
δ, CP-violating phase	$1.23 \pm 0.21\pi\mathrm{rad}\ (\mathrm{S} = 1.3)$	-
$\langle \Delta m_{21}^2 - \Delta \bar{m}_{21}^2 \rangle$	$< 1.1 \times 10^{-4}\,\mathrm{eV}^2$	-
$\langle \Delta m_{32}^2 - \Delta \bar{m}_{32}^2$	$(-0.12 \pm 0.25) \times 10^{-3}\,\mathrm{eV}^2$	-

Considering the time evolution of the mass states after a time t, the two-flavor transition probability is given by

$$P(\nu_e \to \nu_\mu) = P(\nu_\mu \to \nu_e) = P(\bar{\nu}_e \to \bar{\nu}_\mu) = P(\bar{\nu}_\mu \to \bar{\nu}_e)$$

$$= \underbrace{\sin^2 2\theta}_{\text{amplitude}} \cdot \underbrace{\sin^2 \left(\frac{\Delta m_{12}^2}{4} \cdot \frac{L}{E} \right)}_{\text{frequency}} = 1 - P(\nu_e \to \nu_e). \tag{2.8}$$

From Eq. 2.8 it follows that for oscillation to occur both the mixing angle θ and the mass difference Δm_{12}^2 are non-vanishing. From the term determining the oscillation frequency, the characteristic oscillation length L_0 can be derived

$$L_0 = 4\pi\hbar c \frac{E}{\Delta m^2} = 2.48 \frac{E/\mathrm{MeV}}{\Delta m^2 / \mathrm{eV}^2} \mathrm{m}. \tag{2.9}$$

Solar neutrino oscillation

In the core of the sun, nuclear fusion processes generate primarily electron neutrinos, which are produced through the fusion of hydrogen nuclei into helium. Based on our understanding of these fusion reactions, and the Standard Solar Model, precise predictions were made for the expected flux of electron neutrinos that should reach earth. Experimental efforts to detect solar neutrinos, such as the Homestake experiment in the 1960s [Dav64], consistently revealed a deficit in the number of observed electron neutrinos compared to theoretical expectations. The discrepancy was approximately a factor of three, known as the 'solar neutrino deficit'.

The breakthrough for the understanding of the deficit came with the discovery of neutrino oscillations. Neutrino flavor transformation, as demonstrated by the Super Kamiokande [Sup98] and the Sudbury Neutrino Observatory (SNO) [SNO01] experiments, revealed that neutrinos are not necessarily produced and detected in the same flavor state. Instead, they undergo flavor-changing oscillations as they propagate through space. This means that the ν_e produced in the sun can transform into other neutrino flavors (ν_μ or ν_τ) before reaching earth. The observation of neutrino oscillations confirmed that the total number of solar neutrinos ν_e emitted by the sun matched theoretical predictions, thus solving the solar neutrino problem. Note that the detection methods in the early solar neutrino experiments were only sensitive to ν_e, while later experiments were sensitive to the three neutrino flavors of the SM.

In addition to solving the solar neutrino discrepancy, this discovery had further implications for neutrino physics, including the confirmation that neutrinos have mass, revolutionizing the understanding of particle physics beyond the SM.

Theoretical mechanisms for the generation of neutrino masses

In the SM charged fermions obtain their mass via the spontaneous symmetry breaking and the Higgs mechanism [Hig64; Kib67]. The doublet of scalar Higgs fields results in a non-zero vacuum expectation value, which couples to a doublet of left-handed and a singlet of right-handed fermions; this constitutes the so-called Yukawa coupling. For example, for electrons, the corresponding Lagrangian can be written as

$$\mathcal{L}_{\text{Yukawa}} = -c_e \left[\bar{e}_{\text{R}} \phi_0^\dagger \begin{pmatrix} \nu_{e\text{L}} \\ e_{\text{L}} \end{pmatrix} + h.c. \right] \tag{2.10}$$

$$= c_e v \frac{1}{\sqrt{2}} (\bar{e}_{\text{R}} e_{\text{L}} + \bar{e}_{\text{L}} e_{\text{R}}) \tag{2.11}$$

$$= -c_e \frac{v}{\sqrt{2}} \bar{e}e. \tag{2.12}$$

Here c_e is a coupling constant (note that this cannot be predicted by theory and hence has to be determined experimentally), v is the vacuum expectation value of the Higgs field, e is the spinor of the electron, and the Hermitian conjugate is abbreviated by $h.c.$. Evaluation of Eq. 2.12 results in an electron with the mass $m_e = c_e \frac{v}{\sqrt{2}}$.

More generalized, Dirac particles[1] gain their masses from the Lagrangian

$$\mathcal{L} = \bar{\psi} \left(i\gamma_\mu \frac{\partial}{\partial x_\mu} - m_{\text{D}} \right) \tag{2.13}$$

where ψ denotes a four-component spinor, m_{D} is the Dirac mass, and the γ-matrices are defined as:

$$\gamma_0 = \begin{pmatrix} \mathbb{1} & 0 \\ 0 & -\mathbb{1} \end{pmatrix} \quad \gamma_i = \begin{pmatrix} 0 & \tilde{\sigma}_i \\ -\tilde{\sigma}_i & 0 \end{pmatrix} \text{ for } i = 1, ..., 3 \tag{2.14}$$

where $\tilde{\sigma}_i$ are the Pauli matrices [Pau27]. The first term in Eq. 2.13 corresponds to the kinetic energy of the particle, and the second term corresponds to the Dirac mass. The Dirac mass term can be written as

$$\mathcal{L} = m_{\text{D}} \bar{\psi} \psi \tag{2.15}$$

where $\bar{\psi}\psi$ is Hermitian and Lorentz invariant. Given that $\mathcal{L}$ is Hermitian as well, the Dirac mass term can be written in its chiral components (L and R)

$$\mathcal{L} = m_{\text{D}} (\bar{\psi}_{\text{L}} \psi_{\text{R}} + \bar{\psi}_{\text{R}} \psi_{\text{L}}) \quad \text{where } \bar{\psi}_{\text{R}} \psi_{\text{L}} = (\bar{\psi}_{\text{L}} \psi_{\text{R}})^\dagger. \tag{2.16}$$

Here ψ_{L} and ψ_{R} are the Weyl spinors. This is a more general description of Eq. 2.12. Since this mechanism requires both a left- and a right-handed Dirac neutrino to produce the mass term; and only left-handed neutrinos exist, they remain massless in the SM. Any theory that includes a non-vanishing neutrino mass is classified as 'physics beyond the SM'. By introducing a right-handed neutrino singlet state, the SM can be extended. In this way,

---

[1]A particle behaving according to the Dirac theory. This theory describes the general behavior of electrons and muons, except for radiative corrections; it was envisaged as describing the remaining central core of a hadron of spin $\frac{1}{2}\hbar$, after the effects of nuclear forces are removed.

a Yukawa coupling is also possible for neutrinos, and a so-called 'Dirac mass term' is added to the Lagrangian. For neutrinos, Eq. 2.10 can then be written as

$$\mathcal{L}_{\text{Yukawa}} = -c_\nu \left[\bar{\nu}_\text{R} \phi^\dagger \begin{pmatrix} \nu_{e\text{L}} \\ e_\text{L} \end{pmatrix} + h.c. \right] \tag{2.17}$$

$$= -c_\nu v \bar{\nu} \nu. \tag{2.18}$$

Here c_ν is the Yukawa coupling for the neutrino mass. However, with the current upper limits for the neutrino masses, this would require a coupling constant about 1×10^{-12} smaller compared to all other SM particles.

Seesaw mechanism

There are alternative theories for the mechanism to generate neutrinos with mass. One prominent theory assumes that neutrinos are Majorana particles: the neutrinos and anti-neutrinos are the same particle, but the discrimination in handedness remains. The Lagrangian can then be written as

$$\mathcal{L} = -\frac{1}{2} \left[\begin{pmatrix} \bar{\nu}_\text{L} & \bar{N}_\text{L}^c \end{pmatrix} \begin{pmatrix} m_\text{L} & m_\text{D} \\ m_\text{D} & m_\text{R} \end{pmatrix} \begin{pmatrix} \bar{\nu}_\text{R}^c \\ \bar{N}_\text{R} \end{pmatrix} + h.c. \right] \tag{2.19}$$

Here N is a heavy, sterile neutrino and c denotes the charge conjugate state. In addition to the Dirac mass m_D, there are two Majorana masses m_L and m_R. Three specific cases can be distinguished:

- When $m_\text{L} = m_\text{R} = 0$, the resulting mass is the Dirac mass term m_D.

- When $m_\text{L} = 0$ and $m_\text{R} \gg m_\text{D}$, two distinct mass eigenstates can be found, namely:

$$m_1 = \frac{m_\text{D}^2}{m_\text{R}} \tag{2.20}$$

$$m_2 = m_\text{R} \left(1 + \frac{m_\text{D}^2}{m_\text{R}} \right) \approx m_\text{R} \tag{2.21}$$

  This is known as the type I seesaw mechanism. Here m_1 could be in the sub-eV-range, while the mass m_2 of an additional (sterile) neutrino could be in the range of MeV to GeV.

- When $m_\text{R} \gg m_\text{D}$, $m_\text{L} \neq 0$, and $m_\text{L} \ll m_\text{R}$, there is a second contribution to the neutrino mass due to the coupling to the Higgs field. This is called the type II seesaw mechanism and can lead to approximately equal neutrino masses.

Numerous different mass scenarios can be predicted by the different theoretical models. From the experimental point of view, neutrino oscillation experiments can provide the required mass differences and, eventually, the ordering. However, they cannot provide the absolute scale, which is of great interest for discriminating between the different theoretical models. The choice of the mass scenario realized in nature and a hint to the appropriate theory behind it can therefore only be obtained from absolute neutrino mass measurements. An overview of the different scenarios, as a function of the lightest mass eigenstates, is shown in Figure 2.2.
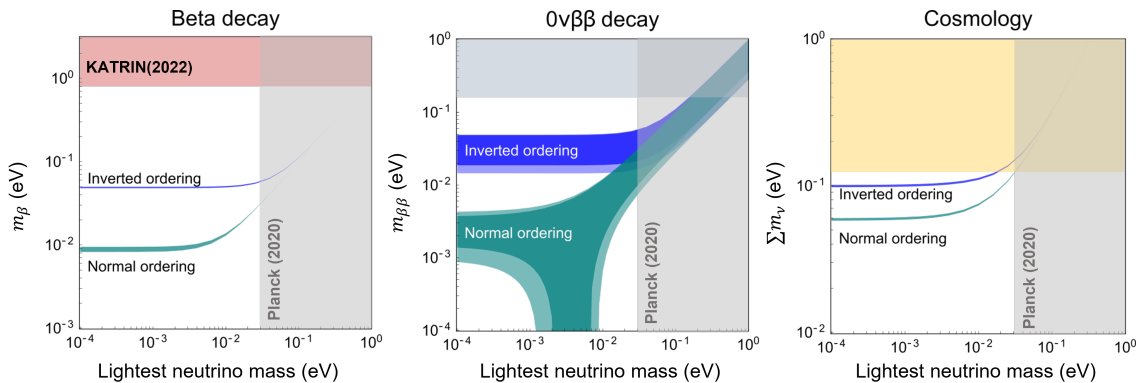
Figure 2.2.: Experimentally observable combinations of neutrino mass in β-decay, neutrino-less double beta decay (0νββ), and cosmology as a function of the lightest neutrino mass. The current β-decay limit is taken from [Ake22b], the Planck result from [Agh20], and the (0νββ)-limit from [Kam23]. Image adapted from [INP21].

2.1.3. Measurements of the neutrino mass

There are several experiments attempting to measure the neutrino mass, often using different and complementary approaches. In general, these are classified in two categories, namely direct and indirect. Direct methods make use of the relativistic energy-momentum relation and use the kinematics of a neutrino process; these are sensitive to an effective neutrino mass squared, m^2. Indirect methods, in addition to experimental data, rely on modeling, simulations and theoretical calculations. These are, in general, associated with additional systematic and model-dependent uncertainties. In the following, key aspects of the different measurement methodologies are collected.

Cosmological and astrophysical observations

Large-scale structures observed in the current state of the universe have been influenced by neutrinos since the early stages of the universe. Specifically, 'smearing' of small-scale fluctuations is sensitive to the sum of the neutrino masses. There are two main methods employed here: (i) studying the structure of today's universe by large galaxy surveys; and (ii) analysis of the cosmic microwave background (CMB). However, it has to be stressed that the associated results are model-dependent and therefore often not trivial to derive, combine, or compare [PDG22; Val22]. The observable in these experiments is the total sum of all neutrino masses, m_{tot}. In 2014, a very detailed map of the CMB was published by the Planck Collaboration [Pla14], which suggested that

$$m_{tot} = \sum_{i=1}^{3} m_i < 0.23\,\text{eV (95\% C.L.)}. \tag{2.22}$$

Data from more recent studies, including SDSS's Baryon Oscillation Spectroscopic Survey (BOSS) data and dark energy surveys (DES), further constrained the sum of the neutrino masses to

$$m_{tot} < 0.14\,\text{eV (95\% C.L.) [Tan22] and} \quad m_{tot} < 0.13\,\text{eV (95\% C.L.) [DES22].} \tag{2.23}$$

However, as pointed out in complementary analyses, described in *e.g.* Refs. [Sgi21; Val22], the data leading to the values in Eq. 2.23 could also be compatible with neutrino masses as large as

$$m_{tot} \sim 0.4 - 0.6\,\text{eV (95\% C.L.).} \tag{2.24}$$

Neutrinoless double β-decay

Neutrinoless double β-decay (0νββ) is a specific weak interaction process that would signal violation of total lepton number conversation. This violation can be resolved if neutrinos are Majorana particles, thus their own anti-particle [Giu12]. If this is the case, two neutrons in the same nucleus can decay simultaneously without the emission of neutrinos. This would correspond to the following nuclear reaction:

$$N(A, Z) \rightarrow N'(A, Z + 2) + 2e^-. \tag{2.25}$$

Following Ref. [Giu12], the half-life $T_{1/2}^{0\nu\beta\beta}$ of the 0νββ-decay can be written as:

$$(T_{1/2}^{0\nu\beta\beta})^{-1} = G_{01} |M^{0\nu\beta\beta}|^2 \left(\frac{\langle m_\nu \rangle}{m_e} \right)^2, \tag{2.26}$$

where $\langle m_\nu \rangle = |\sum_i U_i^2 m_i|$ is the effective Majorana neutrino mass, where U is given by Eqs. 2.5 and 2.6, G_{01} is a phase-space factor, $M^{0\nu\beta\beta}$ is the nuclear matrix element and m_e is the electron mass.

One major experimental challenge is the background reduction due to the long half life and hence very low expected decay rate of the 0νββ-decay at about $T_{1/2}^{0\nu\beta\beta} > 1.4 \times 10^{22} - 2.3 \times 10^{26}$ yr [Bil15]. In addition, the calculation of the nuclear matrix element $M^{0\nu\beta\beta}$ leads to a significant uncertainty in the determination of the effective Majorana neutrino mass. Therefore, the spread in experimental results is still considerable. Most recently, the CUORE (Cryogenic Underground Observatory for Rare Events) collaboration reported no evidence of the 0νββ and derived - using Bayesian analysis [CUO22] - that

$$T_{1/2}^{0\nu\beta\beta} > 2.2 \times 10^{25} \text{ yr} \quad \text{and} \quad \langle m_\nu \rangle < 90 - 305 \text{ meV at } 90\% \text{ C.I..} \tag{2.27}$$

The effective Majorana neutrino mass $\langle m_\nu \rangle$ is in good agreement with the latest results from the KamLAND-Zen (Kamioka Liquid Scintillator Antineutrino Detector-Zen) experiment [Kam23]:

$$T_{1/2}^{0\nu\beta\beta} > 2.3 \times 10^{26} \text{ yr} \quad \text{and} \quad \langle m_\nu \rangle < 36 - 156 \text{ meV at } 95\% \text{ C.L..} \tag{2.28}$$

Note that the values for $T_{1/2}^{0\nu\beta\beta}$ cannot be directly compared, due to the use of different isotopes.

Supernova neutrinos

Core-collapse supernovae (type II supernovae) are strong[2], point-like sources of neutrinos. These neutrinos can be used for time-of-flight measurements. A neutrino with velocity v_ν and total energy E_ν, has a flight time, t_F, of

$$t_F = t - t_0 = \frac{L}{v} = \frac{L}{c} \frac{E_\nu}{p_\nu c} = \frac{L}{c} \frac{E_\nu}{\sqrt{E_\nu^2 - m_\nu^2 c^4}} \approx \frac{L}{c} \left(1 + \frac{m_\nu^2 c^4}{2E^2} \right) \tag{2.29}$$

from the source (emission time t_0) to the detector (arrival time t), at a distance L. Here, it is assumed that $m_\nu c^2 \ll E_\nu$. For two neutrinos with E_1, t_1 and E_2, t_2 ($E_2 < E_1$) the time difference upon detection on earth is:

$$\Delta t = t_2 - t_1 = \Delta t_0 + \frac{L m_\nu^2}{2c} \left(\frac{1}{E_2^2} - \frac{1}{E_1^2} \right). \tag{2.30}$$

---

[2]For example, SN1987A emitted 10^{58} neutrinos, leading to a neutrino flux of over 10×10^{10} neutrinos/cm^2 at the earth. [Don09]

However, the difference of emission times Δt_0 has to be determined based on theoretical models of the time evolution of the supernova neutrino burst. All other parameters in Eq. 2.30 can be determined experimentally. Depending on the theoretical model and the analysis method, detailed analysis of the supernova 1987A data led to upper limits on the neutrino mass of about 5.7 eV [Lor02].

Kinematics of weak decays

Another prominent direct method for the determination of the neutrino mass, is the investigation of the kinematics of weak decays. Of particular interest is the β-decay. In the β-decay, one encounters three possible decay modes:

$$N(Z, A) \rightarrow D(Z + 1, A) + e^- + \bar{\nu}_e \quad (\beta^-\text{-decay}), \tag{2.31}$$

$$N(Z, A) \rightarrow D(Z - 1, A) + e^+ + \nu_e \quad (\beta^+\text{-decay}), \text{ and} \tag{2.32}$$

$$e^- + N(Z, A) \rightarrow D(Z - 1, A) + \nu_e \qquad (\text{electron capture}). \tag{2.33}$$

In the β-decay the ordering number Z of the nucleus changes by one unit, while the atomic mass A remains the same. The observable in β-decay experiments it the average electron neutrino mass square, given by:

$$m^2(\nu_e) = \sum_i |U_i|^2 m_i^2 \tag{2.34}$$

The decay energy, the so-called Q-value, is given by the mass difference between the mother and daughter atoms:

$$Q = (m[N(Z, A)] - m[N(Z + 1, A)]) \, c^2 \tag{2.35}$$

The endpoint energy E_0 of the decay spectrum is given by

$$E_0 = Q - E_{\text{recoil}}, \tag{2.36}$$

where E_{recoil} is the recoil of the daughter nucleus [Ott08]. Eq. 2.36 is only valid for the case of a vanishing neutrino mass and no additional excitations of the daughter nucleus. As will be seen in Section 2.2 these quantities will be relevant in the realization of an experiment, and for the derivation of the neutrino mass: the influence of the neutrino mass on the shape of the β-spectrum becomes significant close to the kinematic endpoint. Therefore, to determine the neutrino mass from the shape of β-spectrum, this small change in spectral shape has to be resolved in any given experiment.

2.1.4. Tritium β-electron spectroscopy

In many past and current neutrino mass experiments, the hydrogen isotope tritium ${}^3\text{H}$, in this work denoted as T, is used as an β-emitter. There are various reasons motivating the use of tritium [Ott08; Bea08; Dre13; Zub20]:

- Tritium has a relatively short half-life of only about 12.3 yr, providing high decay rates per unit amount of radioactive material. At the same time, any tritium source is not depleted all too rapidly.

- The endpoint is one of the smallest for known β-emitters, with about 18.6 keV.

- Tritium has a simple electronic shell with an atomic number of $Z = 1$. Therefore, Coulomb interactions between the emitted electrons and the nucleus are minimal, which allows for making detailed theoretical calculation of the process.

- Typically, tritium presents itself in the form of molecules, T_2. The simple structure of the molecule allows for the quantitative calculation of the excited final states of the daughter molecule $(^3\text{HeT})^+$. However, this molecular form, T_2, is also limiting the sensitivity of tritium neutrino mass experiments. This will be explained in more detail in Section 2.4.

Previous neutrino mass experiments with tritium have returned upper limits on the neutrino mass, *e.g.* the Troitsk [Ase11] and Mainz [Kra05] experiments. Since the first such experiments in 1947 [Kon47], substantial improvements have been made with regard to tritium sources and electrostatic spectrometers of the MAGNETIC ADIABATIC COLLIMATION WITH ELECTROSTATIC (MAC-E) type (see Section 2.2.2). The current experiment of this type is the KARLSRUHE TRITIUM NEUTRINO (KATRIN) experiment.

From the conceptual point of view, the β-decay of tritium is described by

$$\text{T} \longrightarrow {}^3\text{He}^+ + \text{ e}^- + \bar{\nu}_\text{e}. \tag{2.37}$$

Here it should be stressed that in the experimental realizations to date always T_2 was used so that Eq. 2.37 needs to be modified to represent the decay originating from the tritium in its molecular form (see Eqs. 2.46 to 2.48 in Section 2.3 below). The differential decay rate of a tritium nucleus can be derived using Fermi's golden rule [Fer34; Ott08]:

$$\frac{\text{d}\Gamma}{\text{d}E} = \frac{G_\text{F}^2 \cos^2(\theta_\text{C})}{2\pi^3}|M_\text{nuc}|^2 F(Z,E)p(E+m_\text{e}) \cdot \sum_i |U_{ei}|^2 \epsilon \sqrt{\epsilon^2 - m_i^2}\Theta(\epsilon - m_i) \tag{2.38}$$

with the following parameters (see *e.g.* Ref. [Kle19a; Ake22a]). Note that for better readability, natural units ($\hbar = c = 1$) are used in this work.

- G_F: Fermi coupling constant

- θ_C: Cabibbo angle

- $|M_\text{nuc}|^2$: nuclear matrix element

- $F(Z,E)$: Fermi function to account for the interaction with the nuclear Coulomb field, with the atomic charge of the helium daughter nucleus $Z = 2$

- $\epsilon = E_0 - E$: neutrino energy

- $\Theta(\epsilon - m_i)$: Heaviside function to ensure energy conservation

- m_i: neutrino mass eigenstates m_i with $i = 1, 2, 3$

The KATRIN collaboration recently published the results from their second neutrino mass measurement campaign, which returned an m_ν^2 value compatible with zero within the experimental uncertainties and resulting in the currently most stringent upper limit to date:

$$m_\nu^2 = (0.26 \pm 0.34)\,\text{eV}^2 \Rightarrow m_\nu < 0.9\,\text{eV } 90\,\%\text{ C.L..[Ake22b]} \tag{2.39}$$

Combined with the result from the very first neutrino mass measurement campaign in 2019 [Ake19], this results in

$$m_\nu < 0.8\,\text{eV } 90\,\%\text{ C.L..} \tag{2.40}$$

Since the research described in this thesis has been conducted in the context of the KATRIN experiment, its setup and methodology are described in more detail in the next section.

2.2. The KArlsruhe TRItium Neutrino (KATRIN) experiment

Using the experience gained from its predecessor experiments in Troitsk [Ase11] and Mainz [Kra05], the KATRIN experiment aims to improve the sensitivity on the neutrino mass by one order of magnitude from 2 eV before the start of KATRIN to 0.2 eV with its total expected data set [KAT05].

The KATRIN experiment employs a high-luminosity Windowless Gaseous Tritium Source (WGTS) in combination with a Magnetic Adiabatic Collimation with Electrostatic (MAC-E) filter type spectrometer. An overview of the complete setup of the KATRIN experiment is shown in Figure 2.3. For simplicity, the system is normally described as comprising three sub-systems: (i) the Source and Transport Section (STS), (ii) the Source and Detection Section (SDS) and (iii) the Rear Section (RS). These experimental sub-systems of the KATRIN experiment are described briefly in Sections 2.2.1 to 2.2.3. Note that the description follows Refs. [KAT05; KAT21] if not stated otherwise.

2.2.1. The source and transport section (STS)

The Source and Transport Section (STS) includes the Windowless Gaseous Tritium Source (WGTS), a differential pumping section (DPS), and a cryogenic pumping section (CPS); all are integrated into the full tritium loops infrastructure of the TLK. The transport section adiabatically guides the beta electrons from the source to the spectrometers, while at the same time eliminating any tritium flow into the spectrometer. The spectrometer has to be kept practically free of tritium: any tritium in the spectrometer would produce unwanted background signals at the detector.

A schematic of the WGTS and inner tritium loop [Kaz08; Stu10b; Pri15; Stu21] is shown in Figure 2.4. The WGTS is a 10 m long tube with an inner diameter of 90 mm. The tube
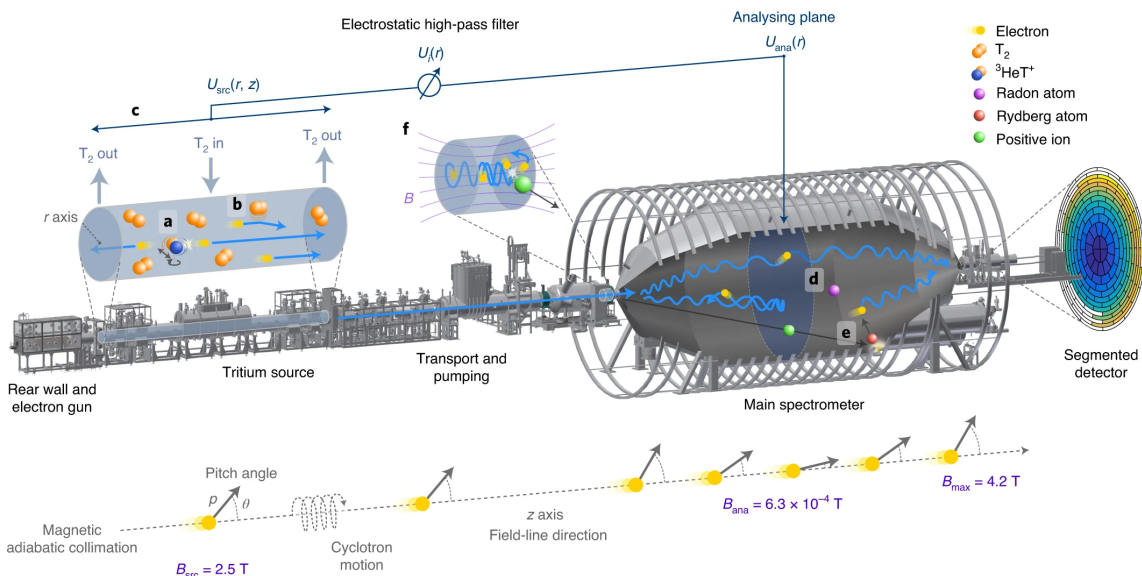
Figure 2.3.: Schematic view of the KATRIN experimental setup. The overall length of the setup is about 70 m. Electrons emitted in the β-decay of tritium in the source are guided adiabatically through the transport section into the Main Spectrometer (MS). The Main Spectrometer (MS) is based on the MAC-E filter principle and acts as an electrostatic high-pass filter for electrons. The β-electrons that pass the MS are recorded, and counted, using the Focal Plane Detector (FPD). Image adapted from [Ake22b].
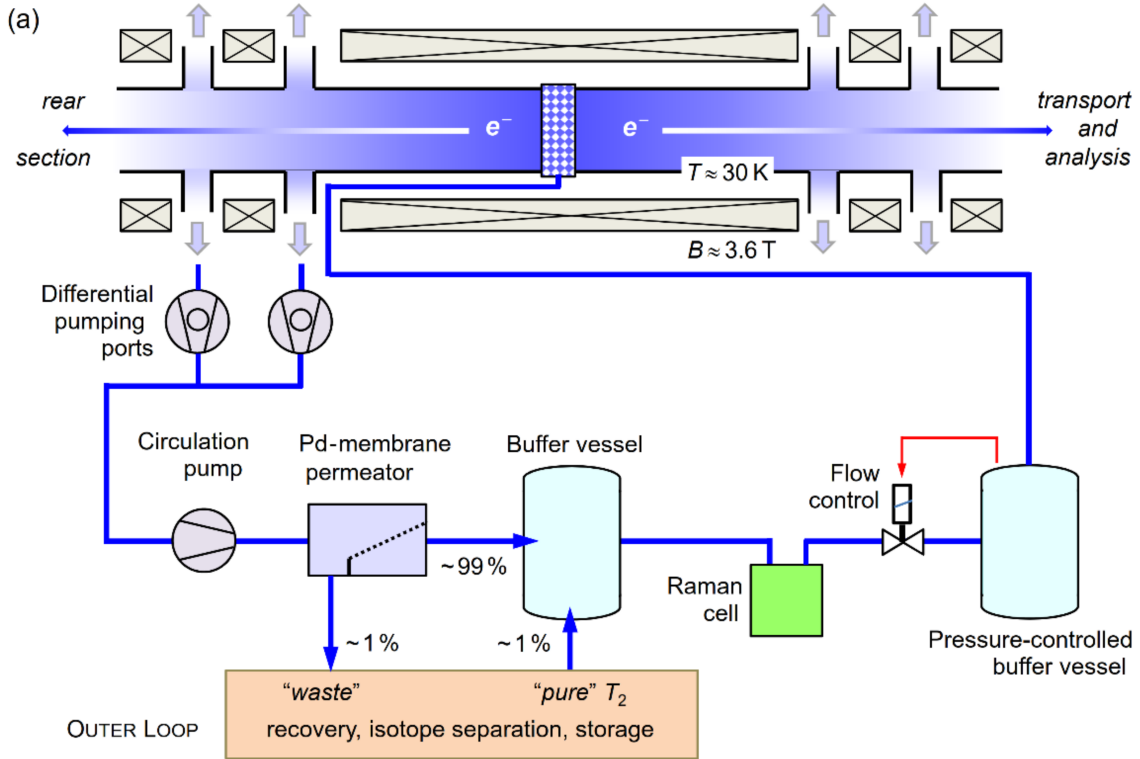
Figure 2.4.: Schematic diagram of the Windowless Gaseous Tritium Source (WGTS) and the Inner Loop. Via a pressure-controlled buffer vessel and a capillary system, tritium gas is injected at the center of the WGTS tube. The gas is pumped off on both ends via turbomolecular pumps. Impurities are removed by a Pd-permeator and returned to the Outer Loop. Pure tritium is supplied as needed from the Outer Loop. The gas composition is constantly monitored via a LARA system. Image adapted from [Ake20b].

is filled with high-purity molecular tritium gas; the gas is injected into the tube through a capillary, roughly at the center. The β-electrons from the tritium decay are guided by a homogeneous magnetic field with up to 3.6 T towards the ends of the tube. The tritium gas is pumped off at both ends of the tube and returned to the inner tritium loop, after passing a Pd-membrane permeator, to remove any non-hydrogen isotopologue contamination. The cleaned tritium gas is stored in a buffer vessel that is replenished with high-purity tritium gas as needed. From this main buffer vessel, the gas flows through the Laser Raman (LARA) cell (see Section 4.1) into a pressure-controlled buffer vessel that releases the gas with a constant flow rate into the WGTS through the injection capillary.

The LARA system is used for source composition monitoring [Stu10a; Ake20b]. Since it forms a major foundation of the present work, an in-depth description of the LARA system is provided in Section 2.3.

Any tritium gas that is not removed by the pumps directly from the end of the WGTS, is pumped off by the DPS and CPS and returned to the Outer Loop [Wel17]. In full operation, the KATRIN source has a throughput of about 40 g of tritium per day [Wel17; Stu21]. For this reason, the KATRIN experiment is located at the Tritium Laboratory Karlsruhe (TLK); it is currently the only scientific laboratory equipped with a closed tritium cycle and licensed to handle the required amount of tritium.

2.2.2. The spectrometer and detector section (SDS)

Within the KATRIN beam line (see Figure 2.3), two MAC-E filter spectrometers are used, the so-called Pre-Spectrometer (PS) and the MAIN SPECTROMETER (MS). As it is an integral part of the KATRIN experiment, the MAC-E filter principle is briefly introduced (a sketch of the MS is shown in Figure 2.5).

The main purpose of these spectrometers is the energy selection; they serve as high-pass filters for electrons by using magnetic adiabatic collimation in combination with an electrostatic energy filter. The required magnetic field is produced by superconducting solenoids at the spectrometer entrance and exit. A β-electron arriving into the spectrometer from the WGTS, is guided by the magnetic field towards the center of the spectrometer, to the so-called analyzing plane[3]. During this process, the magnetic gradient force transforms the cyclotron motion of the electron into the longitudinal component, while maintaining full energy conservation. In a non-relativistic approximation, the orbital magnetic moment μ is conserved according to

$$\mu = |\boldsymbol{\mu}| = \frac{\mathrm{e}}{2m_\mathrm{e}}|\boldsymbol{l}| = \frac{E_\perp}{B} = \mathrm{const.}, \tag{2.41}$$

where $\boldsymbol{l}$ is the electron angular momentum around a magnetic field line, and $E_\perp$ and B are the transversal components of the electron energy and the magnetic field, respectively. The transverse kinetic energy reaches its minimum in the analyzing plane, where the magnetic field is reduced to a small value in the order of $0.5\,\mathrm{mT}$. In addition to the magnetic field,
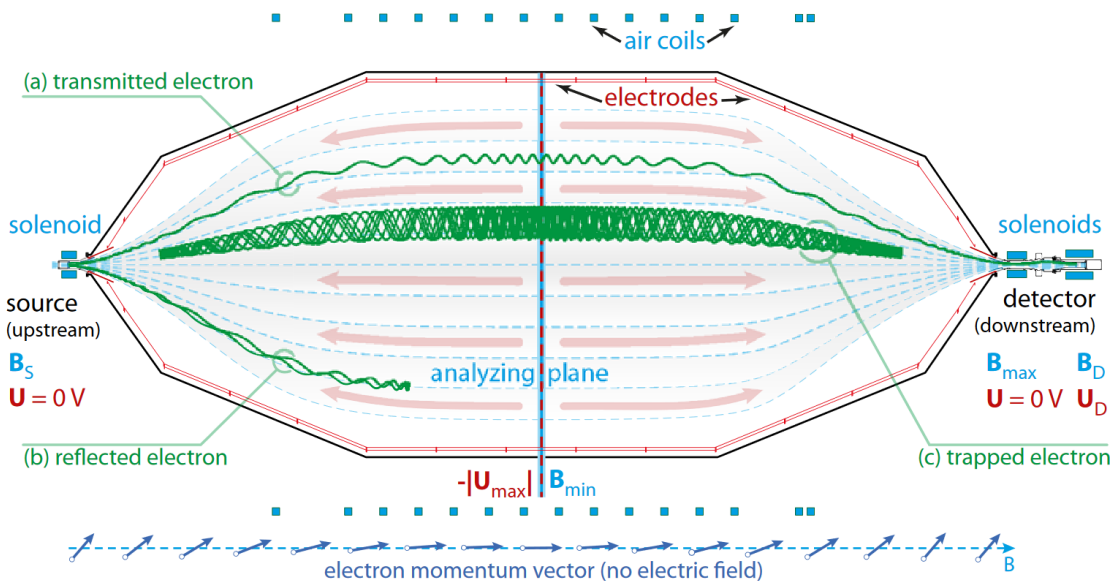
Figure 2.5.: Schematic view of the KATRIN main spectrometer that is based on the MAC-E filter principle. Electrons from the source enter the MS (left). They are guided adiabatically along the magnetic field lines. In the lower part of the image, the evolution of the electron momentum vector is shown. The magnetic field is defined by the superconducting solenoids at the entrance and exit of the spectrometer, and by a system of air coils. Image adapted from [KAT21].

---

[3]The position of the analyzing plane relative to the spectrometer is given by the relative strength of the magnetic field at the entrance and exit. Starting with KATRIN NEUTRINO MASS (KNM)3 campaign, the MS is operated with a shifted analyzing plane (SAP) to reduce background. [Lok22]

an electric field is applied in the MS. The electrons can only pass the spectrometer if their longitudinal energy is larger than the filter energy

$$E_\parallel = E \cdot \cos^2\theta > q \cdot U_{\max}, \tag{2.42}$$

where q is the electron charge, E its kinetic energy and θ the pitch angle. The energy resolution ΔE of such a MAC-E filter is then given by

$$\frac{\Delta E}{E} = \frac{B_{\min}}{B_{\max}} \xrightarrow{\text{KATRIN MS}} \Delta E \approx \frac{0.3\,\text{mT}}{6\,\text{T}} \cdot 18.6\,\text{keV} \approx 1\,\text{eV}. \tag{2.43}$$

In the KATRIN experiment, the β-spectrum is measured in integral form by varying the filter energy, or more precisely, by varying the potential difference between the source and the spectrometer. The key requirements and design criteria for the MS are the vacuum quality (lower 10×10^{-11} mbar regime), high voltage (relative precision of ppm for voltages up to -35 kV), and magnetic field stability, to guarantee optimal electron transport from the source to the detector.

In KATRIN a custom-designed multi-pixel silicon detector, the so-called FOCAL PLANE DETECTOR (FPD) system, is used. The main objective of the FPD system is to detect β-electrons transmitted by the MS. The detector is segmented into 148 pixels of equal area, covering the entire magnetic flux tube. For electrons in the signal region, the FPD has a high efficiency of $\geq 90\,\%$. The energy resolution of the detector is relatively poor, with about 1.5 keV FWHM [Ams15]. However, this constitutes no problem for KATRIN, since the energy resolution in the integral measurement mode is provided by the MS. For the envisaged transition to a differential measurement mode, where the energy analysis is performed by the detector, the FPD system will be replaced by the TRISTAN detector [TRI21; Hou20; Ake22a]. This will be briefly discussed in Section 2.4.

2.2.3. The rear section (RS)

The REAR SECTION (RS) is the section at the far end of the KATRIN beam line. It contains an electron gun (e-gun) that enables studies of the electromagnetic characteristics along the full beam line, including the MS and the FPD, and column density monitoring and measurement of the so-called 'energy-loss' (E-loss) function. The REAR WALL (RW), a stainless-steel disk coated with a 1 μm-layer of gold, also forms part of the RS. The RW is important for determining and manipulating the plasma potential distribution within the WGTS.

During the operation of the KATRIN experiment, accumulation of tritium-mediated contaminants on the RW was observed [Ake23b]. If left untreated, tritiated-compound accumulations lead to an increase in the background signal in the experiment. Currently, these accumulations are intermittently removed *in-situ* by UV/ozone cleaning; however, the actual composition of the tritiated molecules on the surface of the rear wall remains unknown. The best hypothesis is tritiated amorphous carbon (aC:T). The CONFOCAL RAMAN MICROSCOPE (CRM) that was developed within the scope of this work can be used for the characterization of aC:T on a gold surface. Proof-of-principle studies conducted with $\approx 1\,\text{cm}^2$ duplicates of the RW are summarized in Appendix E.

2.3. Importance of source composition monitoring

In the previous sections, it was assumed that β-electrons originate from atomic tritium, to simplify the theoretical treatment. However, in reality, in the KATRIN experiment tritium is present in molecular form, T_2, and Eq. 2.37 becomes

$$T_2 \longrightarrow (^3\text{HeT})^+ + \text{e}^- + \bar{\nu}_\text{e}. \tag{2.44}$$

Therefore, Eq. 2.38 needs to be modified to include excitation of a spectrum of rotational and vibrational final states in the daughter molecule, the so-called FINAL STATES DISTRIBUTION (FSD). The neutrino energy ϵ becomes $\epsilon_f = E_0 - V_f - E$ and thus

$$\frac{\text{d}\Gamma}{\text{d}E} = \frac{G_\text{F}^2 \cos^2(\theta_\text{C})}{2\pi^3} |M_\text{nuc}|^2 F(Z,E) p(E + m_\text{e}) \cdot \sum_f P_f \epsilon_f \sqrt{\epsilon_f^2 - m_\nu^2} \Theta(\epsilon_f - m_\nu) \tag{2.45}$$

with an energy correction V_f, originating from the final state f of the decay product and the final states probability P_f as calculated in quantum chemical theory [Sae00; Dos06]. Here the definition of the effective neutrino mass $m^2(\nu_\text{e}) = \sum_i |U_i|^2 m_i^2$ for $i = 1, 2, 3$ is used.

An ideal source would contain only pure tritium, T_2 [KAT05]; while in general T_2 is the majority molecular component (mole fraction $c_{T_2} > 0.9$), the other tritiated hydrogen isotopologues HT and DT are encountered as well (with $c_\text{HT} + c_\text{DT} < 0.1$) [Ake20b]. Note that minimal traces of the non-tritiated hydrogen isotopologues (D_2, HD, H_2) are also observed.

As a consequence of this, one has to consider the contributions from all three tritiated species to the total number of β-decay electrons, i.e.,

$$T_2 \longrightarrow (^3\text{HeT})^+ + \text{e}^- + \bar{\nu}_\text{e}, \tag{2.46}$$

$$DT \longrightarrow (^3\text{HeD})^+ + \text{e}^- + \bar{\nu}_\text{e} \quad \text{and} \tag{2.47}$$

$$HT \longrightarrow (^3\text{HeH})^+ + \text{e}^- + \bar{\nu}_\text{e}. \tag{2.48}$$

In order to take these into account during the data analysis, constant monitoring of the source gas composition is paramount. In the following, the definition of the source composition parameters is given, and systematic effects, which depend on the source composition, are introduced. Finally, the requirements to the uncertainties in source composition monitoring are summarized.

Definition of source composition parameters

For the successful operation of the KATRIN experiment, key parameters were identified [KAT05; KAT21]. The uncertainties, associated with every key parameter, must not contribute more than

$$\sigma_\text{sys} = 7.5 \times 10^{-3} \, \text{eV}^2 \tag{2.49}$$

to the neutrino mass analysis after three full years (> 1000 days) of β-electron data taking [KAT05; KAT21]. Two key parameters are related to the source gas composition: (i) the isotopic tritium purity ϵ_T (fraction of tritium atoms in the gas); and (ii) the HT/DT ratio κ [Bab12].

The tritium purity is defined as

$$\epsilon_{\mathrm{T}} = \frac{N_{\mathrm{T}_2} + \frac{1}{2}(N_{\mathrm{HT}} + N_{\mathrm{DT}})}{\sum_i N_i}, \tag{2.50}$$

where $i = \mathrm{T}_2, \mathrm{DT}, \mathrm{D}_2, \mathrm{HT}, \mathrm{HD}, \mathrm{H}_2$ and N_x is the number of molecules of the specific isotopologue $x \in i$. It represents the fraction of all tritium atoms relative to the total number of atoms within the source, and KATRIN is designed to operate with $\epsilon_{\mathrm{T}} > 95\,\%$ at all times [Bab12]. This maximizes the source activity (Eq. 2.53). Additionally, the HT-DT-ratio κ, which is defined as

$$\kappa = \frac{N_{\mathrm{HT}}}{N_{\mathrm{DT}}}, \tag{2.51}$$

has to be taken into account, since ϵ_{T} does not contain any information about the number of the individual isotopologues.

Alternatively, the source composition can be represented by the mole fractions of the individual molecular constituents. The mole fraction c_x of a constituent x is defined as

$$c_x = \frac{N_x}{\sum_i N_i}, \tag{2.52}$$

with $\sum_i c_i := 1$. Overall, in the context of the KATRIN experiment, the $\{\epsilon_{\mathrm{T}}, \kappa\}$ representation is preferred because often only the active molecules are of interest. In addition, all the uncertainty requirements are given directly in relation to $\{\epsilon_{\mathrm{T}}, \kappa\}$.

Composition dependent systematic effects

As stated earlier in this section, the isotopic tritium purity ϵ_{T} and the HT-DT-ratio κ are the key parameters specified for the KATRIN experiment [Bab12; Ake22b]. The tritium purity ϵ_{T} directly impacts the source activity S

$$S = C \cdot \epsilon_{\mathrm{T}} \cdot \rho d. \tag{2.53}$$

In this equation C is a constant factor dependent on detector efficiency and other experimental parameters [Bab12], and ρd is the column density in the WGTS, i.e., the areal density of atoms in the source regarding the cross-sectional area of the source tube. The influence of the HT/DT ratio κ is less obvious on first sight; however, there are several systematic effects that are sensitive to the mass of the decaying molecule. If left uncorrected, these would introduce distortions of the shape of the β-spectrum. These are briefly summarized in the following list.

- **Doppler effect:** Due to the thermal motion of molecules in the gas and the resulting Doppler effect, the kinetic energies of the β-decay electrons are shifted. Additionally, within the WGTS, all molecules are moving towards one of the ends in a bulk motion. In the non-relativistic approximation, the energy shift is given by [KAT05]:

$$\epsilon = E_{\mathrm{LAB}} - E_{\mathrm{CMS}} = \frac{1}{2} m_{\mathrm{e}}[(V_{\parallel} + v)^2 + V_{\perp}^2] - \frac{1}{2} m_{\mathrm{e}} v_{\mathrm{e}}^2 \approx m_{\mathrm{e}} \cdot v_{\mathrm{e}} \cdot V_{\parallel}, \tag{2.54}$$

  where $m_{\mathrm{e}}, v_{\mathrm{e}}$ denote the electron's mass and velocity (in the center-of-mass (CMS) system of the molecule), respectively; and $V_{\parallel/\perp}$ is the velocity component of the decaying molecule parallel / transverse to the direction of the electron. At any given temperature, the molecular velocity distribution depends on the molar mass; therefore, the actual composition of the gas has to be taken into account.

- **Elastic electron scattering:** In addition to inelastic scattering, the β-electrons scatter elastically with the molecules in the source. The energy loss of the electron due to elastic scattering is given by [KAT05]

$$\Delta E = 2 \frac{m_e}{M_{Q_2}} E_e (1 - \cos \theta_s), \ Q = H, D, T. \tag{2.55}$$

Here m_e, E_e denote the electron's mass and initial energy, θ_s is the scattering angle and M_{Q_2} represents the molecule's mass. Due to the dependency on M_{Q_2} the knowledge of the source composition is required to calculate the elastic energy loss.

- **Nuclear recoil:** Eq. 2.38 is only valid for an infinitely heavy tritium nucleus. In reality, due to the emission of the β-electron and the electron antineutrino, recoil energy is transferred to the daughter molecule (*e.g.* $(^3\text{HeT})^+$) during β-decay. This recoil energy is not available for the electron as kinetic energy and shifts the spectrum towards lower energies. Close to the energetic endpoint in the β-spectrum, the recoil energy balances the momentum of the electron [KAT05]:

$$E_{\text{rec}} \approx E \cdot \frac{m_e}{M_X}, \ X = HT, DT, T_2. \tag{2.56}$$

Since the recoil energy E_{rec} depends on the mass of the daughter molecule, M_X, the β-spectrum is dependent on the isotopologue composition of the WGTS. In reality, the measured β-spectrum is a weighted superposition of the single spectra of T_2-, DT- and HT-β-decay.

- **Final state distribution (FSD):** The daughter molecule can be excited to different states by the recoil of the β-decay [Sae00; Dos06]. The first electronic excited state of the $(^3\text{HeT})^+$ has an excitation energy of $\sim 27 \, \text{eV}$, and is therefore not relevant for the energy interval relevant for KATRIN [KAT05]. Different rotational-vibrational states are populated. As shown in Figure 2.6, different daughter molecules have different final state distributions. Here, it should be noted that the broadening of the energy spectrum that is associated with the FSD of the molecular decay sets a limit for the sensitivity of neutrino mass experiments with molecular tritium. This will be further expanded on in Section 2.4.
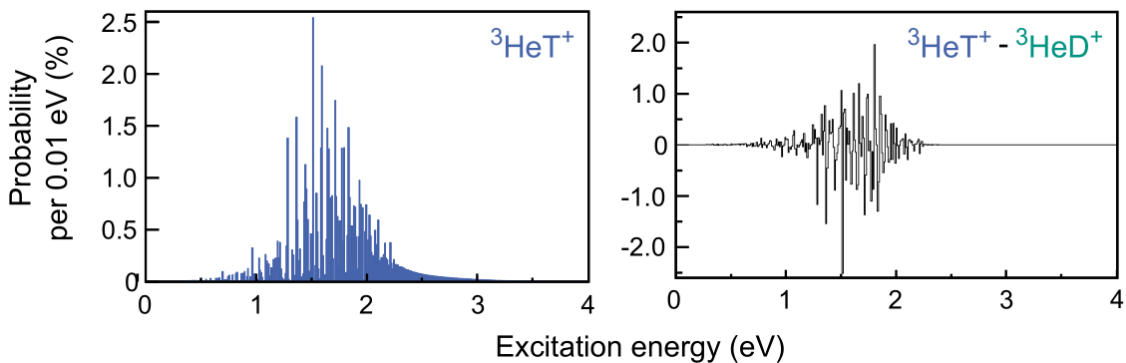
Figure 2.6.: Final state distributions for different daughter molecules. Reprinted with permission from [Sch14]. Copyright 2014 Springer International Publishing Switzerland.

Requirements on the LARA system for source monitoring

Since the source activity (Eq. 2.53) and previously listed systematic effects depend on the source composition, a continuous composition monitoring is necessary. For the KATRIN experiment, the requirements were first defined in Ref. [KAT05], and refined and amended in Refs. [Bab12; Sch14]. In summary, the requirements for the 200 meV goal are:

$$\frac{\Delta\epsilon_{\mathrm{T}}}{\epsilon_{\mathrm{T}}} \leq 1 \times 10^{-3} \,\widehat{=}\, 0.1\,\% \quad \text{(precision)}, \qquad \frac{\Delta\epsilon_{\mathrm{T}}}{\epsilon_{\mathrm{T}}} \leq 3 \times 10^{-2} \,\widehat{=}\, 3.0\,\% \quad \text{(trueness)} \quad (2.57)$$

and

$$\frac{\Delta\kappa}{\kappa} \leq 10 \times 10^{-2} \,\widehat{=}\, 10\,\% \quad \text{(accuracy)}. \tag{2.58}$$

Note that simplified, the precision is related to relative changes, i.e., statistical (stat.) uncertainty; and trueness is associated with the absolute values, i.e., systematic (syst.) uncertainty. Per definition, a measurement is accurate if it is both true and precise [BIP08; ISO23]. These requirements can be fulfilled by using a LARA system with adequate measurement capabilities. Such a LARA system is part of the Inner Loop of the WGTS, see Figure 2.4.

The suitability of the KATRIN LARA system for accurate gas composition measurements has been demonstrated in several studies within the past 10 years, *e.g.* Refs. [Stu10a; Fis14; Sch14; Zel17]. However, the final demonstration that the LARA system can achieve the metrological performance continuously and reliably over the complete operation time of several years, can only truly be demonstrated with the passing of KATRIN operation time. One particular aspect of the LARA system, for which the stability over several years had yet to be demonstrated, is the intensity calibration using a NATIONAL INSTITUTE OF STANDARDS AND TECHNOLOGY (NIST)-certified STANDARD REFERENCE MATERIAL (SRM). Raman spectroscopy and the LARA system itself are described in greater detail in Chapter 3 and Section 4.1, while the long-term metrological performance is demonstrated in Chapter 5.

2.4. Beyond the current KATRIN experiment

At the time of writing, the KATRIN collaboration had published the results from the first two neutrino mass measurement campaigns (KNM1,2) [Ake19; Ake22b]. The data analysis of the KNM1-5 campaigns is ongoing with a release expected soon [Mer23][4]. The data taking has already progressed further, with campaign KNM11 ongoing [Rod23].

In its current configuration, the KATRIN experiment will operate through 2025 to complete >1000 measurement days. With the full data set, the projected and readjusted sensitivity goal is $m_\nu < 0.3\,\mathrm{eV}$ (90 % C.L.) [Lok23]. With this sensitivity, the KATRIN result will likely allow to distinguish between the degenerate and hierarchical ordering scenario (see Figure 2.2 further above). After the neutrino mass measurements are finished, the KATRIN setup will be upgraded with the TRISTAN detector for two years of data taking in the search for keV-scale sterile neutrinos [Hou20; TRI21; Mer23; Ake23a].

Eventually, new technologies are needed to reach the scenario of potential inverted ordering ($m_\nu \approx 0.05\,\mathrm{eV}$). One major reason for the need for new technologies are the limitations associated with molecular tritium. These limitations, and possible solutions, are described in the following Sections 2.4.1 and 2.4.2.

---

[4]The information in this paragraph was made publicly available through conference talks, *e.g.* [Rod23].

2.4.1. Limitations associated with molecular tritium

The limitation is caused by the broadening caused by the FINAL STATES DISTRIBUTION (FSD). In the decay of molecular T_2 to $^3HeT^+$, the molecular FSD of the ground-state rotational and vibrational manifold of the daughter molecule has a standard deviation $\sigma_{FSD} \approx 0.4\,eV$, as shown in Figure 2.7 [Sae00; Bod15].

Even with an unprecedented $1\,\%$ uncertainty on the molecular tritium FSD, a molecular source still limits the sensitivity to about $0.1\,eV$ [Pro22; Hey23]. A (quasi-) atomic tritium source would avoid these limitations. It should be noted that there are other challenges for new technologies, which are not discussed in this work. Namely, these include the resolution of the electron spectrometer, electron energy loss and recombination of atomic to molecular tritium in the source, and backgrounds [Rob91; Pro22].

2.4.2. Proposed atomic tritium source(s)

For the realization of atomic tritium sources, two different approaches are pursued, namely (i) gaseous sources, and (ii) solid-state sources. In the former, the 'Project8' collaboration is working towards an atomic tritium source for which the tritium atoms are magneto-gravitationally confined within the detection vessel, in order to overcome the limitation in energy uncertainty [Pro22]. At the KATRIN experiment and the TLK, R&D for an atomic tritium beam commenced [Rod23; Mer23].

The latter type of source is required in a different approach to measure the neutrino mass, which was suggested by the 'PTOLEMY' (Princeton Tritium Observatory for Light, Early-Universe, Massive-Neutrino Yield) experiment [Bet13]. Rather than measuring the effective electron neutrino mass m_ν via the tritium β-decay, their goal is to study the cosmic neutrino background (CνB) via the monoenergetic signal of electrons produced by relic neutrino capture on atomic tritium:

$$\nu_e + T \longrightarrow {}^3He^+ +\ e^- \tag{2.59}$$
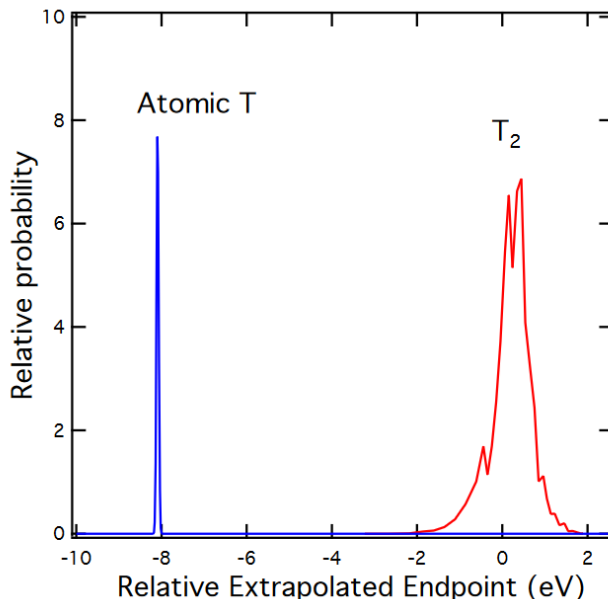
Figure 2.7.: The ground-state sub-level distribution of molecular tritium compared to the ground state of atomic tritium. Reprinted with permission from [For21]. Copyright 2021 Elsevier B.V.

From the study of the CνB, the effective electron neutrino mass could be obtained. This approach needs a solid state tritium target [Bet13]. Due to its excellent hydrogen storage properties, graphene has been proposed, and selected, as the solid-state carrier material [Bet13]. Estimates suggest that PTOLEMY can reach the required sensitivity to assess potential inverted ordering ($m_\nu \approx 0.05\,\mathrm{eV}$) already at the early stages of the experiment, with a target mass of $m_\mathrm{T} = 10\,\mathrm{mg}$ [Bet19b]. Early on it was estimated that, the FSD for atomic tritium bound on graphene would improve significantly compared to molecular tritium, using PTOLEMY's approach; however, recent calculations show that the localization of the initial tritium atom on the graphene sheet induces an intrinsic quantum spread in the energy spectrum of the electron. This uncertainty is predicted to be at least an order of magnitude larger than the energy resolution expected in the PTOLEMY experiment [Che21; Nus22; App22]. This instrumental quantum spread could possibly be avoided by the usage of nano-porous graphene (NPG) or carbon nanotubes [App22].

In addition to the concerns from the theoretical perspective, there are also open questions about the feasibility of tritiated graphene. Tritium is well-known for its aggressive radio-chemical nature, which might hinder the formation of tritiated structures, and negatively affect their stability. In this work, this particular aspect is address by tritiating graphene for the first time.

3. Theory of Raman spectroscopy

The inelastic scattering of light by molecules is called the Raman effect. Predicted by A. Smekal in 1923 [Sme23], the effect was observed for the first time by C. V. Raman and K. S. Krishnan in 1928 [Ram28]. In contrast to infrared spectroscopy, it is also possible to measure homonuclear molecules. This is one of the reasons why it is used for composition monitoring in the KATRIN experiment. In addition, it allows real-time monitoring of the gas composition without sampling.

During Raman scattering, energy is transferred between an incident photon and a probed material / molecule. The material changes its excitation state, and a scattered photon emerges from the process which has gained or lost energy with respect to the incident photon. This shift in energy is characteristic of the chemical and structural properties of the material. In the field of spectroscopy, energies are often given in wavenumbers $\bar{\nu}$. The wavenumbers relate by

$$\bar{\nu} = \frac{E}{hc} = \frac{\nu}{c} = \frac{1}{\lambda} \tag{3.1}$$

to the frequency $\nu = \omega/2\pi$ or the wavelength λ. Here h is Plank's constant and c is the speed of light in a vacuum. When comparing experiments, the refraction index n of the medium (typically air) needs to be taken into account

$$\lambda_{\text{air}} = \frac{\lambda_{\text{vac}}}{n}. \tag{3.2}$$

In the classical picture, the induced polarization vector $\mathbf{P}$ is proportional to the electric field experienced by the dielectric molecules in the medium

$$\mathbf{P}(t) = \varepsilon_0 \cdot \bar{\bar{\chi}} \cdot \mathbf{E}(t), \tag{3.3}$$

where ε_0 is the electric permittivity of free space and $\bar{\bar{\chi}}$ is the electric susceptibility tensor of the medium. On the microscopic scale, for a singular atom or molecule, this can be simplified, and the induced dipole moment is given by

$$\boldsymbol{\mu}(T) = \bar{\bar{\alpha}}\mathbf{E}(t). \tag{3.4}$$

Here $\bar{\bar{\alpha}}$ is the polarizability tensor of the atom or molecule. These two equations can be related, by adding up all N electric dipoles per unit volume in a material:

$$N \cdot \boldsymbol{\mu}(t) = \varepsilon_0 \cdot \bar{\bar{\chi}} \cdot \mathbf{E}(t). \tag{3.5}$$

24

Note that for isotropic media the susceptibility and polarizability tensors, $\bar{\bar{\chi}}$ and $\bar{\bar{\alpha}}$, can often be reduced to constant values, namely $\chi = ||\mathbf{P}||/||\mathbf{E}||$ and $\alpha = ||\boldsymbol{\mu}||/||\mathbf{E}||$.

The description of the theory of the Raman effect mainly follows [Lon02; Jor11; Hak06; Dem08; Yu10; Tel18]. Section 3.1 describes Raman scattering in molecules, starting with Eq. 3.4, with particular emphasis on diatomic molecules and hydrogen isotopologues. Subsequently, in Section 3.2, Raman scattering in solids is explained, with emphasis on graphene (investigated in this work), starting with Eq. 3.3.

3.1. Theory of Raman scattering of (free) molecules

In this section, the theory of Raman scattering of molecules is presented. Unless stated otherwise, the explanation follows Refs. [Lon02; Hak06; Dem08; Tel18]. In addition, this topic is already discussed and summarized in great detail in Refs. [Sch09; Sch14; Fis14; Rup16] regarding the LARA systems at TLK.

In short, the induced dipole moment $\boldsymbol{\mu}_{\mathrm{ind}}$, induced tby the external electric (laser) field $\mathbf{E}_{\mathrm{ext}} = \mathbf{E}_0 \cdot \cos(\omega_0 t)$, can be expressed as

$$\boldsymbol{\mu}_{\mathrm{ind}} = \bar{\bar{\alpha}} \cdot \mathbf{E}_{\mathrm{ext}}(t). \tag{3.6}$$

Here μ is the molecular dipole induced by the external electric field $\vec{E} = E_0 \cdot \cos(\omega_0 t)$. The polarizability $\tilde{\alpha}$ of an atom in a material is one of its properties. The polarizability can be defined as the extent to which the driving field is able to disturb the electron density of the material out of its equilibrium configuration. The components of the polarizability tensor can be expanded into a Taylor series regarding the normal coordinates of a vibration around the equilibrium

$$\alpha = \alpha(Q) = \alpha_0 + \sum_{q=1}^{N} \left[\left(\frac{\partial \alpha}{\partial q} \right)_{q_0} \cdot q + \frac{1}{2} \cdot \left(\frac{\partial^2 \alpha}{\partial q \partial q'} \right)_{q_0 q_0'} \cdot q \cdot q' + O(q^3) \right] \tag{3.7}$$

Taking into account only the first term in the Taylor expansion and assuming a simple harmonic motion around the equilibrium $q = q_0 \cdot \cos(\omega_q t)$, the induced molecular dipole can be written as

$$\mu(t) = \left[\alpha_0 + \left(\frac{\partial \alpha}{\partial q} \right)_{q_0} \cdot q_0 \cdot \cos(\omega_q t) \right] \cdot E_0 \cdot \cos(\omega_0 t) \tag{3.8}$$

which after cosine-wave multiplication evolves into

$$\mu(t) = \alpha_0 \cdot E_0 \cdot \cos(\omega_o t) + \frac{1}{2} \left(\frac{\partial \alpha}{\partial q} \right)_{q_0} \cdot q_0 \cdot \cos[(\omega_0 - \omega_q)t] + \frac{1}{2} \left(\frac{\partial \alpha}{\partial q} \right)_{q_0} \cdot q_0 \cdot \cos[(\omega_0 + \omega_q)t] \tag{3.9}$$

From this equation it follows that Raman scattering is only possible if the polarizability of the molecule changes due to the molecular excitation $\left(\frac{\partial \alpha}{\partial q} \right)_{q_0} \neq 0$. Additionally, it shows that the molecule exhibits three linear induced dipole moments which have different frequencies, namely a dipole moment of frequency ω_0 which is associated with Rayleigh scattering, the Stokes Raman moment of frequency $\omega_0 - \omega_q$, and the Anti-Stokes Raman moment of frequency $\omega_0 + \omega_q$.

3.1.1. Rotational and vibrational states in diatomic molecules

To understand the structure of the Raman spectrum obtained for the six hydrogen isotopologues (T_2, DT, D_2, HT, HD, H_2), a conceptual description of the energy levels in diatomic molecules is introduced. In the context of a rotating diatomic molecule, the generic model often employed is the rigid rotator. In this model, it is assumed that the two nuclei are linked by a massless rod, fixed at the equilibrium distance R_E and that the molecule rotates around the center of mass. The quantized eigenenergy spectrum $\tilde{F}(J)$ is given by

$$\tilde{F}(J) = \mathrm{B_e} \cdot F \cdot (J+1) \tag{3.10}$$

for the rotational quantum number $J = 0, 1, 2, ...$ Here,

$$\mathrm{B_e} = \frac{h}{8\pi^2 c \, \Theta} \tag{3.11}$$

with the molecule specific mass-dependent moment of inertia Θ. The model of the rigid rotator does not provide a complete description of all experimental rotational spectra. This is because the distance vector between the nuclei, $\vec{R}$, is not a constant; it increases with higher rotational quantum numbers J. To correct for this, a spring in place of the rod is introduced, where the stiffness of the connection is characterized by a spring constant, k (see Figure 3.1). This results in a correction terms in the energy spectrum

$$\tilde{F}(J) = \mathrm{B_e} \cdot J(J+1) - \mathrm{D_e} \cdot J^2 \cdot (J+1)^2 + ..., \tag{3.12}$$

where $\mathrm{D_e}$ is a stretching constant

$$\mathrm{D_e} = \frac{\hbar^3}{4\pi \mathrm{k} c \mu^2 R_e^6}. \tag{3.13}$$

In principle, higher-order correction terms can be added [Her63]; however, these are not relevant to this work.
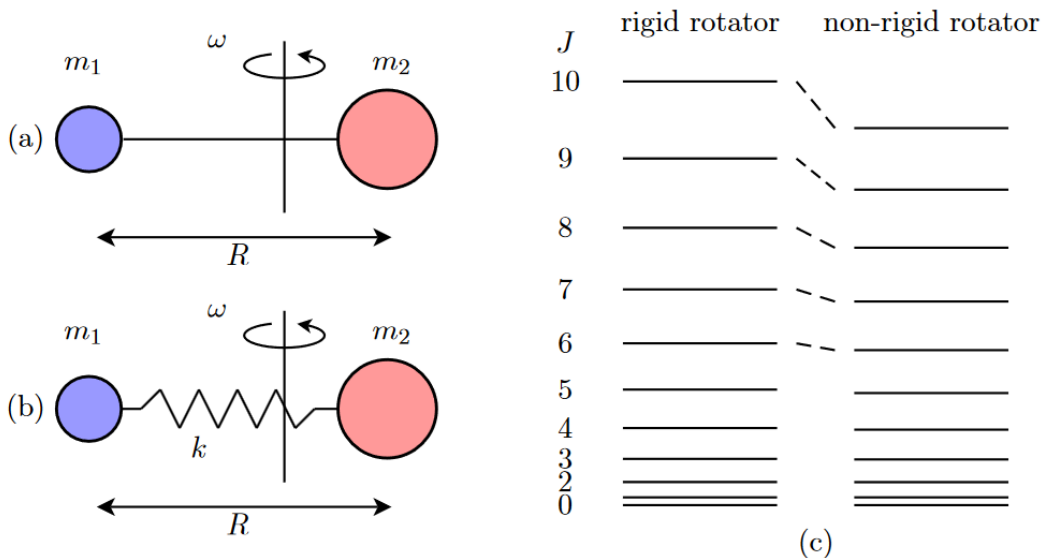
Figure 3.1.: Rotation of diatomic molecules. (a) Rigid rotor with fixed distance R between the atoms. (b) Non-rigid rotor where the atoms can oscillate with the spring constant k (c) Change in the energy scheme. For the non-rigid rotor, the energies are shifted to lower values for higher rotational quantum numbers J. Details are given in the main text. Image taken from [Sch09], based on [Hak06].

An approximation of the harmonic oscillator model is the common approach to characterize the vibrational states of a diatomic molecule. This approximation is based on the assumption of a linear restoring force between the nuclei, resulting in a specific energy spectrum:

$$\tilde{G}(\nu) = \omega_e \left(\nu + \frac{1}{2} \right) \tag{3.14}$$

with the vibrational quantum number $\nu = 0, 1, 2, ...$ and the vibrational constant

$$\omega_e = \frac{\sqrt{k\mu^{-1}}}{2\pi c}. \tag{3.15}$$

The molecule-specific constant ω_e contains the reduced mass μ of the molecule and a restoring-force (spring) constant k. Similar to the description of the rotational states, here the simple model has to be replaced by a more precise model. The harmonic oscillator model is only valid for small values of ν and does not account for molecular dissociation when the finite binding energy E_B is reached. To introduce anharmonic oscillations, the Morse potential can be used, which is one of the simplest, parameterized model potentials. It is based on the molecule-specific constants E_B, R_E and the potential width a. This results in a first-order correction term that changes the energy spectrum to

$$\tilde{G}(\nu) = \omega_e \left(\nu + \frac{1}{2} \right) - \omega_e x_e \left(\nu + \frac{1}{2} \right)^2 + ... \tag{3.16}$$

with

$$\omega_e = \frac{\omega_0}{2\pi c}, \quad \omega_e x_e = \frac{\omega_0^2}{16\pi c^2 E_B} \quad \text{and} \quad \omega_0 = a\sqrt{\frac{2E_B}{\mu}}. \tag{3.17}$$

Rotational and vibrational motions within a molecule are not completely independent. This means that the effect of one type of excitation on the other must be taken into account. Since vibrational excitations are significantly more energetic than rotational excitations, typically by two to three orders of magnitude, it is common to treat the rotational constants as depending on the vibrational quantum number ν. This is applied to B $\rightarrow$ B(ν) and correspondingly to D $\rightarrow$ D(ν). In the case of the Morse potential, specific formulas can be given for B(ν) and D(ν):

$$B(\nu) = B_e - \frac{\alpha}{2} \left(\nu + \frac{1}{2} \right) \quad \text{and} \tag{3.18}$$

$$D(\nu) = D_e - \beta \left(\nu + \frac{1}{2} \right), \tag{3.19}$$

with the molecule-specific specific correction constants α and β. This means the rotational constants are different for each vibrational level, yielding rotational energy levels $\tilde{F}_\nu(J)$. This is reflected in the rotational line spacing for transitions between different vibrational levels.

Finally, the coupled rotational vibrational energy levels for a diatomic molecule can (approximately) be written as

$$\tilde{T}(\nu, J) = \tilde{G}(\nu) + \tilde{F}(\nu, J) \tag{3.20}$$

$$= \omega_e \left(\nu + \frac{1}{2} \right) - \omega_e x_e \left(\nu + \frac{1}{2} \right)^2 + B(\nu) \cdot J(J+1) - D(\nu) \cdot J^2(J+1)^2. \tag{3.21}$$

In terms of precision, the formula presented here offers the essential energy term values with sufficient precision to be valid for the research conducted in this work. More details and correction terms can be found in Ref. [Her63].

Besides describing the general process, it is essential to adhere to certain selection rules when calculating a scattering spectrum for diatomic molecules. In the inelastic scattering process, the spins of the exciting and scattered photons are $S = 1$, resulting in a rotational selection rule of $\Delta J = 0, \pm 2$ for transitions between the corresponding lower state with J'' and upper, excited state with J' due to angular momentum conservation. In the context of vibrational transitions, the selection rule of $\Delta \nu = 0, \pm 1$ is applied. Although so-called overtones with $\Delta \nu = \pm 2, \pm 3$, etc. are theoretically possible, their transition probabilities are often too small (as a consequence of the Franck-Condon principle) to be experimentally observable. It also should be noted that the (anti-Stokes) transitions with $\Delta \nu = -1, -2, ...$ are not accessible when utilizing long-pass edge filters to suppress scattered laser light – as in the experimental setup used during this work; said filters suppress most anti-Stokes lines by a factor of $10^4 - 10^6$. Taking these selection rules for Raman transitions into account, the vibrational / rotational contributions to the transition energies $\Delta \tilde{T} = (\nu, J)$ can be written as following:

$$\Delta \tilde{G}_{\Delta \nu} = \tilde{G}(\nu') - \tilde{G}(\nu'') \qquad [e.g., \ \Delta \tilde{G}_1 = \tilde{G}(1) - \tilde{G}(0)] \qquad (3.22)$$

$$\Delta \tilde{F}_{\Delta \nu}(\mathrm{O}) = \tilde{F}_{\nu'}(J' = J'' - 2) - \tilde{F}_{\nu''}(J'') \qquad [e.g., \ \Delta \tilde{F}_1(\mathrm{O}) = \tilde{F}_1(0) - \tilde{F}_0(2)] \qquad (3.23)$$

$$\Delta \tilde{F}_{\Delta \nu}(\mathrm{Q}) = \tilde{F}_{\nu'}(J' = J'') - \tilde{F}_{\nu''}(J'') \qquad [e.g., \ \Delta \tilde{F}_1(\mathrm{Q}) = \tilde{F}_1(2) - \tilde{F}_0(2)] \qquad (3.24)$$

$$\Delta \tilde{F}_{\Delta \nu}(\mathrm{S}) = \tilde{F}_{\nu'}(J' = J'' + 2) - \tilde{F}_{\nu''}(J'') \qquad [e.g., \ \Delta \tilde{F}_1(\mathrm{S}) = \tilde{F}_1(4) - \tilde{F}_0(2)] \qquad (3.25)$$

A summary of the transition bands resulting from the selection rules and their associated transition energies is given in Table 3.1, together with the corresponding nomenclature scheme. A generic Raman spectrum for a diatomic molecule is depicted in Figure 3.2.

Table 3.1.: Definition of Raman branches based on selection rules in diatomic molecules. Based on Ref. [Lon02]. The various branches are depicted in Figure 3.2.

$\Delta \nu$	ΔJ	Branch	Raman shift $\Delta \tilde{\nu}$	scattering classification
-1	$0, \pm 2$	$\mathrm{O}_{-1}, \mathrm{Q}_{-1}, \mathrm{S}_{-1}$	$\Delta \tilde{G}_{-1} + \Delta \tilde{F}_{-1}(\mathrm{O,Q,S})$	anti-Stokes[*]
0	-2	O_0	$\Delta \tilde{F}_0(\mathrm{O})$	anti-Stokes[*]
0	0	Q_0	0	Rayleigh
0	2	S_0	$\Delta \tilde{F}_0(\mathrm{S})$	Stokes
1	-2	O_1	$\Delta \tilde{G}_1 + \Delta \tilde{F}_1(\mathrm{O})$	Stokes
1	0	Q_1	$\Delta \tilde{G}_1 + \Delta \tilde{F}_1(\mathrm{Q})$	Stokes
1	2	S_1	$\Delta \tilde{G}_1 + \Delta \tilde{F}_1(\mathrm{S})$	Stokes

[*] suppressed by long-pass edge-filter
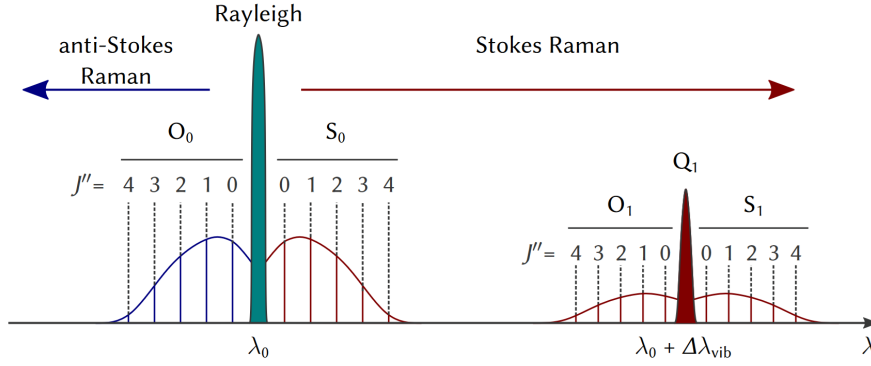
Figure 3.2.: Generic Raman spectrum of a diatomic molecule. The branches are labeled according to Table 3.1. Details are given in the main text. Image repreinted from [Nie21b], based on [Hak06].

3.1.2. Raman transition line strength

According to Ref. [Lon02], the intensity of light scattered by diatomic molecules is given as

$$I(\varphi, \theta)_{p^s, p^i} = k_{\tilde{\nu}} \cdot \tilde{\nu}_s^4 \cdot N_i \cdot \Phi(\varphi, \theta, a, \gamma)_{p^s, p^i} \cdot \Im; \tag{3.26}$$

this formula is based on quantum mechanical calculations. It is only valid if the intensity is measured in units of power [McC06]. If instead the intensity is measured in number of photons, *e.g.* when using a CCD detector, the wavenumber dependency changes from $I(\varphi, \theta)_{p^s, p^i} \propto \tilde{\nu}_s^4$ to $I(\varphi, \theta)_{p^s, p^i} \propto \tilde{\nu}_0 \tilde{\nu}_s^3$ yielding

$$I(\varphi, \theta)_{p^s, p^i} = k_{\tilde{\nu}} \cdot \tilde{\nu}_s^3 \cdot \tilde{\nu}_0 \cdot N_i \cdot \Phi(\varphi, \theta, a, \gamma)_{p^s, p^i} \cdot \Im. \tag{3.27}$$

Additionally it is often useful to use unit wavelength instead of wavenumber; then Eq. 3.27 becomes:

$$I(\varphi, \theta)_{p^s, p^i} = k_\lambda \cdot \lambda_s^{-3} \cdot \lambda_0^{-1} \cdot N_i \cdot \Phi(\varphi, \theta, a, \gamma)_{p^s, p^i} \cdot \Im. \tag{3.28}$$

The constants and variables are summarized in the following list.

$(\varphi, \theta)_{p^s, p^i}$**:** The parameters p^s and p^i indicate the line polarization plane of the scattered and incident light, while φ and θ describe the direction of the scattered beam relative to the scattering plane (see Figure 3.3).

k_λ, $k_{\tilde{\nu}}$**:** Constants, where k_λ is given as

$$k_\lambda = \frac{\pi^2}{\epsilon_0^2} \approx 1.259 \cdot 10^{23} \mathrm{m^2 F^{-2}} \tag{3.29}$$

with ϵ_0 being the permittivity of vacuum.

λ_0, $\tilde{\nu}_0$**:** The wavelength/wavenumber of the incident light.

λ_s, $\tilde{\nu}_s$**:** The wavelength/wavenumber of Raman scattered light with

$$\tilde{\nu}_s = \tilde{\nu}_0 - \Delta\tilde{\nu}_i \tag{3.30}$$

$\Delta\tilde{\nu}_i$ denotes the Raman shift corresponding to a certain molecular state i.

N_i: The population factor, which is given as

$$N_i(E_i) = N \cdot \frac{g_i \exp\left(-\frac{E_i}{k_b T}\right)}{Z} \tag{3.31}$$

and represents the number of molecules in the initial state in thermodynamic equilibrium and is defined by a Boltzmann distribution. Here N is the total number of molecules irradiated, g_i is the statistical weight of the initial state, k_b is the Boltzmann constant, T is the temperature of the sample, E_i is the energy of the initial state and Z is the molecular partition function

$$Z = \sum_j g_j \exp\left(-\frac{E_j}{k_b T}\right). \tag{3.32}$$

The statistical weight consists of a rotational and a vibrational part, namely

$$g_i = g_{J''} \cdot g_\nu. \tag{3.33}$$

For diatomic molecules, the vibrational states are non-degenerate, and therefore $g_\nu = 1$, while the statistical weight $g_{J''}$ depends on the rotational quantum number J'' and the nuclear spin degeneracy g_N:

$$g_{J''} = g_N \cdot (2J'' + 1). \tag{3.34}$$

At this point, a distinction between heteronuclear (*e.g.* $\mathrm{HT}, \mathrm{DT}, \mathrm{DT}$) and homonuclear (*e.g.* $\mathrm{T_2}, \mathrm{D_2}, \mathrm{H_2}$) molecules has to be made. For heteronuclear molecules $g_N = 1$. In the case of homonuclear molecules g_N is J''-depended and different for molecules with two fermionic nuclei ($\mathrm{T_2}, \mathrm{H_2}$) or two bosonic nuclei ($\mathrm{D_2}$). The values are

$$\mathrm{T_2}, \mathrm{H_2}: \quad g_N = 1, 3 \quad \text{for} \quad J'' = \text{even, odd,} \tag{3.35}$$

$$\mathrm{D_2}: \quad g_N = 6, 3 \quad \text{for} \quad J'' = \text{even, odd.} \tag{3.36}$$
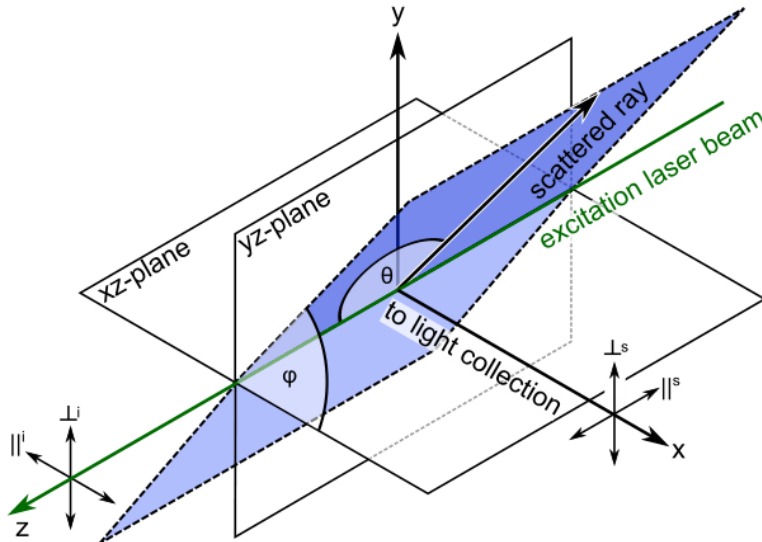
Figure 3.3.: Scattering angles for Raman emission relative to the polarization plane. Details are given in the main text. Reprinted with permission from [Sch14]. Copyright 2014 Springer International Publishing Switzerland.

$\Phi(\varphi, \theta, a, \gamma)_{p^s, p^i}$**:** The line strength functions, which depend on the experiment's geometry and light polarization. The tensor invariants, the mean polarizability a and the polarizability anisotropy γ, are specific for each isotopologue and its molecular transitions. The four line strength functions are [Lon02]

$$\Phi(\varphi, \theta, a, \gamma)_{\perp^s, \perp^i} = a^2 \cos(\varphi)^2 + b^{(2)} \frac{\gamma^2}{45} \left(4 - \sin(\varphi)^2 \right), \tag{3.37}$$

$$\Phi(\varphi, \theta, a, \gamma)_{\perp^s, \|^i} = a^2 \sin(\varphi)^2 + b^{(2)} \frac{\gamma^2}{45} \left(3 + \sin(\varphi)^2 \right), \tag{3.38}$$

$$\Phi(\varphi, \theta, a, \gamma)_{\|^s, \|^i} = a^2 \cos(\varphi)^2 \cos(\theta)^2 + b^{(2)} \frac{\gamma^2}{45} \left(3 + \cos(\theta)^2 \cos(\varphi)^2 \right), \tag{3.39}$$

$$\Phi(\varphi, \theta, a, \gamma)_{\|^s, \perp^i} = a^2 \cos(\theta)^2 \sin(\varphi)^2 + b^{(2)} \frac{\gamma^2}{45} \left(3 + \cos(\theta)^2 \sin(\varphi)^2 \right). \tag{3.40}$$

The factor $b^{(2)}$ is the so-called Placzek-Teller factor and is given as

$$b^{(2)} = \frac{J(J+1)}{(2J-1)(2J+3)} \tag{3.41}$$

for the rotational quantum number J.

$\mathfrak{I}$**:** The irradiance of the incident light. It cancels out during further calculations and has no significance, other than magnifying the Raman signal amplitude. However, for very high irradiance values, non-linear effects may not be negligible.

3.1.3. Quantitative Raman spectroscopy of hydrogen isotopologues

In the previous sections the theoretical structure of Raman spectra for diatomic molecules was explained. This section shifts the focus to experimental aspects, delving into how Raman spectroscopy is employed in the KATRIN experiment, to accurately extract quantitative information on tritium gas mixtures' composition from measured Raman spectra. Throughout the KATRIN measurement runs, the KATRIN LARA system operates autonomously with real-time data analysis, to supply data for neutrino mass analysis and provide feedback to Inner Loop operators. This section summarizes the quantitative evaluation of Raman spectra in the KATRIN experiment and the current status.

Due to the substantial mass differences between the hydrogen isotopes H, D, and T (mass ratio 1:2:3), the Q_1-branches of the isotopologues do not overlap, making them promising candidates for quantitative analysis, see Figure 3.4. With 532 nm laser irradiation, these branches are situated between 612 nm (T_2) and 683 nm (H_2), falling within a visible spectrum range of optical spectrometers and detectors, with sufficient resolution and sensitivity. Additional advantages of the Q_1-branches over other Raman branches are detailed in Refs. [Sch09; Sch14; Fis14]. The optical spectrometer used in the KATRIN LARA system permits the recording of all Q_1-branches within a single spectrum acquisition, although it may not fully resolve the rotational substructure of individual branches. Consequently, the integrals over complete Q_1-branches serve as the basis for quantitative Raman spectrum analysis.

Taylor et al. [Tay01] initiated the development of the KATRIN LARA system, later extended by Lewis [Lew08]. This system was first tested under KATRIN-like conditions in 2010 during the LOOPINO experiment [Fis11]. The test demonstrated a relative precision of 0.1 % within 250 s acquisition time, which was later improved to 60 s [Sch14]. During the first KATRIN tritium campaigns [Ake20a] it met all operational and stability requirements [Ake20b]. Rupp et al. [Rup16; Sim15] carried out further studies to enhance detection limits and reduce measurement time using a capillary Raman system.
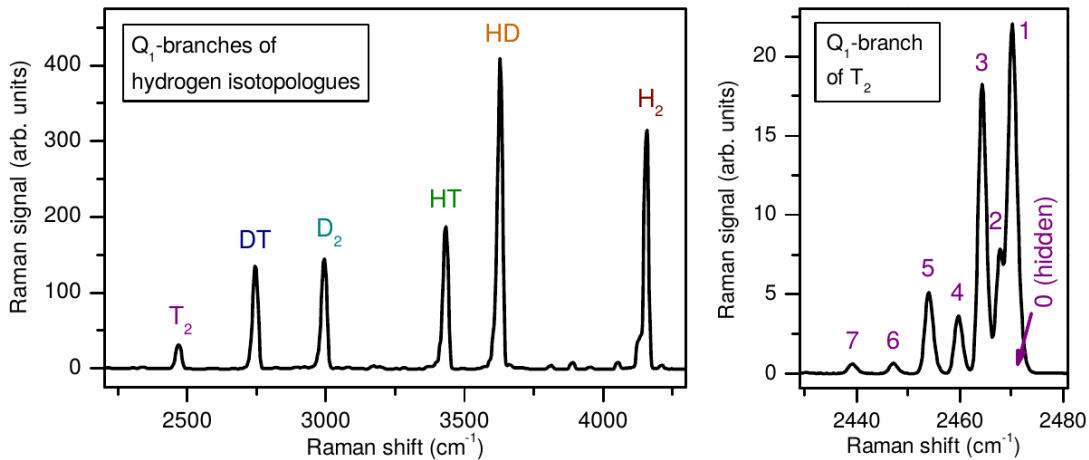
Figure 3.4.: Q_1-branches of the hydrogen isotopologues and a high-resolution spectrum of the Q_1-lines of T_2. Details are given in the main text. Reprinted with permission from [Sch14]. Copyright 2014 Springer International Publishing Switzerland.

In summary, Raman spectroscopy has become a valuable tool for monitoring gas composition in KATRIN, with further potential applications and improvements. A basic LARA system comprises an excitation laser source, sample cell, collection optics, spectrometer, and detector. For monitoring hydrogen isotopologues, the focus is on Q_1-branches with no change in rotational quantum number J (J" = J'). This choice offers several advantages: clear separation between isotopologues, minimal interference from background spectral features, and suitability for real-time gas sampling. A typical spectrum of Q_1-branches for all six hydrogen isotopologues is shown in Figure 3.4. Although overlaps exist, they can be corrected for composition monitoring [Stu10a; Ake20b]. This correction of spectral features overlapping with the Q_1-branches is presented in Section 4.1.3. In general, Section 4.1 discusses the detection setup and Section 4.1.4 the calibration for molar fraction determination.

3.2. Theory of Raman scattering in graphene

In this section, the Raman scattering in graphene is described. The detailed theoretical analysis for diatomic molecules that was given in Section 3.1 is necessary for the quantitative Raman spectroscopy, needed for the KATRIN experiment. In contrast, at this stage, the graphene samples are only analyzed qualitatively to develop an understanding of the graphene-tritium interaction. Similarly, this section only covers the classical and empirical description of Raman spectroscopy of graphene that is necessary for the qualitative analysis, following mainly Refs. [Jor11; Top18]. The quantum mechanical interpretation and derivation can be found in *e.g.* Refs. [Jor11; Yu10; Kit18].

3.2.1. Basics of Raman spectroscopy in solids

In analogue fashion to the derivation of Raman scattering for diatomic molecules (Section 3.1), Raman scattering for solids is derived here. The main difference is that instead of the induced dipole moment μ, the electric susceptibility χ of the material is considered. In the basic application, χ is defined by

$$\mathbf{P} = \varepsilon_0 \chi \mathbf{E} \qquad (3.42)$$

where $\mathbf{P}$ is the induced polarization density, ϵ_0 is the electric permittivity of free space and $\mathbf{E}$ is the electric field. Note that – as pointed out in the introduction to this chapter – in

materials where the susceptibility is anisotropic (i.e., depending on direction), the global susceptibility value χ needs to be replaced by the susceptibility tensor, $\bar{\bar{\chi}}$.

In the presence of an electromagnetic field

$$\mathbf{E}(\mathbf{r}, t) = \mathbf{E}_i(\mathbf{k}_i, \omega_i) \cos(\mathbf{k}_i \cdot \mathbf{r} - \omega_i t) \tag{3.43}$$

the polarization

$$\mathbf{P}(\mathbf{r}, t) = \mathbf{P}(\mathbf{k}_i, \omega_i) \cos(\mathbf{k}_i \cdot \mathbf{r} - \omega_i t) \tag{3.44}$$

is induced. The wavevector and frequency are the same as those of the incident ration, while the amplitude is given by

$$\mathbf{P}(\mathbf{k}_i, \omega_i) = \chi(\mathbf{k}_i, \omega_i) \mathbf{E}_i(\mathbf{k}_i, \omega_i). \tag{3.45}$$

The atomic vibrations in a solid can be quantized into overarching phonons, see *e.g.* Refs. [Yu10; Kit18]. The atomic displacements $\mathbf{Q}(\mathbf{r}, t)$ by the phonons traveling through the material can be expressed as plane waves:

$$\mathbf{Q}(\mathbf{r}, t) = \mathbf{Q}(\mathbf{q}, \omega_0) \cos(\mathbf{q} \cdot \mathbf{r} - \omega_0 t) \tag{3.46}$$

with frequency ω_0 and wavevector $\mathbf{q}$. The atomic vibrations affect χ. Assuming, similar to Section 3.1, that the amplitudes of the vibrations are small compared to the lattice constant, χ can be written as a Taylor series in $\mathbf{Q}(\mathbf{r}, t)$:

$$\chi(\mathbf{k}_i, \omega_i, \mathbf{Q}) = \chi_0(\mathbf{k}_i, \omega_i) + \left(\frac{\partial \chi}{\partial \mathbf{Q}}\right)_0 \mathbf{Q}(\mathbf{r}, t) + \ldots \tag{3.47}$$

with χ_0 defined as the electric susceptibility of the medium with not fluctuations. Using the Taylor expansion, the polarization can be written as:

$$\mathbf{P}(\mathbf{r}, t, \mathbf{Q}) = \underbrace{\overset{\text{in phase with incident radiation}}{\chi_0(\mathbf{k}_i, \omega_i) \mathbf{E}_i(\mathbf{k}_i, \omega_i) \cos(\mathbf{k}_i \cdot \mathbf{r} - \omega_i t)}}_{\mathbf{P}_0(\mathbf{r}, t)} \tag{3.48}$$

$$+ \underbrace{\overset{\text{induced by the phonon}}{\left(\frac{\partial \chi}{\partial \mathbf{Q}}\right)_0 \mathbf{Q}(\mathbf{r}, t) \mathbf{E}_i(\mathbf{k}_i, \omega_i) \cos(\mathbf{k}_i \cdot \mathbf{r} - \omega_i t)}}_{\mathbf{P}_{\text{ind}}(\mathbf{r}, t, \mathbf{Q})}$$

Finally, by substituting $\mathbf{Q}(\mathbf{r}, t)$ from Eq. 3.46, the induced polarization wave $\mathbf{P}_{\text{ind}}(\mathbf{r}, t, \mathbf{Q})$ can be written as

$$\mathbf{P}_{\text{ind}}(\mathbf{r}, t, \mathbf{Q}) = \left(\frac{\partial \chi}{\partial \mathbf{Q}}\right)_0 \mathbf{Q}(\mathbf{q}, \omega_0) \cos(\mathbf{q} \cdot \mathbf{r} - \omega_0 t) \times \mathbf{E}_i(\mathbf{k}_i, \omega_i) \cos(\mathbf{k}_i \cdot \mathbf{r} - \omega_i t) \tag{3.49}$$

$$= \frac{1}{2} \left(\frac{\partial \chi}{\partial \mathbf{Q}}\right)_0 \mathbf{Q}(\mathbf{q}, \omega_0) \mathbf{E}_i(\mathbf{k}_i, \omega_i) \tag{3.50}$$

$$\times \left\{ \cos\left[(\mathbf{k}_i + \mathbf{q} \cdot \mathbf{r}) - (\omega_i + \omega_0)t\right] + \cos\left[(\mathbf{k}_i - \mathbf{q} \cdot \mathbf{r}) - (\omega_i - \omega_0)t\right] \right\}.$$

Here, similar to Eq. 3.9, two different parts can be identified: The Stokes-shifted part with wavevector $\mathbf{k}_S = (\mathbf{k}_i - \mathbf{q})$ and frequency $\omega_S = \omega_i - \omega_0$ and the anti-Stokes part with wavevector $\mathbf{k}_{AS} = (\mathbf{k}_i + \mathbf{q})$ and frequency $\omega_{AS} = \omega_i + \omega_0$. Again, similar to the measurement of diatomic molecules, in this work only the Stokes Raman process is relevant, since it is the dominant process at room temperature without additional excitations of the sample. Also, the related spectral features would be suppressed by the long-pass edge-filter utilized in these experiments, see Chapter 4.

Allowing for n phonons with wavevectors $\mathbf{q}_1, ..., \mathbf{q}_n$ to take part in the Raman process, the energy and momentum conservation laws can be written as

$$\omega_i = \omega_{\mathrm{S}} + \sum_{i=1}^{n} \omega_{\mathbf{q}_i} \quad \text{and} \quad \mathbf{k}_i = \mathbf{k}_{\mathrm{S}} + \sum_{i=1}^{n} \mathbf{q}_i. \tag{3.51}$$

The final state contains one photon with wavevector $\mathbf{k}_{\mathrm{S}}$, energy $\varepsilon_{\mathrm{S}} = \hbar\omega_{\mathrm{S}}$ and frequency ω_{S}. From this derivation, the qualitative Raman spectra in graphene can be described and understood. Using a quantum mechanical approach, the equations for the width, position, and intensity of the Raman peaks can be derived in principle, (see *e.g.* Refs. [Fer13; Ven11; Yu10]). However, for the quantitative studies in this work, these exact calculations are not needed.

3.2.2. Electronic properties of graphene

Graphene was first produced in 2004 by Novoselov and Geim [Nov04]. In 2010, they were awarded the Nobel Prize in Physics '*for groundbreaking experiments regarding the two-dimensional material graphene*'[1]. Graphene consists of a single layer of carbon atoms. The carbon atoms are arranged in a two-dimensional, hexagonal honeycomb structure, as shown in Figure 3.5a. In the crystalline phase, the electronic configuration of carbon is $1\mathrm{s}^2$, $2\mathrm{s}^2$, $2\mathrm{p}^2$. In the pristine graphene lattice, these orbitals are hybridized to sp^2. The sp^2 orbitals form σ-bonds with each other, see Figure 3.5b. Each carbon atom also has a p-orbital projecting into the vertical plane, which is formed by the fourth valence electron. The p-orbitals form the weaker π-bonds with each other, see Figure 3.5c. However, in the presence of defects - *e.g.* edges, vacancies, or adsorbents - the hybridization changes to sp^3.

In the reciprocal space (*e.g.* Ref. [Kit18]), the unit cell can be described by two basis vectors, $\mathbf{a}_1$ and $\mathbf{a}_2$. Starting from these basis vectors and using the tight binding approximation [Sai98; Bet04], it can be shown that the electronic band structure can be described using the equation

$$E_{g2D}^{\pm}(\mathbf{k}) = \frac{\epsilon_{2p} \pm \gamma_0 \omega(\mathbf{k})}{1 \mp s\omega(\mathbf{k})}. \tag{3.52}$$

Here, E_{g2D} is the 2D energy dispersion of graphite, ϵ_{2p} is the site energy of the 2p orbital, $\gamma_0 \approx 2.8\,\mathrm{eV}$ is the nearest neighbor hopping energy, and s the tight-binding overlap integral. $E^{\pm}$ correspond to the valence (π) and conduction (π^*) energy bands. The function $\omega(\mathbf{k})$ is given by

$$\omega(\mathbf{k}) = \sqrt{1 + 4\cos\left(\frac{\sqrt{3}k_x a_0}{2}\right)\cos\left(\frac{k_y a_0}{2}\right) + 4\cos^2\left(\frac{k_y a_0}{2}\right)}. \tag{3.53}$$

In Eq 3.53, k_x, k_y represent the in-plane components of the wave vector $\mathbf{k}$, $a_0 = 1.42\,\text{Å}$ is the lattice constant. The π^*- and π-bands touch at the six corners of the hexagonal first Brillouin zone, known as the K-and K'-points (Figure 3.5d). These are called Dirac points. These Dirac points are crucial to the electronic transport in graphene, serving a role analogous to that of Γ-points in direct band-gap semiconductors. Close to the Dirac points the dispersion relation for graphene is linear, and the Fermi energy is given by

$$E_{\mathrm{F}} = \hbar v_{\mathrm{F}} k_{\mathrm{F}} = \hbar v_{\mathrm{F}} \sqrt{\pi n_{g,2D}}. \tag{3.54}$$

The carrier concentration is denoted as $n_{g,2D}$ and $v_{\mathrm{F}} \approx 1 \times 10^6\,\mathrm{m\,s^{-1}}$ is the Fermi velocity. The linear dispersion relation implies that charge carriers in graphene behave like massless Dirac fermions. The electron band structure is shown in Figure 3.5e.

---

[1]The Nobel Prize in Physics 2010. NobelPrize.org. Nobel Prize Outreach AB 2023. Mon. 6 Nov 2023. https://www.nobelprize.org/prizes/physics/2010/summary/

(a)   **(b)**   **(c)**

(d)   **(e)**
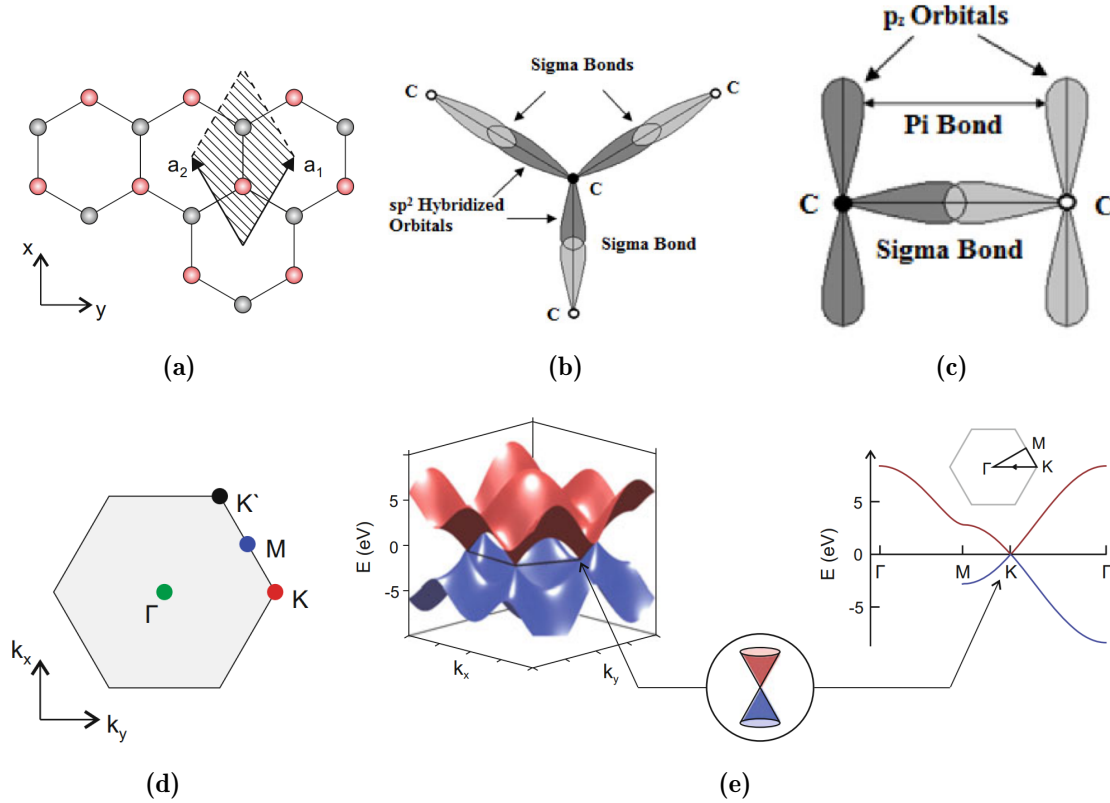
Figure 3.5.: Electronic band structure of graphene. Illustrations of: (a) The graphene lattice. The shaded region indicates a unit cell spanned by the vectors $\vec{a}_1$ and $\vec{a}_2$. (b) The sp^2 hybridized orbitals of carbon atoms between nearest neighbors. (c) The orbitals of the remaining electrons forming π bonds. (d) First Brillouin zone corresponding to the unit cell with high symmetry points Γ, K, K' and M. (e) *Left:* The resulting electronic band structure. The valence band (π) is shown in blue and the conduction band (π^*) in red. The linear dispersion relation at the Dirac points (K, K') is shown in the inset. *Right:* Cut of the 3D view along the high symmetry points. Reprinted (a,d,e) with permission from [Neu18]. Copyright 2018 Springer International Publishing AG. Images (b,c) adapted from [Das14].

3.2.3. Phonon modes in graphene

A crystal with $N \geq 2$ different atoms in the primitive cell exhibits three acoustic modes: one longitudinal (LA) and two transverse acoustic (TA) modes. The number of optical modes is given by $3N - 3$ [Kit18]. For graphene with $N = 2$ different atoms in the primitive cell (Figure 3.5a), there are three optical modes (iLO, iTO, oTO), one longitudinal acoustic mode (iLA) and two transverse acoustic modes (iTA, oTA). Here, **i** and **o** denote **i**n-plane and **o**ut-of-plane phonons. The phonon dispersion is shown in Figure 3.6. Due to the crystallographic symmetry and the resulting selection rules, only the iLO and iTO phonon branches are Raman active [Fer13]. For first-order Raman processes within a defect-free graphene lattice only phonons at the center of the first Brillouin zone, i.e. at the Γ-point, can contribute. At the Γ-point, tthe iLO and iTO modes are degenerate. In real space, these phonons correspond to vibrations of the two sublattices against each other. The phonon at the K-point corresponds to the radial breathing motion of the lattice hexagon. While not directly Raman active, this phonon plays a crucial role for the D and 2D Raman peaks of graphene.
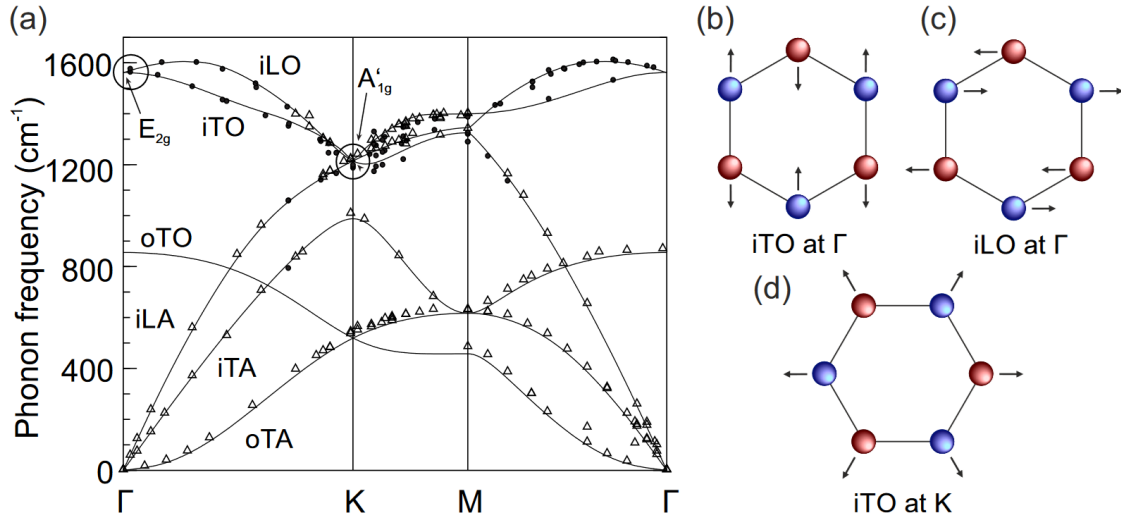
Figure 3.6.: The phonon dispersion of graphene and illustrations of phonon modes. (a) The phonon dispersion is obtained from DFT-GW (density functional theory supplemented by GW) calculations by Venezuela *et al.* [Ven11]. The phonon modes most relevant to Raman spectroscopy of graphene at the Γ- and K-points are highlighted. (b,c) Degenerate phonon modes iTO and iLO at the Γ-point that contribute to the G-peak in the Raman spectrum. (d) Breathing mode (iTO) at the K-point that contributes to the 2D-peak in the Raman spectrum. Reprinted figure (a) with permission from [Neu18]. Copyright 2018 Springer International Publishing AG. Reprinted figure (b) with permission from [Ven11]. Copyright 2011 by the American Physical Society.

3.2.4. Raman spectroscopy of graphene

In the case of defect-free graphene, the sum of the wavevectors of the phonons must be zero:

$$\sum_{i=1}^{n} \mathbf{q}_i = 0. \tag{3.55}$$

Note that the wavevectors of the photons are negligible and do not need to be considered in the momentum conservation law. If defects are present in the sample, the sum of the wave vectors can be different from zero due to electronic scattering at defects. The most prominent Raman processes in graphene involve at maximum two phonons, and only these are described in the following. The corresponding peaks in the Raman spectrum are shown in Figure 3.7.

G-peak: related to one-phonon processes without defects. When only one phonon is involved, it follows from the conservation of momentum (Eq. 3.55) that the phonon momentum has to be equal to zero. Therefore, the phonon must be from the Brillouin zone center (Γ-point). As evidenced in Figure 3.6, the frequencies of acoustic phonons vanish at the Γ-point. From horizontal mirror symmetry, the out-of-plane phonon (oTO) is forbidden. Therefore, for the one-phonon processes the two degenerate, optical in-plane phonons at the Γ-point, iLO and iTO, contribute. Due to the rotation symmetry, they possess the same energy and lead to the same Raman shift. If the rotation-symmetry is broken, *e.g.* by strain in the graphene layer, the degeneracy is broken and the corresponding Raman peak splits. The Raman peak corresponding to these two one-phonon processes is the so-called G-peak, located at around $1580\,\mathrm{cm^{-1}}$ in the Raman spectra of graphene.

The process giving rise to the G-peak can be described in three steps:

1. A photon with energy ε_{in} is absorbed by graphene and creates an electron/hole pair. The electron in the π-band is resonantly excited to the π^*-band.

2. The electron loses energy to a phonon of wave vector $\mathbf{q} = 0$ and transits into a virtual state in the π^*-band.

3. The electron recombines with the hole and emits a photon of lower energy ε_{out}.

2D-peak: related to two-phonon processes without defects. When two phonons are involved, it follows from Eq. 3.55 that $\mathbf{q}_1 = -\mathbf{q}_2 \equiv \mathbf{q}$, i.e., the wave vectors of the phonons need to be oriented in opposite directions. There are no further constrains on $\mathbf{q}$ and it can correspond to any point in the Brillouin zone. As a consequence, the two-phonon peaks are broader than the G-peak since a continuum of phonon frequencies contributes to them. The most prominent two-phonon peak is the 2D-peak at around $2700\,\mathrm{cm}^{-1}$ with dominant contributions from two phonons of the TO-branch, with $\mathbf{q}$ near the K-point. Other two-phonon processes give rise to the 2D'peak (at $\sim 3200\,\mathrm{cm}^{-1}$) and the D+D''-peak (at $\sim 2450\,\mathrm{cm}^{-1}$). The process giving rise to 2D-peak can be described in four steps:

1. A photon with the energy ε_{in} is absorbed by graphene and creates an electron/hole pair. The electron in the π-band is resonantly excited to the π^*-band.

2. The electron loses energy to a phonon and transits into a virtual state in the π^*-band.

3. The hole loses energy to a phonon and transits into a virtual state in the π-band.

4. The electron recombines with the hole and emits a photon of lower energy ε_{out}.
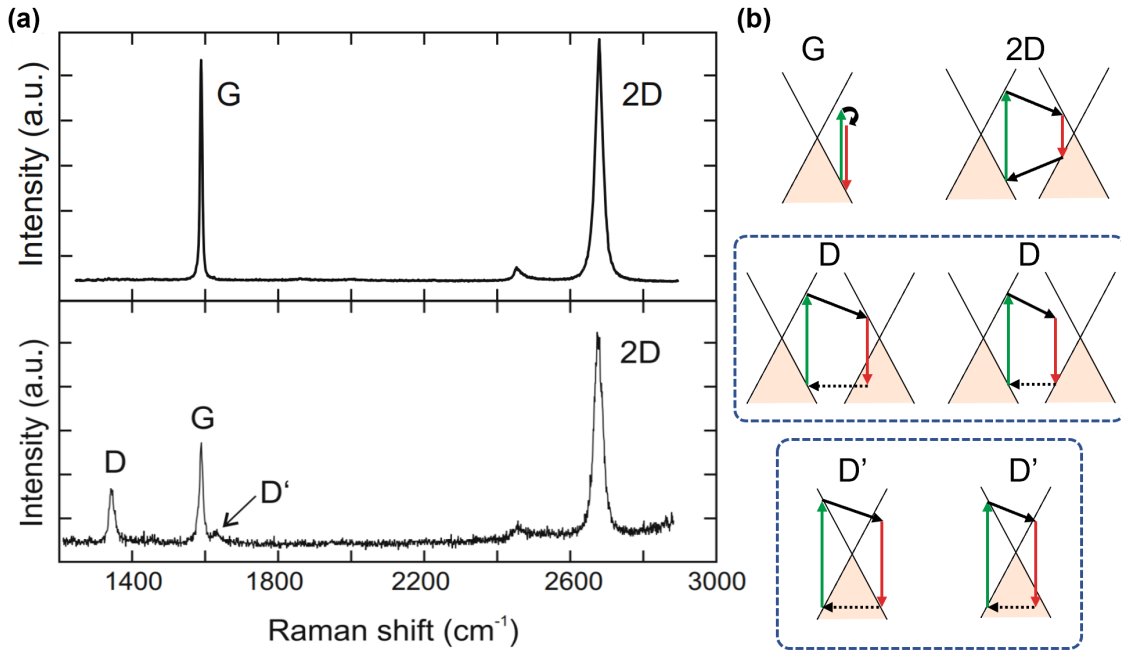
Figure 3.7.: Raman spectra and processes in defect-free and defective graphene. (a) Raman spectra with annotated peaks, *Top:* defect-free, *bottom:* defective. (b) Main corresponding Raman processes: The excitation of electrons by the incident photon is represented by green arrows, the relaxation with the emission of the scattered photon is shown with red arrows. The solid black arrows represent emitted phonons and dashed black arrows phonon scattering on defects. Reprinted figure (a) with permission from [Neu18]. Copyright 2018 Springer International Publishing AG. Figure (b) adapted with permission from [Fer13].

D-peak: related to one-phonon processes with defects. The presence of defects allows phonons away from the Γ-point to contribute to the one-phonon Raman process. The momentum of the phonon can be compensated for by electron-defect scattering. The most prominent peak in this category is the D-peak that is mostly due to a TO-phonon near the K-point and is located around $1350\,\mathrm{cm^{-1}}$ in the Raman spectra of defective graphene. Another peak in this category is the D'-peak (at $\sim 1600\,\mathrm{cm^{-1}}$); the D'-peak can be related to the nature of the defects in graphene, but is often overlapped by the G-peak in low-spectral resolution Raman spectroscopy [Eck12]. This is also the case in this work. The detailed interpretation of the D'-peak is given in Section 3.3.

Two-phonon precesses with defects There are also two-phonon Raman processes, which are only possible in the presence of defects. The two phonons do not have to adhere to $\mathbf{q}_1 = -\mathbf{q}_2$ and thus stem from different points in the Brillouin zone. The most prominent peak in this category is the D+D'-peak (at $\sim 2950\,\mathrm{cm^{-1}}$).

3.2.5. Raman spectroscopy of defective graphene

Raman spectroscopy is a valuable tool to study defective graphene [Fer13; Eck13]. Defective graphene includes *e.g.* strain, doping, edges and defects. However, for this work only edges and defects are relevant.

Edges The first type of defect in graphene, discussed in this section, are edges [Cas09]. Edges can be viewed as extended defects, breaking the translational symmetry and thus leading to the appearance of the D- and D'-peaks. Edges are important to consider in order to understand the Raman spectra from the samples [Gra23a] used in this work. Even though the graphene layer covers the whole $1\,\mathrm{cm^2}$ substrate, the layer is not monolithic, but instead consists of graphene 'flakes' with a maximum size of about $20\,\mathrm{\mu m}$[Gra23a]. When the samples are scanned with the CRM set up and characterized in this work (see Section 4.2 and Chapter 6), it can be assumed that always some flake borders are within within the region illuminated by the laser spot. Therefore, the Raman spectra studied in this work will always have a small D-peak ($I_D/I_G<0.1$) visible, as seen in the data from the manufacturer Figure 3.8.

Defects: In this section, there is no distinction made between sp^3-type and vacancy-type defects. The general characteristic changes in the Raman spectrum of graphene and the description of the defect density covers both defect-types. In Section 3.3 the differences between these defect types are discussed, in particular with respect to hydrogen adsorption.

(a) SEM image   **(b)** Raman spectrum
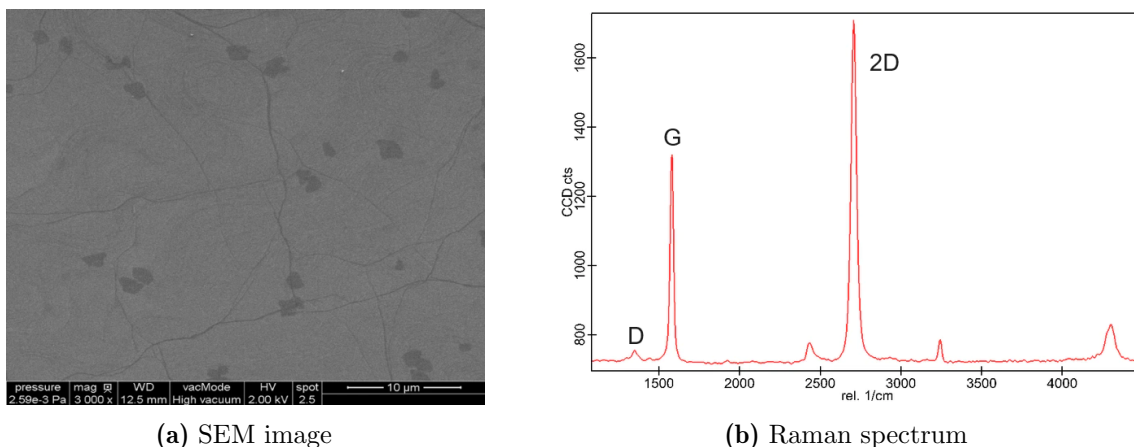
Figure 3.8.: Graphene flakes and edges of graphene samples from *Graphenea*. Reprinted figures with permission from *Graphenea* [Gra23a].

A precise determination of the defect density can be obtained by analyzing the intensity ratio of the D-and G-peaks, (I_D/I_G), for a given excitation energy of the laser [Can11; Luc10]. The respective Raman spectra and the empirical data for different laser energies are shown in Figure 3.9. Based on the work in Ref. [Tui70], the defect density in graphene is usually described by the average distance between two lattice defects, L_D, usually given in units of $[L_D] = $ nm. Using controlled Ar^+-bombardment, an analytic relation between I_D/I_G and L_D was developed [Can11]:

$$\frac{I_D}{I_G} = C_A \frac{r_A^2 - r_S^2}{r_A^2 - 2r_S^2} \left(\exp(-\pi r_S^2/L_D^2) - \exp(-\pi(r_A^2 - r_S^2)/L_D^2) \right) \tag{3.56}$$

Here, r_S is the radius of the **structurally defective area** caused by the impact of an ion; r_A corresponds to the **activated region** where the D-peak scattering occurs, even though the area is intact [Luc10]. The parameter C_A is a scaling factor for the activated region. In this representation, C_A corresponds to the maximum possible I_D/I_G. This maximum would be reached in the ideal case where the D-peak is activated throughout the sample, with no disruption of the hexagonal carbon rings. As shown in the inset in Figure 3.9, C_A strongly depends on the laser energy E_L with $C_A \propto E_L^{-4}$. Using the values found by Cancado *et al.* [Can11], and converting the laser energy E_L to laser wavelength λ_L, Eq. 3.56 can be simplified to

$$L_D^2 \cdot (\text{nm}^2) = (1.8 \pm 0.5) \times 10^{-9} \cdot \lambda_L^4 \cdot \left(\frac{I_D}{I_G} \right)^{-1} \tag{3.57}$$

and using $n_D \cdot (\text{cm}^{-2}) = 10^{14}/(\pi L_D^2)$ the defect density is given by

$$n_D^2 \cdot (\text{cm}^{-2}) = (1.8 \pm 0.5) \times 10^{22} \cdot \frac{1}{\lambda_L^4} \cdot \left(\frac{I_D}{I_G} \cdot \right) \tag{3.58}$$

These equations hold true for $L_D > 10\,\text{nm}$ (Stage 1 of graphene defects) and for all defects that contribute to the D-peak signal.
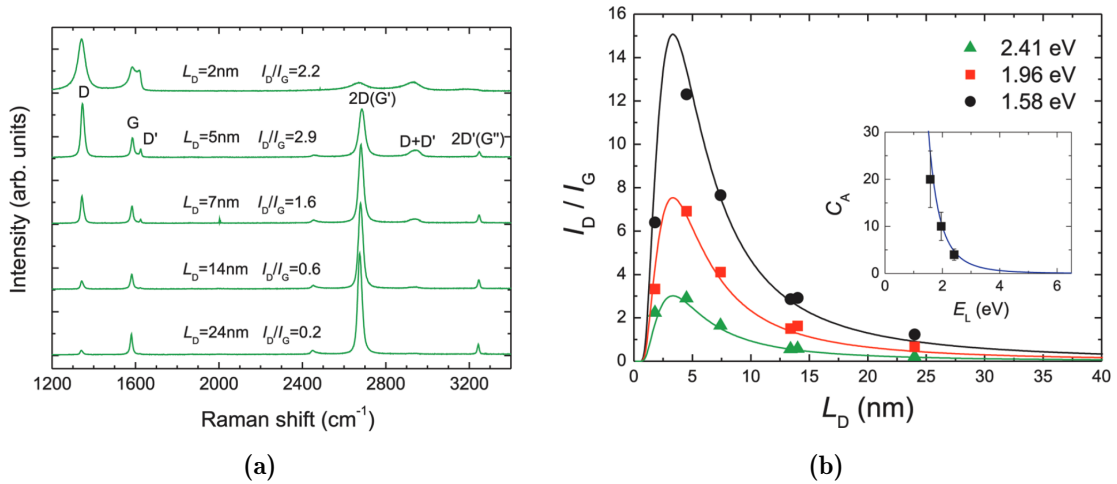
Figure 3.9.: Defect density in graphene in relation to the D/G-peak ratio. (a) Raman spectra for different defect densities, and (b) D/G-peak ratio over defect density for different laser energies. Details can be found within the main text. Reprinted with permission from [Can11]. Copyright 2011 American Chemical Society.

3.2.6. Raman spectroscopy of multi-layer graphene

Raman spectroscopy can also be used to determine the number of layers in multi-layer graphene. In the context of thickness analysis, the usual monolayer graphene is referred to as SINGLE-LAYER GRAPHENE (SLG) and graphene with two layers as BILAYER GRAPHENE (BLG).

The 2D-peak is a robust indicator of the number of carbon layers in graphene, due to its close relationship with the number of electronic bands and the precise band structure. For instance, single-layer graphene is typically characterized by a single Lorentzian model for its 2D-peak. In contrast, bilayer graphene exhibits the influence of an expanded number of electronic bands, resulting in the presence of four individual Lorentzian components within its 2D-peak profile. This phenomenon directly emerges from the increased electronic bands and the associated Raman processes (see Figure 3.10). Depending on the spectral resolution of the Raman system, used for analysis, this change may only be hinted at by broadening of the 2D-peak profile envelope. However, even with a low-spectral resolution Raman system, the line position shift is significant (about 15-30 cm^{-1} depending on the laser wavelength).

This common description is only valid for a specific stacking of bilayer graphene (so-called *Bernal*) or AB stacking; see Figure 3.10b) [Pon08; Pon09; Mal09]. In misoriented bilayer graphene the characteristics of a Bernal bilayer are completely lost, and the 2D-line shape is more typical of monolayer graphene with no broadening, as shown in Figure 3.10c. In addition, in the misoriented bilayer, the line position shift is only about 9 cm^{-1}.

In Section 6.8 multi-layer graphene samples from *Graphenea*[2] are characterized with the CRM. In addition, it is studied if in SLG overlapping regions can be identified.
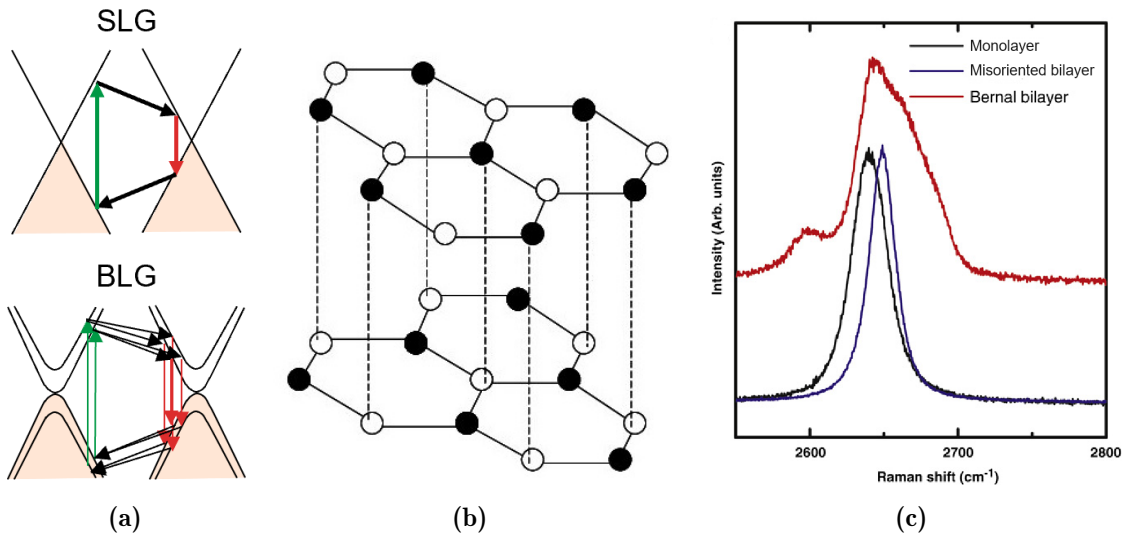
Figure 3.10.: Differences in the 2D-peak shape for single- and multi-layer graphene. (a) Relevant Raman processes in SLG and BLG; (b) Structure of Bernal (AB) stacking; and (c) Typical Raman spectra of SLG, misoriented BLG and Bernal stacked BLG. Figure (a) based on [Top18]. Reprinted figure (b) with permission from [Yan11]. Copyright 2011 by the American Physical Society. Reprinted figure (c) with permission from [Pon08]. Copyright 2008 by the American Physical Society.

---

[2]Graphenea Inc., San Sebastián, Spain

3.3. Characteristic changes for hydrogenated graphene

Hydrogenation (Tritiation) of graphene is defined as the adsorption of atomic hydrogen, H (tritium, T) on the graphene surface by formation of covalent bonds between the H (T) atom and one carbon (C) atom of graphene. Fully hydrogenated graphene is also referred to as 'graphane'. Although a range of possible configurations for graphene exist (including *chair*, *boat*, *armchair*, *stirrup*, ...[Sah15]), the differences will not be discussed here any further. This is because the measurement equipment at present does not allow to identify them. Specifically, the CRM (Section 4.2 and Chapter 6) used in this work does neither possess sufficient spectral nor the spatial resolution to distinguish the different graphane configurations.

In principle, there are a range of basic analysis methods which may be used to characterize the hydrogenation of graphene; in this work two methods are used, namely electronic (resistance) measurements and Raman analysis.

Electronic measurements: By hydrogenation, the electron, and phonon dispersion of graphene change significantly. The changes depend on the amount of hydrogenation and on the graphane configuration. As a consequence of the hydrogen-carbon bonds, the π electrons are no longer available as charge carriers, which leads to an increase in the electrical sheet resistance with increasing hydrogenation levels, see *e.g.* Refs. [Gui14; Son16]. This measurement methodology was used for *in-situ* monitoring of the tritiation progress, as discussed in Chapter 7.

Raman analysis: A consequence of the hydrogenation is hybridization of the corresponding carbon atom from sp^2- to sp^3-configuration. This change of hybridization is associated with a local deformation of the graphene layer. As a direct consequence of this symmetry breaking, the D-peak Raman processes are possible and the 2D-peak Raman processes are less likely.
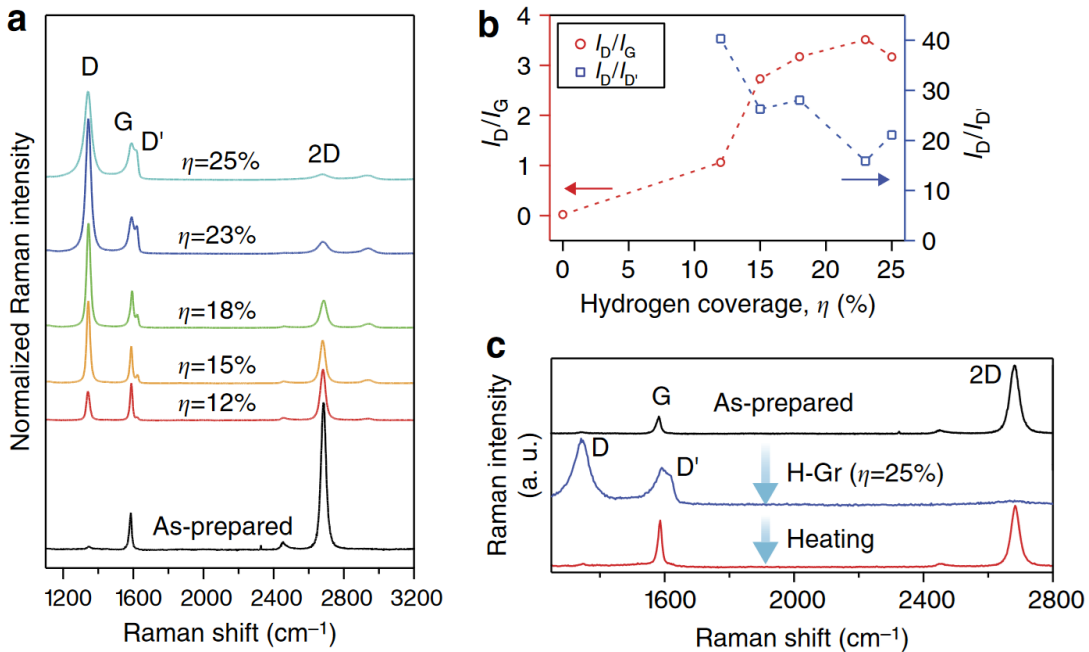
Figure 3.11.: Raman parameters of graphene with different hydrogenation levels. (a) Raman spectra for increasing hydrogenation levels, (b) D/G-peak ratio and D/D'-peak ratio as a function of hydrogen coverage, (c) Raman spectra of hydrogenated and heated graphene, demonstrating the reversible hydrogenation. Images adapted from [Son16].

According to Figure 3.9 an increasing defect density leads to an increase of the D-peak intensity and the D/G-peak ratio in the low defect density regime ($L_D > 10\,\text{nm}$). To a certain degree, hydrogenation may be interpreted as a 'defect', and the degree of hydrogenation coverage therefore affects the defect density. However, the D/G-peak ratio is not sensitive to the type of defect, and during the tritiation experiments it proved to be difficult to ascertain whether the sample was tritiated, or if other defects were induced during tritium exposure.

In typical hydrogen loading experiments with commercially available atomic hydrogen sources, the hydrogenation can be performed without creating vacancy-type defects when the source intensity and energy are set appropriately [Cha22]. In principle, this could also be achieved with an atomic tritium source, but at the time of writing, no such source did exist. The development of an atomic tritium source is the goal of *e.g.* the 'Project8' collaboration [Mon15].

Instead, in this work, the self-radiolysis of tritium is taken advantage of to produce the needed tritium atoms. This is described in more detail in Section 7.2. The properties of the ions, atoms, and electrons created in the β-decay of tritium cannot be controlled directly. Therefore, it cannot be excluded or avoided that vacancy-type defects are created.

In principle, Raman spectroscopy can be used to distinguish vacancy- and sp^3-type defects [Eck12]. However, as will be shown in Chapter 6, the spectral resolution of the CRM used in this work was insufficient to resolve the D'-peak. Therefore, mainly the intensity of the D-, G- and 2D-peaks and the intensity ratio D/G are used to characterize the defects after tritium exposure. In addition, the width of the 2D-peak is used as an indicator for graphene layers with high symmetry, since the width can broaden significantly in highly damaged graphene [Che13]. Finally, it should be noted that – as shown in Figure 3.11 – hydrogenation of graphene was shown to be largely reversible by heating (see *e.g.* Ref. [Son16]). The same is expected for tritiation.

4. Experimental setup of the Raman systems

In this chapter, the two different Raman systems used in this work are described. In Section 4.1 the LARA system, which was developed for source monitoring in the KATRIN experiment, is covered. This LARA system was developed during the period 2010 – 2020 at the TLK [Stu10a; Fis11; Jam13; Sch14; Fis14] and was already described in great detail [Ake20b]. Therefore, here in this work only the most important characteristics regarding the results presented in Chapter 5 are given: a brief overview and the working principle (Section 4.1.1), the optical setup and components (Section 4.1.2), the data flow within the KATRIN framework (Section 4.1.3) and, lastly, a short summary of the calibration procedure using spectral sensitivity measurements and theoretical calculations (Section 4.1.4).

In contrast to the LARA system, the CRM [Dia22] was constructed and commissioned within the framework of this thesis research, using the experience of the KATRIN LARA group. In particular, the setup and alignment of the CRM were performed together with Deseada Diaz Barrero from the UNIVERSIDAD AUTÓNOMA DE MADRID (UAM). Thus, the CRM is presented and discussed in detail. First, the general principle, the optical components, and the experimental setup are presented in Section 4.2.1. Second, the software requirements and implementations necessary for the operation of the CRM are described in Section 4.3. Finally, in Section 4.4 the data structure obtained from the CRM and the data analysis are explained.

4.1. The KATRIN Laser Raman (LARA) system

4.1.1. Overview and working principle

The KATRIN - its conceptual setup is shown in Figure 4.1 - LARA system is divided into two main sections. These sections are separated by black anodized aluminum walls to prevent light leaking from one segment to another. There are openings in the walls where laser or Raman light needs to pass. Furthermore, the whole setup in enclosed in black anodized aluminum for safety reasons.

Segment A The laser light is directed to the sample cell via two mirrors and focused into the sample cell by a focusing lens. There are several components installed in the beam path to clean and rotate the polarization of the laser light. Additionally, the laser power is monitored; for this, there is a second compartment located after the sample

cell, which is also considered as part of Segment A. In this second compartment a mirror is installed, which back-reflects the laser beam into the sample cell – enabling the so-called double-pass operation mode.

Segment B The second segment is the light collection arm, where the Raman light from the laser excitation region in the sample cell is collected by a fiber bundle, carrying the Raman light to the spectrometer and CCD.

Additionally, there is the sample cell itself. The sample cell is part of the Inner Loop of the WGTS (see Section 2.2.1) and the source gas passes through the cell before injection into the WGTS. For intensity calibration and beam alignment, the sample cell can be replaced by a calibration cell (Figure 4.2).

4.1.2. Components and optical setup

Segment A - Excitation laser

Laser The laser is a diode pumped solid state (DPSS), continuous wave (cw) laser with a maximal output power of 5 W, at the nominal output wavelength of 532 nm. Although the laser itself is located in Segment B, there is no visible laser light in Segment B: the opening of the laser sits flush with a laser shutter system, which again is flush against the wall between the segments. Here the laser light enters Segment A.

Mirrors (M1 and M2) The two mirrors are used to guide and align the laser beam.

Optical isolator (OI) An optical isolator consists of two polarizers and a Faraday rotator. The polarization of the laser beam is rotated twice by 45° as it passes through
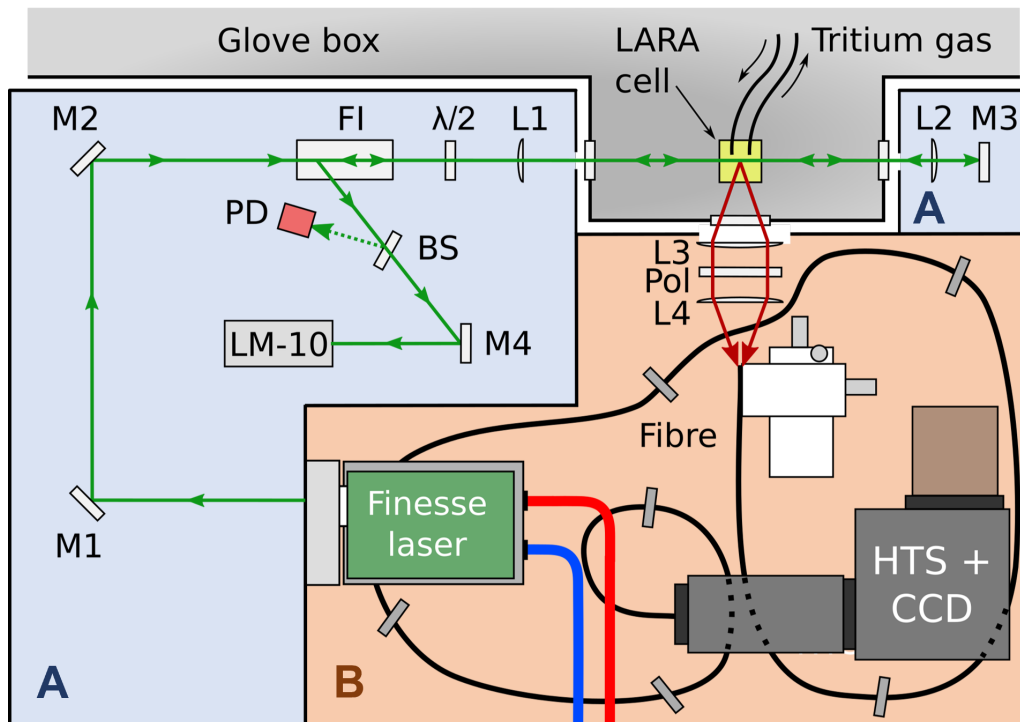
Figure 4.1.: Experimental setup of the KATRIN LARA system. The setup is be divided into Segment A (Laser beam guidance) and Segment B (Raman light collection). Relevant elements are annotated; further details are given in the main text. Image adapted from [Fis14].

the Faraday rotator in the forward and backward directions. As a result, the first polarizer blocks the return beam. In this setup, the blocked beam is not absorbed internally by the polarizer but is deflected sideways to be dumped. This dumped beam is conveniently used for external power monitoring with the LM-10.

Thermopile power meter (LM-10) The reflected laser beam enters a thermopile power meter (LM-10) which absorbs the beam and measures the beam intensity and position.

Half-Wave-plate ($\lambda/2$) The polarization of the laser beam is rotated by a fixed angle. This is useful in two different measurement scenarios: (i) In standard operation the $\lambda/2$-plate is set to a fixed position, which changes the laser light polarization from horizontal to vertical, (ii) For the intensity calibration, the spectrum of the standard reference material (SRM) needs to be measured at $\pm45°$ relative to the position set in standard operation.

Focusing lens L1 The laser beam is focused by an anti-reflection (AR) coated lens of focal length $f = 150\,\mathrm{mm}$ into the sample cell, generating an elongated, near-cylindrical interaction volume of about $6\,\mathrm{mm}$ in length and a beam waist of $\approx 100\,\mathrm{\mu m}$.

Focusing lens L2 This lens is identical to L1. The divergent laser beam is collimated to be reflected by mirror M3 for double-pass operation.

Mirror M3 Reflects the laser beam, which is then focused into the sample cell by L2 for double-pass operation.

Segment B - Raman light collection

Pickup lenses (L3 and L4) Raman light from the elongated excitation volume is focused onto the fiber by a pair of achromatic lenses.

Polarizer The polarization angle is set to match the setting of the $\lambda/2$-plate in standard operation mode for an improved Raman signal. It is inserted in between lenses L3/L4.

Fiber The light passing through the polarizer is collected by an optical fiber bundle. The fiber bundle is custom-fabricated and consists of 48 individual fibers of core diameter $100\,\mathrm{\mu m}$. The individual fibers are arranged in a line ('slit'-configuration) at both ends to match the laser beam profile.
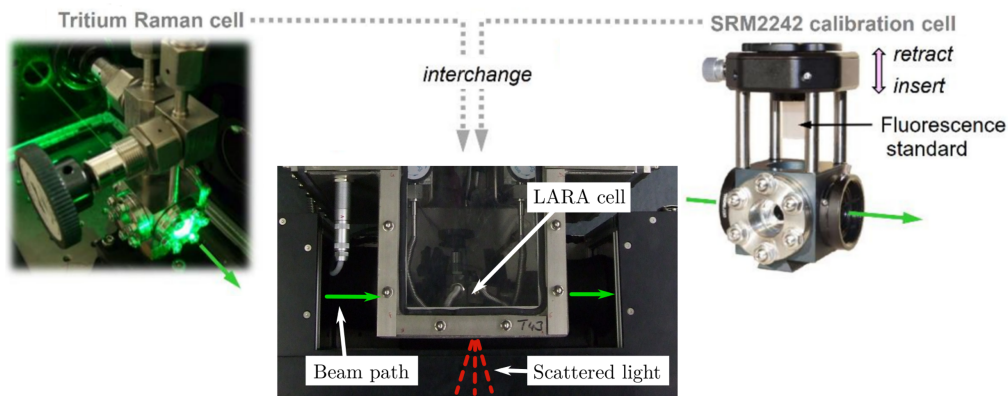
Figure 4.2.: Top view into the glove box appendix, with the LARA cell installed. The laser beam path and the Raman scattered light are indicated. For intensity calibration, the Raman cell can be exchanged with a calibration cell incorporating the SRM 2242 standard. Image adapted from [Fis14; Ake20b].

Spectrometer and charge-coupled device sensor (CCD) For the spectral analysis, a HTS-type spectrometer with large-NA achromatic lens-multiplets (PI Acton) - in combination with a Pixis-2k CCD-array detector (Princeton Instruments) is used.

4.1.3. Description of data analysis and database connection

Similar to the hardware setup the data analysis routine was developed at TLK by Sebastian Fischer, Timothy James and Magnus Schlösser [Jam13; Sch14; Fis14; Sch15a]. The data stream within TLK was later developed and finalized by Sebastian Fischer. The system control, recording of operating parameters, Raman spectrum acquisition, and real-time data treatment and analysis are under the control of an integrated, dedicated LabVIEW program, LARAsoft. `LARASoft` is the successor to SpecTools [Jam13] and was developed and commissioned by Timothy James, Florian Kassel and Sebastian Fischer [Fis14; Kas13]. Since then, the data analysis routing has been extended by incorporating the ability to deconvolve overlapping spectral lines features [Ake20b].

The concept of the data analysis routine is shown in Figure 4.3. First, the 2D readout of the CCD detector is first cleaned and corrected in several steps. These include (i) region of interest selection, (ii) cosmic ray removal, (iii) astigmatism correction and (iv) intensity calibration. Next, the bins of the 2D data set are summed up to generate a 1D spectrum. The background (*e.g.* from fluorescence) is then removed by the application of the ROLLING CIRCLE FILTER (RCF)- or SAVITZKY–GOLAY COUPLED ADVANCED ROLLING CIRCLE FILTER (SCARF)-algorithm. Optionally, this step can also be performed before the summing of bins. The overlapping spectral lines are removed and the Q_1-lines of the hydrogen isotopologues are fitted using ShapeFit. Finally, the ShapeFit results are corrected using theoretical calculation data [Roy11] and the source composition is calculated.

Deconvolution of overlapping spectral lines

The deconvolution of overlapping spectral lines in `LARASoft` is based on a method and calculations from Helmut H. Telle (see Ref. [Ake20b]). The mathematical description is given in Section 3.1.2 and the required, relevant numeric values can be found in [Lon02; Fis14; Sch14]. Under standard KATRIN operating conditions ($c(T_2) > 90\,\%$), only the interference between DT Q_1- and T_2 $S_1(2)$-lines is relevant for the determination of isotopologue concentrations. Therefore, the implementation is exemplified using this interference using KNM1 LARA data (Figure 4.4). Assuming that the intensity ratio of the calculated overlap-line (OL) and the reference-line (RL) replicates the intensity ratio of the respective measured lines. Note that this assumption is only correct when there are no unknown systematic effects. The unknown overlapping line can be determined by following the listed steps:

1. Fit the reference line(s) with a Gaussian function to determine the line profile and the reference line(s) experimental amplitude(s) $A_1(J''_{\mathrm{RL}})$.

2. Calculate the expected experimental line amplitude $A_1(J''_{\mathrm{OL}})$ of the interfering line according to

$$A_1(J''_{\mathrm{OL}}) = A_1(J''_{\mathrm{RL}}) \cdot \frac{S_1(J''_{\mathrm{OL}})}{S_1(J''_{\mathrm{RL}})}. \tag{4.1}$$

3. Convolve $A_1(J''_{\mathrm{OL}})$ with the line profile determined in the first step.

4. Subtract this line profile from the experimental spectrum, centered at the known position in the spectrum.

In order to consolidate `LARASoft2` and its numerous additions, the software was rewritten from scratch by András Bükki-Deme at TLK. Since this was a large update, the version number was incremented to `LARASoft2`. `LARASoft2` is programmed modular and follows up-to-date National Instruments design principles. The modularity enables `LARASoft2` to be adapted to different measurement systems, *e.g.* as needed for the CRM (Section 4.3).

Connection to the KATRIN database

For the KATRIN experiment, the LARA system is treated as a gas composition sensor and needs to be included in the database structure of the whole experiment [KAT21]. The complete data flow of the LARA data is shown in Figure 4.5.

After every CCD acquisition and the full data analysis, `LARASoft2` collects all the parameters from the different hardware components (laser, power meter, water chiller, temperature sensors) and sends the data to Advanced Data Extraction Infrastructure (ADEI). The ADEI platform integrates all available data sources and makes them available to end users in a unified, understandable and user-friendly fashion [Chi10b]. It should be noted that the data sent to ADEI does not include the raw spectra, the analyzed spectra, and the analysis settings. The distribution/export from the EU of this data is regulated by the Federal Office for Economic Affairs and Export Control (BAFA), due to dual-use possibility. Specifically, data regarding tritium analysis and monitoring cannot be distributed freely, not even within the KATRIN collaboration [Fis14].

For the backup of the protected data, it is bundled with all the data that is sent to ADEI and synchronized to a TLK-internal server (LARA-server) with RAID-5 capabilities. The
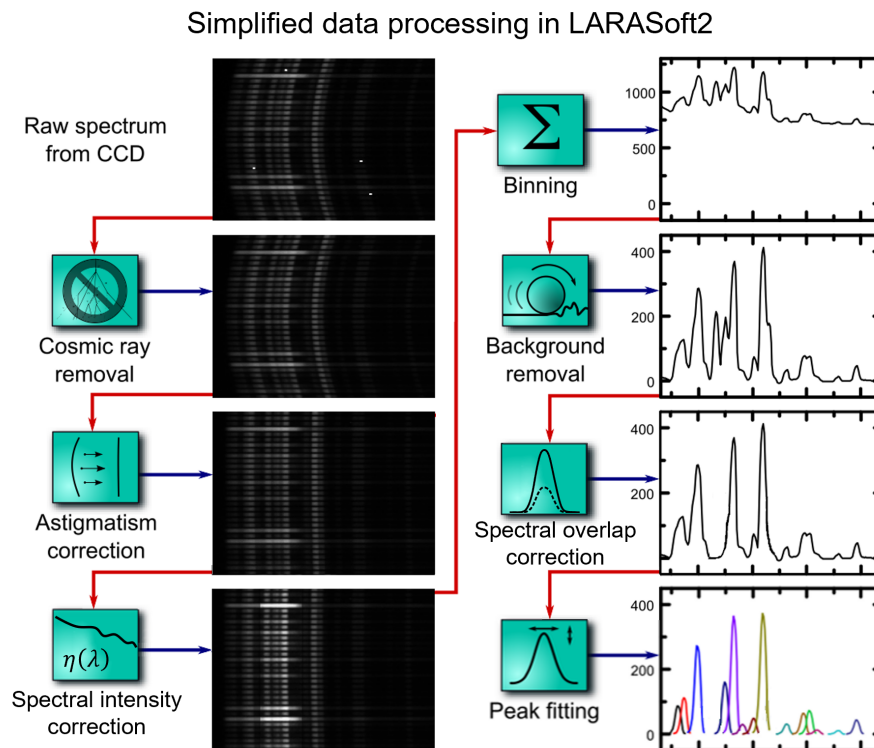
Figure 4.3.: Flow-chart of data analysis in `LARASoft2`. Only analysis procedures are shown. Not displayed: Region of interest selection, correction with theoretical intensities and calculation of gas composition. Details can be found within the text. Image adapted from Ref. [Jam13]
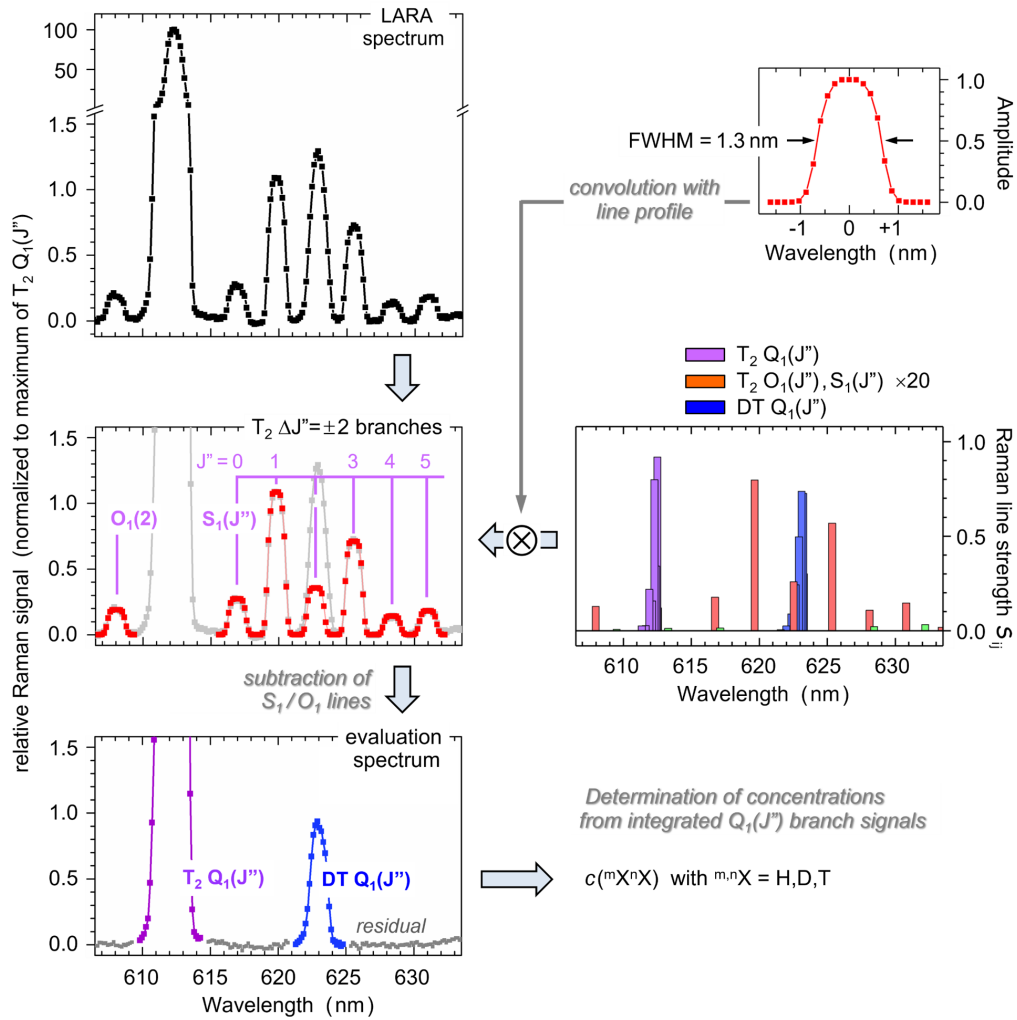
Figure 4.4.: Method for the deconvolution of overlapping lines. For illustration, a spectrum from the first KATRIN neutrino mass campaign is used. Details can be found within the main text. Image adapted from [Ake20b].
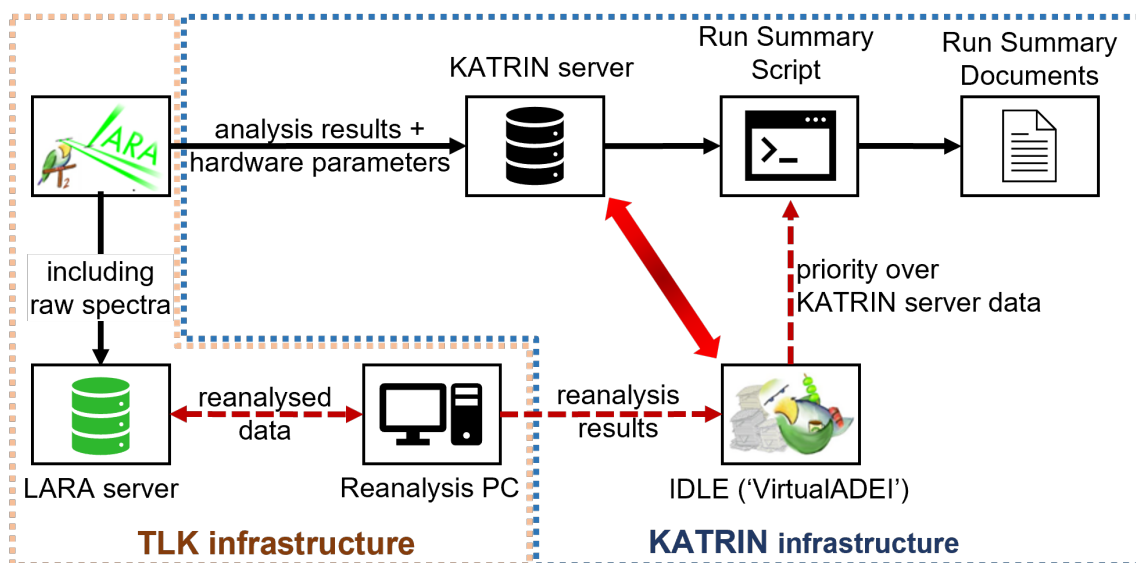
Figure 4.5.: Data flow of the KATRIN LARA system. The arrows shown in red are optional and are only used, when a re-analysis of LARA-data is required.

LARA-server can be accessed via a dedicated computer by selected users, which need the spectra and analysis settings for their work. The main purpose of this PC is the reanalysis of LARA data. Since LARA data is recorded and analyzed automatically in nearly real-time in 24h-operation, there can be the need to reanalyze the data afterward. Hardware failures, user errors or improved analysis routines can trigger a reanalysis of LARA data for an affected timeframe. Here it is important to note, that ADEI is made for real-time sensor data and cannot be overwritten with reanalyzed results. Therefore, the reanalyzed data is sent to the INTERMEDIATE DATA LAYER FOR EVERYONE (IDLE) instead. In the context of LARA data, IDLE is often referred to as 'VirtualADEI'.

Finally, the relevant data from all KATRIN sensors are combined into RUN SUMMARY (RS) documents that are primarily used as input for tritium spectrum fitting. The RS documents are produced by C++ scripts and stored in IDLE [KAT21]. The respective script for LARA data first checks VirtualADEI and uses any data found there. If there is no data on VirtualADEI for the specified neutrino mass scan, the script defaults to ADEI for data.

4.1.4. Calibration strategy: spectral sensitivity and theoretical intensities

There are two principal methods for the intensity calibration of any Raman system [Sch13a; Sch13b; Sch14]. The first is using a well-known gas sample to determine the system's response function. For tritium, this method is especially difficult due to its radioactive decay nature. Every sample containing tritium will undergo radio-chemical changes in its composition, usually within hours. This means that for every calibration a new, accurate gas sample needs to be prepared and transported safely and timely to the system, which needs to be calibrated. At TLK the TRITIUM-HYDROGEN-DEUTERIUM (TRIHYDE)-facility was set up for this purpose [Nie21a; Nie21b]. Although it is not routinely used for the calibration of the KATRIN LARA system, it provides an improved uncertainty on the theoretical correction factors and is an important tool to validate the second calibration method.

The second possible calibration approach combines theoretical intensities from *ab initio* calculations with the measured spectral sensitivity in order to determine the system's response function. In the first part of this section the theoretical framework for this calibration procedure [Rup12; Sch13a; Sch13b; Sch14; Zel17] is presented. In the second part the standard reference material (SRM) 2242 is presented as a way to measure the spectral sensitivity of a Raman system.

Equation (3.28) from Chapter 3 can be re-written for any hydrogen isotopologue, x, as

$$I_{\text{Raman,x}}(\lambda_s, N_x) = k_\lambda \cdot \lambda_s^{-3} \cdot \lambda_0^{-1} \cdot N_x \cdot \Phi(\varphi, \theta, a, \gamma)_{p^s, p^i, x} \cdot \mathfrak{I}. \tag{4.2}$$

In order to obtain the actual Raman signal, two further aspects must be considered. First, Eq. 4.2 represents a theoretical Raman signal. The spectral sensitivity $\eta(\lambda_s)$ of the experimental setup must be included in order to obtain the measured Raman signal. The spectral sensitivity is unique for each system and setup, and describes the wavelength-dependent efficiency of the photon detection. The measured Raman Signal is then given as

$$S_x = \eta(\lambda_s) \cdot I_{\text{Raman,x}}(\lambda_s, N_x) \tag{4.3}$$
$$= \eta(\lambda_s) \cdot k_\lambda \cdot \lambda_s^{-3} \cdot \lambda_0^{-1} \cdot N_x \cdot \Phi(\varphi, \theta, a, \gamma)_{p^s, p^i, x} \cdot \mathfrak{I}. \tag{4.4}$$

Second, in the previous derivation shown in Section 3.1 it was assumed that the Q_1-branches are equal to single lines. In reality, this is not the case, as shown in Figure 3.4. The Q_1-branches are unresolved single lines of different J'' initial states. If this is taken into account, the formula changes to

$$= k_\lambda \cdot \lambda_0^{-1} \cdot N_x \cdot \Im \sum_{J''} \left(\eta(\lambda_{s,J''}) \cdot \lambda_{s,J''}^{-3} \cdot \Phi_{x,J''} (2J''+1) g_N \exp\left(-\frac{\tilde{F}(J'')hc}{kT} \right) / Q \right), \tag{4.5}$$

where Q is the molecular partition function [Lon02]

$$Q = \sum_{J''} \left((2J''+1) g_N \exp\left(-\frac{\tilde{F}(J'')hc}{kT} \right) \right) \tag{4.6}$$

and $\tilde{F}(J'')$ are the rotational term energies. These can be obtained by accurate measurement of the line positions; alternatively, one may utilize the theoretical values calculated by Schwartz und LeRoy [Sch87].

It is reasonable to approximate that the spectral sensitivity does not change over the width of a Q_1-branch (see Figure 3.4) and therefore does not depend on J'':

$$S_x = \underbrace{k_\lambda \cdot \lambda_0^{-1} \cdot \Im}_{\text{const.}} \cdot N_x \cdot \eta(\lambda_s) \underbrace{\sum_{J''} \left(\lambda_{s,J''}^{-3} \cdot \Phi_{x,J''} (2J''+1) g_N \exp\left(-\frac{\tilde{F}(J'')hc}{kT} \right) / Q \right)}_{r_x}, \tag{4.7}$$

$$= C \cdot N_x \cdot \underbrace{\eta(\lambda_s) \cdot r_x}_{R_x}. \tag{4.8}$$

The spectral sensitivity $\eta(\lambda_s)$ and the theoretical intensities r_x are both necessary in order to obtain N_x from the measured Raman signal S_x. They can be combined into the response function if necessary (i.e. for cross validation of different calibration methods). The constant C cancels out during the calculation of any relative values.

The theoretical intensities r_x are calculated according to

$$r_x = \sum_{J''} \left(\lambda_{s,J''}^{-3} \cdot \Phi_{x,J''} (2J''+1) g_N \exp\left(-\frac{\tilde{F}(J'')hc}{kT} \right) / Q \right). \tag{4.9}$$

The spectral sensitivity $\eta(\lambda_s)$ has to be determined experimentally by measuring some kind of known/certified spectrum using the LARA system. The ratio of the measured and theoretically known spectrum defines the spectral sensitivity:

$$\eta(\lambda_s) = \frac{I_{\text{meas.}}}{I_{\text{theo.}}}. \tag{4.10}$$

The Standard Reference Material (SRM) 2242(a)

The luminescence standard SRM 2242(a) is manufactured, certified and distributed by the National Institute of Standards and Technology (NIST) [NIS08; NIS19]. The standard was developed specifically for the calibration of Raman systems. The luminescence standard is a glass plate doped with MnO_2. There are three different versions of the standard material:

(i) Original SRM 2242:
  The original version has one frosted and one polished surface and measures $10.7\,\mathrm{mm} \times 30.4\,\mathrm{mm} \times 2.0\,\mathrm{mm}$. Both lateral surfaces are unpolished.

(ii) New SRM 2242:
  The newer version has two polished surfaces and is $10.7\,\mathrm{mm} \times 30.4\,\mathrm{mm} \times 1.6\,\mathrm{mm}$ in size. Thus, this version is $0.4\,\mathrm{mm}$ thinner. Both lateral surfaces are unpolished.

(iii) SRM 2242a:
  After the certificates of the SRM 2242 expired in 2018, NIST completely revised the SRM 2242. The new dimensions are $10.0\,\mathrm{mm} \times 10.0\,\mathrm{mm} \times 1.65\,\mathrm{mm}$ with both surfaces optically polished. The SRM 2242a is significantly smaller and is incompatible with the default LARA calibration cell. Both lateral surfaces are unpolished.

When any of these SRM are excited with $532\,\mathrm{nm}$ laser light, they emit a broadband spectrum, which is certified for the associated Raman shift region $150\,\mathrm{cm}^{-1}$ and $4000\,\mathrm{cm}^{-1}$ (Figure 4.6). For the SRM 2242, the shape of the spectrum is described by a fifth-order polynomial

$$I_{\mathrm{SRM}}(\lambda) = \frac{10^7}{\lambda^2} \cdot \sum_{i=0}^{5} A_i Y(\lambda)^i \quad \text{with} \quad Y(\lambda) = 10^7 \cdot \left(\frac{1}{532\,\mathrm{nm}} - \frac{1}{\lambda} \right), \qquad (4.11)$$

which is provided and certified by NIST. Additionally, NIST provides certified 95% confidence curves in polynomial form. For the region outside $4000\,\mathrm{cm}^{-1}$ (relevant for H_2) an extended set of measured data was requested from and provided by from NIST. The certification is valid for measurement temperatures between $20\,^{\circ}\mathrm{C}$ and $25\,^{\circ}\mathrm{C}$. If the SRM 2242 is employed in different conditions, a correction has to be used:

$$(\Delta\nu, T)_{\mathrm{SRM}} = (T_{\mathrm{meas}} - 21\,^{\circ}\mathrm{C}) \cdot (-1.9\,\mathrm{cm}^{-1}/\,^{\circ}\mathrm{C}) + (\Delta\nu)_{\mathrm{SRM}}. \qquad (4.12)$$
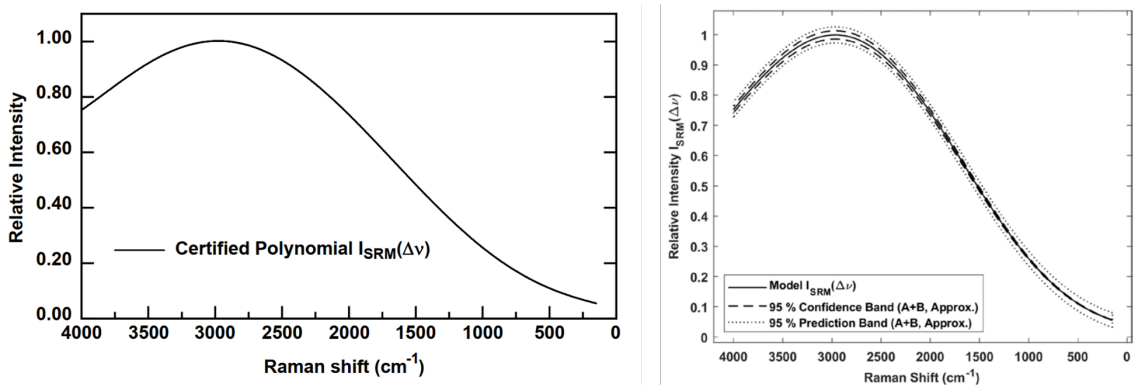
Figure 4.6.: Certified spectral curves of SRM 2242(a). Figures from [NIS08; NIS19].

For the SRM 2242a, the shape of the luminescence spectrum is defined by a linearly shifted log-normal model:

$$I_{\text{SRM}}(\lambda) = \frac{10^7}{\lambda^2} \cdot \left(H \cdot \exp \left[\frac{-\ln 2}{(\ln \rho)^2} \left(\ln \left[\frac{(z - x_0)(\rho^2 - 1)}{w \cdot \rho} + 1 \right] \right)^2 \right] + m \cdot z + b \right), \quad (4.13)$$

where

$$z = 10^7 \cdot \left(\lambda_{\text{L}}^{-1} - \lambda^{-1} \right) \tag{4.14}$$

and λ is the wavelength in nanometers, λ_{L} is the wavelength of the laser in nanometers, and H, w, ρ, x_0, m and b are coefficients of the model. NIST provides the mean values for the coefficients, as well as values to calculate the lower and upper confidence and prediction limits. For the region outside $4000\,\text{cm}^{-1}$ the equation and coefficients can be used without any changes[1].

The SRM 2242(a) is designed for the calibration of Raman systems with a 180° scattering geometry (as is common for Raman microscopes). However, as the described in Section 4.1 the KATRIN LARA system is a 90° configuration. In this configuration, the laser beam enters the SRM 2242(a) through one of the lateral surfaces instead of the intended and certified front surfaces. For adapting the SRM 2242 to the 90°-scattering setup, detailed investigations and studies were conducted [Rup12; Sch14; Sch13a; Sch15b; Zel17]. In the 90°-scattering setup, the spectrum emitted from the SRM 2242 depends on the lateral position of the laser beam passing through the material. In order to find the correct position of the laser beam, the original version of the SRM 2242 was used, since it has one polished and one unpolished (frosted) surface. For the measurement, the beam position is varied with different sides facing the collection optics. As shown in Figure 4.7, when the beam position is varied, the resulting spectral sensitivities are only in agreement when the beam position is directly below the surface facing the collection optics. This result was confirmed by round-robin measurements of the same gas sample with different LARA systems. Based on this requirement for the beam position, a bespoke positioning procedure was developed; it was shown that with this procedure and the SRM 2242, the trueness requirements for the KATRIN LARA system are fulfilled.
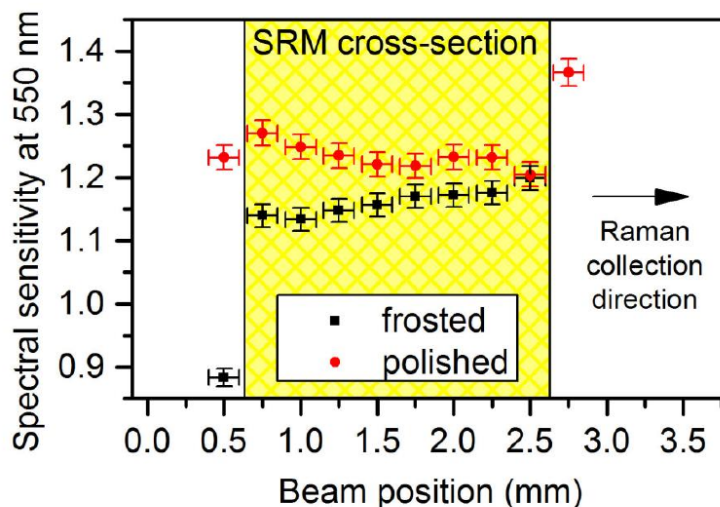
Figure 4.7.: Measurements were taken with different sides facing the collection optics. Only the values directly under the surface agree. Figure from [Sch15b].

---

[1]Personal communication with A.A. Urbas of the NIST Chemical Sciences Division

4.2. The Confocal Raman Microscope (CRM) for tritiated samples

In this section, the experimental setup of the CRM is described. First, in Section 4.2.1 a brief introduction to confocal microscopy in general is given. Second, an overview of the CRM is presented in Section 4.2.2. Finally, in Section 4.2.3 and Section 4.2.4 the detailed experimental setup and measures for tritium compatibility are described.

4.2.1. Introduction to confocal Raman microscopy

Confocal Raman microscopy is a potent tool for characterizing materials at the molecular species level. The fundamental functional mechanism is based on the combination of confocal microscopy and Raman spectroscopy. The generic principle of a confocal microscope is shown in Figure 4.8.

For confocal microscopy, a point-like light source is needed. This can be achieved by using a free-space laser with a pinhole placed in the path of the laser. Alternatively, a fiber-coupled laser with a single-mode optical fiber [Gu91; Dab92] can be used. The divergent light from the point-like source is then collimated by a lens. Using a dichroic beam splitter, the light is directed through an objective and focused to a specific point in the focus plane. The sample of interest is positioned in the focus plane of the confocal microscope. The laser beam interacts with the sample molecules through Raman scattering, in addition to common Rayleigh scattering and fluorescence. A detailed introduction and summary of the Raman effect for gaseous and solid samples was given in Chapter 3.

The focus point typically has a diameter in the micrometer range and defines the area from which the scattered light is emitted and detected. In addition, this configuration enables spatial scanning of the sample. By moving the objective or the sample, the laser focus can be moved across the sample to create a three-dimensional image. The scattered light passes the objective and the beam splitter and is then focused by a second lens onto a pinhole. It is located in front of the detector (or optical fiber coupled to the detector) and allows only
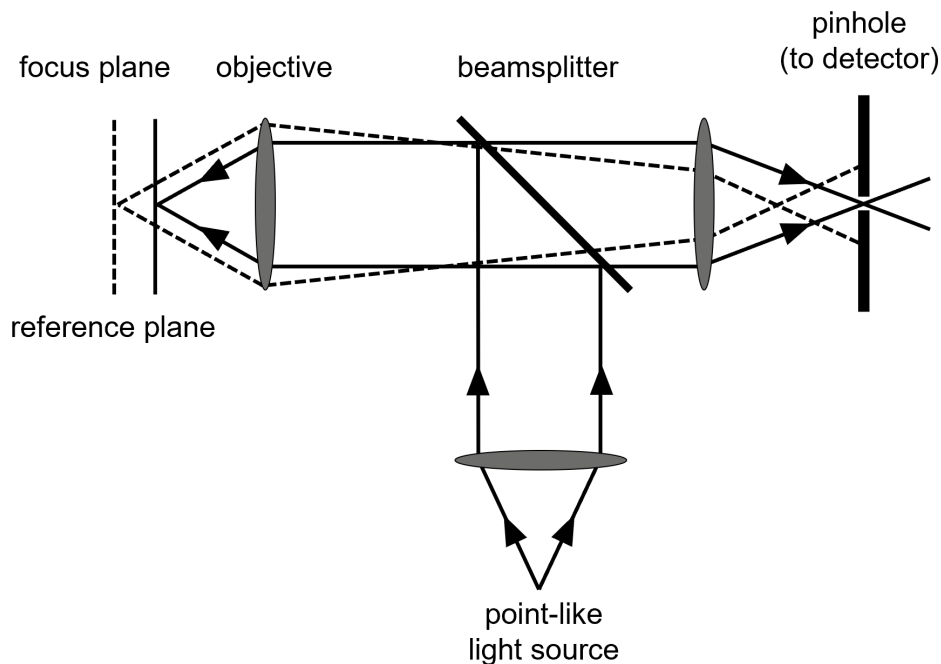
Figure 4.8.: Principal concept of a confocal microscope. Details can be found within the text. Image based on [Top18].

light from a specific focal region of the sample to pass through. This improves the lateral (xy-plane) and axial (z-plane) resolution, as only the light from the focal volume can pass the pinhole, while emitted light from other areas of the sample is suppressed, as depicted in the beam path of the reference plane in Figure 4.8.

By scanning the sample, confocal microscopy can produce high-resolution images in both the lateral and axial directions, allowing three-dimensional analysis of the sample. This principle can be adapted to optimize the system to work with different types of scattering. Achieving optimal transmission and analysis of the desired scattering requires careful selection of appropriate optical components, thereby fine-tuning the system for the specific scattering of interest. In this work, all components are selected for optimal collection of Raman scattered light.

4.2.2. Design of the tritium-compatible CRM

The CRM's overall concept is illustrated in Figure 4.9, depicting a schematic drawing and an overview photo. Similar to commercial CRM implementations, the entire system can be divided into several essential functional groups. In addition to the main optical system, there is the motorized sample stage, the DPSS excitation laser and the spectrometer with CCD detector combination. The main optical setup is divided into three functional groups:

Segment A The purpose of this first segment is the *excitation laser coupling and collection of Raman light*. The laser light is coupled into the CRM using a single-mode (SLM) optical fiber. Optionally, the laser power can be monitored. Furthermore, the laser and Raman light are guided through the microscope objective.

Segment B The second segment is the *wide-field imaging arm*. Here a CMOS camera is positioned which is used for sample positioning and to record images of the sample.

Segment C The final segment is the *confocal light collection arm*, where the Raman light from the laser excitation region on the sample is imaged onto the confocal pinhole and collected by a fiber bundle, carrying the Raman light to the spectrometer.

Segment A - Excitation laser coupling and Raman light collection

Laser The selected laser is a diode-pumped solid-state (DPSS) laser with a maximal output power of 120 mW and a nominal wavelength of 532 nm. Normally, confocal microscopes utilize free-space coupling of the laser radiation in combination with a pinhole to create a point-like light source (Figure 4.8) [Dab92; Gu91]. In this system, the excitation laser is coupled into the CRM by using a single-mode FC/PC fiber optic patch cable. The core diameter of common single-mode fibers has a MODE-FIELD DIAMETER (MFD) of the order of $\approx 3.5\,\mu$m. Therefore, it acts equivalently to the aforementioned pinhole. The fiber is then connected to a fixed-focus collimation package, which generates a collimated laser beam with a diameter of about 2 mm. Additionally, the fiber-coupling allows for increased flexibility in the position of the laser. The laser can be easily placed outside potentially toxic or radioactive environments, while the fiber optic patch cable is fed through, *e.g.*, the enclosure of a glove box.

Laser line filter The laser line filter installed in the laser path directly after the collimation package removes any fluorescence and stimulated Raman light, which might have been generated in the fiber, while most of the laser light can pass the filter (T > 90 % for 532 nm).
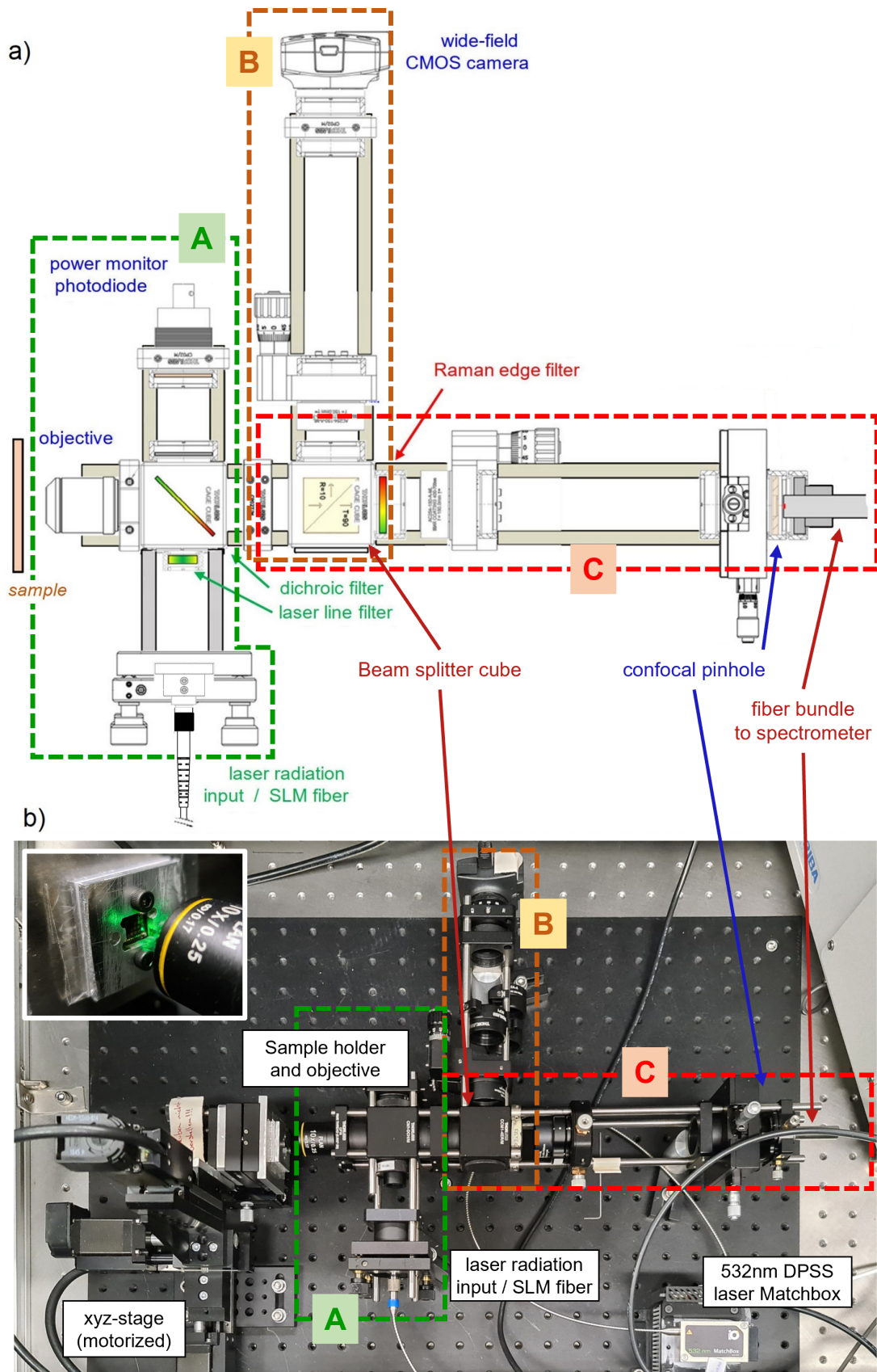
Figure 4.9.: Overview of the confocal Raman microscope a) technical drawing and b) photograph of the system. The three main sections are: A - excitation laser coupling and Raman light collection, B - the wide-field imaging arm and C - the confocal light collection arm. Details can be found in the main text and in Ref. [Dia22].

Dichroic beam splitter Using a single-edge dichroic beam splitter with $R_{532\,nm} \approx 95\,\%$ and $T_{Raman} > 93\,\%$, the laser beam is directed to the microscope objective. The remaining transmitted laser light is used for laser power monitoring.

Microscope objective A low-cost infinity-corrected objective with 10x magnification and 0.25 NUMERICAL APERTURE (NA) is used to focus the laser beam onto the sample. This objective with rather low NA was chosen since the areas to be raster-scanned are rather large and for the planned studies larger magnifications were not needed. However, an objective with a larger NA can be used and will be tested with this CRM in the future. The laser light scatters off the sample. The scattered light is then collimated by the microscope objective. At this stage, the scattered light comprises not only Raman scattering, but Rayleigh scattering as well. All scattered light hits the dichroic beam splitter, where 93 % of the Raman scattered light can pass. Only a sub-percent of the 532 nm light can pass the mirror.

Segment B - Wide-field imaging arm

Beam splitter cube Both, the remaining 532 nm light as well as the Raman light passing through the dichroic beam splitter, hits the beam splitter cube and is split in the ratio 10:90 (R:T). The reflected light (R) is used in the wide-field imaging arm (Segment B) while the transmitted light (T) propagates in the confocal light collection arm (Segment C). Note that the beam splitter cube is common to both segments (B) and (C).

Focusing lens L1 The reflected light is focused by an achromatic lens of focal length $f = 150\,mm$ onto a color CMOS camera. The focusing is equal to that in the confocal light collection arm; therefore, a direct comparison of the wide-field and the confocal Raman images is possible.

CMOS camera The CMOS camera has an imaging area of 1440×1080 pixel (about $5.0 \times 3.7\,mm^2$). When the same lens is used in segment B and segment C and the lenses are aligned so that the distances between L1 ⇔ CMOS sensor and L2 ⇔ pinhole are equal, then information from either arm can be used to determine whether the sample is in focus. This is the main use for the CMOS camera. Since the intensity of the remaining 532 nm light is much higher than the Raman signal, the image on the CMOS camera has sufficient illumination within a few milliseconds compared to $> 10\,s$ for a clear Raman image. Therefore, the movement of the sample through the focus point of the laser spot can be observed in real-time and the positioning of the sample in focus is rather easy and quick.

Segment C - Confocal light collection arm

Beam splitter cube Common element with Segment B.

Long-pass edge filter As described in segment A, the light which is generated on the sample does not originate from Raman scattering alone. Additionally, Rayleigh scattering and laser light reflections are collimated by the microscope objective. This light has the same wavelength as the excitation laser light of 532 nm. The intensity of the Rayleigh light alone is already at least three orders of magnitude higher than the Raman intensity [Hen70]. For this reason, a long-pass filter is installed into the Raman light pass prior to the focusing lens. Note that for alignment of the beam pass, this filter has to be removed.

Focusing lens L2 The remaining Raman light is focused onto the confocal pinhole by an achromatic lens of focal length $f = 150\,mm$. This is the same type of lens as L1 in the wide-field imaging arm.

Pinhole Two different pinhole diameter were used in this work, namely 75 µm and 100 µm, which are close to the optimal value for the current configuration of the CRM. The optimal pinhole diameter depends on (i) the NA of the objective, (ii) the focal length of the achromatic lens L2, and (iii) the focal beam diameter on target. If either of these parameters is changed, the pinhole diameter has to be adjusted accordingly.

Fiber The light passing through the pinhole is collected by an optical fiber bundle. The fiber bundle is custom-fabricated and comprises of 48 individual fibers of core diameter 100 µm. The individual fibers are arranged into a circular area of diameter 1 mm.

Key technical details for all aforementioned CRM components are collated in Table 4.1. In addition, a description of said CRM elements and the alignment procedure for the setup can be found in Ref. [Dia22]. Characterization measurements for the CRM are discussed in Chapter 6.

4.2.3. Mechanical system for sample positioning and movement

The schematic of this motorized sample motion assembly is shown in Figure 4.10. The motion of the sample is realized by three coupled, motorized translation stages. The directions of motion across the target surface are designated as the x- and y-axes, while focusing on the surface occurs along the optical axis (designated as the z-axis). The three translators are 8MT173-20-EN1 units (*Standa*[2]) that allow motorized motion in all three directions with minimum step intervals of <1 µm.

To enable quick sample exchange without major or tedious mechanical manipulation of the measurement setup, a special sample holder was designed, based on a pair of magnetically connected kinematic baseplates (KB50/M by *Thorlabs*[3]). The principle of this plug-and-play mount is shown in Figure 4.11. This design allows the tritium-contaminated sample to be mounted inside a glove box on the detachable holder part, and then to attach it magnetically to the xyz-translator in a plug-and-play manner. The magnetic connection has a combined reproducibility in the x-y plane of <12 µrad. The holding force of the magnetic connection is 2.8 kg. With a weight of the holding plate + graphene sample of <100 g, a robust fixation is ensured. With this holding method, the time for handling the radioactive sample outside the glove box is reduced to a minimum.

The sample itself is held in a type of 'sandwich'; this holder was specially designed for the *Graphenea*[4] substrates. However, the design can be easily adapted to other samples, as long as the design can be screwed onto the separable kinematic holder. The substrate (of dimension 10 mm×10 mm) is centered on a baseplate and fixed with a cover plate that has a recess of the appropriate size. This unit is then screwed onto the separable kinematic holder. The functionality is outlined in Figure 4.12.

---

[2]Standa Ltd.,LT-08221 Vilnius, Lithuania

[3]Thorlabs Inc., Newton, New Jersey 07860, United States

[4]Graphenea Inc., 20009 - San Sebastián, Spain

Table 4.1.: Overview of CRM components

Component	Part #	Manufacturer	Remarks
Laser	0532L-13B-NI-AT-NF	Integrated Optics[a]	532 nm DPSS laser, single mode fiber, FC/APC
Spectrometer	iHR320	Horiba[b]	1200 g/mm grating
CCD array detector	Syncertiy FI-UV-VIS	Horiba[b]	
Mechanical system for sample positioning and movement			
Motorized stage	8MT173-20-EN1	Standa[c]	coupled for motorized motion in all three directions
Kinematic platform	KM100B	Thorlabs[d]	Base plate for magnetic sample holder, adjustable tilt
Magnetic holder	KB50/M	Thorlabs[d]	Plug-and-play sample holder
Segment A - Excitation laser coupling and Raman light collection			
Fixed-focus collimator	P260FC-A	Thorlabs[d]	FC-coupled fiber collimator
Kinematic mount	KC1-S/M	Thorlabs[d]	Laser beam steering
Laser line filter	LL01-532-12.5	Semrock[e]	Laser clean-up filter
Laser beam separator	Di02-R532-25x36	Semrock[e]	Single-edge dichroic beam splitter
Microscope objective	LIO-10X	Neuport/MKS[f]	10x infinity corrected, 0.25 NA
Laser power monitor	SM1PD1A	Thorlabs[d]	SM1-mounted Si photodiode
Beam splitter cube	BS025	Thorlabs[d]	Non-polarizing, ratio 10:90 (R:T)
Segment B - Wide-field imaging arm			
Focusing lens	AC254-150-A-ML	Thorlabs[d]	AR-coated achromat, f=150mm
Color camera	CS165CU/M	Thorlabs[d]	Color CMOS camera, USB2
Segment C - Confocal light collection arm			
Raman edge filter	LP03-532RU-25	Semrock[e]	Long-pass 532nm edge filter
Focusing lens	AC254-150-A-ML	Thorlabs[d]	AR-coated achromat, f=150 mm
Confocal pinhole	PxxK	Thorlabs[d]	SS-foil pinhole, xx = diameter in μm
Pinhole xy-adjustment	ST1XY-S/M	Thorlabs[d]	xy-translator, micrometer drive
Spectrometer fiber bundle	Custom-made	CeramOptec[g]	48-fiber-bundle, circular to slit

[a] Integrated Optics UAB, Vilnius 08221, Lithuania
[b] HORIBA Ltd, Kyoto, 601-8510 Japan
[c] Standa Ltd.,LT-08221 Vilnius, Lithuania
[d] Thorlabs Inc., Newton, New Jersey, United States
[e] IDEX Health & Science LLC, Rochester, New York, USA
[f] MKS Instruments, Andover, Massachusetts, United States
[g] CeramOptec GmbH, Bonn, Germany
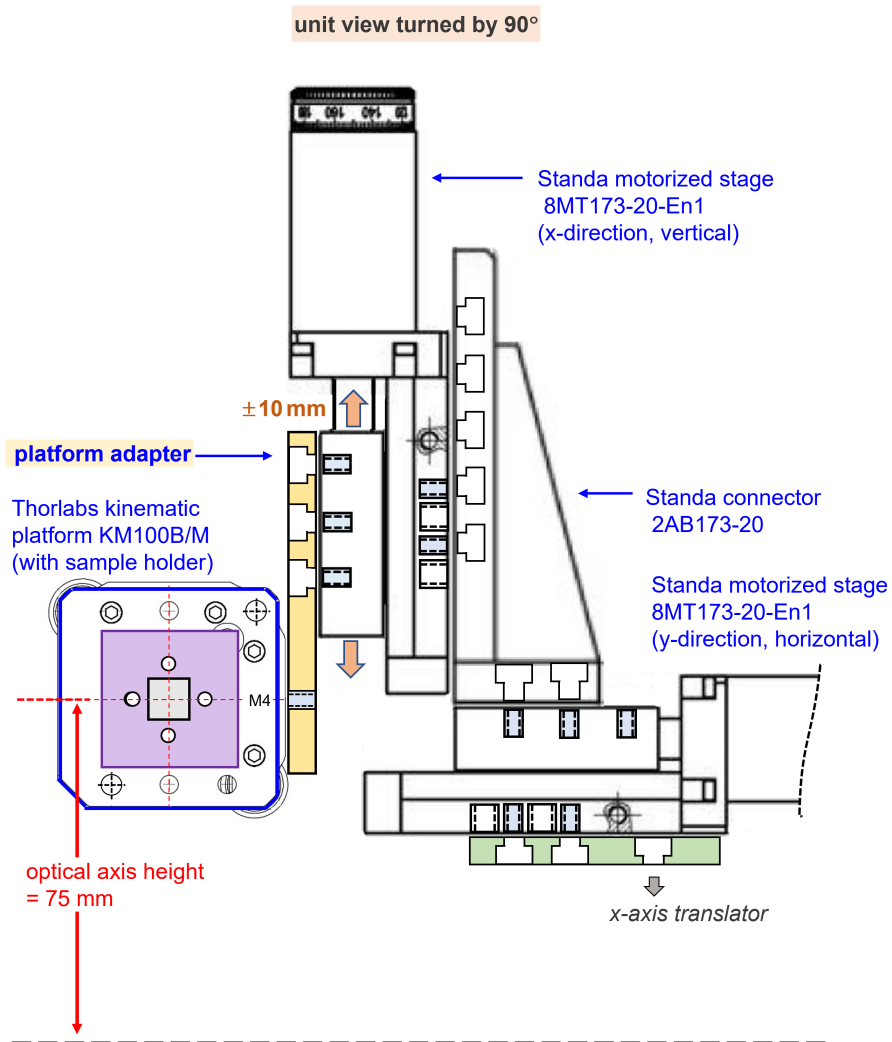
Figure 4.10.: Schematic sketch of the motorized system for moving the sample, in x, y and z directions. The system is based on three mechanically coupled, stepper motor-driven translation stages. Note: for clarity, the translator for the z-direction is not shown.
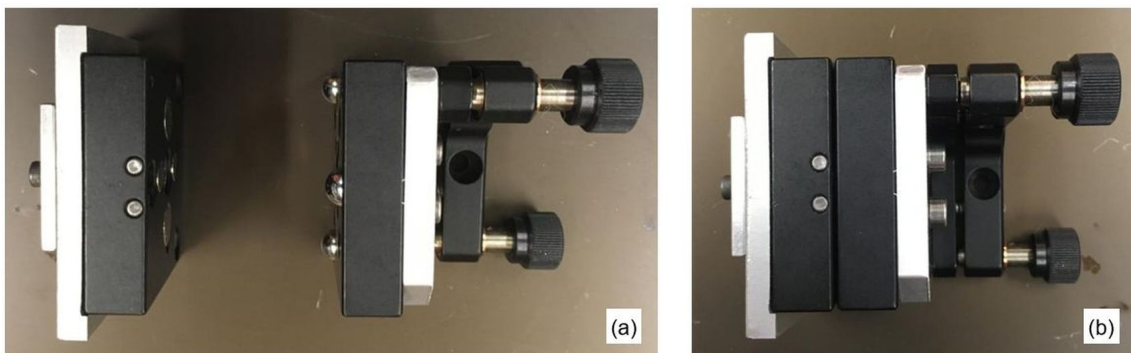
Figure 4.11.: Schematic of the magnetic plug-and-play holder for tritium-loaded samples; (a) detached state; (b) attached state. The kinematic part (right in the pictures) is screwed to the translator unit, the sample holder (left in the pictures) is a combination of magnetic baseplate and sample plate.
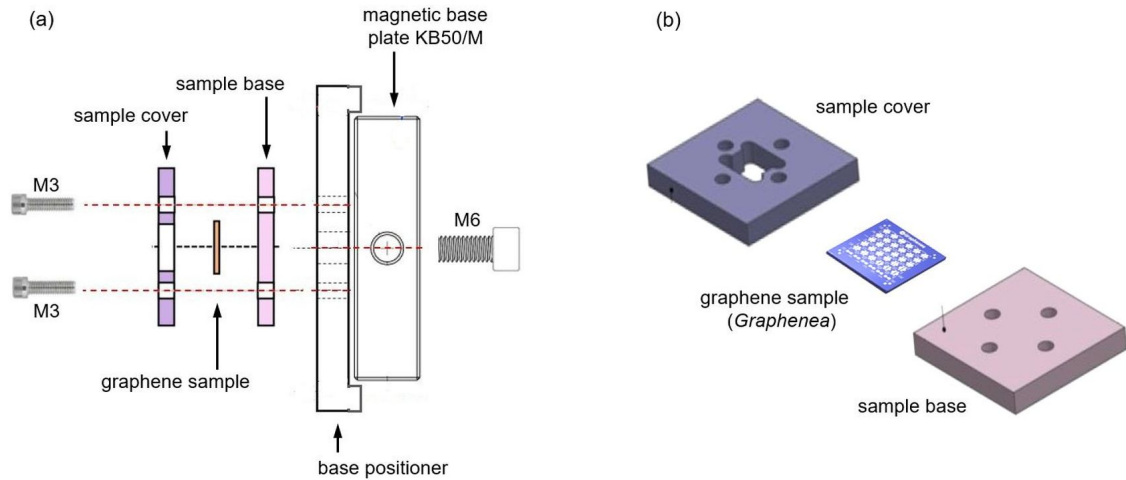
Figure 4.12.: Schematic structure of the sample holder for tritium-loaded samples. (a) Design of the sample holder, with magnetic base KB50/M (Thorlabs); (b) Sample 'sandwich', consisting of sample base, (graphene) sample and sample cover.

4.2.4. Tritium compatibility

To minimize the risks of tritium release into the laboratory and of the contamination of all optical components, the entire sample stage is surrounded by an enclosure, which is connected to a mobile suction unit of the TLK. Specifically, the sensitive CRM is completely isolated from the tritium-loaded sample with only a single opening for the microscope objective. For better visibility of all components, this enclosure is not shown in Figure 4.9; when installed, it covers the motorized stage and the sample holder.

With this design, there is no need for a window between the microscope objective and the sample, which would potentially produce a fluorescence background. The suction unit ensures a constant exchange of the air surrounding the sample stage and a directed flow away from the rest of the optical system. The volume flow of the suction unit is $300 - 600 \, \mathrm{m^3 \, h^{-1}}$, which, with an enclosure volume of about $100 \, \mathrm{L}$, corresponds to about 3000-6000 air changes per hour, i.e. 0.8-1.7 air changes per second.

Experimental operation with tritium may only be carried out when the ventilation system of the tritium laboratory is in operation. The enclosure is monitored by means of a mobile ionization chamber. Therefore, when a tritium contaminated sample is placed in the CRM only the motorized stage and the microscope objective are directly exposed to potential tritium contamination. With this particular setup, the total activity on a sample can be as high as $1 \times 10^{10} \, \mathrm{Bq}$.

4.3. Software for the operation of the CRM

As described in Section 4.1.3, `LARAsoft` was revised by András Bükki-Deme and incremented to `LARASoft2`. The new software version is more stable for long-term operation (see Chapter 5) and programmed in a modular fashion, which improves maintainability, scalability, and extendability. All features present in `LARASoft2` are also available in `LARASoft2`. Therefore, only the new features will be presented and discussed in this section. Details about the functionality of `LARASoft2` can be found in Ref. [Fis14]. For the following sections, the version with added support for the CRM, is called `LARASoft2-CRM`[5].

4.3.1. Review of pre-existing software

In Figure 4.13 the main window of `LARASoft2` is shown; here the core features for a particular data acquisition run are selected. Using the (1)-bar on the left, the different submodules can be loaded into the central (2)-subpanel. Every submodule has a custom front panel (User Interface, UI), which is often divided into (3)-tabs for different functionalities. As an overlay, the (4)-window controls (print, scrollbars, window size, about and exit) are always visible and accessible. The corresponding block diagram is shown in Figure 4.15. All (2)-submodules are loaded when `LARASoft2` is started. The submodules communicate with each other and the main module via access to the same `User Events`.

When a submodule is selected via the (1)-bar task selector, it is loaded into the (2)-subpanel by the event loop block (3), as indicated in the corresponding block diagram in Figure 4.15. This improved software architecture results in the increased long-term stability and expandability. All submodules have a dedicated error handling, which does not affect the other submodules, unless it is specifically required. For example, a minor error or warning produced by the water-chiller-submodule does not affect the data taking. However, a major error - like the overheating of the laser - could be programmed to stop the data taking and shut down the entire system.
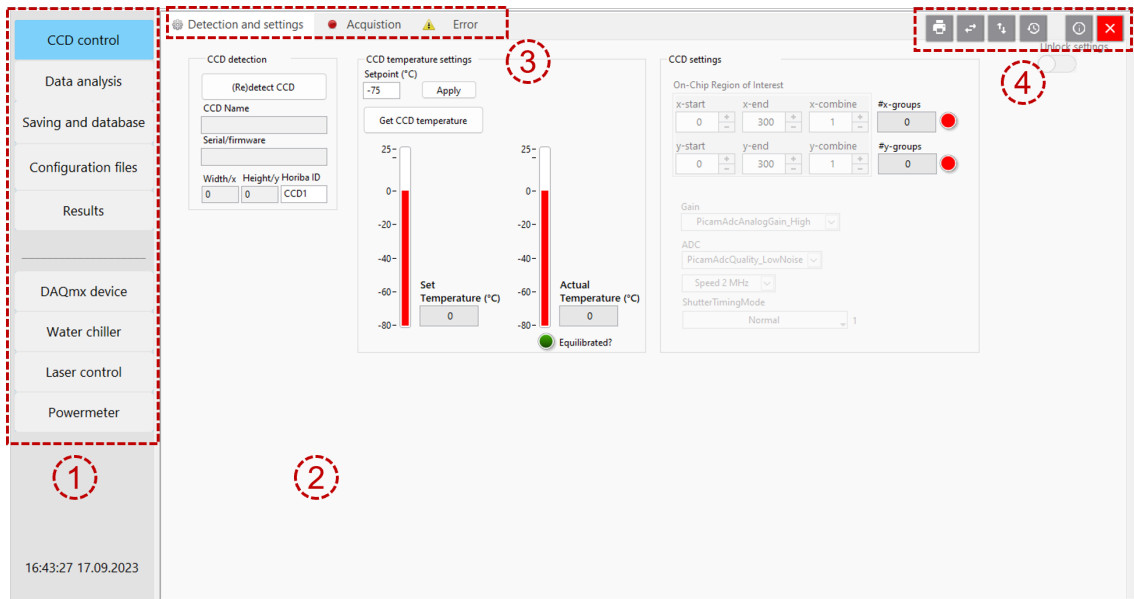
Figure 4.13.: Front panel of `LARASoft2`. (1) - sidebar to select different submodules, (2) - subpanel into that the front panel of the select submodule is loaded, (3) - tab separator of the 'CCD control'-submodule, and (4) - general window controls.

---

[5]`LARASoft2-CRM` corresponds to the version numbers upwards of `LARASoft2.7.0`

4.3.2. Automatic control of the motorized stages for Raman raster imaging

Within the scope of this work, `LARASoft2` was extended by a submodule for the control of the xyz-motion-stage. Apart from the manual control of the xyz-motion-stage, the main additional functions in `LARASoft2-CRM` are (also see Figure 4.14):

(a) Detection of and connection to the xyz-motion-stage: The system can detect and distinguish two different xyz-motion-stages at this point in the software development. First, the xyz-motion-stage from Standa (Table 4.1) employed in this CRM. Second, is a stage built from Thorlabs components, which is employed in the CRM at the UAM.

(b) Angle correction: For keeping samples in the laser focus during raster scans, the tilt angles need to be determined. A detailed description of the procedure is given in Section 4.3.3.

(c) Automatic scans: The user can specify a starting position (x_s, y_s, z_s), the step size $(\Delta_x, \Delta_y, \Delta_z)$, and upper and lower boundaries $(x_{(\min,\max)}, y_{(\min,\max)}, z_{(\min,\max)})$ for an automatic scan. In addition, the number of spectra n taken at every point can be controlled. When data taking is started, the xyz-motion-stage will be moved to the starting position of the specified scan. After n spectra are recorded, the x-position is incremented by the step size Δ_x. This is repeated until the x-position reaches the upper boundary $x_{\max}$, meaning one x-line was scanned. The x-position is then reset to the lower boundary $x_{\min}$, the y-position incremented by the step size Δ_y and the next x-line scanned. When the y-position reaches the upper boundary $y_{\max}$, a full xy-plane has been scanned (xy-slice). The z-position is incremented by Δ_z and the next xy-slice is recorded. When all values reach the upper boundaries, the scan (xyz-cube) is completed and stopped.

4.3.3. Automatic control for keeping samples in the laser focus during raster scans

For the generation of planar (xy-direction in our geometry frame) images of a sample, during the scan the sample surface needs to stay within the laser focus (z-direction). Due to unavoidable offset and rotations in the assembled xyz-motion-stage and uneven mounting in the sample holder, the sample, and the laser focus planes are not necessarily parallel to each other on a sub-degree level. Thus, the sample surface would likely move out of focus during a full planar scan. This is a general problem in whole-slide (laser) microscopy, in which topographic variability may severely affect in-focus imaging [Bia20].

In the raster-scan Raman imaging described here, which at present only utilizes a low-magnification 10x objective, normally topographical variations are well within the standard focal depth of several µm. However, as mentioned earlier, the sample surface may not be absolutely in-plane for lateral xy-scans, i.e. the sample might be mounted with a tilt.

Therefore, the surface may severely run out of focus during a full-area raster scan; for a compensated scan-procedure, knowledge of the particular sample tilt is required. In order to correct for the tilt of the sample, the tilt angles $\theta_{x,y}$ need to be measured. Using the CMOS camera three different points P_1, P_2, P_3 on the sample surface are selected such that all points are in the focus of the laser beam. From these three points, two vectors $\vec{r}_{x,y}$ on the sample surface are constructed. Finally, the vector dot-product of $\vec{r}_{x,y}$ with the normal vector $\vec{n}_z = (0, 0, 1)$ is used to calculate the angles

$$\theta_{x,y} = \cos^{-1} \left(\frac{\vec{n}_z \cdot \vec{r}_{x,y}}{|\vec{n}_z| \cdot |\vec{r}_{x,y}|} \right). \tag{4.15}$$

The coordinate system of the xyz-motion-stage is then rotated using basic rotation matrices R_x and R_y, according to

$$P_i = R_y(\theta_y) \cdot R_x(\theta_x) \cdot P_i',\tag{4.16}$$

where $P\prime$ denotes the original tilted system and P is the corrected coordinate system.

This procedure is implemented in `LARASoft2` in such a way that the user enters coordinates only in the corrected coordinate system, which then are back-transformed and transmitted to the xyz-motion-stage for movement. With the corrected coordinate system, the z-coordinate remains constant during the planar scan and the sample is kept in the laser focus. This procedure is applied first, whenever a new sample is installed in the sample holder.
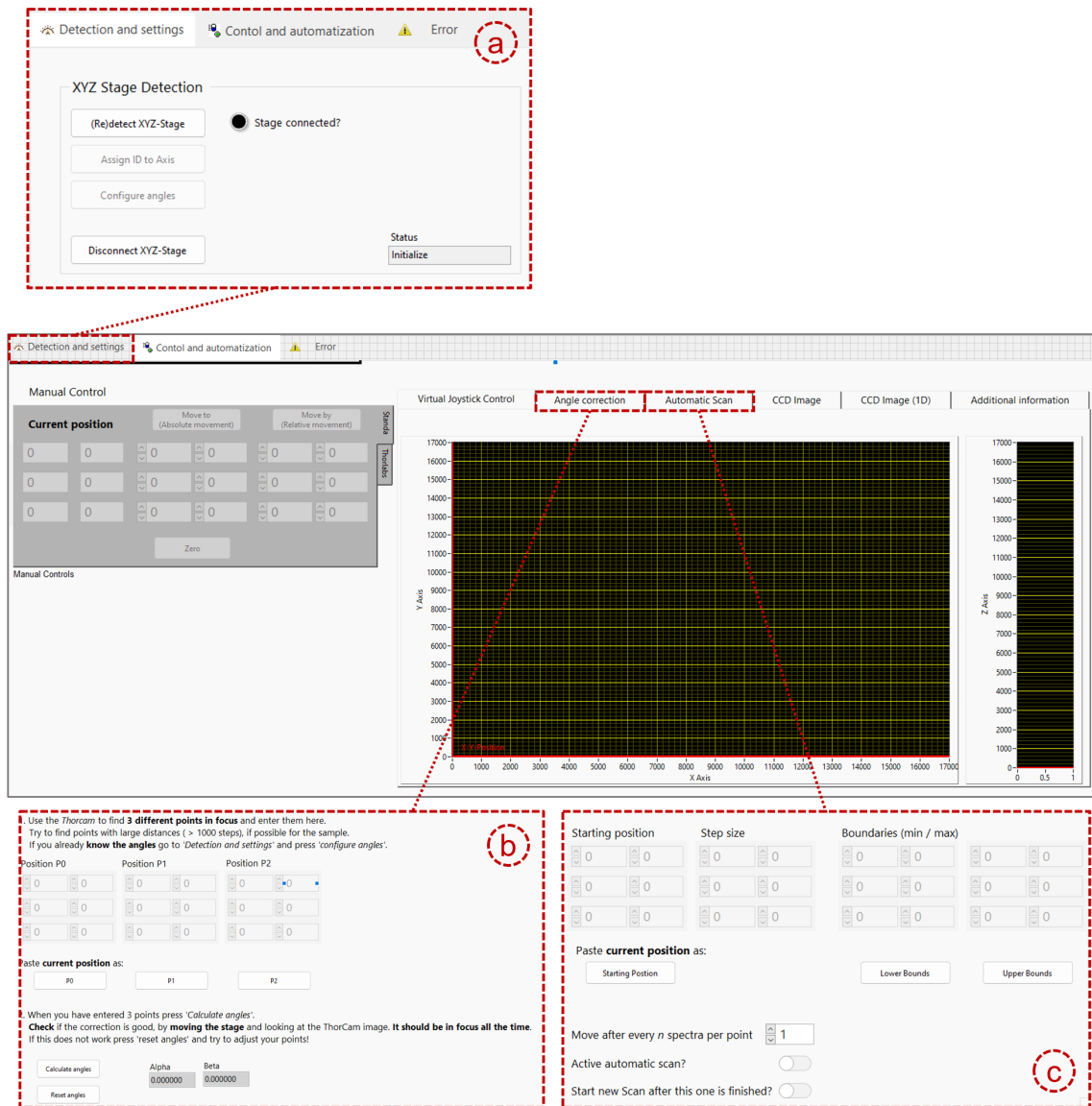
Figure 4.14.: Front panel functionality of CRM submodule. (a) - detection of and connection to the xyz-motion-stage, (b) - angle correction for a raster scan area, and (c) – setup of automatic scans.
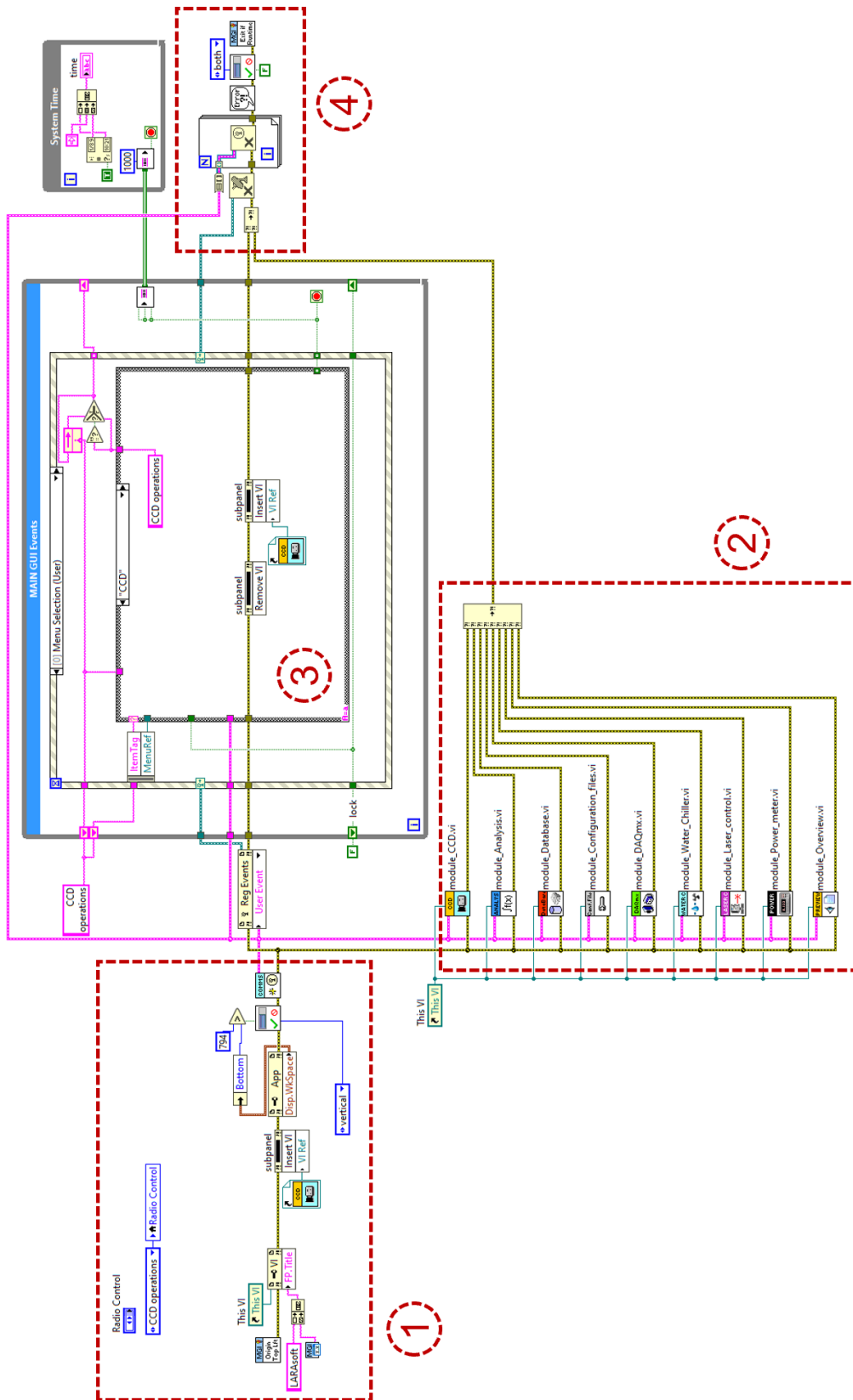
Figure 4.15.: Block diagram of `LARASoft2`. (1) - initialization of the window and subpanel, (2) - initialization of all submodules, (3) - main loop to switch submodules based on user input and communication to submodules, and (4) - clean up procedure executed on software exit.

4.4. Data analysis for Raman imaging

4.4.1. Description of acquired data sets (hyperspectral data cubes)

During a scan, a complete Raman spectrum is recorded for every pixel position. When all three spacial dimensions are scanned, this results in a 4D-data cube (four-dimensional = xyz-spatial + s-spectral), where the S-dimension (or spectral-dimension) is associated with the recorded Raman spectra. However, the more commonly employed scans are xy- or xz-scans, which are represented by a 3D-date cube. Such data sets are referred to as *hyperspectral data sets.* For 2D visualization of the hyperspectral data sets, the information contained within each spectrum needs to be reduced to a single value for each spatial pixel position (see *e.g.* Refs. [Kes02; Top18; Tel18; Sch22]); this procedure is often referred to as 'slicing'. When multiple slices are extracted from the Raman spectra, each image can either be displayed individually or they can be combined into a color image stack.

It should also be noted that the hyperspectral data sets typically consist of a large amount of individual Raman spectra. A full-special-resolution (step-size $\approx 7\,\mu$m $\equiv$ laser FBD) xy-scan of a $1\,cm^2$ sample would contain $1430 \times 1430 \approx 2 \times 10^6$ individual Raman spectra. Considering the typical measurement time of the CRM of 10 seconds, such a scan would take more than 230 days to complete. Therefore, full-special-resolution scans are often reduced to a smaller area of about $300\,\mu$m $\times 300\,\mu$m with total scan times in the order of 10 - 20 hours. Alternatively, the step-size is increased significantly (*e.g.* to $50\,\mu$m or more) - resulting in under-sampling - to obtain a coarse image of the whole sample in a total scan time of a few days.

The large amount of data is a challenge for data analysis. Especially, the analysis of samples with unknown chemical composition, potentially varying with spatial position, is complicated, since it is not feasible to check every individual Raman spectrum manually. Any data analysis solution needs an option to reduce the size of the data set, or easy data exploration.

4.4.2. Pre-processing of spectra

The raw intensity signal from the CCD is cleaned and calibrated through a series of pre-processing steps to obtain a Raman spectrum for quantitative analysis. If not stated otherwise, the pre-processing procedures are based on Refs. [Jam13; Fis14; Zel17; Ake20b] and more details can be found there. The main pre-processing steps applied in this work are:

(i) **Cosmic Ray Removal:** Interactions between cosmic radiation and the atmosphere lead to the creation of muons, which, when traversing the CCD detector, yield high pixel reponse intensity. For the removal of these 'cosmic rays' it is utilized that the events are short-term and only affect one spectrum. Given the number of pixels on the CCD and the cosmic ray event rate of about 1 event/10 s, it is unlikely that two consecutive cosmic ray events will affect the same pixel. Therefore, by comparing consecutive Raman spectra against an optimized threshold value, cosmic ray peaks can be identified and removed by using the mean value of the neighbouring pixels. This pre-processing step is always used and integrated within `LARASoft2`.

(ii) **Background removal:** Depending on the scanned sample, a background removal algorithm is applied. Either the SCARF-algorithm, implemented in `LARASoft2`, a MATLAB implementation of the 'Whittaker Smoother' [Eil03] or the 'Vancouver Raman Algorithm' [Zha07] is used.

(iii) **Spectral sensitivity correction:** For intensity calibration, the SRM 2242a was scanned and the spectral sensitivity of the CRM calculated (see Section 6.5). It should be noted that the intensity calibration is incomplete without the theoretical intensities of the studied materials, which are often unknown. The correction using the spectral sensitivity is implemented in `LARASoft2`.

4.4.3. Generation of 2D spectral-slice images

For the generation of the 2D spectral-slice images '('heatmaps') custom-written Python- and MATLAB-scripts are used. For data extraction, sorting, and combination, Python-scripts based on the work of J. Demand[6] are used. For the spectra analysis, optional spectra processing and the generation of the heatmaps, a custom MATLAB-script is used (see Appendix B). As described in Section 4.4.1, most often a xy- or xz-raster scans were performed during this work, resulting in a 3D-data set (2 spatial dimensions + 1 spectral dimension). In addition, for optimal cosmic ray removal (Section 4.4.2) at least $n = 2$ spectra are recorded for every point/coordinate of the scan.

After the pre-processing steps, the spectra are sorted by their coordinates and the mean spectrum for every coordinate is calculated. The mean spectrum and its coordinates are the inputs for the MATLAB-script for the data analysis and heatmap generation. In general, the script (i) reads the data, (ii) performs optional pre-processing steps, (iii) extracts some spectral information from the data, and, finally, (iv) displays the spectral information in heatmap form using the coordinate information.

Note that step (iii) requires specific refinements, depending on the studied sample and the spectral information of interest. In general, one or more of the following refinements were included:

(A) **Summed area:** A simple method is to define spectral slices by wave numbers and calculate the mean or summed value within these slices. This method is highly flexible, but sensitive to the background and normalization, and can produce skewed results when these effects are not corrected for. However, in some samples the background is of special interest and is not removed (see *e.g.* some results discussed in Appendix E). In these cases, this method provides an easy-to-use tool, without the need for a model function.

(B) **Fit of model function:** Instead of spectral slices, the position of known peaks can be used to fit a model function. The model function is dependent on the sample; *e.g.* , for graphene peaks a Lorentzian model is used. Using this method, different spectral features can be extracted from the data set, *e.g.* peak area, peak height, peak position and peak width. More complicated models can be used for the simultaneous fit of multiple spectral features at once, or for the fit of a background shape. Provided that the model function includes a parameter for the background offset, this method is less sensitive to background fluctuations. In addition, if the peak positions are well known, this method can be used to fit slightly overlapping peaks.

(C) **Intensity ratios:** Using the results from either method A or B, peak intensity ratios can be calculated and shown in heatmap form. In this approach, effects like the fluctuation of the laser intensity cancel out. This method is often used to normalize the results to a reference peak in the spectrum, *e.g.* the Si-peak in graphene on Si/SiO_2 samples. Additionally, *e.g.* in graphene studies, the ratio of two peaks is also of interest in itself.

---

[6]J. Demand: 'Characterization of a Laser-Raman-Microscope for the examination of hydrogenated graphene'. Bachelor's thesis. Karlsruhe: Karlsruhe Institute of Technology, 2021

(D) **Principal component analysis (PCA):** PCA[Pea01; Hot36] is a statistical technique for the analysis of large data sets without the requirement of *prior*-knowledge about the sample, like its chemical composition or specific Raman peak positions. However, PCA is very complex and requires significant effort to achieve quantitative results. Therefore, in this work, PCA (see Appendix B) is used only for data exploration of the large data sets. The information is then compiled and utilized as input for methods A, B, or C.

It should be noted that further evaluation options could be utilized in the data analysis, including different multivariate analysis techniques, and neutral network approaches; however, these were not used in this work.

5. Long-term operation of the KATRIN LARA system during the KNM1-KNM11 (KATRIN Neutrino Mass) campaigns

5.1. Motivation and overview

The KATRIN LARA system has been successfully operated during all KATRIN Neutrino Mass (KNM) campaigns, starting with the 'first tritium´ campaign in mid-2018 [Ake19]. In this chapter, this long-term operation over a timespan of five years is presented.

The KATRIN LARA system was fully available since the start of the KATRIN operation with tritium on the 18th of May 2018. More than five years later, at the time of writing, the LARA system is monitoring the source gas composition during the KNM11 data taking. In the meantime, during the actual β-scan periods of the KATRIN experiment, over 1.7 mio Raman spectra were recorded, and analyzed.

During the full set of β-scan time periods, the LARA data taking was unintentionally interrupted only five times. Four of these stops were caused by an unknown memory error in LARAsoft; however, this error only appeared once since the upgrade to `LARASoft2` (see Section 4.1.3). Unintentional interruption of the LARA recording was noticed and fixed within 7-20 h, resulting in a total downtime of the LARA system of only 0.36 % during β-scan time periods.

Due to the large amount of data collected over the KATRIN run time, in this section only selected, representative data sets are presented. Apart from the Raman spectra and the analysis settings, the data is available in ADEI for members of the KATRIN collaboration (see Section 4.1.3).

In Section 5.2, the performance of the LARA system is quantified by scrutinizing the performance parameters, spectra quality and hardware stability. In addition, the combination of the LARA system with the Forward Beam Monitor (FBM) [Beg22], that was used during the 'Very First Tritium' (VFT) and 'First Tritium' (FT) campaigns, and overall achievements are highlighted.

A significant challenge for the successful long-term operation of the LARA system is the Raman response calibration with the Standard Reference Material (SRM) (NIST standard reference material) sample. Prior to the KATRIN campaigns, no long-term studies

existed on how, for example, the properties of the SRM or the spectral sensitivity of a LARA system would evolve over the time span of a few years. As the LARA system is usually calibrated between each measurement campaign, these datasets can be used for such long-term studies. Another challenge was that the SRM 2242 certification was only valid until the end of 2018 [NIS08]. A year later, as described in Section 4.1.4, the SRM 2242a was made available by NIST [NIS19]. In Section 5.3, the long-term studies on both theSRM 2242 and the spectral sensitivity of the KATRIN LARA system are described, as well as the application of the new SRM 2242a.

5.2. Definition and evaluation of performance parameters

First, a brief summary of the performance parameters that are used for the discussions and analysis in the following sections is given here.

As defined in Section 2.3, KATRIN puts rather stringent requirements on the tritium, ϵ_T, and the ratio of impurities, κ. In summary, the requirements for the 200 meV goal are:

$$
\begin{aligned}
\delta_{\text{prec.}}\epsilon_T &= \frac{\Delta\epsilon_T}{\epsilon_T} \leq 1 \times 10^{-3} \mathrel{\widehat{=}} 0.1\,\% \quad \text{(precision)}, \\
\delta_{\text{cal.}}\epsilon_T &= \frac{\Delta\epsilon_T}{\epsilon_T} \leq 3 \times 10^{-2} \mathrel{\widehat{=}} 3.0\,\% \quad \text{(trueness)}, \\
\delta_{\text{cal.}}\kappa &= \frac{\Delta\kappa}{\kappa} \leq 10 \times 10^{-2} \mathrel{\widehat{=}} 10\,\% \quad \text{(trueness)}.
\end{aligned} \tag{5.1}
$$

Related to these definitions and requirements, the following nomenclature is used in this chapter:

$$
\begin{aligned}
X &: \text{measured quantity}, \\
\Delta X &: \text{absolute uncertainty on the measured quantity}, \\
\delta X &: \text{relative uncertainty on the measured quantity}.
\end{aligned} \tag{5.2}
$$

Unless stated otherwise, the 1σ standard deviation (coverage $k = 1$ in the GUM[1] framework) is stated as the uncertainty.

In previous works, it was shown that these requirements could be fulfilled, in principle [Stu10a; Fis11; Zel17; Nie21b]. However, the accuracy of the LARA system depends on changing factors, *e.g.* the intensity calibration, the analysis settings, the hardware stability, and the actual gas composition in the WGTS. It is therefore not automatically given that the requirements are always fulfilled over years of operation. Here it should be stressed that the LARA system is a monitoring system; the actual source composition is determined by the purification of tritium in the TRITIUM SEPARATION SYSTEM (TSS) [Wel17; Stu21].

Even though there are other common quality indicators in spectroscopy, *e.g.* LIMIT OF DETECTION (LOD) and the signal-to-noise ratio (SNR), the requirements based on the final KATRIN aim (Eq. 5.1) are the most important quality indicators. For example, a low LOD is not useful if it does not lead to the KATRIN requirements being fulfilled. Note that the results reported in this section for the (V)FT and KNM1 campaigns have been published in Ref. [Ake20b].

---

[1]ISO/IEC Guide 98-3:2008-09: Uncertainty of measurement - Part 3: Guide to the expression of uncertainty in measurement (GUM:1995). Burau Interational Genève, Switzerland, 2008

5.2.1. Spectra quality

The data presented in this section is used to quantify the quality of the Raman spectra.

Figure 5.1 shows representative Raman spectra from the KATRIN measurement campaigns, namely the FT campaign and the KNM1-11 campaigns. To obtain these spectra from the raw images of the CCD detector, several data analysis steps were applied; these have been summarized in Figure 4.3 in Section 4.1.3. The applied processing steps are: (i) removal of cosmic rays, (ii) astigmatism correction, (iii) spectral sensitivity calibration, (iv) binning, (v) background removal via the SCARF algorithm, and (vi) the spectral overlap correction. In order to make it easier to compare the spectra, they are each individually normalized to $I_{\mathrm{max}} = 100$; this is not done in regular data analysis.

In Figure 5.1, in addition to the Q_1-branches of six hydrogen isotopologues, the O_1- and S_1-lines are annotated when they are visible. In the KNM1-11 campaigns ($\epsilon_{\mathrm{T}} > 95\,\%$), these are mainly visible for T_2, while in the FT campaign ($\epsilon_{\mathrm{T}} < 1\,\%$) mainly the O_1- and S_1-lines of D_2 ($c_{D_2} > 90\,\%$) are visible. Comparing the FT-Raman spectrum with the spectrum from *e.g.* KNM1, clearly demonstrates the problem of overlapping spectral lines: In the FT-Raman spectrum, the DT-Q_1-branch does slightly overlap with the $D_2O_1(3)$-line; however, there is enough separation that a fit of the DT-Q_1-branch is possible. In KNM1, where the main gas component is T_2 instead of D_2, the $T_2S_1(2)$-line that is almost at the exact position of the DT-Q_1-branch has a significant intensity, and thus rendering a separate fit of the DT-Q_1-branch impossible without additional analysis. In this case, the spectral lines are deconvoluted following the procedure depicted in Figure 4.4 in Section 4.1.3.

For the extraction of the source gas composition from the respective Raman spectra, the Q_1-branches are fitted with the `ShapeFit` procedure [Jam13], determining the signal intensity I_{Q_2} of every hydrogen isotopologues. The signal intensities are then corrected using the molecule-specific theoretical correction factors, and the concentrations c_{X}, the tritium purity ϵ_{T}, and the HT/DT-ratio κ are calculated according to the equations given in Section 2.3.

Because of the radioactive β-decay of tritium and the carbon-release from the stainless-steel walls of the Inner Loop (IL) and the WGTS, which gives rise to unwanted ^{3}He and several molecular species, about $1\,\%$ of the gas is constantly removed by the permeator in the IL (see Figure 2.4). This raises the need for regular gas refills. Due to technical reasons, this is realized by batch gas transfers rather than a constant stream of new gas. These batch gas transfers often have different gas compositions than the actually circulating gas in the IL, causing a shift in the chemical equilibrium and a changing gas composition for up to several days after the refill. Therefore, the source gas composition changes every time the processed gas batches are injected into the KATRIN loop (see Figure 2.4 in Chapter 2).

As an example, this is shown in Figure 5.2 for the KNM4 campaign; every batch refill of the KATRIN loop with a different gas composition is associated with an exponential temporal evolution of tritium purity. However, these variations are no problem for the KATRIN experiment as long as they are monitored with the required precision. Figure 5.2b and Figure 5.2c show the precision that is derived from the time series data. Every exponential temporal evolution of tritium purity is fitted with an exponential curve, and the residuals of this fit correspond to the precision of the measurement [Fis14]. Figure 5.2b shows a zoomed region, corresponding to the time between two batch refills, together with the associated exponential fit curve. The statistical histogram of the residual of the exponential fit is shown in Figure 5.2c. The standard deviation of this histogram is the precision of this data 'snapshot'. For the data shown $\delta_{\mathrm{prec.}}\epsilon_{\mathrm{T}} = 0.046\,\%$, easily fulfilling the KATRIN requirement of $\delta_{\mathrm{prec.}}\epsilon_{\mathrm{T}} = 0.1\,\%$.
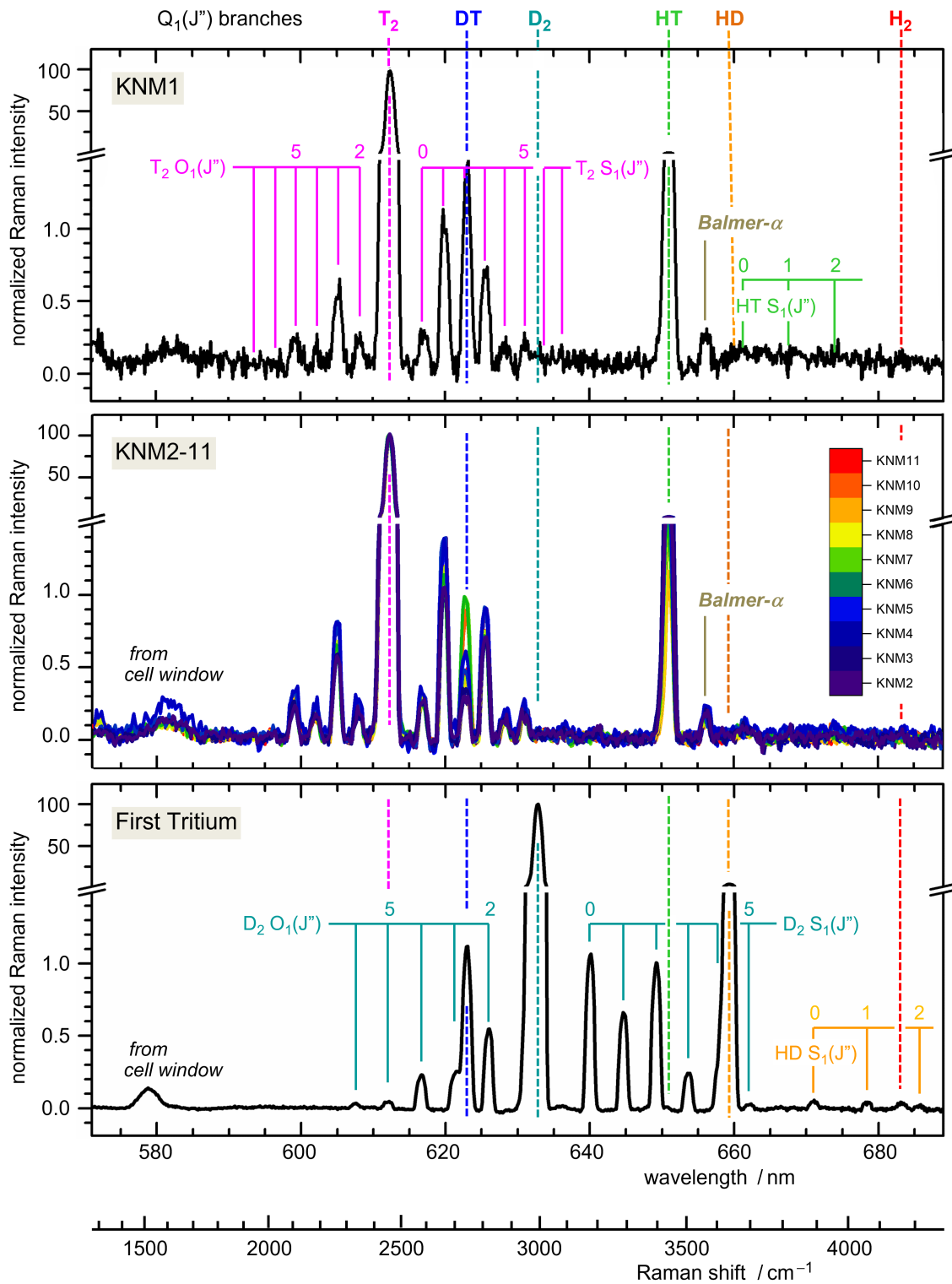
Figure 5.1.: Raman spectra from all KATRIN NEUTRINO MASS (KNM) campaigns. Data updated and adapted from [Ake20b]; details can be found in the text.

This analysis is performed for data 'snapshots' from every KNM campaign that was conducted, up to the time of writing. In addition, the trueness requirement is also examined in the data 'snapshots'. The results are summarized in Table 5.1. One finds that the KATRIN requirements were met in all KNM campaigns, despite the different source gas compositions.
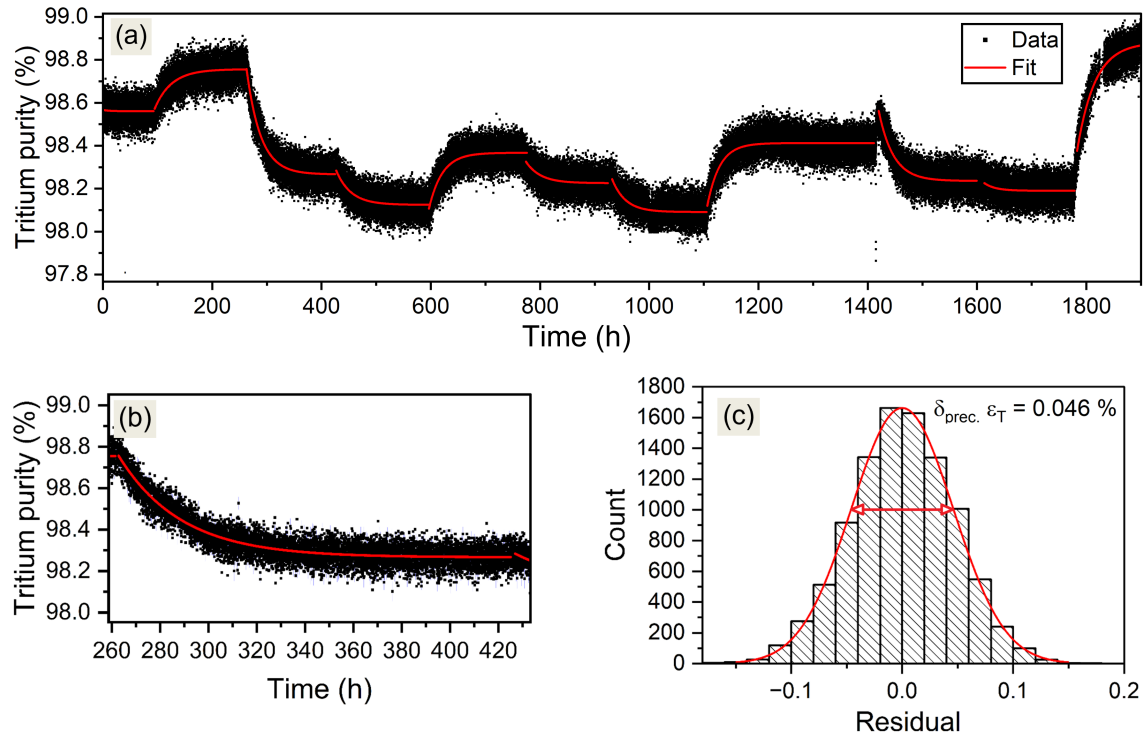
Figure 5.2.: Source gas composition during KNM4. Every batch refill of the KATRIN loop with a different gas composition is fitted with an individual (exponential) curve. From the spread of the residuals, the precision can be determined; details can be found in the text.

Table 5.1.: Typical monitoring parameters for the gas composition in KATRIN: comparison of the specification requirements and the values achieved during KNM1-11 data taking. Precision and trueness are given relative to the respective values, $|\delta X = \Delta X/X|$.

		c_{T_2}	c_{DT}	c_{HT}	ϵ_T	κ
Require-ments	Value	-	-	-	> 0.95	-
	Precision	-	-	-	$< 1 \times 10^{-3}$	-
	Trueness	-	-	-	$< 3 \times 10^{-2}$	$< 10 \times 10^{-2}$
KNM1	Value	0.950 16	0.012 81	0.035 68	0.962 20	2.785 51
	Precision	2.15×10^{-4}	6.34×10^{-3}	4.31×10^{-3}	5.20×10^{-4}	8.76×10^{-3}
	Trueness	9.72×10^{-3}	9.26×10^{-2}	1.45×10^{-1}	1.49×10^{-3}	3.37×10^{-2}
KNM2	Value	0.974 32	0.005 57	0.019 33	0.986 75	3.475 51
	Precision	3.76×10^{-4}	2.44×10^{-2}	1.18×10^{-2}	1.96×10^{-4}	1.50×10^{-2}
	Trueness	7.67×10^{-3}	7.56×10^{-2}	7.79×10^{-2}	1.42×10^{-3}	7.94×10^{-2}
KNM3	Value	0.971 15	0.005 22	0.020 92	0.984 22	4.007 56
	Precision	1.95×10^{-4}	1.33×10^{-2}	4.21×10^{-3}	1.58×10^{-4}	1.44×10^{-2}
	Trueness	1.58×10^{-3}	5.72×10^{-2}	5.50×10^{-2}	1.97×10^{-4}	3.40×10^{-2}
KNM4	Value	0.965 47	0.005 53	0.026 27	0.981 37	4.750 69
	Precision	2.43×10^{-4}	1.29×10^{-2}	4.40×10^{-3}	1.86×10^{-4}	1.32×10^{-2}
	Trueness	1.82×10^{-3}	5.66×10^{-2}	5.35×10^{-2}	4.05×10^{-4}	3.29×10^{-2}
KNM5	Value	0.980 90	0.005 07	0.010 44	0.988 65	2.063 66
	Precision	2.79×10^{-4}	2.95×10^{-2}	8.43×10^{-3}	2.08×10^{-4}	2.85×10^{-2}
	Trueness	1.34×10^{-3}	5.58×10^{-2}	5.56×10^{-2}	5.68×10^{-4}	5.81×10^{-2}
KNM6	Value	0.976 50	0.007 33	0.013 48	0.986 92	1.844 41
	Precision	3.09×10^{-4}	1.82×10^{-2}	1.30×10^{-2}	1.61×10^{-4}	9.12×10^{-3}
	Trueness	1.57×10^{-3}	7.36×10^{-2}	5.47×10^{-2}	8.76×10^{-4}	6.91×10^{-2}
KNM7	Value	0.977 31	0.008 78	0.011 75	0.987 57	1.338 64
	Precision	1.09×10^{-4}	6.41×10^{-3}	3.82×10^{-3}	7.69×10^{-5}	7.17×10^{-3}
	Trueness	1.45×10^{-3}	7.28×10^{-2}	5.40×10^{-2}	8.04×10^{-4}	6.89×10^{-2}
KNM8	Value	0.980 61	0.004 59	0.012 77	0.989 29	2.784 15
	Precision	1.96×10^{-4}	1.13×10^{-2}	1.13×10^{-2}	1.06×10^{-4}	9.46×10^{-3}
	Trueness	1.24×10^{-3}	7.85×10^{-2}	5.53×10^{-2}	6.95×10^{-4}	7.31×10^{-2}
KNM9	Value	0.972 15	0.006 68	0.019 13	0.985 06	2.863 86
	Precision	9.22×10^{-5}	6.17×10^{-3}	2.55×10^{-3}	6.55×10^{-5}	6.64×10^{-3}
	Trueness	1.64×10^{-3}	7.61×10^{-2}	5.43×10^{-2}	9.02×10^{-4}	7.05×10^{-2}
KNM10	Value	0.974 65	0.009 04	0.014 15	0.986 25	1.566 67
	Precision	1.32×10^{-4}	4.62×10^{-3}	7.16×10^{-3}	8.03×10^{-5}	8.11×10^{-3}
	Trueness	1.57×10^{-3}	7.41×10^{-2}	5.47×10^{-2}	8.72×10^{-4}	6.84×10^{-2}
KNM11	Value	0.976 93	0.005 02	0.015 88	0.987 38	3.165 25
	Precision	1.30×10^{-4}	1.23×10^{-2}	4.13×10^{-3}	7.95×10^{-5}	1.05×10^{-2}
	Trueness	1.05×10^{-3}	7.70×10^{-2}	5.49×10^{-2}	8.18×10^{-4}	7.14×10^{-2}
Average	Value	0.972 74	0.006 88	0.018 16	0.984 15	2.535 30
	Precision	2.07×10^{-4}	1.32×10^{-2}	6.83×10^{-3}	1.67×10^{-4}	1.19×10^{-2}
	Trueness	2.79×10^{-3}	7.18×10^{-2}	6.50×10^{-2}	8.22×10^{-4}	6.00×10^{-2}

5.2.2. Hardware stability

Regarding the hardware of the LARA system, only the CCD detector, and the spectrometer caused any problems at all. The original PIXIS 2k CCD had to be exchanged for a PIXIS 400B[2] in March 2020 (in between KNM2/KNM3) because the aging PIXIS 2k CCD detector (purchased in 2009) had developed `TimeOutErrors` with increasing frequency, causing the loss of about 1-5 spectra per day. As a preventive measure, the CCD was therefore replaced before the start of KNM3.

During KNM5, the internal shutter of the HTS spectrometer, which is usually opened and closed for every Raman measurement, started to cause problems and would become stuck in either one of the positions for prolonged times, affecting the data taking. Since replacing the mechanical shutter mechanism would require a large intervention at the spectrometer (if it were possible at all), it was decided to leave the shutter in the 'open' position for all future measurements.

For the evaluation of the stability of the hardware, data from the latest complete measurement campaign, KNM10, are shown and discussed. At the time of the KNM10 data taking, every hardware component was already at least five years old and was in operation for at least half of every single year. Therefore, any hardware problems would have more time to manifest themselves, and would be more likely to appear. In addition, there was a problem with the software of the LM-10 power meter (see Figure 4.1) during KNM1-7, and it could not be used for the external power monitoring during these campaigns; in KNM10 it could be used again, and provides helpful insight.

In total, six hardware stability parameters were investigated; these are summarized and described in the following list. The statistical histogram data is shown in Figure 5.3, and the corresponding data evolution during KNM10 is shown in Figure 5.4. The hardware itself was already described in Section 4.1.

- **CCD temperature:** The 2D light sensor of the CCD-detector is constantly cooled via thermoelectric cooling to minimize the dark current and thus the dark noise. The set temperature in operation is $-75.0°$C. According to the temperature read-out, this temperature is always reached (except for one international warm-up), and stable is within the numerical precision of the read-out, namely $0.01°$C.

- **Water chiller temperature:** The laser head is installed on a water-cooled baseplate. In operation, the water chiller set temperature is $24.0°$C. This is the most stable set value as shown in Ref. [Fis14]. The water chiller can keep the temperature of the cooling water stable at $(24.000 \pm 0.018)°$C (0.73% relative) during the full 1300 h of the KNM10 campaign.

- **Laser output power:** The set value is 4 W, and according to the internal readout of the laser, the value is maintained at (4.000 ± 0.002) W (0.05% relative).

- **External power meter:** According to the external power meter, the laser power is stable to 0.65% relative. This is one order of magnitude worse, when compared to the internal readout of the laser. However, this is not surprising, considering that the power meter is positioned at the end of the optical beam path in the double-pass configuration. At this point, the laser beam has already passed several lenses, the Glen-Taylor polarizer, and several optical windows. The laser power arriving at the position of the LM-10 power meter is only (0.2453 ± 0.0016) W. During the initial commissioning, in Ref. [Fis14], the power meter was placed in the

---

[2]both from Teledyne Princeton Instruments, Trenton, New Jersey, USA

beam path without any windows or lenses present. In Ref. [Fis14], the measured value was (4.558 ± 0.004) W (0.09 % relative). When comparing these two values, it appears that the power stability measured at present using the LM-10 sensor head is worse than during commissioning of KATRIN LARA. However, predominantly this is a consequence of the measurement resolution of the LM-10 sensor head, which according to the manufacturer's data sheet is 1 mW. Thus, at the low power values received at the current measurement position, the readout becomes resolution-dominated. In Figure 5.3 power readings for the laser-internal (i.e., at the laser output) and laser-external (i.e., after passage through all optical components in the LARA beam path) measurements are compared. From those data and the comparison to the original commissioning data one can deduce that the absolute power stability has not deteriorated. It is noteworthy that, while the externally measured power data are seemingly less precise, as a bonus, a comparison between the continuously monitored laser-internal and laser-external values will reveal any deterioration of optical components in the LARA beam path, and thus help in deciding when to service certain optical elements.

- **Laser head / base temperature:** These values show the largest variations of the hardware parameters, only being stable for a couple of hours at a time. They are also almost 100 % correlated, with an offset of about 4°C. However, the overall spread of the variations is small with 0.2 % relative for the laser head temperature and 2.7 % for the laser base temperature, respectively.

In summary, the hardware stability is excellent and has not worsened since the first commissioning of the components in 2014 [Fis14].
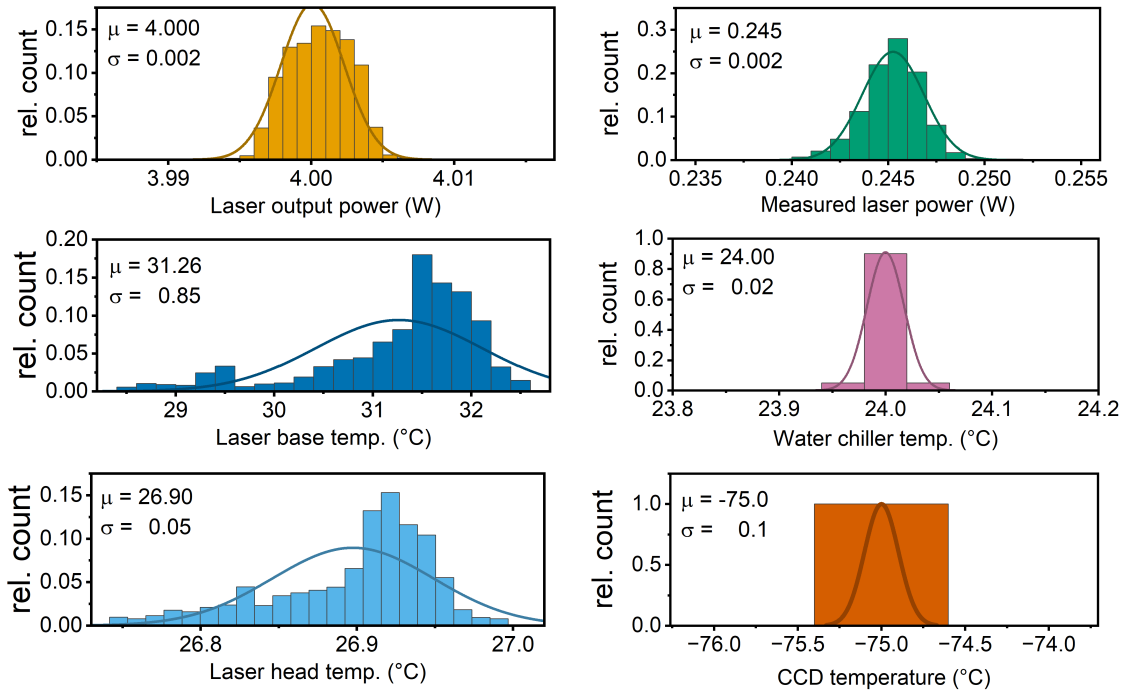
Figure 5.3.: Histograms of hardware parameters of the KATRIN LARA system during KNM10. In every histogram, a Gaussian distribution, and the corresponding mean (μ) and standard deviation (σ) are included. The corresponding time series data is shown in Figure 5.4. Details can be found in the text.
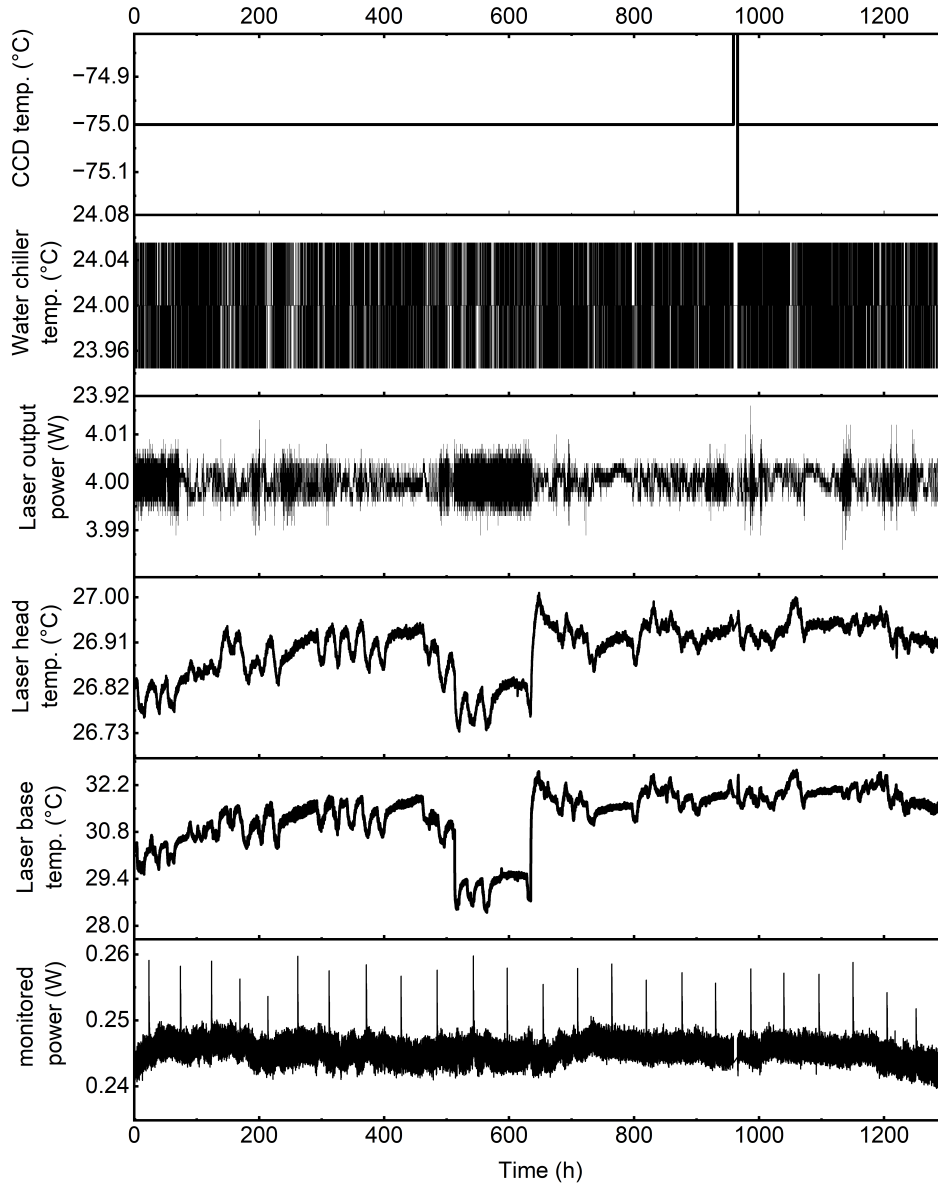
Figure 5.4.: Time evolution of hardware parameters of the KATRIN LARA system during KNM10. The corresponding histogram data is shown in Figure 5.3. Details can be found in the text.

5.2.3. Combination with activity measurements during the 'very first tritium (VFT)' and 'first tritium (FT)' campaigns

During the first KATRIN measurement campaigns with tritium in 2018, referred to as 'Very First Tritium' (VFT) and 'First Tritium' (FT), only small amounts of tritium ($\epsilon_T < 1\%$) were circulated in the WGTS. As Deuterium (D_2) was used as the main carrier gas; because of the permeator in the inner loop tritium, the tritium was mostly present in the form of DT [Ake20b].

The KATRIN LARA system is optimized for the measurement and analysis of high-tritium purity gas-mixtures. To measure the gas mixture accurately during the VFT/FT campaigns without increasing the acquisition time was a challenge, specifically on the data analysis. In order to fulfill the KATRIN requirements and provide an accurate result, different data analysis strategies were employed. In relation to that, the LARA results were combined with the activity measurements of the FBM.

Representative for the (V)FT-campaigns, the time series data of the DT-concentration from a single KATRIN run is shown in Figure 5.5a. The run length is about three hours (3 hour), and is divided into different sub-runs corresponding to different high voltage set-points of the MS (see Figure 2.5). As for the set-point with lower energies, more electrons can pass the MAC-E-filter, these sub-runs can be shorter and still reach the necessary statistics [Ake22a]. Therefore, when the time series data is shown as a function of the sub-run as in Figure 5.5a, the timescale is not linear. Note that LARA data was recorded every 60 s, and there are sub-runs which are shorter and thus do not contain a LARA value. During the (V)FT-campaigns, because of the low tritium content and the corresponding small Raman peak (see *e.g.* Figure 5.1), the precision that is reached is only about $\delta c_{DT} \approx 0.4\%$. As established earlier in this section and in Section 2.3, this directly contributes to the systematic uncertainty in the KATRIN experiment. Two complementary methods were applied to improve the precision and thus to mitigate the impact of the systematic uncertainties.

(a)

(b)
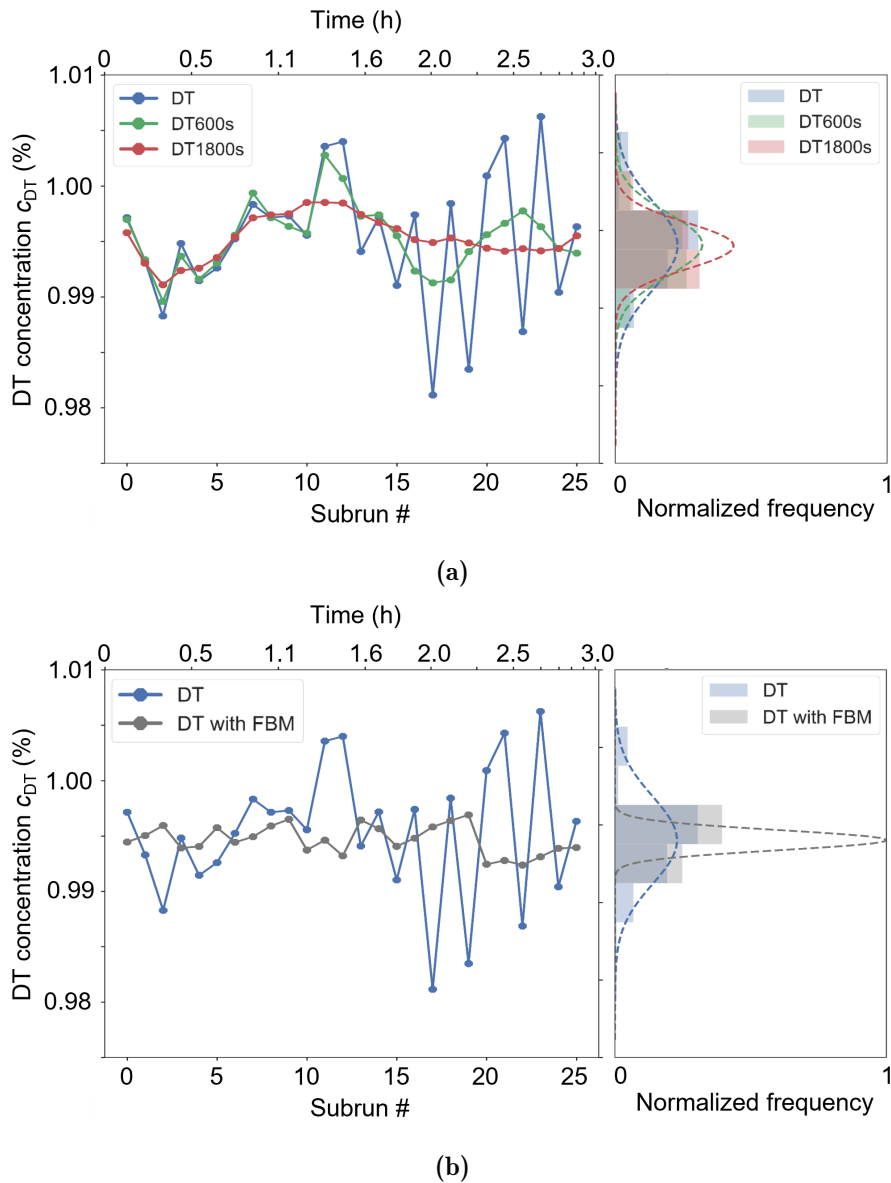
Figure 5.5.: DT-concentration during a selected run of the FT campaign. (a) With moving average of 600 s and 1800 s. (b) Combination of LARA and FBM data according to Eq. 5.3. Details can be found in the text.

Moving average

In addition to the time series data, Figure 5.5a also shows the DT-concentration with different moving averages, with averaging windows of $600\,\mathrm{s}$ and $1800\,\mathrm{s}$, respectively. This improves the precision to about $\delta c_{\mathrm{DT}} \approx 0.2\,\%$ because the short-time fluctuations are removed. However, this can introduce an unknown systematic shift on the neutrino mass and is thus not recommended overall.

Use of FBM data

The FBM directly monitors the source activity, A. During the (V)FT-campaigns, the FBM data showed a long-term drift of about $0.4\text{-}1.0\,\%\,\mathrm{d^{-1}}$, but was significantly more precise than LARA on short time scales. Assuming that the source activity is directly proportional to the DT-concentration, i.e., $A \propto c_{\mathrm{DT}}$, the FBM data can be combined with the LARA data, to improve the precision of the latter, according to

$$\mu(c_{\mathrm{DT,\ Subrun}}) = \frac{\mu(c_{\mathrm{DT,\ Run}})}{\mu(A_{\mathrm{FBM,\ Run}})} \cdot \mu(A_{\mathrm{FBM,\ Subrun}}). \tag{5.3}$$

Here μ denotes the mean value of the respective (sub-)run. The mean DT-concentration of the run is normalized to the mean activity as measured with the FBM for the same run. Multiplying this with the mean value of the activity in a given sub-run, the effective DT-concentration in the sub-run can be estimated. Applying this to the previously shown KATRIN run, results in a precision of $\delta c_{\mathrm{DT}} \approx 0.1\,\%$, reaching the KATRIN requirement, while at the same time maintaining the sensitivity to short-term fluctuations. This is shown in Figure 5.5b for a single run and in Figure 5.6 for all FT runs.
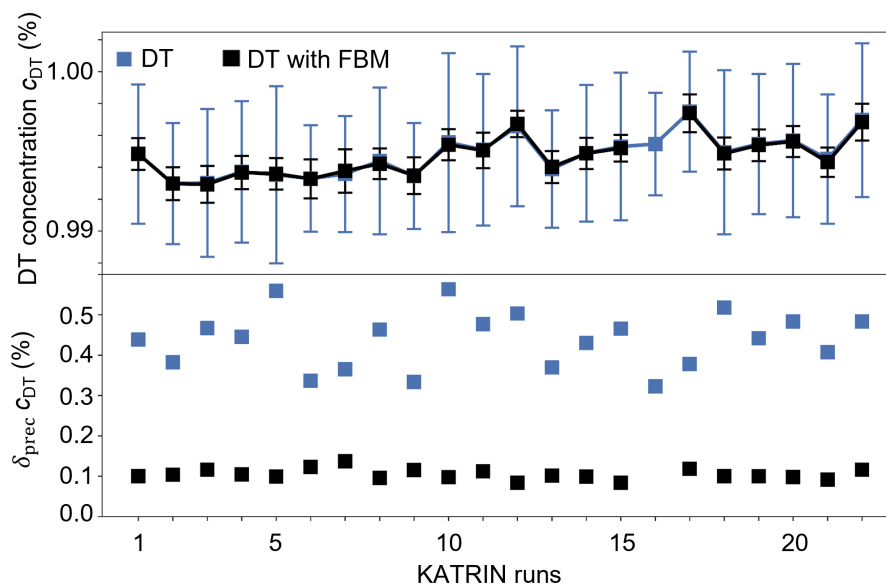
Figure 5.6.: Effect of the combination of LARA and FBM data for a set of runs of the VFT campaign. *Top:* DT-concentration c_{DT} with statistical error bars $\Delta_{\mathrm{prec.}}c_{\mathrm{DT}}$. *Bottom:* Relative statistical uncertainty $\delta_{\mathrm{prec.}}c_{\mathrm{DT}}$ Details can be found in the text.

5.3. Intensity calibration with the standard reference material (SRM) 2242

The KATRIN LARA system was calibrated repeatedly since its commissioning more than a decade ago, using an SRM 2242 fluorescence standard (see Section 4.1.4). Since the SRM 2242 is certified for 180° Raman system, but is used for the calibration of the 90° Raman system 'KATRIN LARA', the calibration is not straightforward. The SRM 2242 has to be positioned in such a way that the laser beam passes the SRM sample as close to the surface as possible. This is achieved by a positioning procedure in which the laser beam spot is monitored using a webcam [Zel17].

This positioning procedure is done at least ten times ($j = 10$) to determine the uncertainty of this procedure and finally the spectral sensitivity. In addition, NIST uses a polarization scrambler for the certification measurements, and it is recommended to use one for the intensity calibration [NIS08]. However, it can be demonstrated that instead of polarization-scrambling, one can use a $\lambda/2$-plate to rotate the polarization of the incoming laser light by $\pm 45°$ [Rup12; Sch15b]. The mean of these two measurements is equivalent to a measurement with a polarization scrambler. Therefore, for every position of the SRM 2242 two spectra with $\pm 45°$ are recorded. Note that in specific measurements, *e.g.* for the direct comparison of two different SRM, this step can be skipped.

The completed measurement procedure and data analysis required to determine the spectral sensitivity is summarized in flow-chart representation in Figure 5.7. The background signal without laser light is subtracted from every measured spectra to remove signal from stray light. Finally, the measured and theoretical intensities of the SRM are normalized to 1 at the same wavelength[3], before the spectral sensitivity is calculated as the ratio of the two intensity curves. This is performed for every vertical bin *(i)* of the CCD detector. This is repeated *j*-times to obtain multiple spectral sensitivity curves that can be analyzed to determine the systematic uncertainty of the positioning method.
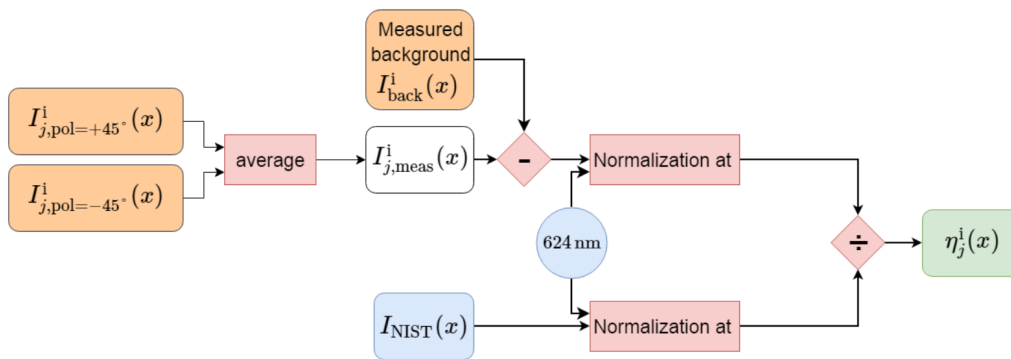
Figure 5.7.: Schematic flow-chart illustration of the data analysis of the SRM 2242 measurements. Measured input quantities are shown in orange, predefined input quantities in blue, data operations in red and output quantities in green. Image adapted from [Zel17].

---

[3]Usually at 624 nm because the uncertainty of the data provided by NIST is smallest at this point. However, in principle other normalization wavelength can be used.

5.3.1. Challenges encountered

Although, the demonstration of intensity calibration with the SRM 2242 was established in Refs. [Rup12; Sch14; Sch13a; Zel17], there were open questions regarding the long-term operation of the LARA system.

1. The SRM 2242 certification was only valid until the end of 2018 [NIS08]. Over a year later, as described in Section 4.1.4, the SRM 2242a was made available by NIST [NIS19]. The SRM 2242a has an entirely different form factor and would require a complete redesign of the LARA calibration cell for it to be usable for intensity calibration.

2. The long-term aging effects on the material properties of the SRM 2242 are unknown. These need to be quantified and and it has to be proven that the aging of a standard does not impact the intensity calibration.

3. Some KNM campaigns had to be performed without evacuating the inner loop of the WGTS in between them. Therefore, the LARA cell remained filled with a tritium gas mixture during the short maintenance time, and could not be removed from the cell holder. This made it impossible to install the calibration cell and perform the calibration. Instead of the planned calibration interval of one calibration per 60 days, the timespan between calibrations was on average much larger and up to a full year.

The systematic investigations and solutions regarding these challenges are presented here.

Table 5.2.: Summary of the intensity calibrations in between KNM campaigns and maintenance work that potentially changes the spectral sensitivity of the system.

Campaign	Before the start of the campaign	Calibrated?	Date
	Maintenance work		
VFT		yes	18/05/2017
FT		yes	27/07/2018
KNM1	Realignment of the beam path	yes	20/02/2019
KNM2		yes	01/09/2019
KNM3	Exchange of the CCD detector (10/03/2020) from PIXIS:2K* to PIXIS:400B*	yes	12/03/2020
KNM4		yes	27/08/2020
KNM5		yes	23/02/2021
KNM6		no	-
KNM7		no	-
KNM8		no	-
KNM9		no	-
KNM10		yes	14/06/2023
KNM11		no	-

(*) Both from Teledyne Princeton Instruments, Trenton, New Jersey, USA

5.3.2. Validity of the SRM 2242 certification

One possible way to demonstrate that the spectrum emitted from the employed SRM 2242 can still be used for the calibration of a Raman system, even when the certification is expired, is to calibrate the expired SRM against a new and certified SRM 2242a.

However, there are two main problems associated with such a *re-calibration*:

(i) The employed SRM 2242 is considered contaminated[4]. The standard activity measurement of the TLK is a so-called wipe-test, which could alter the properties of the SRM 2242 by leaving residual material on the glass slide. Therefore, the direct re-calibration has to be made by placing the new SRM into the same glove box.

(ii) The new SRM 2242a, the only available reference material for Raman systems with laser excitation of 532 nm with valid certification, has entirely different dimensions compared to the original SRM 2242. Therefore, a new calibration cell design is necessary, which - according to experience - is a time-consuming task, and could introduce new systematic effects and uncertainties, complicating the comparability of results.

In order to avoid these problems, an indirect re-calibration can be used: During the finalization of the studies regarding the calibration of the LARA system in 2017, a total of three different SRM 2242 standards were used and compared to one another [Zel17]. It was found that with the developed calibration procedure, the spectra from the three SRM samples agreed with each other within the uncertainties provided by NIST. One of the SRM was then brought into the KATRIN LARA glove box appendix and used for all successive calibrations of the KATRIN LARA system (called LARA-SRM in the following). The second SRM was moved to the TRiHyDE glove box and used for calibrations of the TRiHyDE LARA system [Nie21b]. The third SRM was stored in the laser laboratory of the TLK (called Lab-SRM in the following).

If aging of the material affected the LARA-SRM and the Lab-SRM to a similar extent, it is possible to make a statement about the LARA-SRM by measuring the Lab-SRM. This
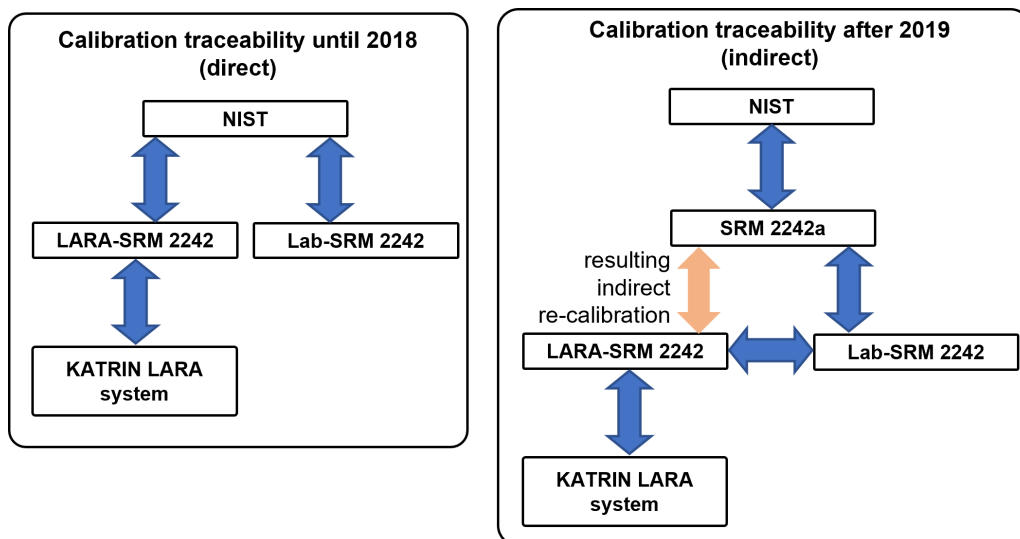
Figure 5.8.: Direct and indirect calibration traceability procedure for the KATRIN LARA system. Details can be found in the text.

---

[4]According to TLK standards, everything leaving the glove box environment is treated as radioactively contaminated until activity measurements prove the opposite.

procedure and the changed calibration traceability diagram is summarized in Figure 5.8. More specifically, the Lab-SRM can be re-calibrated against a new, certified SRM 2242a. If (i) the spectra emitted by the Lab-SRM and the SRM 2242a agree, and (ii) the assumption about the aging of the LARA-SRM and the Lab-SRM is valid, then the spectra from the LARA-SRM and the SRM 2242a should also agree. In the following, the validity of both these conditions is addressed.

For proving the first point, i.e., the comparative spectral measurements of Lab-SRM and SRM 2242a, a simple laser Raman system was set up in the laser laboratory of the TLK. Since in these measurements only the general properties of the SRM are of interest, there was no need to mimic the setup of the KATRIN LARA system; instead a 180° scattering geometry (as used by NIST) can be employed. This removes the additional uncertainty that is introduced in 90° scattering geometry by the positioning procedure. In addition, this enabled the use of a μRa-systems (described in Ref. [Pri22]), making the setup easy and removing the need for any optical alignment. The μRa-systems are equipped with a laser and detection system in 180°-scattering configuration. As a consequence of using a μRa-system for detection, all recorded spectra are one-dimensional, in contrast to the two-dimensional images recorded with the typical spectrometer and CCD-detector combination (see Section 4.1.2). This makes data analysis and comparison of the two SRM standards easier and straightforward; although some finer details in the spectra may be lost because of the lower spectral resolution of the μRa-system.

In Figure 5.9, the spectral sensitivity of the test setup from a calibration with the Lab-SRM and the SRM 2242a is shown. In the spectral intervals [560 nm, 600 nm] and [690 nm, 720 nm] the difference between the curves is noticeable, but still $< 1.3\%$. However, in the KATRIN relevant region (600 nm, 690 nm), which contains all Q_1-lines of the hydrogen isotopologues, the differences are $< 1\%$ and mostly within the uncertainty limits provided by NIST. For example, at the Q_1-branch of T_2 (at ~ 612 nm) the difference is only 0.7%. This is
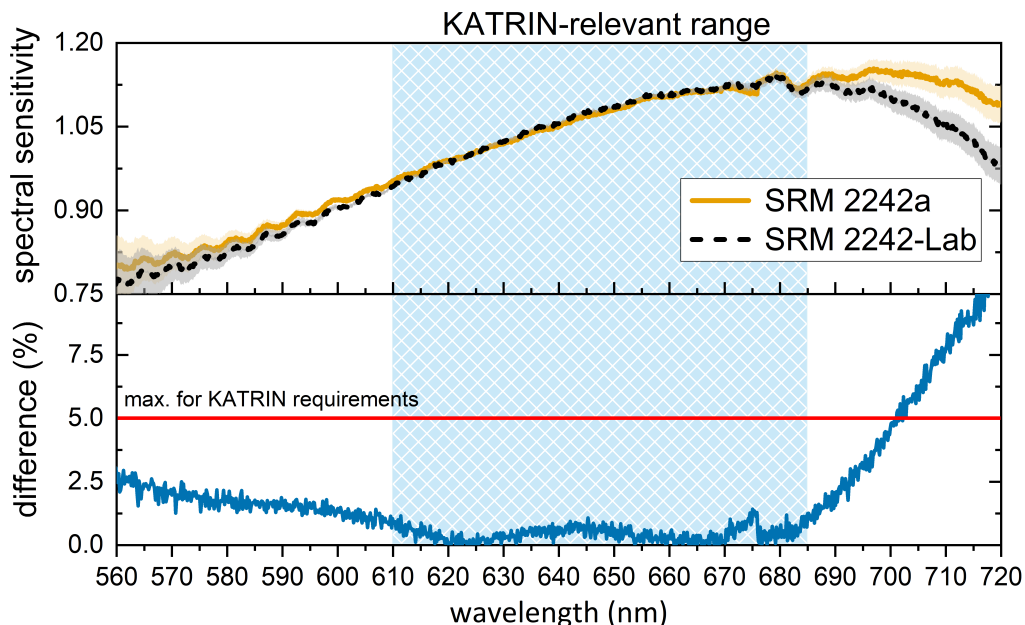
Figure 5.9.: Difference between spectral sensitivity using Lab-SRM and SRM 2242a. *Top:* Mean spectral sensitivity with 1σ standard deviation. *Bottom:* Relative difference between the mean spectral sensitivity. The KATRIN relevant wavelength range (600 nm, 690 nm) is marked. In addition, the red line indicates an upper limit for the difference in a KATRIN-like scenario ($\epsilon_T > 95\%$, $\kappa \approx 2$) as shown in Figure 5.10. Details can be found in the text.

smaller than the typical systematic uncertainty ($\sim 1.0\,\%$) associated with the calibration procedure in the 90° scattering configuration [Zel17]. In conclusion, the differences between Lab-SRM and SRM 2242a within the KATRIN relevant wavelength region are negligible when compared to the overall uncertainties. Thus, even though the Lab-SRM will certainly have aged, and the certification is no longer valid, it can still be used for the calibration of the KATRIN LARA system without any restrictions or disadvantages.

Second, the assumption that the aging of Lab-SRM and LARA-SRM are comparable needs to be discussed. In Ref. [NIS19] it is stated: *'The glass substrate is susceptible to surface corrosion when exposed to elevated levels of humidity. Therefore, when not in use it is strongly recommended that the SRM unit be stored in an environment with a stable humidity of 20 % or lower.'*

On the one hand, the Lab-SRM was stored in an open container in the laser laboratory. Even though the laboratory is equipped with an air conditioning system, it is not always in use and the humidity is neither controlled, nor monitored. Since it is a laboratory, which is in regular use, it can be assumed that the humidity is between 40-60 %. Even though the Lab-SRM was not stored in optimal and recommended conditions, the calibration result agrees with a new SRM 2242a, as highlighted in the previous paragraph.

On the other hand, LARA-SRM was stored in a glove box filled with $98\,\%$ N_2 and $2\,\%$ O_2. The gases are constantly circulated, cleaned and dried as part of the tritium retention system (TRS). The mean temperature and relative humidity in the glove box were $T = (26.5 \pm 1.6)°C$[5] and RH$< 1\,\%$[6] on average over the last year.

It is therefore a substantiated assumption that the LARA-SRM is in an overall better condition than Lab-SRM and was less affected by aging and humidity. In conclusion, this demonstrates that even though the validity of the certification of LARA-SRM is expired, and it cannot be accessed for a direct re-calibration, it is justified to use the LARA-SRM for the intensity calibration of the KATRIN LARA system. In the next section, the actual long-term evolution of the spectral sensitivity of the KATRIN LARA system is presented.

5.3.3. Stability and reproducibility of the system's spectral sensitivity over time

As described in Section 5.3.1, the calibration could not always be performed in between every KNM campaign. All calibrations of the KATRIN LARA system are listed in Table 5.2. In addition, the maintenances actions and other changes to the LARA system are noted. If anything was changed during the maintenance period, the spectral sensitivity cannot be compared directly to the previous calibration. After the exchange of the CCD-detector in 2020, four campaigns with linked intensity calibration can be identified: KNM3, KNM4, KNM5, and KNM10; covering about three years. Using data from these campaigns, the temporal evolution of the spectral sensitivity of the KATRIN LARA system can be studied. In order to quantify the change over time, two methods are employed:

(i) Direct comparison of the spectral sensitivities, including their respective uncertainties.

(ii) Re-analyzing the LARA data with the spectral sensitivity from a different period, *e.g.* using the KNM5 spectral sensitivity to analyze the KNM3 data and vice versa. This can be described as sort of a round-robin data analysis. In contrast to the first method, this method allows directly quantifying how the KATRIN-relevant parameters are affected.

---

[5]Internal sensor name for reference: ISS-A-RT201
[6]Internal sensor name for reference: ISS-A-RM201

Direct comparison

As the KATRIN requirements (see Eq. 5.1) are stated in relation to $\{\epsilon_T, \kappa\}$, it is useful to calculate the requirements in terms of the uncertainty of the intensity calibration. The goal is to answer the question: *'When the operator of the KATRIN LARA system measures the spectral sensitivity of the system, is there a simple formula that they can check, to determine if the observed variation in the spectral sensitivity is within the region that is allowed by the KATRIN requirements?'*

In general, the calibration uncertainty $\Delta_{\text{cal}}X$ $(X = c_{\text{Q2}}, \epsilon_T, \kappa)$ is given by

$$\Delta_{\text{cal}}X = \sqrt{\Delta\eta^2 + (\Delta_{\text{theo.}}X)^2}, \tag{5.4}$$

where $\Delta_{\text{theo.}}X$ is the theoretical uncertainty [Roy11; Nie21a; Nie21b], and $\Delta\eta$ is the total, system-specific spectral sensitivity uncertainty, which itself is given by

$$\Delta\eta = \sqrt{(\Delta_{\text{NIST}}\eta)^2 + (\Delta_{\text{meas.}}\eta)^2}, \tag{5.5}$$

where $\Delta_{\text{NIST}}\eta$ is the uncertainty stated by NIST [NIS08], and $\Delta_{\text{meas.}}\eta$ the uncertainty associated with the calibration procedure [Sch15b; Zel17]. Note that the uncertainties related to the spectral sensitivity are two-dimensional arrays, and thus a function of the (x,y)-pixels on the CCD detector [Sch15b]. Using the equations 5.4 and 5.5, the definitions of $\{\epsilon_T, \kappa\}$, and Gaussian uncertainty propagation without correlations (formulas are given in Appendix A), the KATRIN requirements can be used to calculate requirements on δ_η. The results of these calculations are summarized in Figure 5.10. The following observations can be made:

- For ϵ_T, the calculations for the uncertainty strongly depend on the actual value of ϵ_T. Therefore, the calculations are performed for three different scenarios: (i) $\epsilon_T > 97\%$, which is assured in the standard KATRIN operation mode [Stu21], (ii) $\epsilon_T \approx 90\%$, and (iii) $\epsilon_T \approx 80\%$.

- None of the curves start at (0,0), since according to Eq. 5.5, $\Delta_{\text{cal}}\eta = \Delta_{\text{theo.}}\eta$ for $\Delta\eta = 0$. The uncertainty of the theoretical calculations therefore constitutes a lower limit on the total calibration uncertainty $\Delta_{\text{cal}}\eta$.

Although in reality $\Delta\eta$ is a function of the wavelength λ (x-pixel of the CCD), with a minimum typically around $630\,\text{nm}$, for the calculations here a 'worst-case' scenario is

(a) ϵ_T **(b)** κ
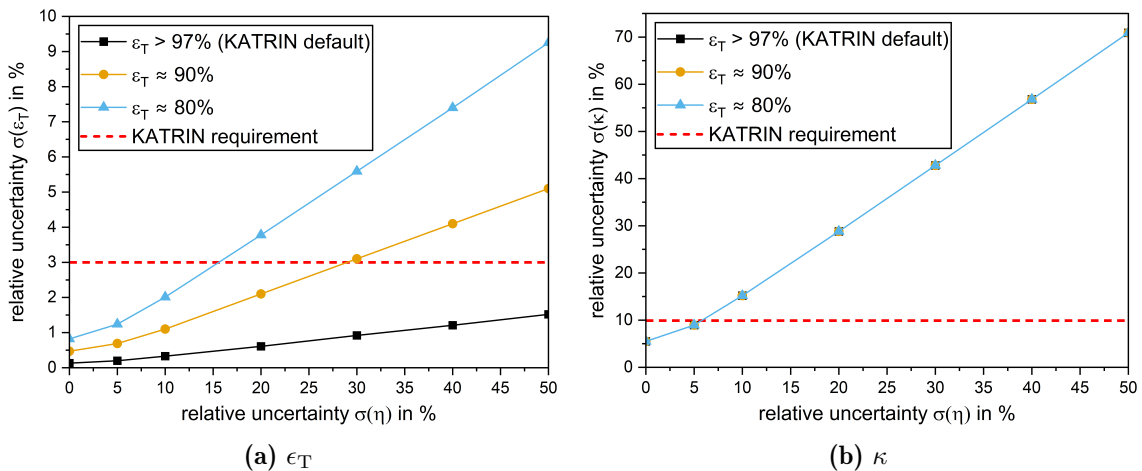
Figure 5.10.: Upper limit on the calibration uncertainty. Details on the definitions and calculations can be found within the text.

assumed, namely that the uncertainty is uniform on the complete spectral range. As a consequence, it can be assured that the limits derived here are indeed upper limits and are not underestimated.

In the KATRIN-like scenario, the relative uncertainty of the spectral sensitivity can even surpass 50 % and the requirements on ϵ_T are still fulfilled. Even with a lower tritium purity of only $\epsilon_T \approx 80\%$, there is no stringed requirement on the spectral sensitivity uncertainty of $\delta_\eta < 15\%$. This is not the case for the HT/DT-ratio κ. Here, the evolution of the relative uncertainty δ_κ is not dependent on the gas composition[7], and therefore the uncertainty is more sensitive to changes in the uncertainty of the spectral sensitivity. Even a relative uncertainty of the spectral sensitivity $\delta_\eta > 5\%$ would lead to an uncertainty on κ that is not acceptable for the KATRIN experiment.

Thus, in summary, as long as

$$\delta\eta = \frac{\Delta\eta}{\eta} < 0.05 \equiv 5\%$$
(5.6)

is fulfilled, the KATRIN requirements on the tritium purity ϵ_T and the HT/DT-ratio κ are also fulfilled. Note that the opposite is not necessarily true. As for the KNM10 data shown in Figure 5.11, if the spectral sensitivity uncertainty in the region of the H_2-peak is above 5 %, the KATRIN requirements can still be fulfilled. Thus, in the case of $\delta\eta > 5\%$, the data needs to be analyzed in more detail to determine whether the KATRIN requirements are still fulfilled.
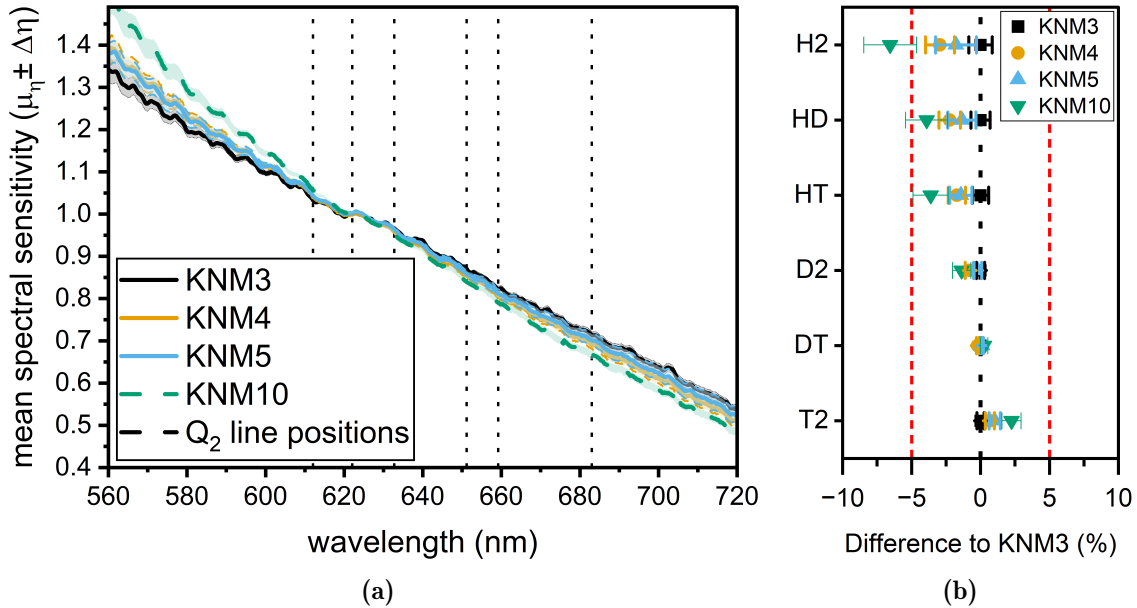
Figure 5.11.: Direct comparison of mean spectral sensitivity in the KNM3-5 campaigns. (a) Mean spectral sensitivity of bins $i = 3, ..., 18$ with 1σ-uncertainties. The line positions of the hydrogen isotopologues Q_2 are indicated. (b) Difference relative to KNM3 at positions of the hydrogen isotopologues. The maximum for the KATRIN requirements are indicated with red dotted lines. Details on the definitions and calculations can be found within the text.

---

[7]As shown in Appendix A

Round-robin data analysis

For the round-robin data analysis, the four aforementioned data sets are used. Each data set contains about 10 hour of LARA data that was selected randomly, using two criteria: (i) the data should correspond to KATRIN measurement runs during the β-scan time, and (ii) the source gas composition should be stable for the full 10 hour periods - a changing source gas composition can also be used; however, this severely complicates data analysis. The data sets are taking from the KNM3, KNM4, KNM5, and KNM10 campaigns (these are the campaigns that are preceded by an intensity calibration, see Table 5.2).

During KATRIN operation, analysis parameters were adjusted from time to time; to remove this influence on the round-robin analysis, all analysis inputs are fixed apart from the intensity calibration array. Note that due to this restriction, the results change, and the values do not agree with the results presented in other sections of this work, or in other works. Each data set is re-analyzed four times, *e.g.* , the KNM3 data set is analyzed using the intensity calibrations from KNM3, KNM4, KNM5, and KNM10; thus one 'correct' intensity calibration, and three 'incorrect' intensity calibrations are used. The re-analysis is done using `LARASoft2`, and includes all analysis steps shown in Section 4.1.3.

The resulting tritium purity ϵ_T from the KNM4 and KNM10 data sets is shown in Figure 5.12, while the complete results for all four sets are given in Figure 5.13. In Figure 5.12, the tritium purity ϵ_T from the KNM4(10) data set, analyzed with the four different spectral sensitivities η, is shown in a single plot with different regions corresponding to the different η. As expected from Figure 5.11, there is a difference, when using different $\eta(\text{KNMx})$ for the intensity calibration of up to $\Delta_{\text{rr}}\epsilon_T \approx 0.1\,\%$. However, this is significantly smaller than the calibration uncertainty $\Delta_{\text{cal}}\epsilon_T \approx 0.3\,\%$, and one order of magnitude smaller than the KATRIN requirements given in Eq. 5.1.
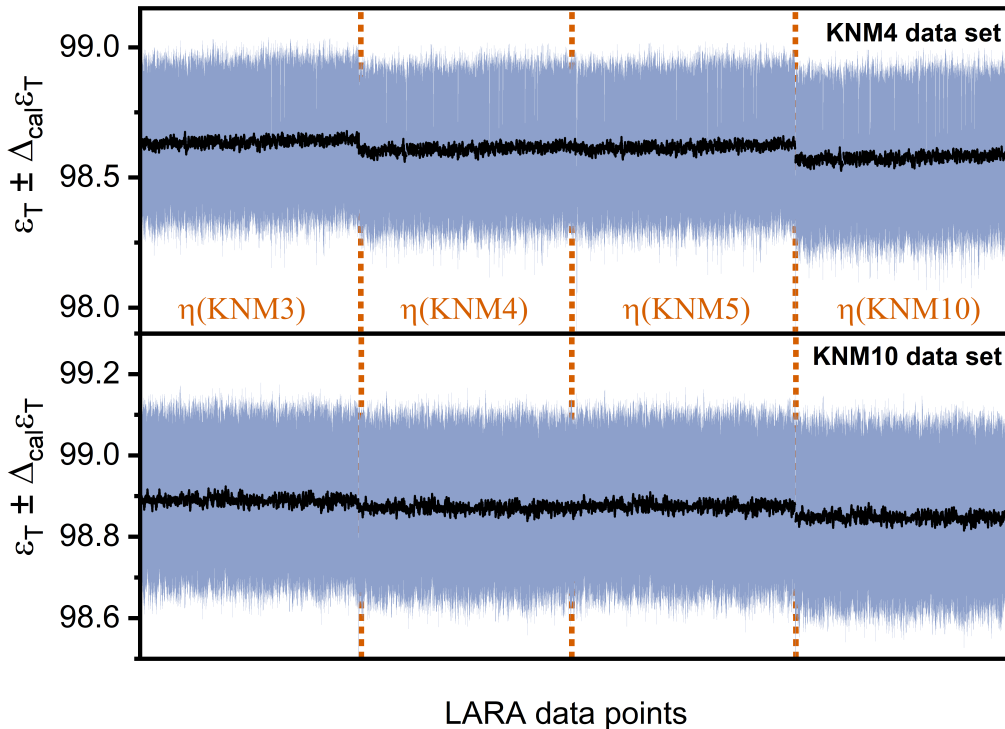
Figure 5.12.: Round-robin data analysis of the intensity calibration. Shown are the KNM4 and KNM10 data sets with the spectral intensity correction from KNM3,4,5, and 10. Details can be found in the text.
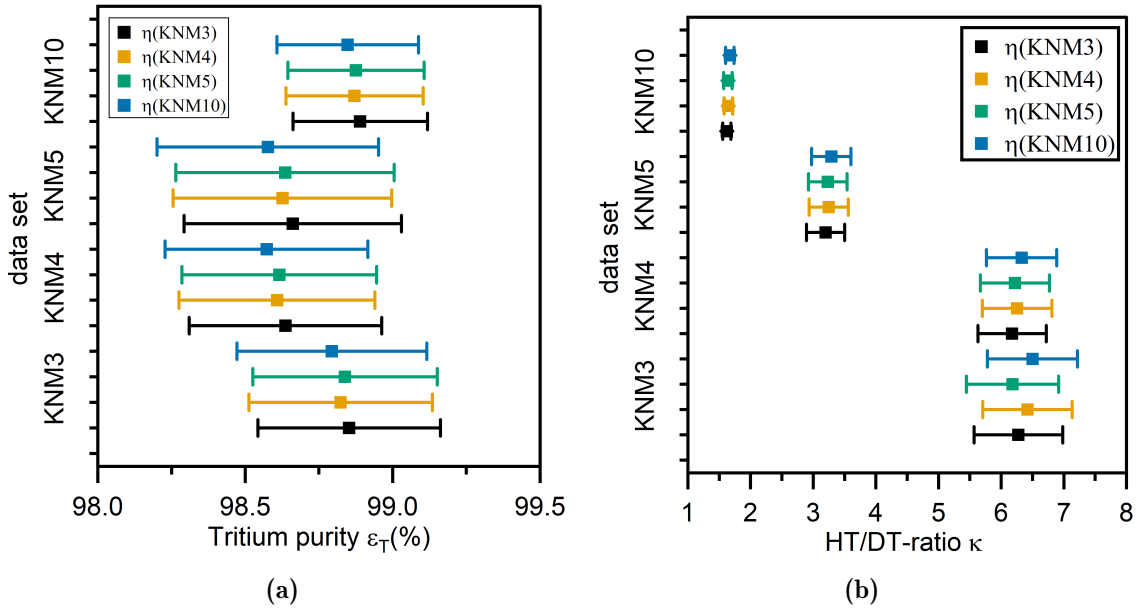
Figure 5.13.: All values of the round-robin data analysis of the spectral sensitivity. Shown are the KNM3,4,5, and 10 data sets with the spectral intensity correction from KNM3,4,5, and 10. Details on the definitions and calculations can be found within the text.

5.4. Concluding remarks

The KATRIN LARA system has been in operation for all KNM campaigns with a minimal unplanned downtime of only $0.36\,\%$ during β-electron data taking. For all measurement campaigns, the LARA system fulfills the KATRIN requirements (see Equation 5.1) for the 200 meV-goal (see Table 5.1). In addition, it was shown how the combination of LARA and FBM data can be used to improve the precision of the LARA data in low tritium purity $\epsilon_T < 1.0$ operation. It can be expected that the LARA system will also fulfill the requirements in the upcoming KNM campaigns.

Moreover, the studies presented in this section demonstrated the successful use of an SRM 2242 standard over several years of KATRIN LARA operation. It was shown that both the spectrum produced by the SRM 2242 standard, and the spectral sensitivity of the LARA system, are stable over a minimum timeframe of three years (provided that no system components are changed).

As for now, the LARA-SRM can still be used for the calibration of the KATRIN LARA system. It shows no signs of deterioration, and even the Lab-SRM that was stored in an environment with higher humidity could still be used for an intensity calibration that is sufficient to fulfill the KATRIN requirements on the tritium purity and the HT/DT-ratio.

The new SRM 2242a should be used in regular intervals, to assess the of stability of the Lab-SRM. If large changes ($> 5\,\%$) were observed, this should trigger a reexamination of the LARA-SRM. In addition, a new calibration cell could be developed that would allow the direct use of the SRM 2242a standard with its changed form-factor for the intensity calibration of a LARA system. However, it should be noted that the certification of the SRM 2242a standard is only valid until 31/12/2024. At the time of writing, it is not clear whether NIST will re-release the SRM 2242a with an extended certification, or if a new standard material, with a new form factor and new properties will be released, making a new calibration cell design obsolete. Note that between the end of the certification of the SRM 2242 and the release of SRM 2242a more than one year passed, during which no

certified reference material was available; this could also happen at the end of the SRM 2242a certification.

With regard to the calibration interval, it was shown that the spectral sensitivity of the system is stable enough that about one calibration procedure every few years was sufficient. This is in contrast, to the previously recommended calibration interval of 60 days [Fis14]. As stated in the introduction section, often between KATRIN measurements campaigns, the Inner Loop - including the LARA cell - is not always evacuated (*e.g.* because the tritium in the WGTS is needed for studies of systematic effects in the KATRIN experiment), which renders a calibration impossible because the LARA cell cannot be exchanged for the calibration cell. During most years, there is at least one longer maintenance break that can and should be used for the calibration of the LARA system. Regardless, even though the spectral sensitivity was stable within the last three years, having more data points is always useful to quantify an effect. When the LARA cell is evacuated, the calibration is rather fast (about two working days) and low-risk for the KATRIN operation.

6. Commissioning and characterization of the confocal Raman microscope (CRM)

This chapter discusses commissioning and characterization measurements of the CONFOCAL RAMAN MICROSCOPE (CRM) which was constructed within the framework of this thesis. The experimental setup, including the tasks and properties of the individual subcomponents, is described in detail in Section 4.2; unless stated otherwise, all measurements are performed with the CRM configuration presented therein. This chapter is structured as follows.

In Section 6.1 the aim of the studies in this chapter is given; including a brief overview of the critical experimental parameters, and the methods and samples used. The determination of the spectral resolution and the spectral range is presented in Section 6.2. Following this, the determination of the spatial resolution, both in the lateral (Section 6.3) and axial (Section 6.4) directions, is described.

In Section 6.5 the topic of intensity calibration using a SRM2242a standard is addressed. Subsequently, two important hardware related quantities are demonstrated: the positioning reproducibility of the employed motorized stage in Section 6.6, and the laser power stability in Section 6.7.

In Sections 6.8 and 6.9, two benchmark CRM measurements are discussed: (i) the study of multi-layer graphene to determine the number of layers from the Raman spectra; and (ii) the comparison of the Raman images with different imaging techniques, namely light microscopy and SCANNING ELECTRON MICROSCOPY (SEM).

Finally, in Section 6.10, the performance of the system is evaluated in relation to the requirements for the quantitative study of tritium-exposed graphene, as those described in Chapter 7 and required in future efforts of the TLK.

6.1. Motivation and overview

The characterization of microscale samples with a Raman microscope is associated with a number of fundamental practical aspects of analytical instrument performance and experimental design. To distinguish the Raman signal of one chemical component from another on a sample requires proper alignment of the CRM, understanding of the spectral and spatial resolution of the system, and hardware stability and reproducibility, to ensure sufficient measurement accuracy. These aspects of the CRM were studied and the results are presented here.

Throughout this chapter, numerous samples are used multiple times. In the following list, an overview and key details of these samples is given:

- **Graphene-on-quartz:** A monolayer of graphene on a $500\,\mu$m-thick quartz substate. The substrate is transparent to visible light ($> 97\,\%$), is $1\,$cm $\times\,1\,$cm large, and fully covered ($> 95\,\%$) with graphene. The manufacturer is *Graphenea*[1].

- **Graphene-on-SiO$_2$/Si:** The substrate is made of a silicon (Si) monocrystal with a $<100>$ surface orientation, that is covered with $90\,$nm of SiO_2 on both sides. The total substrate thickness is $(525 \pm 20)\,\mu$m. Due to the SiO_2 coating, the substrate looks blue. It is $1\,$cm $\times\,1\,$cm in size, and fully covered ($> 95\,\%$) with a monolayer of graphene. The manufacturer is *Graphenea*.
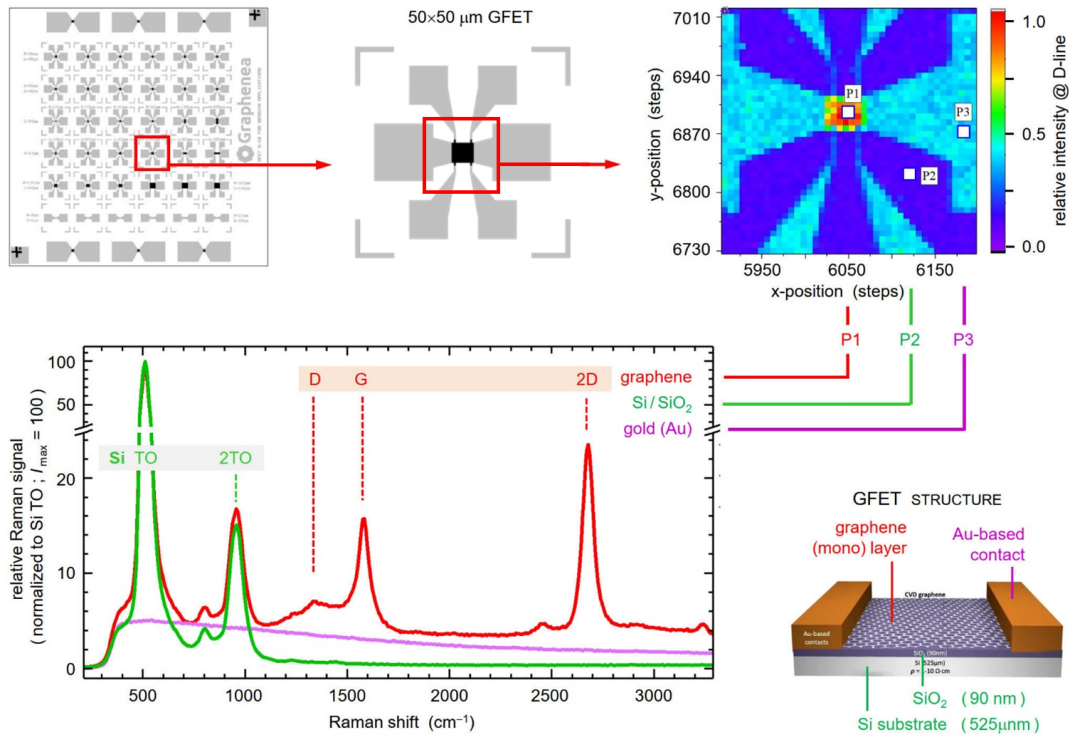
Figure 6.1.: Overview of the **GFET-sample**. From *top-left* to *bottom-right*: Technical drawing of the complete **GFET-sample**; zoomed image of one of the GFET-devices on the sample; Raman image of the central region of the GFET-device; Raman spectra from the three compounds on the GFET-sample (graphene, Si/SiO$_2$, gold); and a schematic 3D view of the cross-section of the GFET-sample, highlighting the layer structure. Image adapted from [Dia22].

---

[1]Graphenea, 20009 San Sebastián, Spain

- **GFET-sample** This is the Graphene Field-Effect Transistor (GFET) Chip *S10* from *Graphenea*. The GFET-sample is based on the same substrate as the **Graphene-on-SiO$_2$/Si** sample. However, instead of a full graphene coverage, there are 36 individual graphene areas of varying sizes (from $5\,\mu m \times 5\,\mu m$ to $200\,\mu m \times 200\,\mu m$) arranged on the substrate. Each graphene area is contacted with either two (2) or six (6) gold contacts, which can be used for *e.g.* Hall measurements on the respective graphene area. For Raman microscopy, these samples have some advantages compared to the full-coverage samples: (i) the graphene areas are small enough so that they can be scanned completely with full spatial resolution, within a reasonable time (see Section 4.4 for more details on the spatial resolution and sampling), (ii) there are three different materials (SiO$_2$, gold, graphene) on one sample, and thus (iii) different material transitions (graphene $\leftrightarrow$ gold, graphene $\leftrightarrow$ SiO$_2$) that can be studied. The technical drawing of the S10 chip, a Raman image, and representative Raman spectra are shown in Figure 6.1.

- **Si-Grid-Finder** This sample is produced by *Micro to Nano*[2]. The $12\,mm \times 12\,mm$ sample is made of a silicon (Si) monocrystal with a <100> surface orientation. A $1\,mm \times 1\,mm$ raster grid, composed of chromium (Cr) with a nominal width of $20\,\mu m$, is deposited onto this substrate. Each resulting field of the grid has a unique alphanumeric label in the lower-right corner, with an approximate height of $80\,\mu m$. In addition, the samples are ultra-flat with a total thickness variation $\leq 1.5\,\mu m$ and warp $\leq 30\,\mu m$. Although primarily designed for SEM applications, it has good properties for the alignment and characterization of the CRM. Namely, these are:

  - First, the sample can act as a mirror for the laser wavelength employed ($\lambda_{\text{laser}} = 532\,nm$), due to its high reflectivity of $\approx 37\,\%$ at this wavelength [Asp83; Gre95].

  - Second, it has a strong Raman peak at $520.9\,cm^{-1}$ [Des09].

  - Lastly, as determined experimentally, the thickness of the Cr-lines is sufficient to completely suppress the Raman peak of Si, providing specific areas on the sample with no Raman signal. In this chapter, the sample is used in Sections 6.3 and 6.6.

  Note that, this sample is also used for the alignment of the wide-field imaging arm of the CRM [Dia22].

6.2. Determination of spectral resolution

The spectral resolution and spectral range of a Raman system mostly depend on the employed spectrometer and spectrometer grating. During this work, as described in Section 4.2.2, a *HORIBA iHR 320* spectrometer was used. The spectrometer is equipped with a $300\,gr/mm$ grating with blaze at $500\,nm$. This spectrometer and grating configuration, and the alignment of the system, result in a spectral range of

$$\lambda_{\text{R}} = [516.8\,nm, 781.4\,nm] \equiv [-556.8\,cm^{-1}, 5994.6\,cm^{-1}] = \Delta\tilde{\nu}_{\text{R}}. \qquad (6.1)$$

The spectral range and the wavelength (λ_{R}) / Raman shift ($\Delta\tilde{\nu}_{\text{R}}$) calibration are determined used a spectral calibration pen lamp with Neon[3], which provides a sufficiently large number of Neon emission lines in the spectral range of the CRM for accurate wavelength calibration. The same pen lamp is also used for the measurements to determine the spectral resolution.

---

[2]EM-Tec silicon SEM finder grid substrate, Micro to Nano, 2031 ET Haarlem, Netherlands
[3]Spectral Calibration Lamp, Neon, *Newport* Corporation, 92606 California, USA

The AMERICAN SOCIETY FOR TESTING MATERIALS (ASTM INTERNATIONAL) suggests two principal methods to determine the spectral resolution $\delta\tilde{\nu}_{\text{system}}$ of a Raman system [AST14]. Although, the determination using pen lamps is not the preferred option, it still yields often adequate results. The main disadvantage of this method is that the line width of the laser $\delta\tilde{\nu}_{\text{laser}}$, which can contribute significantly to the spectral resolution, is neglected. Following Ref. [Liu12], the measured line width of an observed (Raman) line can be described by

$$\delta\tilde{\nu}_{\text{meas.}} = \sqrt{(\delta\tilde{\nu}_{\text{real/theo.}})^2 + (\delta\tilde{\nu}_{\text{system}})^2 + (\delta\tilde{\nu}_{\text{laser}})^2}. \tag{6.2}$$

Here a Gaussian approximation of the line profile is assumed. As mentioned, when using spectral emission lines for the determination of spectral resolution, $\delta\tilde{\nu}_{\text{laser}} = 0$. Furthermore, for Neon emission lines $\delta\tilde{\nu}_{\text{theo.}} \ll \delta\tilde{\nu}_{\text{system}}$, and thus Eq. 6.2 can be simplified to

$$\delta\tilde{\nu}_{\text{meas.}} = \delta\tilde{\nu}_{\text{system}}. \tag{6.3}$$

By fitting a Gaussian function to the measured Neon emission lines, the resolution can be determined across almost the complete range, as shown in Figure 6.2. As usual, the data is shown as a function of the Raman shift. As stated in the ASTM INTERNATIONAL guide, the resolution is not constant across the whole Raman shift range, $\Delta\tilde{\nu}_{\text{R}}$. The pen lamp does not emit lines with measurable intensity below $< 1715\,\text{cm}^{-1}$; therefore, the spectral resolution has to be estimated by extrapolation. The mean spectral resolution is $\delta\tilde{\nu}_{\text{system}} = (32.6 \pm 4.0)\,\text{cm}^{-1}$, and the maximum spectral resolution is $\delta\tilde{\nu}_{\text{system}} = (41.4 \pm 10.7)\,\text{cm}^{-1}$. To provide a conservative estimate, for calculations in this work, the maximum spectral resolution

$$\delta\tilde{\nu}_{\text{CRM}} = (41.4 \pm 10.7)\,\text{cm}^{-1}. \tag{6.4}$$

is used across the full spectral range. Thus, for example, when measuring the 2D-peak of graphene (at around $2700\,\text{cm}^{-1}$ with $\delta\tilde{\nu}_{\text{theo}} \approx 20\,\text{cm}^{-1}$ [Mal09]), the expected, measured peak width is:

$$\delta\tilde{\nu}_{\text{meas.}} = \sqrt{\delta\tilde{\nu}_{\text{2D-peak, theo.}}^2 + \delta\tilde{\nu}_{\text{CRM}}^2} \tag{6.5}$$

$$\approx \left(\sqrt{20^2 + 41.4^2}\right)\text{cm}^{-1} = 46\,\text{cm}^{-1} \tag{6.6}$$
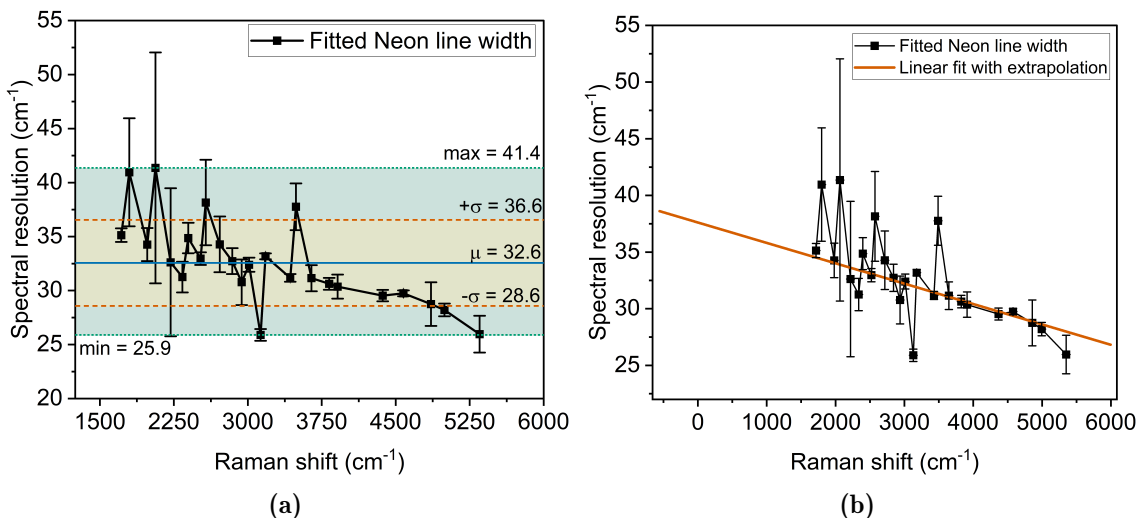
Figure 6.2.: Spectral resolution of the CRM. Fitted widths of Neon emission lines with (a) indication of the mean, standard deviation and min-max values, (b) linear fit with extrapolation for the complete spectral range.

From this, it becomes clear that the G-peak (at $1590\,\text{cm}^{-1}$ with FWHM $\approx 30\,\text{cm}^{-1}$) and the D'-peak (at $1622\,\text{cm}^{-1}$ with FWHM $\approx 15\,\text{cm}^{-1}$) [Eck12], cannot be resolved with the spectrometer configuration used in this work. As a further consequence of this relatively low spectral resolution, the system is less sensitive to chemical changes that affect the width of the graphene peaks.

Finally, the assumption that the laser spectral width $\delta\tilde{\nu}_{\text{laser}}$ can be neglected, is briefly examined. According to certification by the manufacturer for this specific laser, the spectral width of the laser is $\delta\tilde{\nu}_{\text{laser}} < 0.027\,\text{nm} \,\widehat{=}\, 2.0\,\text{cm}^{-1}$ (see Appendix C). If this is included in *e.g.* Eq. 6.5, the result would only change by $0.2\,\text{cm}^{-1}$ and is thus negligible compared to the uncertainty of the determined spectral width.

6.3. Determination of the laser focal beam diameter

Commercial laser beam profilers, often based on CCD arrays, are widely used to capture and analyze spatial intensity profiles of laser beams. These devices, which illuminate the camera sensor directly, are a popular choice. However, their effectiveness is compromised when dealing with laser beams whose diameter is close to or smaller than the pixel size of the camera sensor, typically in the range 2-5 µm. This limitation is particularly pronounced when measuring the spot size of a laser beam focused through a microscope objective, become the limiting factor. In addition, positioning the beam profiler in the focal plane of a microscope can be physically challenging.

Therefore, the indirect knife-edge technique is often used as an alternative. This method, involves intercepting the laser beam with a slit or knife-edge before detection by a power/intensity detector [Zha17]. The original beam profile is reconstructed by systematically recording the integral intensity profile for a series of cuts.

In a variant to the standard knife-edge method, one moves the focal spot of the laser beam across a sharp boundary that exhibits different responses to laser radiation. This is akin to measuring the integrated laser intensity, which is partially obscured by the knife-edge.

For the determination of the laser beam radius with the knife-edge technique, the beam is assumed to be a radially symmetric Gaussian laser beam with intensity distribution

$$I(x,y) = I_0 \cdot \exp\left(-\frac{(x-x_0)^2 + (y-y_0)^2}{w^2},\right) \tag{6.7}$$

where I_0 represents the peak intensity at the beam's center (x_0, y_0) and w is the beam radius, measured at the $1/e$ point in the intensity distribution [Ara09]. The normalized transmitted power is given by an integral expression

$$P_N = \frac{\int_{-\infty}^{x} \int_{-\infty}^{\infty} I(x',y)dydx}{\int_{-\infty}^{\infty} \int_{-\infty}^{\infty} I(x',y)dydx}. \tag{6.8}$$

Evaluation of this equation at each position x of the incremental knife-edge scan gives, according to [Ara09],

$$P_N(x) = \frac{1}{2}\left[1 + \text{erf}\left(\frac{x-x_0}{w}\right)\right] \tag{6.9}$$

involving the error function (erf). The erf-function is equivalent to the cumulative distribution function of the standard normal distribution. In the particular knife-edge scan variant used in this work, $P_N(x)$ does not represent the actual laser power, but rather the Raman response signal resulting from the applied laser power. This approach is particularly effective in combination with a Raman signal response of different molecular sample compounds.

For laser spot size determination, two samples with distinct structural 'edges' are used: (i) a **Si-grid-finder** sample[4] and (ii) a **GFET-sample**[5]. In addition, the beam diameter is determined using an image of the laser spot as recorded by the CMOS camera of the CRM. The results of these three different methods are summarized in Figure 6.3.

6.3.1. Using edge scans of a silicone grid finder sample

For this measurement, the laser beam is focused onto the **Si-grid-finder** sample, minimizing its diameter as observed via the CMOS camera of the wide-field imaging arm. Subsequently, the sample is moved in one direction (termed a 'horizontal' scan), in step increments of $\Delta S = 0.5 \equiv 0.625\,\mu m$ across four consecutive grid lines, both in forward and backward directions. The scan over a single Cr-grid line is illustrated in Figure 6.3a. The average over the eight leading/trailing edges of the four grid lines contained in the scan yields an average focal beam diameter (FBD) of

$$\text{FBD} = (7.23 \pm 0.13)\,\mu m \tag{6.10}$$

on target. Additional observations and insights are derived from this grid-finder scan.

- First, the spacing between Cr-grid lines was determined experimentally as 800 ± 0.2 steps, which is equivalent to $(1000.00 \pm 0.25)\,\mu m$. This agrees with the nominal grid line spacing, falling within the uncertainties of the mechanical accuracy of the stepper driver of the translation stage.

- Second, the experimental width of the Cr-grid lines, as determined from the half-intensity points of the knife-edge scan(s), is found to be $w_S = (20.7 \pm 0.3)\,\mu m$. This value is slightly larger (about 2-3 %) than the nominal value stated in the data sheet, which is most likely associated with the uncertainty in the analysis methodology based on Eq. 6.9.

- Finally, various structured reference materials are well-suited for applying the knife-edge method in confocal (Raman) microscopy. Trägårdh *et al.* [Trä15] employed a simple transmission electron microscopy (TEM) grid specimen. When very high magnification is required, as in the case of using a 100x objective, substrates with ultra-precise edge structures on a smaller scale become necessary. In this latter context, Itoh and Hanari [Ito20] utilized a tungsten-dot array on a silicon substrate as a certified reference sample in their confocal Raman microscope, enabling them to determine the lateral resolution of their system and, in turn, the laser focal beam diameter on target.

6.3.2. Using edge scans of a graphene-gold sample

A different approach is demonstrated by Sacco *et al.* [Sac21]. It involves using a graphene layer on a Si-substrate to determine the laser spot size. This method underscores the principle that samples with a sharp transition between materials can effectively determine the laser beam waist using the knife-edge method, even in the absence of a standard reference like a grid-finder sample. In this work, a line scan data-subset from a raster scan of a **GFET sample**[6] across the graphene boundary is extracted. The evaluation of this 'edge' scan yields

$$\text{FBD} = (7.10 \pm 0.40)\,\mu m \tag{6.11}$$

on target (see Figure 6.3b). In addition, two key observations emerged from this analysis:

---

[4]EM-Tec silicon SEM finder grid substrate, Micro to Nano, 2031 ET Haarlem, Netherlands
[5]GFET-S10 from Graphenea, 20009 San Sebastián, Spain
[6]GFET-S10 from Graphenea, 20009 San Sebastián, Spain

(a) CRM RAMAN SPECTROSCOPIC EDGE SCAN OF A SI SEM-FINDER SAMPLE
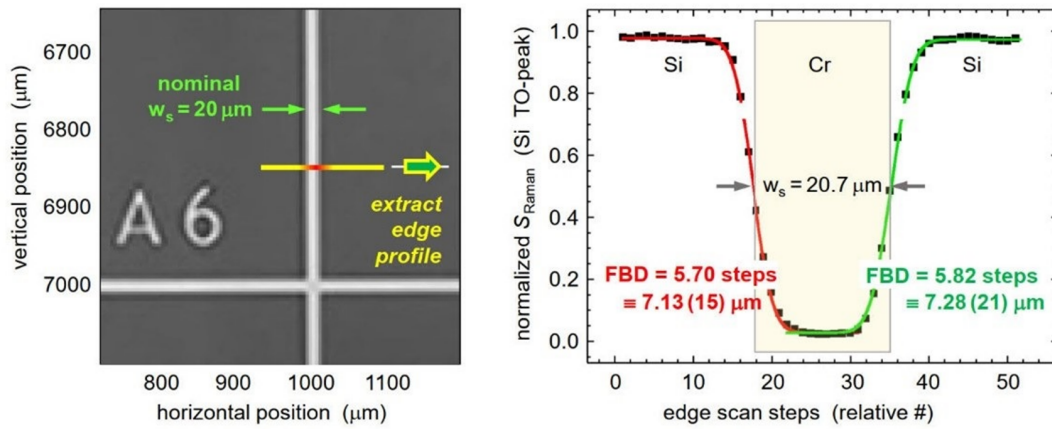
(b) CRM RAMAN SPECTROSCOPIC EDGE SCAN OF A GFET GRAPHENE SAMPLE
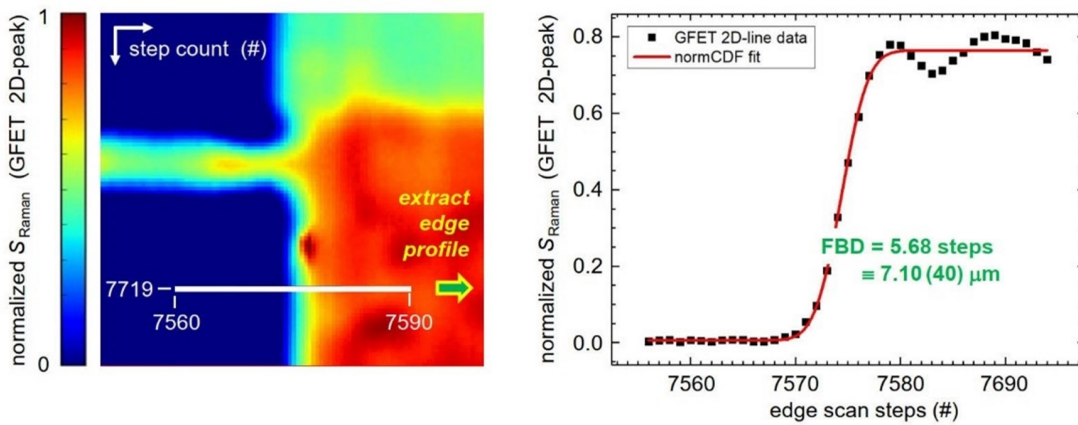
(c) CRM IMAGE OF LASER SPOT ON SI SAMPLE RECORDED BY CMOS CAMERA
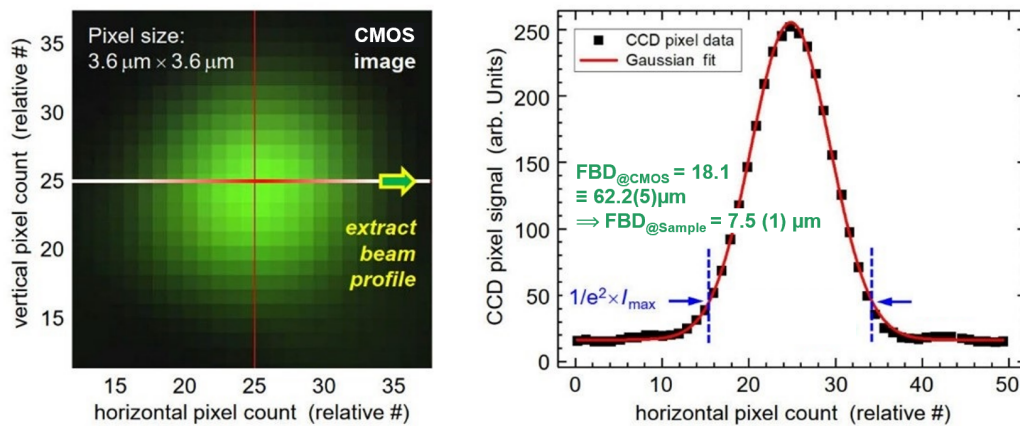
Figure 6.3.: Determination of the laser focal beam diameter (FBD) on the target surface. (a) Line-scan across a Cr-grid-line of the **Si-grid-finder** sample. The extracted intensity is fitted using Eq. 6.9. (b) Line-scan on a **GFET** sample. The extracted intensity is fitted using Eq. 6.9. (c) Laser beam spot imaged onto the CRM CMOS-camera, and the determination of the beam waist from a Gaussian fit. Details are given within the text. Image adapted from [Dia22].

95

- First, the raster scan map revealed that the edge is not perfectly straight but exhibits a 'rugged' appearance, with varying steepness in the 'vertical' scan coordinate. This suggests that averaging over multiple line scans might be necessary for a more accurate and reliable result. The x-y structural shape of the edge likely reflects the methods used in creating and mounting the graphene flake on the GFET substrate.

- Second, the knife-edge data displayed in Figure 6.3b demonstrate an 'oscillatory' behavior, leading to a less precise fit when applying Eq. 6.9, especially when compared to data from SEM finder grid scans. This fluctuation in the Raman data, also noted by Sacco *et al.* [Sac21], could be attributed to stress in the graphene flake, particularly near its edges when mounted on a substrate with a different lattice constant.

6.3.3. Using the wide-field imaging camera

For this method, first, the beam spot size on the wide-field imaging camera is determined. Using the camera software, a beam profile across the center of the beam spot can be extracted. This is then plotted over the pixel count and fitted with a Gaussian function, as shown in Figure 6.3c. Converting the pixel count to the dimension of µm, the focal laser beam waist on the CMOS sensor is $w_{0,@CMOS} = (65.2 \pm 0.5)\,\mu\text{m}$. Using this information, the spot size on the sample can be calculated by back-reconstruction. Applying Gaussian beam propagation principles, the relation between the focal laser beam waist on the target (@sample) and the beam waist on the CMOS sensor (@CMOS) can be expressed as

$$w_{0,@\text{CMOS}} = \frac{\lambda \cdot f_{\text{L}}}{\pi \cdot w_{\text{f,L}}} \iff \frac{\lambda \cdot f_{\text{obj}}}{\pi \cdot w_{\text{f,obj}}} = w_{0,@\text{sample}} = \text{FBD}. \tag{6.12}$$

Here f_{L} and f_{obj} are the focal length of the achromatic lens and the microscope objective, respectively. The indices '0' and 'f' denote the focused and collimated beam waist parameters, respectively; and λ is the laser wavelength. There are two important assumptions that need to be made to establish the direct back-reconstruction relation given in Eq. 6.12.

- There is exact collimated beam propagation within the CRM, meaning $w_{\text{f,L}} = w_{\text{f,obj}}$. This is not necessarily the case, since the beam from the entrance fiber collimator is slightly divergent. Therefore, there is an unknown systematic uncertainty associated with the result from the method.

- Eq. 6.12 is derived for the propagation through thin lenses; neither the objective nor the imaging achromatic lens can be treated as thin optical elements. Therefore, there is an additional systematic uncertainty on this method.

Inserting the values $\lambda = 532\,\text{nm}$, $f_{\text{L}} = 150\,\text{mm}$, $f_{\text{obj}} = 18\,\text{mm}$ and the experimentally determined $w_{0,@CMOS} = (65.2 \pm 0.5)\,\mu\text{m}$ into Eq. 6.12, results in

$$w_{0,@\text{sample}} = (7.5 \pm 0.1)\,\mu\text{m} \equiv \text{FBD}. \tag{6.13}$$

Note that uncertainty here only stems from the uncertainty of the measurement of the FBD on the CMOS sensor; no additional uncertainty estimation, regarding the two assumptions made, is included.

This result is in reasonable agreement with the other two measurements given in this section, Eqs. 6.10 and 6.11. The most reliable result is given by the method using the Si-grid-finder since it is a well-defined standard sample, with known lines and line widths, and many scans over several grid lines can be taken into account for the calculation of the FBD, with the bonus to conduct statistical error analysis. Nevertheless, the agreement of all three methods demonstrates that there is not necessarily the need for a standard sample. In addition, the method using the CMOS camera could be used in the future to monitor the FBD *in-situ* during a scan, if the scanned sample is reflective enough to obtain a clear image.

6.4. Determination of focal depth

Graphene or ultra-thin graphite are ideal samples to determine the focal depth of a confocal Raman microscope [Top18; Sac21]. These samples are only a few nm-thick at most, but produce a strong Raman signal. Here, two different graphene samples from *Graphenea* are used; namely a monolayer of graphene on $500\,\mu m$ quartz, and a GFET sample[7] with a monolayer of graphene on $90\,nm$ SiO_2 / $525\,\mu m$ Si substrate (see Section 6.1 for more details on the samples).

For the measurements, the focus position was determined using the usual procedure with the wide-field imaging camera [Dia22]. The respective sample was then moved out-of-focus by about $200\,\mu m$. At this position, the axial (z-direction) scan with a step-size of $5\,\mu m$ was started. The axial scan was stopped at about $200\,\mu m$ below the sample surface. In total, about $400\,\mu m$ were scanned in the z-direction. For the most intense Raman lines, namely the TO-Line of $Si(O_2)$ and the 2D-line of graphene, relevant interval slices were selected, integrated, and normalized to $I_{max} = 1$. In addition, for the GFET sample, the D-peak of graphene is analyzed. The absolute intensity of the D-peak is low (only a few 100 counts above the background signal); therefore, the data is noisier. The results are shown in Figure 6.4.
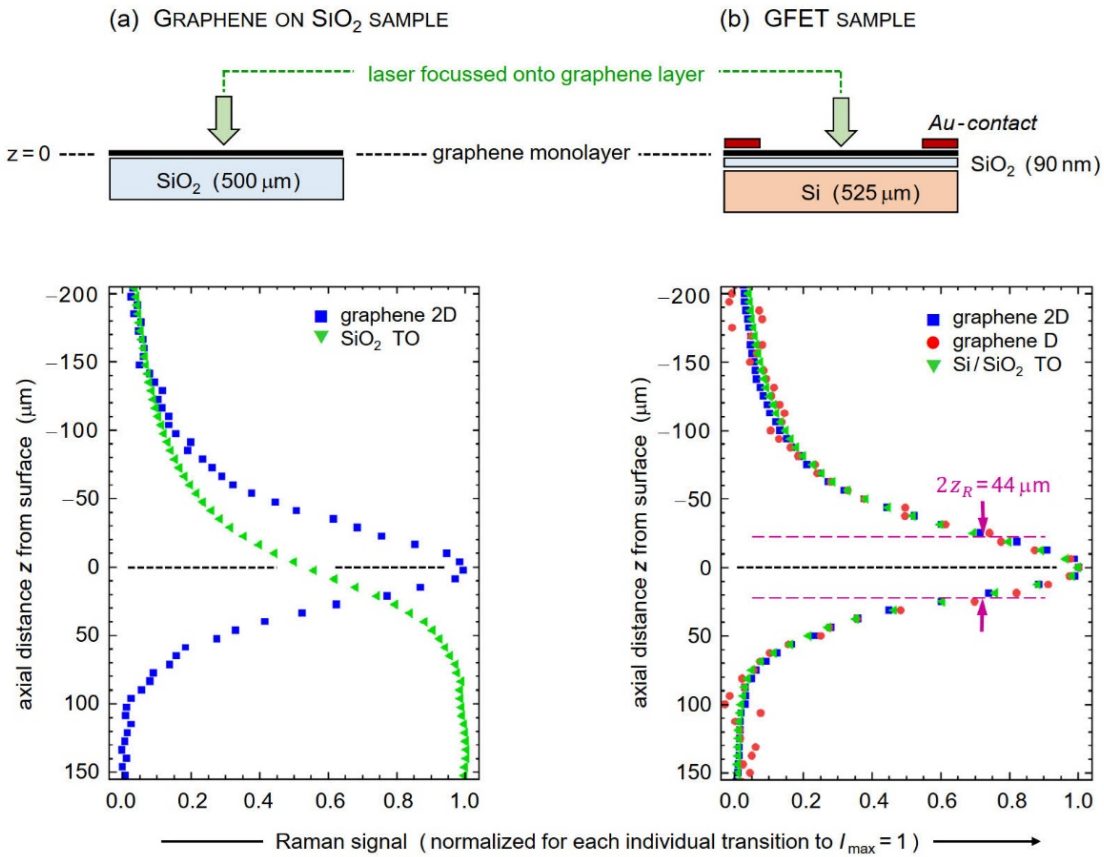
Figure 6.4.: Axial (z-direction) scans on two samples to determine the focal depth of the CRM. (a) Axial scan of the **graphene-on-quartz** sample. (b) Axial scan of the **GFET** sample. For both scans, the axial distance is plotted over Raman peak intensities. In the representation, the focal depth can be determined by fitting a Lorentzian shape to the intensity profile. For clarity, this is only indicated in (b). Image adapted from [Dia22].

---

[7]GFET-S10 from Graphenea, 20009 San Sebastián, Spain

97

For the **GFET sample**, all three extracted curves agree: approaching the graphene surface, the intensity increases. When the focal point has passed the graphene surface, the intensity decreases again. For the graphene on quartz sample, the graphene 2D-peak intensity follows the same general behavior. However, the intensity of the TO-line of $Si(O_2)$ reaches its maximum when the focal point is about $50\,\mu m$ below the surface and remains at that value even at $150\,\mu m$ below the surface. The reason for this different intensity curve is that, the quartz substrate is transparent to visible light. In contrast, the laser penetration depth in crystalline Si is only about $0.8\,\mu m$ [Top18].

Using the common definition of the focal depth L (Rayleigh length):

$$L = 2z_{\mathrm{R}} = \frac{2\pi w_0^2}{\lambda_{\mathrm{laser}}}, \tag{6.14}$$

a Lorentzian fit to the data in Figure 6.4 is performed to determine the experimental focal depth of the current CRM configuration, resulting in

$$L_{\mathrm{exp}} = (44 \pm 5)\,\mu m. \tag{6.15}$$

This is in reasonably agreement (2σ uncertainty) with the theoretical value $L_{\mathrm{theo}} = (38 \pm 2)\,\mu m$ obtained from the laser spot size measured on target.

6.5. Intensity calibration with SRM 2242a

The CRM has to be intensity-calibrated before the resulting Raman intensities can be compared with other experiments. The calibration is performed with the NIST SRM2242a standard material, which was likewise used for the measurements in Section 4.1.4. Compared to the KATRIN LARA system, the calibration of the CRM is much simpler. The KATRIN LARA system has a 90° scattering geometry, for which the SRM2242a is not designed, and therefore a specifically developed calibration procedure was required [Sch15b; Zel17]. However, the CRM utilizes the 180° scattering geometry for which the SRM2242a is certified. Therefore, the SRM2242a can simply be placed in the focus of the CRM to measure the emitted spectrum. The spectral sensitivity of the CRM can subsequently be calculated (*e.g.* see Figure 5.7). The resulting spectral sensitivity from such a calibration measurement is shown in Figure 6.5.
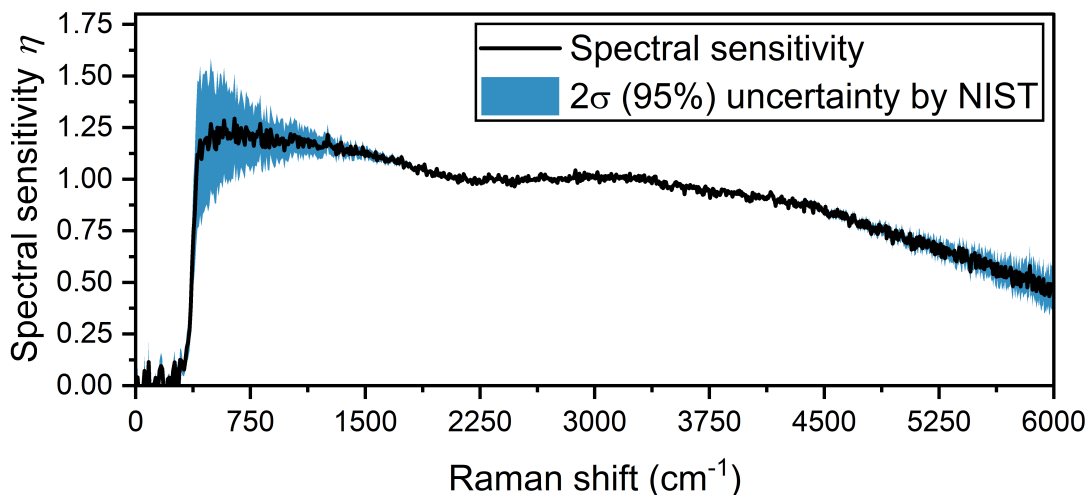
Figure 6.5.: Mean spectral sensitivity of the CRM with 2σ-uncertainty provided by NIST [NIS19].

Several important aspects have to be considered regarding the intensity calibration:

- As described in Section 4.1.4, the spectral sensitivity is only one part of the intensity calibration. For the complete calibration, the theoretical line intensities have to be calculated and accounted for as well.

- Most published data on Raman spectroscopy of graphene do not include information about the calibration of the respective system. Therefore, it cannot be ascertained whether the systems are calibrated, or not: direct comparability of absolute values is difficult to verify, even with this CRM being correctly calibrated.

- The spectral and spatial resolution of the current CRM configuration is not sufficient to perform quantitative studies on graphene. All conclusions drawn in this work are of a qualitative nature. A more accurate intensity calibration is not necessary and would only insignificantly change the results presented at this point. This statement is supported by the fact the spectral sensitivity of the CRM is $\eta \approx 1.0 \pm 0.1$, as extracted from Figure 6.5, in the relevant spectral range 1600-3000 cm^{-1}, in which the graphene Raman peaks are located.

6.6. Positioning reproducibility of motorized stage

For this measurement, the **Si-grid-finder** sample is placed in the focus of the CRM. Using the wide-field camera, the grid lines can be easily located since the sputtered Cr-lines reflect the laser spot diffuse. The laser spot was positioned close to a grid-line and a horizontal scan, in step increments of $\Delta S = 2 \equiv 2.25\,\mu\mathrm{m}$ across the grid lines, is performed in both directions, forward and backward. This *bidirectional* scan was then repeated several times. For the data analysis, the TO-line of Si is fitted with a Lorentzian peak and the normalized intensity is plotted over the scanned coordinate, similar to Section 6.3.1. The edges can then be fitted with Eq. 6.9. Two representative bidirectional scans are shown in Figure 6.6.

Notably, the position of the transition edges are shifted between forward and backward scans by $(1.8\pm0.3)\,\mu\mathrm{m}$. This is caused by the inherent backlash in the motorized translation stages. The measured value is in good agreement with the value given by the manufacturer for the
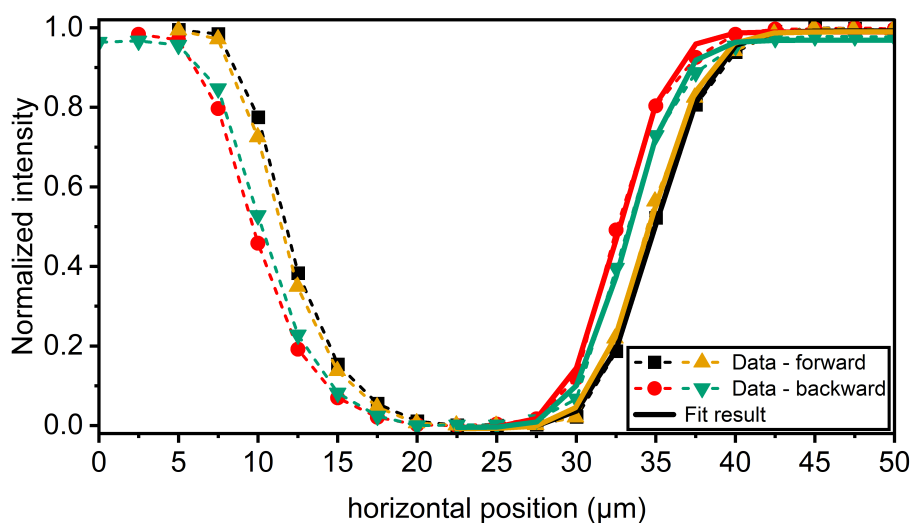
Figure 6.6.: Bidirectional positioning reproducibility of the motorized stage. The normalized TO-line intensity of Si of two bidirectional scans of a grid line is shown. The dashed lines are only for visualization. The solid lines are fits according to Eq. 6.9. For clarity, the fits are only shown for the right edge.

bidirectional reproducibility, $2\,\mu$m[8]. In contrast, the measured unidirectional reproducibility is only about $(0.5 \pm 0.1)\,\mu$m. This is also in good agreement with the value given by the manufacturer, 0.5-$1\,\mu$m[8].

6.7. Laser power stability

During the commissioning of the CRM, the stability of the laser power output was determined. High intensity stability is paramount when conducting full raster scans over larger areas, which can last for one day, or even longer. The output fiber of the fiber-coupled single mode 'matchbox' laser (see Table 4.1) was set up directly in front of a *S142C* - integrating sphere photodiode power sensors with a *PM100D* handheld digital power meter console, both from *Thorlabs*[9]. The output laser power was set to $P_{\text{set}} = 25\,$mW. In addition to the power measurement, internal laser parameters (laser diode (LD) current, base temperature, and LD temperature) were read out from the device. The laser was switched on and remained active for the next four days without any interruptions. The measured laser power and the read-out laser parameters are shown in Figure 6.7. Analyzing the data, the following observations can be made:

- Both, the base and LD temperature, are stable to $\leq 0.05°$C without any significant correlations to the LD current, measured power, and day-night-temperature changes of the laboratory. Both temperatures stabilize within minutes after the laser is switched on. The base temperature stabilized at $(26.650 \pm 0.025)°$C and the LD temperature stabilized at $(36.30 \pm 0.05)°$C.

- After about $12\,$h the measured laser power stabilized to $(22.0 \pm 0.1)\,$mW. Within the first $12\,$h, the measured power changes by $\pm 2\,$mW $\approx \pm 10\,\%$.

- The LD current takes significantly longer to reach a stable value. Only after about $36\,$h a stable value of $(1250 \pm 20)\,$mA is reached.

- There is a strong anti-correlation between the measured power and the LD current. While the LD current is increasing, there is a decrease in the measured power.

In conclusion, the laser output power is sufficiently stable after $12\,$h of operation. However, the maximal observed change in measured power of $\pm 2\,$mW $\approx \pm 10\,\%$ within the first $12\,$h, could lead to misinterpretation of qualitative data. This problem can be circumvented by either (i) starting the laser about $12\,$h before the data taking, or (ii) measuring and correcting for the laser power instabilities. Since the CRM is equipped with a laser shutter, the laser can run continuously without the need to power down between measurements. Currently, the CRM is used for many measurements with little downtime in between, and the laser has been in continuous operation for about the last twelve months. Therefore, the stabilization period is often no issue. Nevertheless, monitoring the laser power and, if necessary, correcting for instabilities is valuable for the interpretation of the measurement data. This can be done in one of the following ways during the measurement: direct monitoring, LD current monitoring, and indirect monitoring.

LD current monitoring

The commissioning with the external power meter demonstrated the read-out of the LD current can be used to estimate the stability of the power output. In praxis, there were problems with this approach, limiting its usability. The laser control software from

---

[8]Personal communication with Vision Lasertechnik GmbH, 30890 Barsinghausen, Germany; an authorized reseller of the *Standa* 8MT173-20XYZ motorized stage.

[9]Thorlabs Inc., Newton, New Jersey, USA
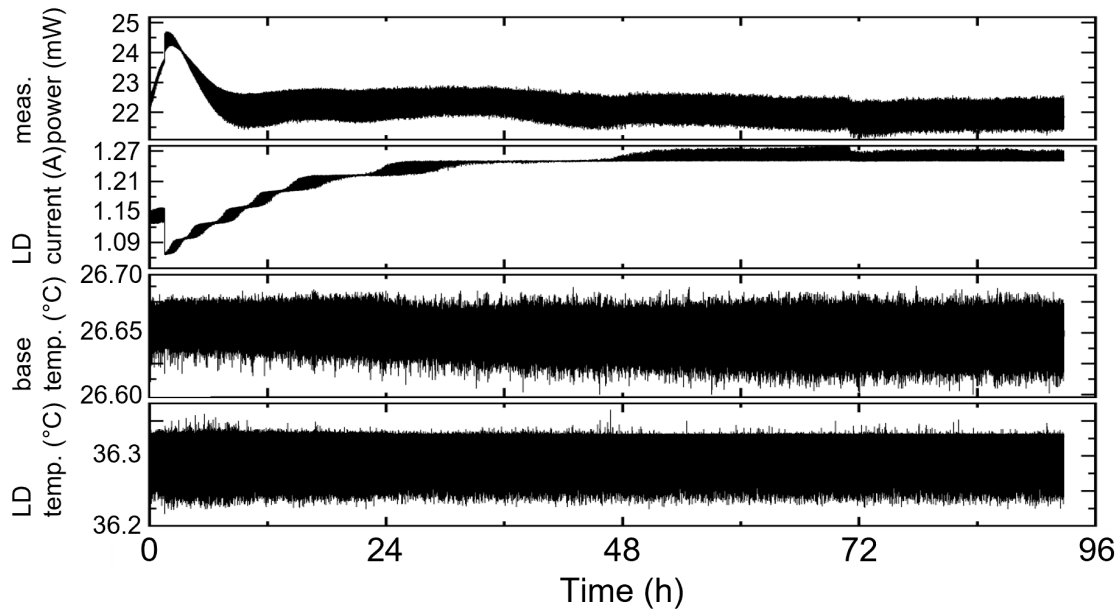
Figure 6.7.: Evolution of the Matchbox laser power and temperature. Details are given in the main text.

the manufacturer has a built-in logging function, but often crashes after about 100 h. Therefore, the laser control was integrated into `LARASoft2-CRM` (see Section 4.3). Some hardware parameters could not be accesses reliability with this solution, leading to crashes of `LARASoft2-CRM`. These software problems will be addressed in the future. This method could only be used for selected measurements with logging times of up to 100 h.

Direct power monitoring

Measuring the laser power directly after the first beam splitter cube, see Figure 4.9, **Segment A**. This is the most accurate power measurement, since it can measure the laser beam directly. Although at this point the beam is slightly divergent, it is still focused enough for the entire beam to hit the power meter. It also needs to be considered that only about 5 % of the laser beam passes the dichroic beam splitter in the direction of the power meter, while 95 % of the laser light is directed to the microscope objective. Therefore, even when the matchbox laser is operated at full power of 120 mW - due to the laser line filter and the dichroic beam splitter - only about 2-5 mW arrive at the position of the power meter. However, the high-sensitivity power meter was only available for the first commissioning measurements.

Indirect power monitoring

To monitor the stability of the laser output power during raster scans of graphene on Si/SiO_2 samples, a method involving the Raman signal of the TO-peak of $Si(O_2)$ is used. This technique assumes minimal variation in the graphene film's layer number [No18], and a constant sample focus. The observed intensity of the TO-peak of $Si(O_2)$, always visible within the set spectral range of the CRM, is directly proportional to the laser output power. By normalizing the recorded Raman spectra to the Si-TO signal, this method not only monitors but also corrects for possible instabilities in the laser power.

One example of the TO-peak signal of $Si(O_2)$ during a x-y-raster scan of a graphene-on-Si/SiO_2 sample is shown in Figure 6.8 (duration of the scan about 90 h); the corresponding
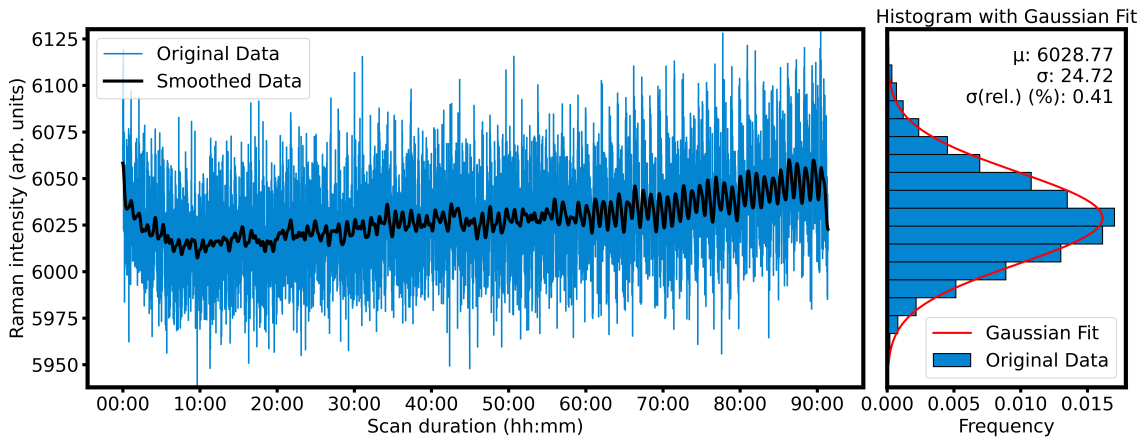
Figure 6.8.: Evolution of the TO-peak intensity of $Si(O_2)$ during a raster scan. The peak intensity is determined by fitting a Lorentzian function. For visualization of the overall trend, the data is also shown with smoothing applied. The histogram with the Gaussian fit shows the distribution of the signal and demonstrates the good stability, with a relative standard deviation of only 0.41% over the full measurement period of about $90\,h$.

heatmap of this x-y-raster scan is shown later in Figure 7.11. There is a clear linear drift in the TO-peak intensity during the measurement time. However, the relative standard deviation is only about 0.41% for the complete scan. Even if left uncorrected, this drift is significantly smaller than the change in Raman spectra studied in this work. However, as described, this data is used to normalize the Raman spectra, and therefore the measurement is not affected by this drift at all.

6.8. Measurement of multi-layer graphene

The purpose of this measurement is to explore whether the current configuration of the CRM is sensitive enough to distinguish the number of graphene layers. As determined in Section 6.2, the mean spectral resolution in this configuration is $\delta\tilde{\nu}_{CRM} = (41.2 \pm 10.7)\,cm^{-1}$. Using the theoretical width of the 2D-peak in SLG, BLG, and TRILAYER GRAPHENE (TLG) (see Figure 3.10), the expected experimental widths for Bernal stacked layers are $\delta\tilde{\nu}_{SLG} = (46 \pm 10)\,cm^{-1}$, $\delta\tilde{\nu}_{BLG} = (66 \pm 10)\,cm^{-1}$, and $\delta\tilde{\nu}_{TLG} = (75 \pm 10)\,cm^{-1}$, respectively [Pap20]. Therefore, even with the current CRM configuration with a low-spectral resolution grating, the number of graphene layers should be extractable from the width of the 2D-peak, if the graphene is Bernal stacked. The graphene samples used for these measurements are from *Graphenea* and similar to the **Graphene on SiO_2/Si** samples, only with a varying number of graphene layers [Gra23b].

A representative Raman spectrum from each graphene sample is shown in Figure 6.9. Since the intensity of the TO-line of $Si(O_2)$ correlates with the number of graphene layers [No18], the data is normalized to the G-peak instead. For these multi-layer graphene samples, the 2D-peak width is not proportional to the number of graphene layers; there is only a $1\,cm^{-1}$ difference between the SLG and TLG. The shift of the 2D-line position between the SLG and BLG is about $5\,cm^{-1}$. In addition, the I_{2D}/I_G-ratio is proportional to the number of graphene layers [Pap20].

In combination, these observations demonstrate that the multi-layer graphene sample from *Graphenea* are indeed multi-layer, however, it appears that the samples are misoriented and not Bernal stacked. It should be noted here that in misoriented multi-layer graphene, the determination of the number of layers is not conclusive without prior information
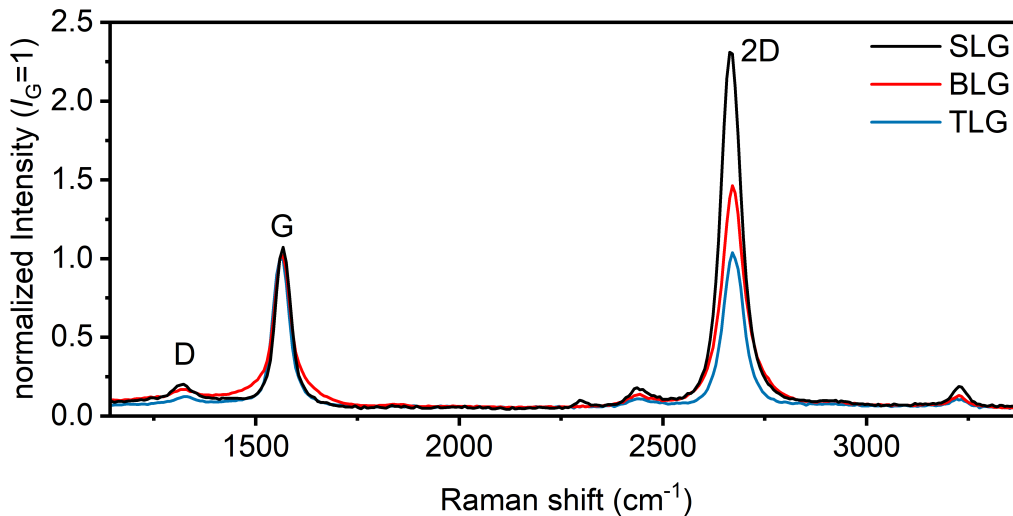
Figure 6.9.: Measured spectra of multilayer graphene, namely SLG, BLG, and TLG. The spectra are normalized to the G-peak intensity. Details are given in the main text.

(*e.g.* from a trustworthy manufacturer), additional characterization, or imaging techniques (*e.g.* TEM). The decrease in the I_{2D}/I_G-ratio is also, in general, observed in lower-quality graphene layers. The small blue shift of the 2D-peak position of only $5\,\mathrm{cm}^{-1}$ for misoriented BLG, can be hidden or mimicked by *e.g.* temperature or structural instabilities of the Raman system. Therefore, the conclusion derived here, is assuming that the TEM images provided on the *Graphenea* website are trustworthy [Gra23b].

6.9. Comparison with complementary imaging techniques

A series of test measurements were performed, comparing the spectroscopic raster maps with images of the same area taken using different imaging techniques, to verify that the apparent spectro-spatial features could be associated with real differences in the sample. Specifically, SEM images of small surface areas of the **GFET sample** and broad-field light images of a large surface area of **graphene-on-quartz** sample were taken.

6.9.1. Light-microscope imaging

In the context of the Bachelor's thesis of J. Demand[10], an electrochemical hydrogenation method was tested with a **graphene-on-quartz** sample. A piece of platinum wire is attached to two neighboring corners of the graphene surface using conductive silver. The wire, and thus the sample, is then connected in series with a Picometer and a voltage source to a platinum anode, making the sample the cathode of an electrolysis cell. A small platinum plate is used as the anode in the setup. By applying a voltage between the cathode and anode, electrolysis of water occurs. The produced hydrogen ions should, in principle, be attracted to the graphene layer. This configuration allows measuring the electrolysis current for different voltages and immersion depths. Using this simple approach, no successful hydrogenation could be demonstrated, but the graphene layer was damaged instead.

In Figure 6.10a, a white-light wide-field image of a **graphene-on-quartz** sample used in said study is shown. Ruptures in the surface as well as ruggedized edges are visible; any chemical changes are not revealed in the white-light image. In order to confirm if hydrogenation (or

---

[10]J. Demand: 'Characterization of a Laser-Raman-Microscope for the examination of hydrogenated graphene'. Bachelor's thesis. Karlsruhe: Karlsruhe Institute of Technology, 2021

(a)   **(b)**

(c)
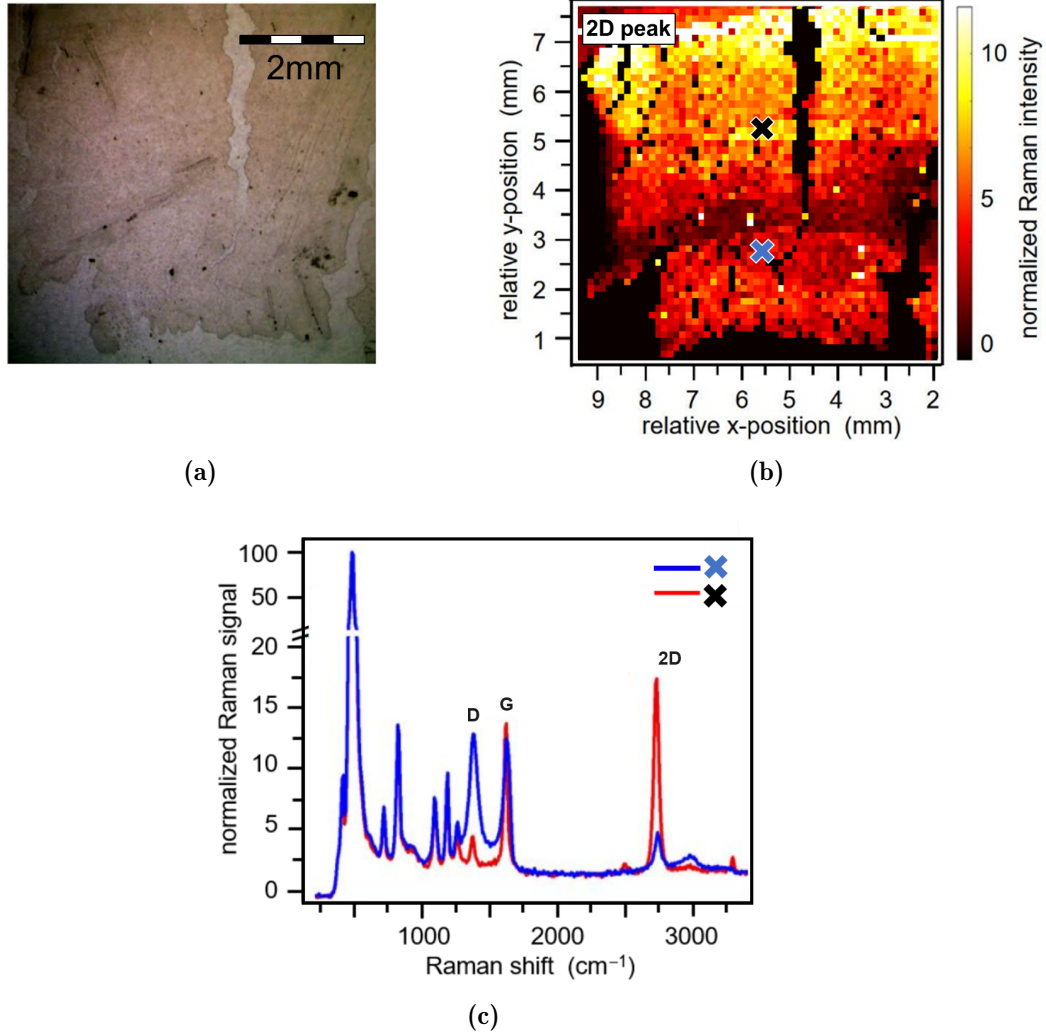
Figure 6.10.: Comparison of confocal Raman spectral maps with a light microscope image. The imaged region is about $7.5\,\text{mm} \times 9.5\,\text{mm}$ in the center of a **graphene-on-quartz** sample. (a) Wide-field image obtained using a light microscope; the graphene layer is damaged and darkened by an electrochemical hydrogenation attempt. (b) Raman image of the 2D-graphene peak in the same region. The Raman image is undersampled with $\Delta S = 100\text{steps} \equiv 125\,\mu\text{m}$. (c) Raman spectra from the positions marked on the map. Images adapted from [Dia22].

other chemical changes) of graphene has occurred, a Raman raster scan was performed, covering the complete area shown in the white-light image. The sample was scanned in increments of $\Delta S = 100$ steps $\equiv 125\,\mu\text{m}$ resulting in about 60×60 raster points. This does not generate gapless maps of the sample, but only probes it at sparse spatial locations.

The heat map for the 2D-peak of graphene is shown in Figure 6.10b. The ruptures and edges are replicated well in the Raman map, associated with a zero-2D-peak signal (black in the amplitude scale of the map). Finer details visible in the white-light image cannot always be directly correlated to the Raman map; this is a consequence of the widely spaced raster points across the sample surface. Raman spectra from two different locations on the sample are shown in Figure 6.10c; revealing that the reduced 2D-peak intensity is correlated with an increased D-peak, with a D/G-peak intensity ratio of about 1.

6.9.2. Scanning electron microscope (SEM) imaging

The SEM image of the **GFET** sample, shown in Figure 6.11a, reveals two structural features. These are (i) graphene-flake boundaries, evident from the faint "black" lines in the image, and (ii) a series of local, circular-shaped features – most likely from deposits during chip manufacture, or adhesion of small dust particles during sample handing in ambient air. Note that both types of features are also present in the SEM images of GFET devices included in the Graphenea GFET-S10 data sheet and on their webpage [Gra22a]. Using the edge of the gold surface for orientation, the area shown in the SEM image was scanned in increments of $\Delta S = 2$ steps $\equiv 2.5\,\mu\text{m}$. The overlay of these features from the SEM image and the Raman raster map for the D-peak of graphene is shown in Figure 6.11b. The D-peak is shown since it is sensitive to the defects present at graphene-flake boundaries.

The thin borders between graphene-flakes are not recognizable in the Raman map. This is expected, considering the limited spatial resolution of this CRM configuration that was determined in Section 6.3. However, most of the circular features show reasonable

(a) SEM image

(b) D-peak map

(c) 2D-peak map
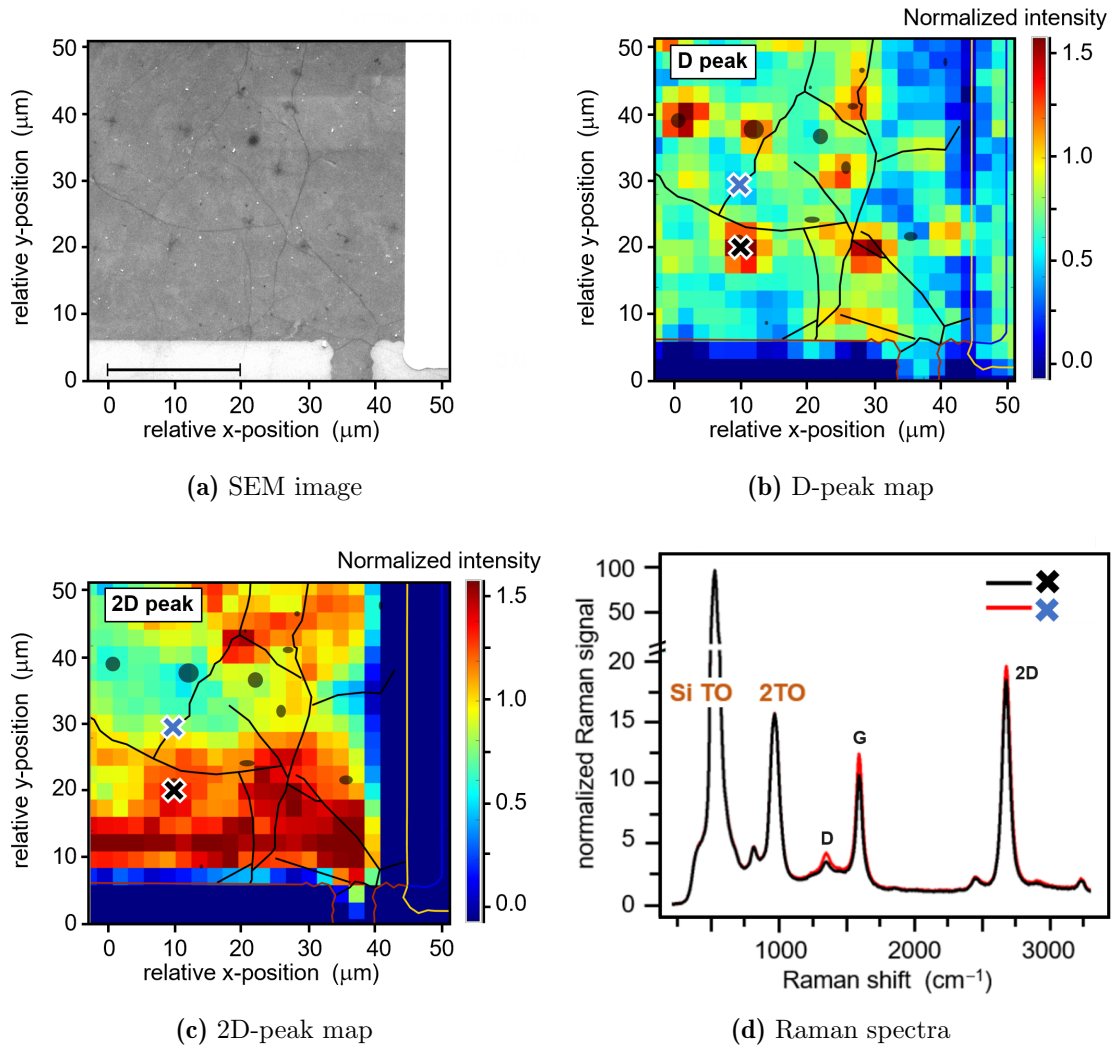
(d) Raman spectra

Figure 6.11.: Comparison of confocal Raman spectral maps with SEM image. The imaged region is about $50\,\mu\text{m} \times 50\,\mu\text{m}$ in the corner of a GFET device on the **GFET sample**. (a) SEM image with increased contrast to improve the visibility of graphene flake borders. (b,c) Raman map of the normalized D-peak and 2D-peak intensity; overlaid with lines and spots indicating the darker regions in the SEM image. (d) Normalized Raman spectra from the points indicated (x) on the Raman maps.

correlation between the two images. For comparison of the on-deposit / off-deposit Raman signals, the spectra at the related spatial positions are shown in Figure 6.11c. From these, small differences in the spectral fingerprints are evident, with the most prominent change in Raman response in the D-peak that is expected for defects in the graphene layer. In principle, darker regions in SEM images can also correspond to graphene flake overlaps. When examining the Raman spectra, it becomes clear - in comparison to Figure 6.9 - that this is not the case here.

Overall, the CRM imaging results discussed here show that, in general, spatial features in the Raman maps can be linked to the features detected by alternative analysis methods at the same position.

6.10. Concluding remarks

The test of the matchbox laser showed that the laser reaches sufficient power output stability of $< 0.5\,\%$ in $> 50\,\mathrm{h}$ after an initial stabilization time of about $12\,\mathrm{h}$. By analysis of the Si TO-peak Raman signal, it was shown that even during prolonged raster scans for several days, up to weeks, the produced Raman signal does not significantly change. This effect is small enough ($4.6 \times 10^{-3}\,\%\,\mathrm{h^{-1}}$) to not impact the conducted measurements negatively. Anyhow, this slight drift can be corrected for by normalization of the Raman spectra with regard to the Si TO-peak.

The spatial resolution of about $(7.5 \pm 0.3)\,\mathrm{\mu m}$ is far below that of commercially available confocal Raman microscopes, in which resolutions $\mathcal{O}(100\,\mathrm{nm})$ can be achieved. However, this is intentional. The employed low NA (10x magnification) microscope objective can only achieve a spatial resolution of about $2.5\,\mathrm{\mu m}$ with a $532\,\mathrm{nm}$ wavelength laser at the diffraction limit. Although, the choice limits the spatial resolution, it also offers several advantages: (i) macroscopic sample areas (up to $1\,\mathrm{cm^2}$) can be completely scanned within a reasonable time of a few days; and (ii) a larger area of the sample is probed at once, increasing the Raman signal and reducing the acquisition time. As it was shown by comparison with light microscope and SEM images, the spacial resolution is good enough to identify mm-scale damages as well as μm-scale defected regions on graphene. Therefore, the selected magnification resembles an optimum in the trade-off between acquisition time and spacial resolution. In principle, the CRM can be equipped with higher magnification objectives, if a higher spacial resolution is needed for future qualitative (graphene) studies. Preliminary results indicate that the CRM performs as expected under higher magnification, too.

Raster scans of $1\,\mathrm{cm^2}$ samples demonstrate that the tilt of the sample and motorized stage can be corrected, and the sample is in focus at all times. The deviation from the determined focal plane is less than $0.1\,\%$ during a full $1\,\mathrm{cm} \times 1\,\mathrm{cm}$ scan. The inherent backlash for bidirectional movement in the motorized translation stages was determined to be ~ 1.8 full-steps $\hat{=} 2.25\,\mathrm{\mu m}$. The uni-directional reproducibility is ≤ 1.0 full-steps $\hat{=} 1.25\,\mathrm{\mu m}$. When compared to the spacial resolution of the system, this reproducibility is sufficient to conduct repeated scans of the same area. Of course, should the CRM be equipped with a higher magnification objective in future experiments, the reproducibility of the motorized translation stages needs to be reassessed.

As the CRM is not designed for graphene samples specifically, but for toxic or radioactive samples in general, a spectrometer and grating combination was chosen, that covers a large spectral range at once. The spectral resolution of this combination is about $(41.4 \pm 10.7)\,\mathrm{cm^{-1}}$. For example, for the measurements of the RW sample (see Appendix E) almost the full spectral range is taken advantage of to find peaks, which were not expected prior to the measurements. With regard to graphene specifically, the large spectral range

($\sim 6000\,\mathrm{cm}^{-1}$) is not needed. Changing the spectrometer grating from $300\,\mathrm{gr/mm}$ to $600\,\mathrm{gr/mm}$ would still cover the whole spectral range of the graphene peaks, including the TO-peak of Si for normalization, with an improved spectral resolution.

For future quantitative measurements of graphene samples, the improved spectral resolution is necessary to allow resolving the G- and D'-peaks that can be used to probe the nature of graphene defects [Eck12]. A higher spectral resolution would also make the CRM more sensitive to the broadening of the 2D-peak that is predicted for multi-layer graphene. With the current system, these effects are rather small and can be hidden by more pronounced effects. Multi-layer graphene samples will be exposed to tritium in the future to study the nature of the graphene-tritium interaction.

In summary, the CRM in its current configuration is well suited for first, qualitative experiments with graphene and tritium. It is also suited for upgrades in both, the spectral and spatial resolution, if desired. The system is fully characterized and well understood. The CRM was used for several measurements and studies on graphene and RW samples, some of which are shown in Appendix D, Appendix E, and published in Ref. [Dia22]. In the future, it will also be used for chemical analysis of different tritium exposed and contaminated parts, *e.g.* to study the depositions on LARA cell windows.

7. Exposure of graphene samples to tritium

In this chapter, the tritium loading experiments are presented and discussed. First, in Section 7.1 a brief introduction into the main ideas is given. Second, in Section 7.2 the loading principle using the self-radiolysis of tritium is described in more detail. Third, in Section 7.3 the experimental setup of the tritium loading chamber is described. Specifically, the theory and the implementation of the sheet resistance measurement using the VAN DER PAUW method is highlighted. Fourth, the results of pre-measurements and 'lessons-learned' are summarized in Section 7.4. Last, the tritium exposure of graphene samples is described in Section 7.5. This includes the *in-situ* resistivity measurements, the temperature dependence of resistance, Raman imaging, and the heating of tritium-exposed samples. The main results of this chapter are published in Ref. [Zel23].

7.1. Motivation and overview

Due to the radioactive and volatile nature of tritium, there are many considerations that must be made regarding regulatory requirements, safety, and contamination of the equipment. This severely limits the choice of possible characterization measurements.

In contrast to most experiments with *e.g.* hydrogen, most steps of a tritium experiment are time-consuming and laborious. For example, in order to extract the samples from a tritium loading chamber, the chamber needs to be evacuated for at least a few days to minimize contamination of the surrounding glove box. Therefore, for experiments with tritium, it is essential to incorporate at least one *in-situ* characterization procedure.

One simple method for *in-situ* monitoring is the resistance measurement of graphene, as demonstrated in *e.g.* Ref. [Gui14]. When using a two-point-measurement, there is an offset of the resistance measurement from the wires used. By using a four-point-resistance measurement via the VAN DER PAUW method [Pau58], the sheet resistance of the graphene sample can be measured offset-free and compared to similar experiments by other groups.

However, using sheet resistance measurements, it is not possible to distinguish between the types of defects introduced to the graphene layer. As described in Section 3.3, there are two main types of defects in graphene, which are relevant to this work, vacancy- and sp^3-type defects. In the literature, there are three main methods employed to distinguish between these defect types:

1. X-ray Photoelectron Spectroscopy (XPS) can be used to measure the bond energy directly and is therefore the method of choice when it is available [Spe07]. XPS systems are expensive and therefore not favorable for the use with radioactive tritium samples, which could experience out-gassing of tritium. For this work, no XPS system was available; however, XPS data from the literature for exposure to atomic hydrogen is used for cross-comparison of the sheet resistance and Raman measurements. This is discussed in great detail in Section 7.6.

2. High-spectral resolution Raman spectroscopy has been used to resolve the D'-peak of defected graphene. Details on this method were already given in Section 3.3. This method was unavailable for this work.

3. By thermal annealing, it can be investigated whether the observed changes to the graphene layer are reversible [Son16]. Although graphene has self-healing properties [Che13], severe damages (vacancy-type defects) are only completely reversible in the presence of hydrocarbon gases [Lóp09].

In this work, *ex-situ* low-spectral resolution Raman characterization measurements, in combination with thermal annealing in a tritium-compatible oven, are used to investigate the nature of graphene defects introduced by exposure to tritium. The Raman measurements are conducted with the CRM described in Chapter 6, which was designed and built specifically for radioactive or toxic samples.

7.2. Introduction to the loading principle

Hydrogenation is usually performed with thermal crackers (via atomic hydrogen) or with plasma sources (via atomic and ionic hydrogen) [Sof07; Eli09; Whi18]. Building tritium compatible equipment operated in a licensed laboratory – especially when involving complex equipment such as thermal crackers, plasma sources and pumps – is expensive, laborious, and time-consuming. Implementing such equipment within the time-constraint of this work was not viable. Therefore, the tritiation is performed with tritium atoms/ions, which are generated naturally because of β-decay and subsequent ionization/dissociation within the tritium gas environment.

The generated β-electrons lead to secondary ionization, significantly increasing the concentration of ions. In addition to Equation 2.44, other possible final states from the β-decay are:

$$T_2 \longrightarrow {}^3\mathrm{He}^+ \quad + T \quad + e^- \quad + \bar{\nu}_e, \tag{7.1}$$

$$T_2 \longrightarrow {}^3\mathrm{He} \quad + T^+ + e^- \quad + \bar{\nu}_e, \text{ and} \tag{7.2}$$

$$T_2 \longrightarrow {}^3\mathrm{He}^{++} + T \quad + 2e^- + \bar{\nu}_e. \tag{7.3}$$
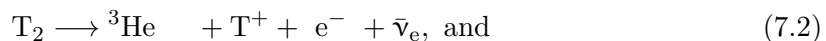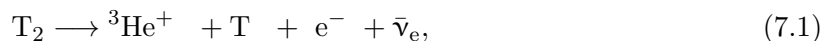
with branching ratio of 32 % for Eq. 7.1 and 0.8 % for Eq. 7.3, respectively [Fie92]. Besides that, secondary ionization of T_2 molecules with the β-electrons can take place, which generates a cold-plasma, thus further increasing the T and T_n^+ densities. For the proof-of-principle study, the expected tritiation rate should be sufficient without the need for a more complex tritium cracker or plasma setup.

Most of the dissociation processes lead to ions/atoms with kinetic energies in the range 3-13 eV[Bod15]. These primary ions are quickly thermalized down to just a few tens of meV by collisions with the gas at room temperature. For initial ion energies of $\mathcal{O}(1\,\mathrm{eV})$ the inelastic scattering cross-section (of H_2^+ on H_2) is about $\sigma_{\mathrm{IS}} 10 \times 10^{-15}\,\mathrm{cm}^2$ [Tab00]. This implies in a mean free path of about $1\,\mu\mathrm{m}$. About four to five scattering events are required to drop the kinetic energy below the threshold for absorption. For the $1\,\mathrm{cm}^2$ graphene

sample, this corresponds to a volume of $1\,\mathrm{cm} \times 1\,\mathrm{cm} \times 4-5\,\mu\mathrm{m}$, in which ions are generated with sufficient energy for tritium adsorption at the surface. By interacting with the gas, further processes take place [Kle19b], including ionization, gas phase formation of larger ion clusters, and the recombination of the ions with electrons. The resulting $\mathrm{T}_n^{(+)}$ species receive kinetic energy in the range 0-15 eV, peaking at about 8 eV.

The calculation of the rate of ions generation regarding initial β-decay is more complex, but may be obtained via Monte-Carlo modelling methods. In principle, a sufficient quantity of tritium ions/atoms can be produced in the energy range of interest to provide significant tritium adsorption during the exposure time; on the other hand, a fraction of the ions will have energies which are high enough to be able to introduce damage to the graphene layer.

7.3. Experimental setup of the loading chamber

A custom-made loading chamber was used for tritium exposure of the graphene samples, which offers *in-situ* sheet resistance measurements. The main components of the loading chamber are shown in Figure 7.1 with a full list of the components given in Table 7.1. All the components are fully tritium and high-vacuum compatible, and are made of stainless steel, aluminum, cooper, and ceramic materials.

The graphene samples are contacted directly via four spring-loaded contacts[1], which are used for the measurement of the graphene sheet resistance via the VAN DER PAUW method. The sheet resistance measurements are conducted using a *DAQ6510* with a *7709-matrix switching card*[2]. The VAN DER PAUW method and the details of the electrical installation are given in Section 7.3.2. In order to characterize the temperature dependence of the graphene sheet resistance and desorption measurements, an electrical heater[3] and a temperature sensor[4] are installed in thermal contact with the sample holder (see Section 7.3.1 for more details). Close-up images of this setup are shown in Figure 7.2.
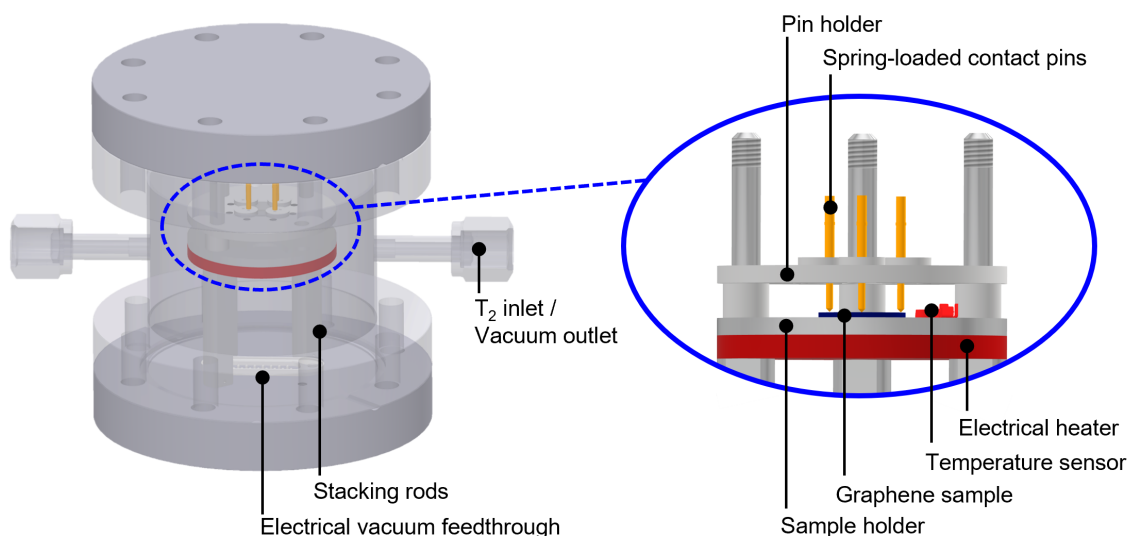
Figure 7.1.: Technical drawing of loading chamber. Important components are annotated. Details can be found within the text and Table 7.1. Image adapted from [Zel23].

---

[1]PTR HARTMANN GmbH, 59368 Werne, Germany
[2]Both from Keithley, Cleveland, USA
[3]Thermocoax, Heidelberg, Germany
[4]Allectra GmbH, 16567 Schönfliess, Germany

Table 7.1.: Overview of main loading chamber components

Component	Material	Manufacturer
Intermediate piece DN63CF with two 1/4-inch VCR connectors	stainless steel 304L	*VACOM*[a]
Flanged D-Sub feedthrough DN63CF SUB-D-15-FM	stainless steel 304L	*VACOM*[a]
Blank flange DN63CF	stainless steel 304L	*VACOM*[a]
SUB-D 15-Pin Connector	Macor	*VACOM*[a]
Spring-loaded contacts	bronze, steel	*PTR Hartmann*[b]
Insulators	ceramic (Al_2O_3 96 %)	*Quick-cool*[c]
PT100 resistor on ceramic	ceramic, glass, platinum	*Allectra*[d]
Stacking rods	aluminum	in house
Sample holder	aluminum	in house
Pin holder	aluminum	in house
UHV wire	silver plated copper, kapton insulated	*Allectra*[d]

[a] VACOM Vakuum Komponenten & Messtechnik GmbH, 07751 Großlöbichau, Germany

[b] PTR HARTMANN GmbH, 59368 Werne, Germany

[c] Quick-Ohm Küpper & Co. GmbH, 42349 Wuppertal, Germany

[d] Allectra GmbH, 16567 Schönfliess, Germany

(a)

(b)

(c)
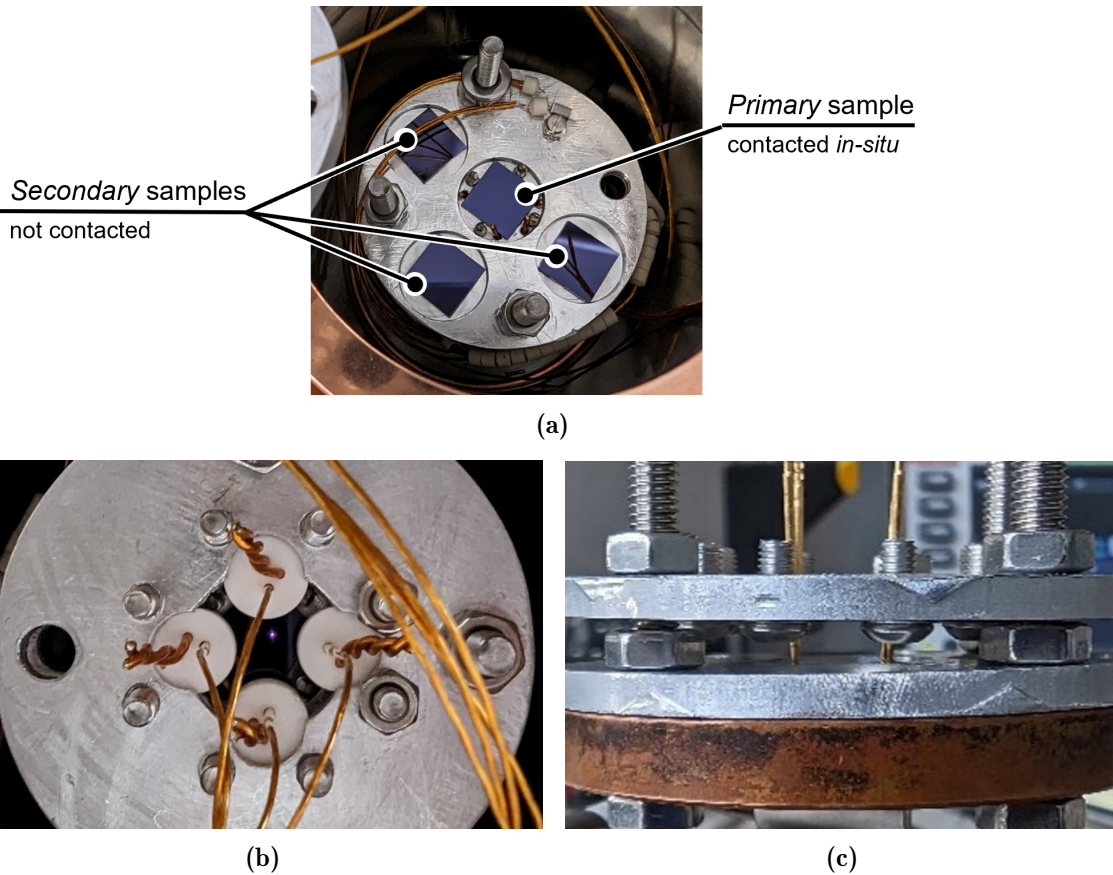
Figure 7.2.: Images of the loading chamber. (a) Top-down image without the pin-holder, showing the placement of the primary and secondary samples within the sample holder. (b) Top-down image showing the pin-holder with the spring-loaded contacts and their ceramic connector insulators. (c) Side-view image of the internal stack, highlighting the spring-loaded contacts.

Note that for the pre-measurements with a RW sample, used for proof-of-principle measurements and described in Appendix E, a different, prototype loading chamber was used, which is described in the respective section.

7.3.1. Electrical heating element

The electrical heating element consists of a copper plate with a *Thermocoax*[5] heating system fitted on the underside. It was manufactured by the KIT Technik-Haus (TEC). The dimensions and electrical properties are summarized in Table 7.2.

The heating element is located within the loading chamber and is used to heat the graphene samples. The graphene sample holder lies flush on the electrical heater for this purpose. The temperature on the top of the sample holder is measured via a Pt100 temperature sensor[6]. For safety reasons, pre-experiments were conducted to determine the relation between the temperature of the sample holder and the inner and outer wall temperatures of the loading chamber. The maximum temperature of the electrical heater is limited such that the inner wall and outer wall temperatures of the loading chamber do not rise beyond max. $200\,°C$ and max. $50\,°C$, respectively. When the loading chamber is evacuated to $1 \times 10^{-6}\,mbar$ (standard operation condition), the temperature of the outer wall is not exceeding $40\,°C$ when heating the samples to $200\,°C$ for $1\,h$.

During the commissioning of the loading chamber, it was found that the electrical connection to the graphene layer can become unstable (evident by the increased signal noise), and the circuit can open completely, causing an OVERFLOW error in the sheet resistance measurement[7]. It was found that these problems correlated with the heating of the samples. Although, the OVERFLOW temperature could not be fully reproduced in every measurement run, these problems almost completely disappeared when the heating temperature was limited to $110°C$. This severely limits the functionality of the loading chamber. The planned *in-situ* desorption measurements are not possible at $110°C$; however, this was the only possible solution to continue with any tritium-loading experiments, without the need for an overall redesign of the loading chamber.

Table 7.2.: Properties of the electrical heating element

Property	Value
Material	Copper (Cu)
Size	$\varnothing\ 50\,mm$, thickness $d = 5\,mm$
Heating	Thermocoax D1
Length	$321\,mm$
Specific Resistance	$10\,\Omega\,m^{-1}$
Loop resistance	$4.4\,\Omega$
Maximum power	$100\,W$
Maximum load	$21\,V$

---

[5]Thermocoax, Heidelberg, Germany

[6]Allectra GmbH, 16567 Schönfliess, Germany

[7]P. Wiesen: 'Commissioning of a graphene-loading stage and conductivity measurements during first tritium exposure'. Bachelor's thesis. Karlsruhe: Karlsruhe Institute of Technology, 2023

7.3.2. Sheet resistance measurement using the Van der Pauw method

The sheet resistance of the graphene sample is measured *in-situ* and continuously via a four-point-resistance measurement using the VAN DER PAUW method [Pau58]. The definitions, explanations, and derivations in this section closely follow Refs. [Hea03; Sch06], in which more details can be found.

Definition of the sheet resistance

For a three-dimensional conductor, the resistance R is defined as

$$R \equiv \rho \cdot \frac{l}{h \cdot w}, \tag{7.4}$$

where ρ is the specific bulk resistivity of the material and l, w and h are the length, width, and thickness of the sample. The sheet resistance is then defined as:

$$R_\square \equiv \frac{\rho}{h} \implies R = R_\square \cdot \frac{l}{w} \tag{7.5}$$

and thus for a square sample with $l = w$:

$$R = R_\square = \frac{\rho}{h}. \tag{7.6}$$

Although, the units for the sheet resistance are Ω, commonly $\Omega/\square$ is used to differentiate between the resistance and sheet resistance

$$[R_\square] = \frac{[\rho]}{[h]} = \frac{\Omega \cdot \mathrm{m}}{\mathrm{m}} = \Omega = \Omega/\square. \tag{7.7}$$

The sheet resistance $R_\square$ numerically corresponds to the resistance of a square piece of the material. However, measurements of the area and thickness of a sample are often difficult to implement. For example, in graphene-based samples, which can be assumed to be a two-dimensional material, there is no material thickness in the classical sense, but only a covalent atomic radius of a carbon atom, which differs depending on the hybridization. The VAN DER PAUW method offers a solution to this problem.

Van der Pauw method

The VAN DER PAUW method is a four-point measurement technique. Using this method, the sheet resistance of a sample with arbitrary shape and thickness can be measured, as long as the following conditions are fulfilled [Pau58]:

1. The four contacts (labelled A, B, C, and D) are placed on the circumferences of the sample.

2. The contacts are sufficiently small compared to the area of the sample.

3. The thickness of the sample is homogenous.

4. The surface has no isolated holes.

When these conditions are not fulfilled, the measurement is only valid to a lesser degree, but can still be used to monitor the change in sheet resistance. In his original paper [Pau58], L. J. VAN DER PAUW first proved that the following equation holds:

$$\exp\left(-\frac{\pi h}{\rho} \cdot R_{\mathrm{AB,\,CD}}\right) + \exp\left(-\frac{\pi h}{\rho} \cdot R_{\mathrm{BC,DA}}\right) = 1, \tag{7.8}$$

where $R_{\mathrm{AB,\,CD}}$ is the resistance calculated by measurement of the current flow along one edge of the sample and the voltage across the opposite edge of the sample. If $R_{\mathrm{AB,\,CD}}$ is the measurement across the horizontal edge of the sample, then $R_{\mathrm{BC,DA}}$ is the measurement across the vertical edge of the sample, and vice versa. In order to improve the measurement accuracy, usually reciprocal and reversed polarity measurements are added [Kei16], resulting in the following combination of eight resistance measurements:

$$R_1 = \frac{U_{\mathrm{AB}}}{I_{\mathrm{CD}}}, \quad R_2 = \frac{U_{\mathrm{BA}}}{I_{\mathrm{DC}}}, \quad R_3 = \frac{U_{\mathrm{CD}}}{I_{\mathrm{AB}}}, \quad R_4 = \frac{U_{\mathrm{DC}}}{I_{\mathrm{BA}}} \tag{7.9}$$

$$R_5 = \frac{U_{\mathrm{AD}}}{I_{\mathrm{BC}}}, \quad R_6 = \frac{U_{\mathrm{DA}}}{I_{\mathrm{CB}}}, \quad R_7 = \frac{U_{\mathrm{BC}}}{I_{\mathrm{AD}}}, \quad R_8 = \frac{U_{\mathrm{CB}}}{I_{\mathrm{DA}}}.$$

All configurations are shown in Figure 7.3. Returning to the original idea of one horizontal and one vertical resistance measurement, these resistances can be combined, yielding

$$R_{\mathrm{H}} = \frac{R_1 + R_2 + R_3 + R_4}{2} \quad \text{and} \quad R_{\mathrm{V}} = \frac{R_5 + R_6 + R_7 + R_8}{2}, \tag{7.10}$$

and Eq. 7.8 becomes

$$\exp\left(-\frac{\pi h}{\rho} \cdot R_{\mathrm{H}}\right) + \exp\left(-\frac{\pi h}{\rho} \cdot R_{\mathrm{V}}\right) = 1. \tag{7.11}$$

The resistivity ρ can then be expressed as

$$\rho = \frac{\pi h}{\ln 2} \cdot \frac{R_{\mathrm{H}} + R_{\mathrm{V}}}{2} \cdot f, \tag{7.12}$$

where f is a function of the ratio $Q = R_{\mathrm{H}}/R_{\mathrm{V}}$ and satisfies the following equation:

$$\frac{Q-1}{Q+1} = \frac{f}{\ln 2}\mathrm{arcosh}\left(\frac{\exp(\ln 2/f)}{2}\right). \tag{7.13}$$

Combining Eqs. 7.6 and 7.12 results in

$$R_{\square} = \frac{\pi}{\ln 2} \cdot \frac{R_{\mathrm{H}} + R_{\mathrm{V}}}{2} \cdot f, \tag{7.14}$$

which is independent of the thickness and area of the sample and depends solely on R_{H} and R_{V} as defined in Eq. 7.10.
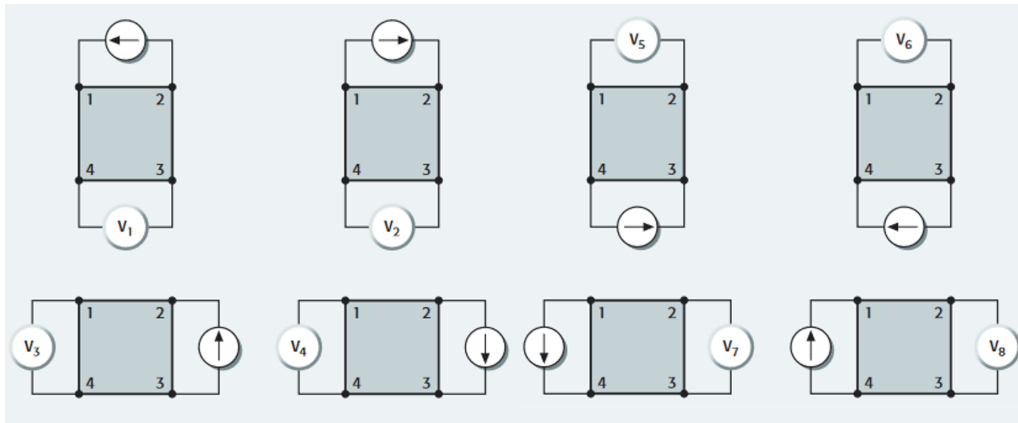
Figure 7.3.: Reciprocal and reversed polarity resistance measurement configurations for the Van der Pauw method. Image adapted from [Kei16].

Experimental implementation

For the sheet resistance measurement via the VAN DER PAUW method, the graphene layer is contacted directly with four spring-loaded contacts from above. The spring-loaded contacts are secured in a pin holder. The vacuum- and tritium-compatible wire are fed through a Sub-D connector in the bottom flange. More details on particular parts were already given in Table 7.1.

The resistances are measured with a *Keithley*[8] *DAQ6510* multimeter. In order to perform the reciprocal and reversed polarity resistance measurements, the *DAQ6510* system is equipped with a programmable *7709-matrix switching card*[8]. In Figure 7.4 a schematic of the internal wiring of the DAQ6510 system and the connections to the graphene sample via the matrix card are shown. The DAQ6510 system automatically selects a suitable test current[9], which flows from INPUT HI to INPUT LO. Between the SENSE HI and SENSE LO connections, the corresponding voltages are measured. The device automatically computes and returns the resistance value. Afterward, a switch-command is sent to the matrix card, changing the connections to the next configuration, as defined in Eq. 7.10. The read-out of the DAQ6510 system, the synchronization with the matrix card, and the computation of the sheet resistance according to Eq. 7.14 is handled by a custom LabVIEW[10] program.

In addition to the eight configurations, which are needed for the sheet resistance measurement, during each measurement cycle also the two-point resistances between the four contacts are measured. A full measurement cycle with eight four-wire measurements and six two-wire measurements takes about 2-5 s to complete.

The two-point resistance measurements provide additional information, in case there is a problem with the four-point measurement. For example, if exactly one of the contacts is damaged, all four-point measurements are affected. However, only three of the six two-point measurements are affected. This information can be used to determine which of the contacts is damaged.
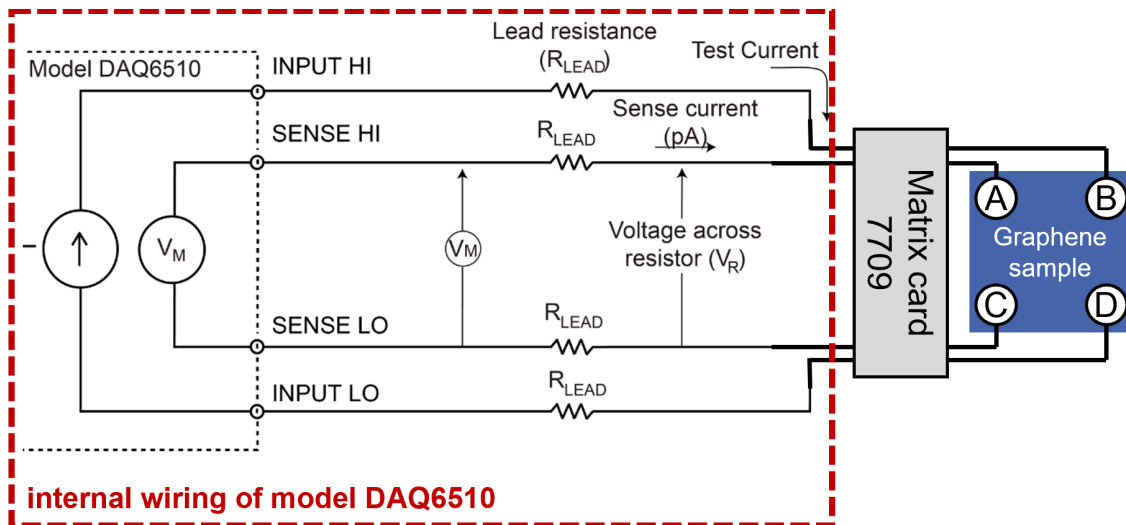
Figure 7.4.: Schematic of the internal wiring of the DAQ6510 system and the connections to the graphene sample via the matrix card 7709.

---

[8]Keithley Instruments, LLC, Solon, Ohio, USA

[9]https://download.tek.com/manual/DAQ6510-900-01B_Aug_2019_User.pdf

[10]National Instruments, Austin, Texas, USA

7.4. Commissioning of the loading chamber with hydrogen

The safety-related and scientific commissioning of the loading chamber with hydrogen were performed together with Paul Wiesen; these were discussed in full detail within his bachelor's thesis[11]. In this section, only the most important results regarding the tritium loading experiment are briefly summarized.

System bake-out

The evacuated loading chamber including a contacted graphene sample was placed in a bake-out oven. The system was baked out at 110 °C for approximately 24 h. During the bake-out, the loading chamber was constantly evacuated via a turbomolecular pump to remove the out-gassing substances from the system. In general, a bake-out of stainless-steel vacuum systems is recommended due to the large amount of H_2O which can be retained in the stainless-steel walls. This makes it more difficult to obtain a good vacuum ($<1 \times 10^{-6}$ mbar) in the system, which is needed to to demonstrate that the leak rate for a tritium system was not surpassed, using a pressure rise test. In addition, it was observed that during the measurement of the TEMPERATURE COEFFICIENT OF RESISTANCE (TCR) the graphene sheet resistance continued to increase, even though a stable temperature of 120 °C was reached (Figure 7.5).

One interpretation of this observation is that by heating of the sample, some of the H_2O from the stainless-steel parts of the system is released and adsorbed on the graphene surface, thus increasing its sheet resistance. After the system bake-out and three additional TCR measurement cycles, this effect disappeared and the sheet resistance of the graphene sample was stable even at elevated heating temperatures. It should be noted that the system was opened in laboratory atmosphere for an exchange of graphene sample before the main tritium loading, without an additional bake-out.

(a) Before system bake-out **(b)** After system bake-out
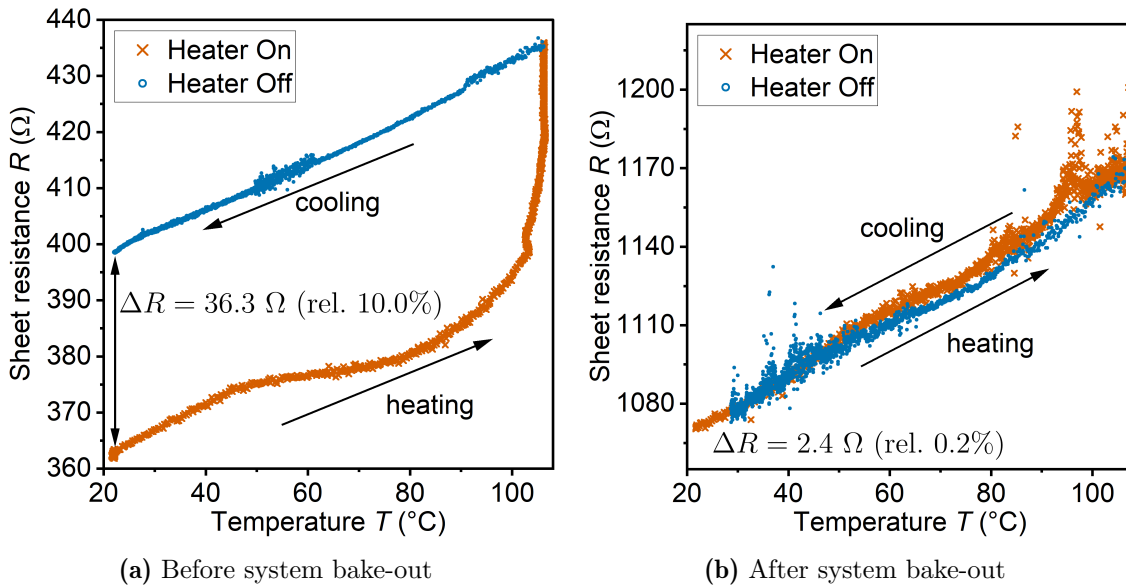
Figure 7.5.: Effect of system bake-out on TCR. Details can be found within the text.

---

[11]P. Wiesen: 'Commissioning of a graphene-loading stage and conductivity measurements during first tritium exposure'. Bachelor's thesis. Karlsruhe: Karlsruhe Institute of Technology, 2023

Temporal stability of graphene sheet resistance

When the sheet resistance was measured overnight, a relative drift of only $0.011\,\%\,\Omega\,h^{-1}$ was observed. The relative statistical uncertainty is of the order of $0.1\,\%$. Both effects are small compared to the increase during heating ($\approx 0.5\,\Omega/°C$) and the expected increase during tritium loading (several orders of magnitude).

Temperature dependence of graphene sheet resistance

After the system bake-out, the TCR of the measured graphene sample was $TCR = 1.13 \cdot 10^{-3}$, which is comparable to similar experiments conducted by other groups[Lei22]. A more detailed discussion and comparison to the TCR after tritium exposure is given in Section 7.5.2

Graphene sheet resistance in hydrogen atmosphere

As expected, the graphene sheet resistance is not affected by the presence of molecular hydrogen. The relative drift during an overnight measurement increased ($1\,\%\,h^{-1}$), in comparison to the evacuated system. Notably, during the inlet of hydrogen, the sheet resistance was not affected (see Figure 7.6). A more detailed discussion and comparison with the inlet of tritium and the drift during and after tritium exposure is given in Section 7.5.1.

(a) During H$_2$ inlet

(b) Overnight stability in H$_2$
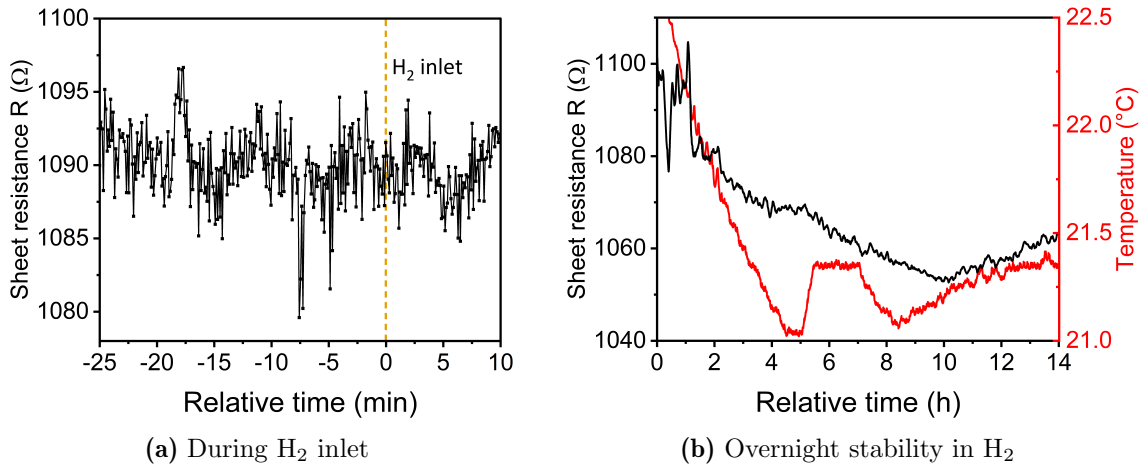
Figure 7.6.: Sheet resistance during hydrogen inlet, and stability for several hours thereafter. Data shown in (b) is recorded after several heating cycles during the day. Additionally, a Savitzky-Golay filter is applied to reduce noise and improve the visibility of the data trend. Details can be found within the text.

7.5. Characterization of tritium-exposed graphene

For the tritium exposure of the graphene samples, the loading chamber and experimental setup described in Section 7.3 are used. The graphene samples are monolayer graphene on a silicon substrate with a 90 nm SiO_2 buffer layer (SiO_2/Si) citeGraphenea.MonolayerGrapheneon from *Graphenea*[12]. Four identical samples are placed in the loading chamber, one *primary* sample (**Sample A**), which is contacted *in-situ* for the sheet resistance measurement, and three *secondary* samples (**Samples B, C, D**) (see Figure 7.2a). The *secondary* samples are not-contacted, but are exposed to tritium during the same loading process as the *primary* sample. It can therefore be assumed that they are comparable to the *primary* sample *e.g.* regarding the amount of tritium adsorbed on the sample. They can be used for destructive activity, cross-check, or stability measurements.

An overview of the full tritium loading experiment, the different graphene samples, and their use after tritium exposure is sketched in Figure 7.7. As long as the samples are in the loading chamber, the sheet resistance measurement is running continuous to monitor any changes. First, the loading chamber is closed; it is evacuated to $< 1 \times 10^6$ mbar and a pressure-rise test is used to demonstrate a leak rate of less than 1×10^{-9} mbar L s^{-1}. Second, the manual value to the TRIHYDE sampling port I is opened, and the loading gas mixture expands into the loading chamber.

The loading gas mixture was provided to TRIHYDE via the TSS of the TLK and consisted of 97.2 % T_2 with the remaining 2.8 % being mainly HT and DT. The pressure in the loading chamber, determined by a pressure sensor located at the sampling port I, was about 400 mbar during the exposure. Given the chamber volume of about 0.2 L, this corresponds to a total activity of 7.6×10^{12} Bq. Based on the branching ratios described in Eqs. 7.1 and 7.3, this yields 3.3×10^7 tritium atoms per second. Third, after $\sim$ 55 h of tritium exposure, the loading chamber is again evacuated the $< 1 \times 10^6$ mbar. The manual value to the TRIHYDE system remains open, and the loading chamber is continuously evacuated during the following measurements.
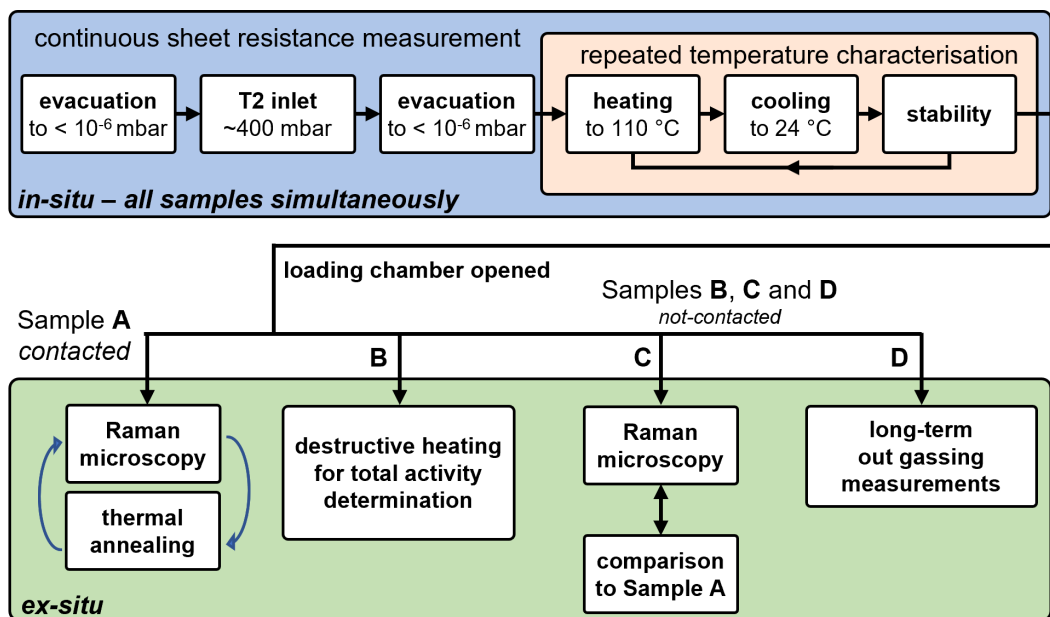
Figure 7.7.: Measurement procedure for tritium loading. Details can be found in the text.

---

[12]Graphenea Inc., 20009 - San Sebastián, Spain

Fourth, the TCR is measured by heating the sample to 110°C and letting it cool down again, similar to the pre-measurements outlined in Section 7.4. Fifth, the stability of the sheet resistance at constant temperature is monitored while the loading chamber is evacuated for several days.

Finally, the loading chamber is opened, and the samples are transferred to a small container, where they are stored within the nitrogen atmosphere of the glove box until further measurements. During this work, three of the four loaded graphene samples, were used for different measurements. For clarity, they are numerated in the following sections:

- **Sample A** This is the *primary* sample, which was contacted *in-situ* for the VAN DER PAUW measurements. After it was removed from the loading chamber, it was transported to the CRM for Raman microscopy measurements. The sample was then heated several times in a tritium compatible oven and again scanned with the CRM.

- **Sample B** One of the secondary samples, which were not contacted *in-situ* during the tritium exposure. It was used for a destructive total activity measurement.

- **Sample C** One of the secondary samples, which were not contacted *in-situ* during the tritium exposure. It was later scanned with the CRM for comparison with **Sample A**.

- **Sample D** One of the secondary samples, which were not contacted *in-situ* during the tritium exposure. It was stored in a sealed plastic bag, to be used later for long-term out-gassing measurements; these measurements were outside the scope of this work.

7.5.1. *In-situ* sheet resistance measurement

The initial increase in sheet resistance at the start of the exposure is shown in Figure 7.8A. Within 5 min, the sheet resistance of the graphene sample increases from $R_\square = (551 \pm 2)\,\Omega/\square$ to $R_\square = (5830 \pm 5)\,\Omega/\square$, reaching a local maximum. During the inlet of H_2, shown in Figure 7.6a, no significant change in $R_\square$ was observed.

Due to the sensitivity of the spring-loaded contacts to outside influences, and therefore the sheet resistance measurement, it cannot be claimed with certainty that this initial increase is related to the inlet of tritium specifically. Speculating, in this experiment the gas stream could have affected the spring-loaded contacts, moving them slightly. To conclusively determine whether this is a chemical effect of the tritium on the graphene layer, or something else, the loading needs to be repeated several times, which was not possible within the time frame of this work, due to the substantial amount of time associated with any individual tritium experiments.

In the subsequent 1.5 h, the sheet resistance initially decreases slightly, but increases again thereafter. The increase approximately follows a logistic function. The complete measurement of $R_\square$ with a fitted general logistic function [Ric59] is shown in Figure 7.8C. When comparing these results to the change in sheet resistance in H_2 atmosphere, shown in Figure 7.6b, it is clear that in the presence of T_2 a chemical process is taking place. From this measurement alone, it is not possible to distinguish vacancy- and sp^3-type defects in the graphene layer, as mentioned earlier. Nevertheless, it serves as proof that by β-decay and self-radiolysis of tritium either electrons or tritium ions/atoms are created with sufficient energy to damage the graphene, or adsorb to the graphene layer.

According to Ref. [Cho16], the electron energy of 18.6 keV from the β-decay is not sufficient to damage the graphene layer. Other groups have reported damaged graphene in low-energy (20 keV) electron beams [Chi10a; Bal11; Hua11; Dor13]. In their work, Choi *et al.* question the validity of these claims and present measurements and observations to disprove them [Cho16].
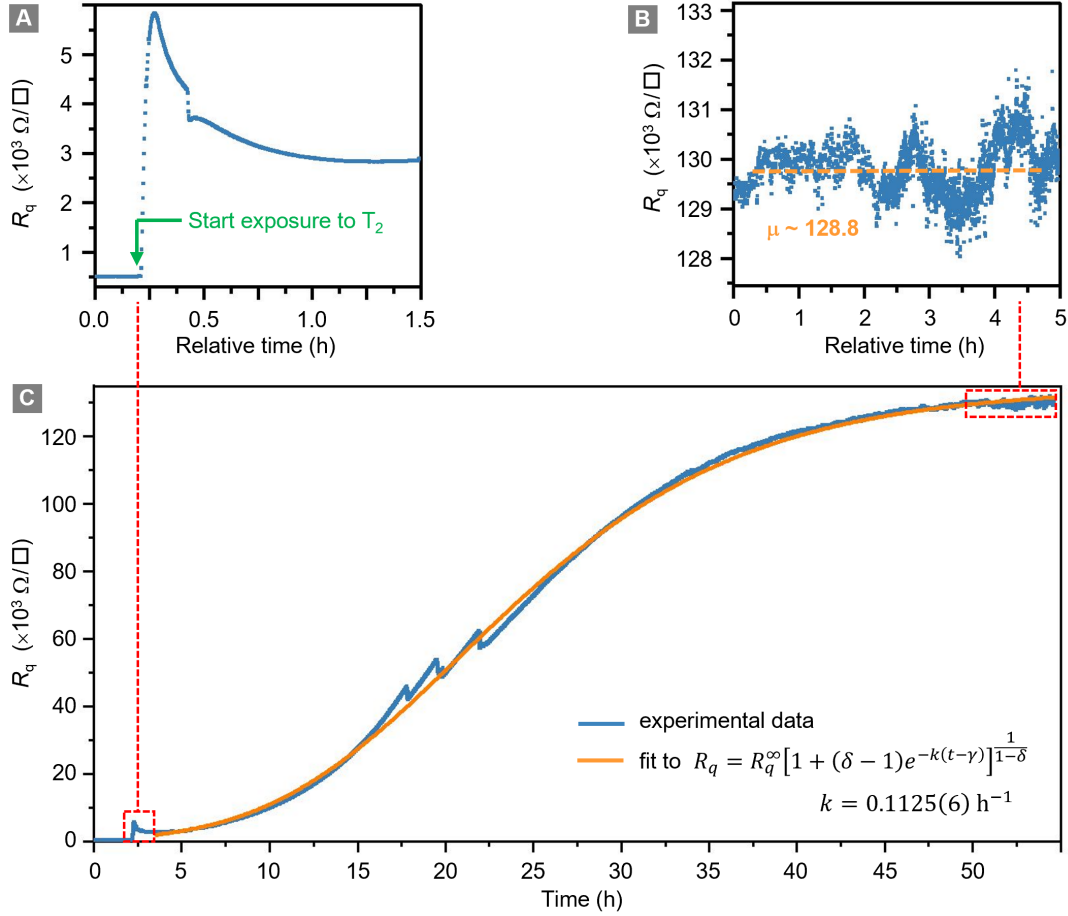
Figure 7.8.: Graphene sheet resistance during tritium exposure. A - Initial increase at the start of tritium exposure; B - plateau reached after 55 h of tritium exposure; and C - full measured curve. Details can be found within the text. Image adapted from [Zel23].

After an exposure time of about $55\,\mathrm{h}$, the surface resistance reaches a plateau at about $R_\square^\infty \approx 120 \times 10^3\,\Omega/\square$, corresponding to a total relative resistivity increase by a factor of ~250. This plateau is shown in Figure 7.8B. It should be noted that the setup used for these measurements can measure resistances up to $\mathcal{O}(1 \times 10^6\,\Omega)$. Therefore, the measured value reflects the actual value of the graphene sample even at the plateau. It can be concluded that enough graphene remains to conduct the measurement current after $55\,\mathrm{h}$ of tritium exposure, and the graphene layer has not completely disintegrated.

7.5.2. Temperature dependence of resistance

These measurements are conducted after the loading chamber is evacuated for $18\,\mathrm{h}$ to $< 1 \times 10^{-6}\,\mathrm{mbar}$. The loading chamber was not opened in between the tritium loading and the TCR measurement. In order to determine the TCR after tritium exposure, the sample was heated using the *in-situ* electrical heating element.

When the sample temperature increases, the sheet resistance decreases. This contrasts with the TCR measurement performed with clean graphene in air, vacuum, or hydrogen atmosphere (Section 7.4). However, this change in TCR is in agreement with measurement of hydrogenated graphene [Bur11; Son16] and graphene-oxide [Muc14]. As in the literature, the graphene samples show metallic transport characteristics when clean. The TCR<0 after tritium exposure, corresponds to insulator-like transport characteristics.

By plotting the natural logarithm of the sheet resistance $\ln(R_\square)$ versus the inverse temperature T^{-1} (see Figure 7.9), an Arrhenius-like equation for the temperature-dependent sheet resistance

$$R_\square(T) = R_\square^0 \exp\left(\frac{E_g}{k_b T}\right) \tag{7.15}$$

can be fitted to the data. Here, E_g is the activation energy and k_b is the Boltzmann constant. Fitting this to the data, pre- and post-tritium exposure, results in

$$E_{\mathrm{g,pre}} = (10.21 \pm 0.04)\,\mathrm{meV} \qquad \text{and} \qquad E_{\mathrm{g,post}} = -(39.33 \pm 0.05)\,\mathrm{meV}. \tag{7.16}$$

The uncertainties given here are only the uncertainties of the linear fit; no other systematic or statistical uncertainty is taken into account.
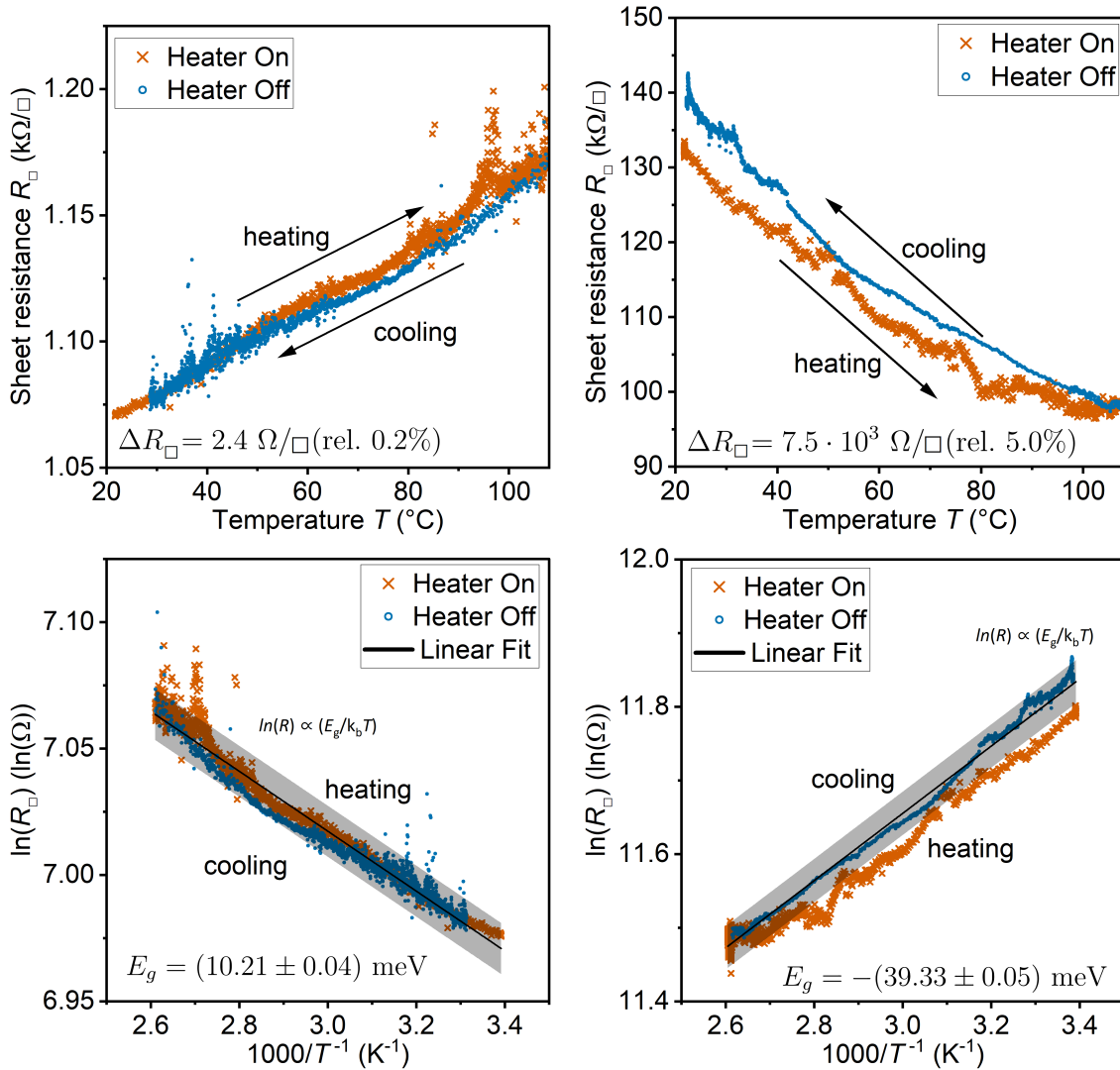
Figure 7.9.: Temperature-dependence of the sheet resistance. Details can be found within the text. Image adapted from [Zel23].

7.5.3. Raman imaging

The *primary* sample (**Sample A**) was scanned with the CRM after tritium exposure. Although, there is no scan of this exact sample prior to the tritium exposure, other clean *Graphenea* samples were scanned during this work and are shown in detail in Appendix D.1. With the low spatial resolution (7.3 µm) of the CRM, the pristine samples look rather homogeneous. In this context, it should be noted that all scanned pristine graphene samples from *Graphenea* are comparable and high quality (see Appendix D.1).

Representative Raman spectra from a pristine and the tritium exposed sample are shown in (Figure 7.10). Before tritium exposure, the sample is in pristine condition with a small D-peak intensity and the intensity ratio $I_D/I_G < 0.1$. After exposure to tritium, the intensity of the 2D-peak is significantly reduced, while the G-peak intensity increases, resulting in an intensity ratio $I_G/I_{2D} = 4.8$. In addition, the D-peak intensity increases by a factor of ~ 70, becoming the dominant Raman band. The intensity ratio $I_D/I_G = 1.7$ indicates a significant increase in the defect density.

Two different scans of **Sample A** were made : First, a HIGH-SPATIAL RESOLUTION (HSR) ($\Delta S = 6.25$ µm) scan of a 350 µm × 350 µm region, roughly in the center of the sample. Second, a LOW-SPATIAL RESOLUTION (LSR) ($\Delta S = 50$ µm) scan of the full 1 cm × 1 cm sample. For the Raman spectra analysis, Lorentzian peak functions are fitted (see Section 4.4 for details). The individual spectra are discussed in more detail in Section 7.5.6. The Raman maps generated from the HSR and LSR scans are shown in Figure 7.11.

The LSR scan demonstrates that the graphene layer is mostly intact and was not destroyed by the exposure to tritium. In addition, the LSR scan of the whole graphene sample, revealing the following:

(i) The sample is installed slightly tilted in the sample holder; this is evident from the 'gray' upper-left corner of the image, indicating a 'non-signal' area.

(ii) In the three visible corners of the sample, severe damages (color-coded black) of the graphene layer can be seen. These damages correspond to the spring-loaded contacts of the sheet resistance measurement. It becomes clear that the contacts were moving
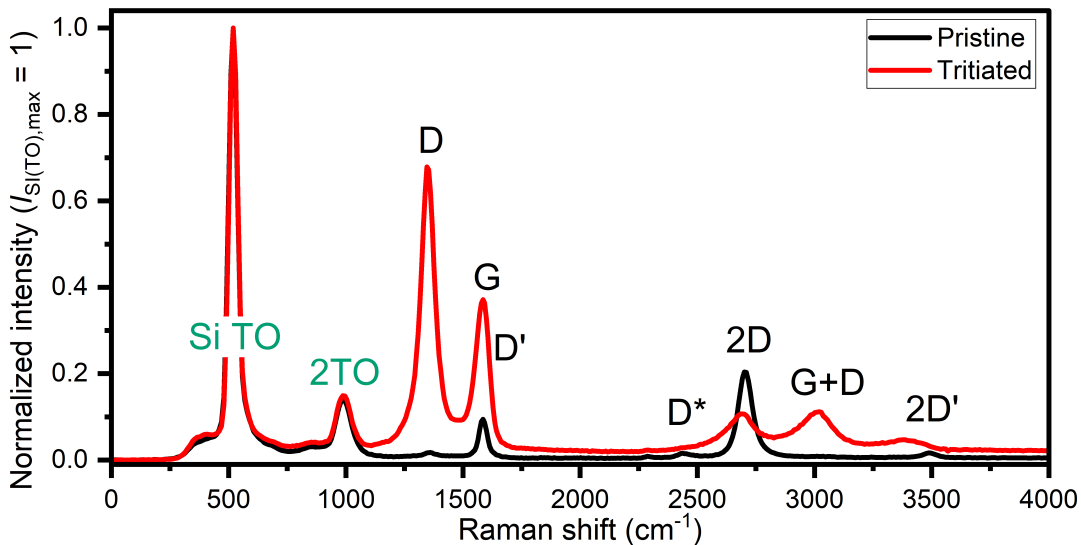
Figure 7.10.: Raman spectra of pristine and tritium-exposed graphene. Important spectral features of Si and graphene are annotated. Details can be found within the text. Image adapted from [Zel23].

on the sample surface. An additional HSR scan was performed on the damaged region in the lower-left corner. The respective Raman image is shown in Figure 7.11b; it will be discussed later in this section.

(iii) In an area surrounding the damaged pin-contact areas there is a radial gradient in the spectral modifications, *e.g.* the G-peak intensity increases with increasing distance from the damaged areas. This could be caused be shadowing of the pin-holder or by electrochemical effects induced by the measurement current, which is passed through the contacts during the VAN DER PAUW measurement.

(iv) In the area of the HSR scan, which was performed first, a reduced G-Peak intensity is observed in the LSR scan. This likely indicates that a laser-induced or laser-accelerated change occurs; the systematic investigation of this effect is summarized in Section 7.5.4.

(v) Apart from the effects listed above, the spectral modifications of the graphene are rather homogenous and are present across the full sample area.

(a) LSR scan of full sample

(b) HSR scan of the area damaged by spring-loaded contact

(c) HSR scan of central region (G-peak)

(d) HSR scan of central region (D/G-peak intensity ratio)
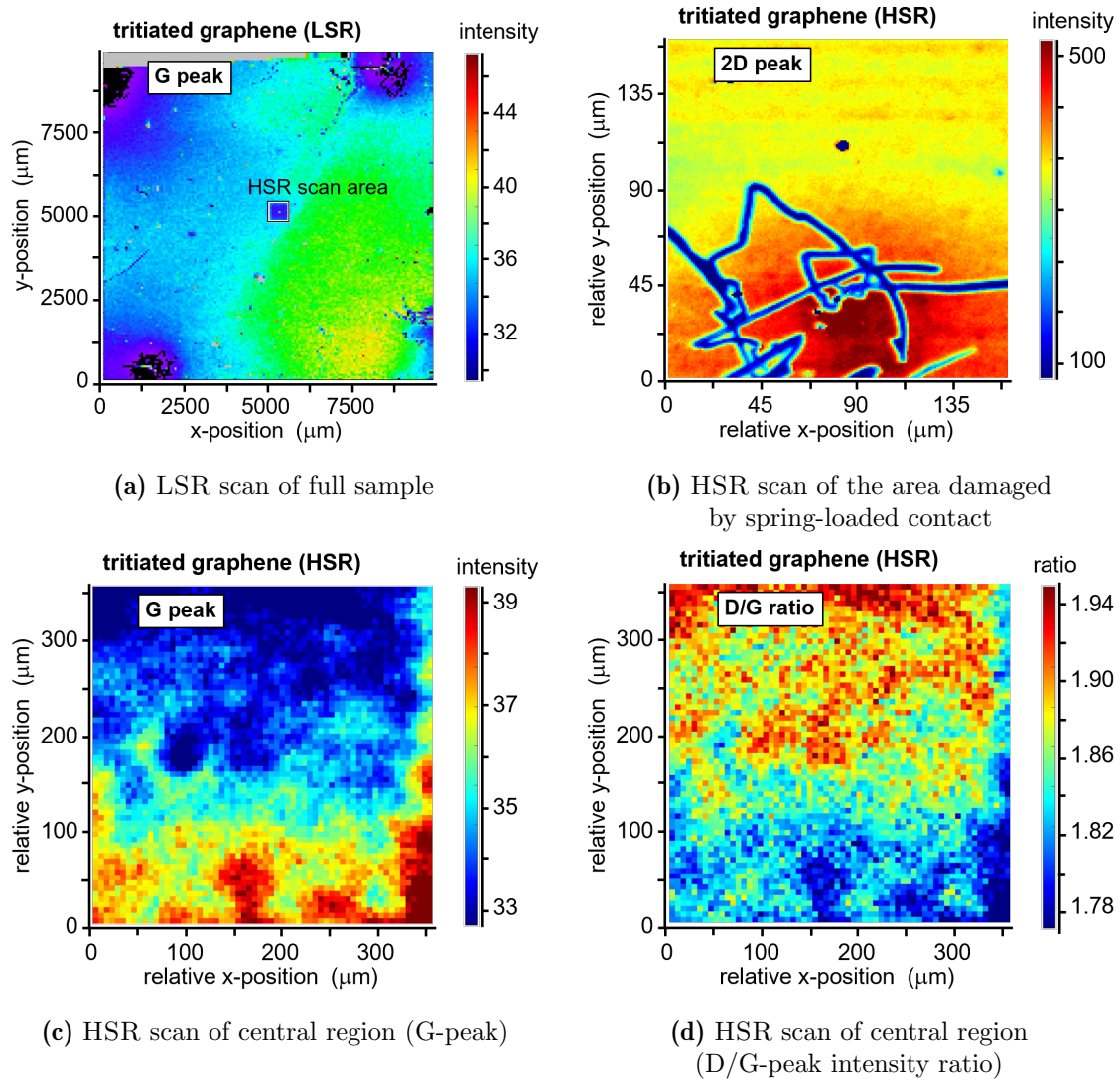
Figure 7.11.: Raman images of tritium-exposed graphene sample (**Sample A**). Details can be found within the text. Images adapted from [Zel23].

7.5.4. Laser-induced spectral changes

After the laser-affected G-peak intensity was observed during the analysis of the HSR and LSR scans of **Sample A**, systematic investigations were conducted. These investigations include the prolonged (24 h) laser irradiation of a single spot on the graphene sample; the results are summarized in Figure 7.12. The intensities are determined using a Lorentzian fit and the D-, G-, and 2D-peak are normalized to the signal of the TO-peak of $Si(O_2)$ to eliminate influences which affect all peak intensities simultaneously, *e.g.* fluctuations of the laser power, or temperature. In addition, the D/G-intensity ratio is shown. While the D- and G-peak intensities show an almost linear decrease of $-0.3\,\%\,h^{-1}$, the 2D-peak intensity and the D/G-intensity ratio are stable, and the linear fit slope is conform with $0.0\,\%\,h^{-1}$. For all peaks, the other Lorentzian fit parameters (width, position, offset) are stable to $< 0.01\,\%\,h^{-1}$. The measurement was repeated two weeks later, and this effect could not be replicated: all peak intensities then were stable to $< 0.01\,\%\,h^{-1}$. Although the cause of the observations in Figure 7.12 is not understood at present, even in the worst-case scenario of $-0.3\,\%\,h^{-1}$, the standard measurements with typical acquisition times of 5-90 s are not affected.
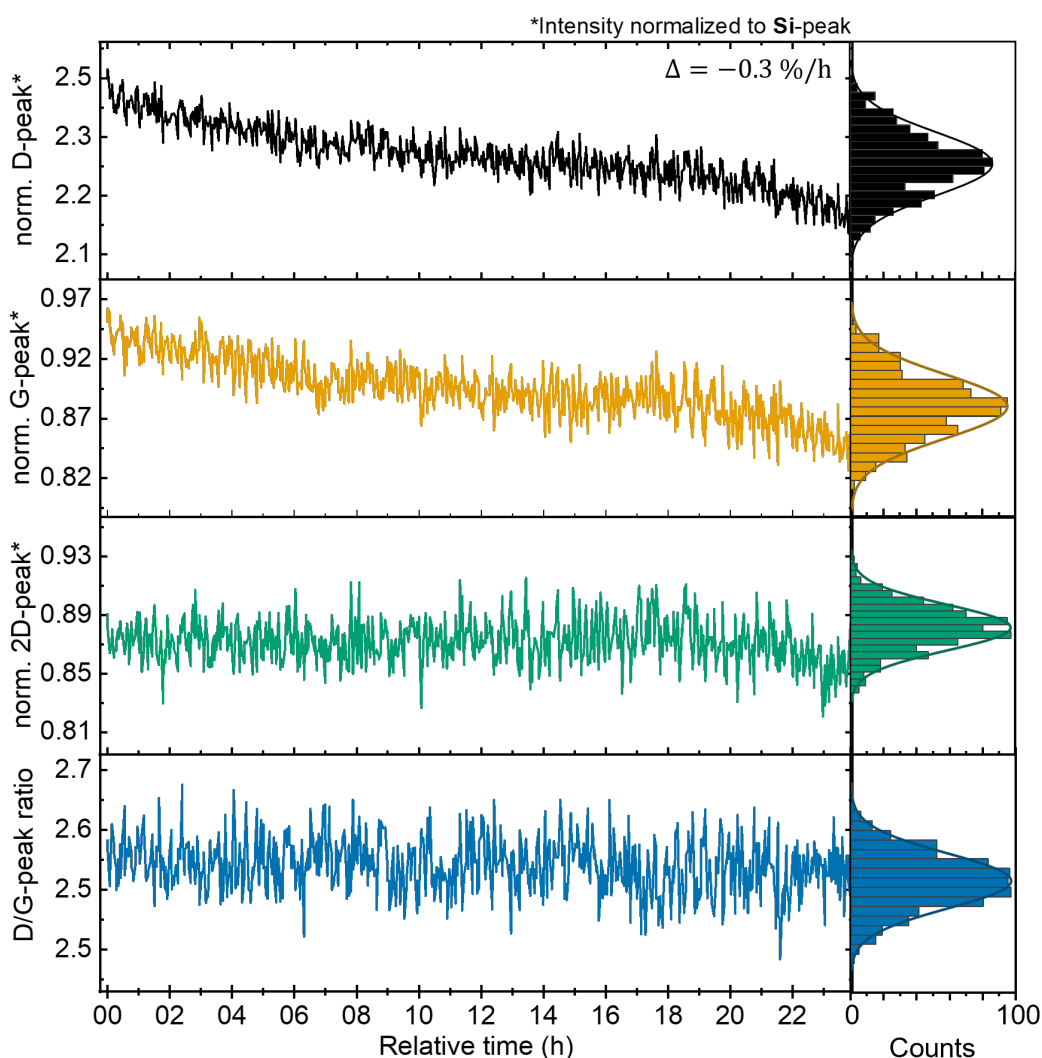
Figure 7.12.: Laser-related spectral changes in tritiated graphene. The intensities of the D-, G-, and 2D-peak are normalized to the TO-peak of $Si(O_2)$ to eliminate fluctuations of the laser power. Details can be found within the text.

7.5.5. Comparison of different graphene samples

In order to test if the measurement current supplied for the *in-situ* sheet resistance measurements affected the graphene⇔tritium interaction, Raman measurements of two different samples are compared. The comparison is made between **Sample A** and **Sample C**.

A HSR scan of a central region of **Sample C** was recorded. The Raman images and representative Raman spectra from each sample are shown in Figure 7.13. In general, the spectral changes are the same. However, a detailed analysis shows that the D-peak and G-peak intensity is consistently lower on **Sample C**, which was not contacted during the tritium exposure. From this observation, it does not necessarily follow that the origin of this difference is the measurement current. As is visible in Figure 7.2, the *secondary* samples are completely shadowed by the pin-holder, while there is an opening directly above the *primary* sample.

(a)

(b)

(c)
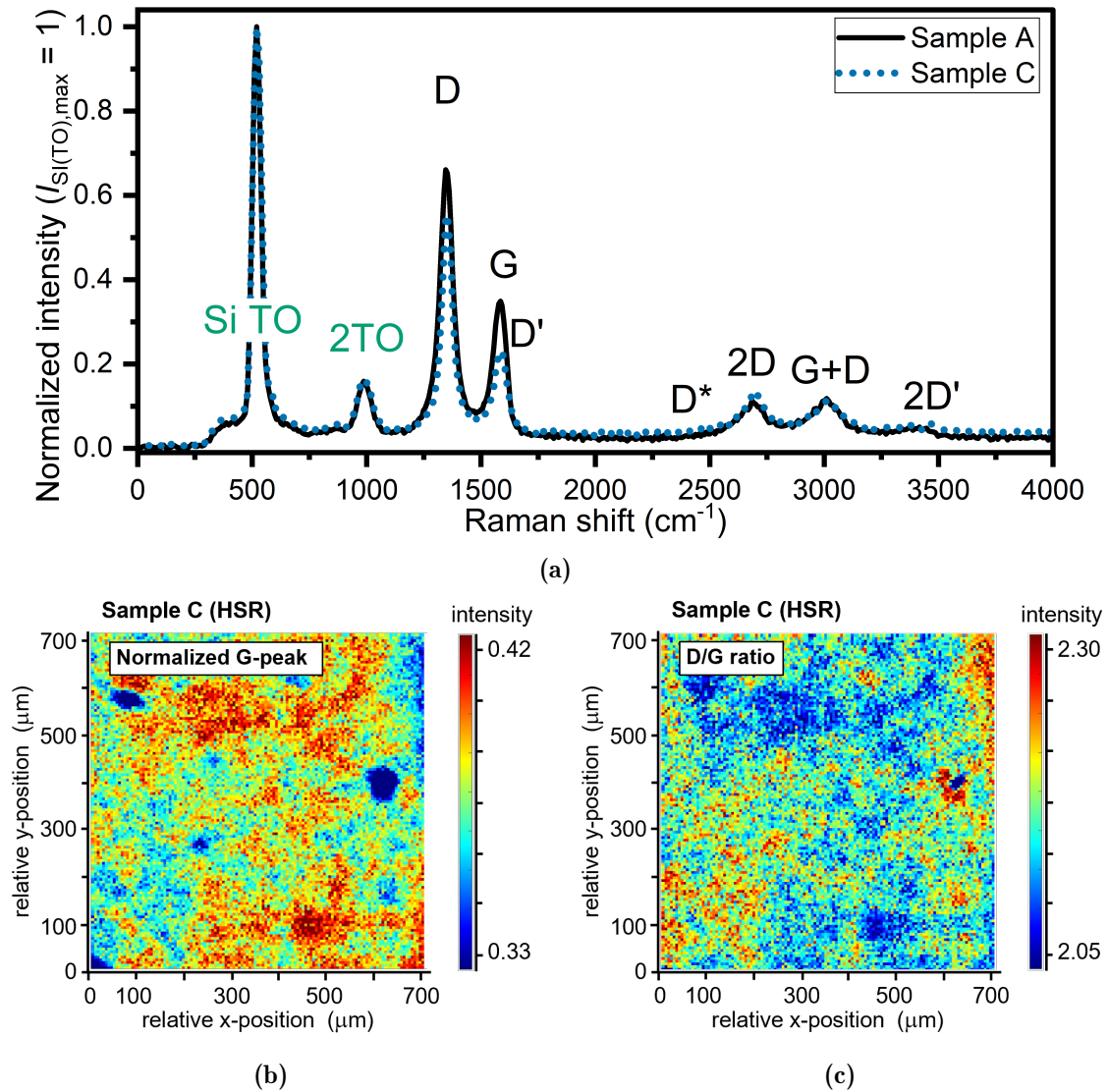
Figure 7.13.: Comparison of different tritium exposed graphene samples. **Sample A** was contacted in-situ, while **Sample C** was not contacted (see Figure 7.2): (a) representative Raman spectra, HSR scan of **Sample C** (b) map of the G-peak and (c) map of the D/G ratio. All spectra are normalized to the TO-peak of $Si(O_2)$. The HSR scan of **Sample A** is shown in Figure 7.11.

7.5.6. *Ex-situ* heating of tritium-exposed samples

As described in Section 7.3.1, the *in-situ* electrical heater had to be limited to 110°C. Due to this restriction, *in-situ* heating and desorption measurements are not possible with the loading chamber. In literature, desorption of hydrogen from graphene is only reported at temperatures above 200°C, *e.g.* Ref. [Che13]. This was confirmed during the TCR measurement of the tritiated graphene sample, described in Section 7.5.2. No significant change in sheet resistance was observed, when the sample was held at 110°C for 6 h.

Therefore, in order to demonstrate whether the changes to the graphene layer by tritium exposure are reversible, the heating at higher temperatures is conducted *ex-situ* in a tritium-compatible oven. In this oven, the graphene samples can be heated *ex-situ* to up to 1600°C. Additionally, the exhaust from the oven is passed through water bubblers, where the released tritium is retained as HTO. The tritiated water is then used to determine the total activity released during the sample heating via LIQUID SCINTILATION COUNTING (LSC). This can also provide additional information about the nature of the C↔T interaction. Before the 1st heating, the oven was flushed with Argon gas, to prevent oxidation of the graphene layer during heating. In the setup employed here, argon is flowing through a wash bottle, which saturates it with water vapor. This gas flow is connected to the pipe-oven, which comprises a ceramic tube into which the sample is placed in a boat for laboratory ceramics. The wet argon gas is heated in the pipe-oven, thus heating the sample as well. The gas and sample temperatures are not measured directly and are certainly lower than the nominal temperature of the ceramic tube of the pipe-oven. In summary, during this external thermal annealing of the samples, Ar and H_2O are present.

After each heating, a HSR scan of a $100\,\mu m \times 100\,\mu m$ area is recorded with the CRM. Because the sample contacting in the loading chamber can lead to damage to the samples, as demonstrated during the commissioning[13], it was decided to not repeat the sheet resistance measurement after the heating.

Raman microscopy

One representative Raman spectrum from the HSR scans after each step, namely for tritium exposure and after three different heating steps, is shown in Figure 7.14A. By fitting Lorentzian peak functions, graphene quality indicators - the intensity I_D/I_G and the 2D-peak width w_{2D} - are extracted from the spectra, which are shown in Figure 7.14B.

After the first heating, the I_D/I_G ratio decreases from $I_D/I_G = 1.7$ to $I_D/I_G = 1.0$, but the D-peak does not disappear completely. The 2D-peak intensity is also mostly recovered, reaching $\sim 83\,\%$ of the original value of the pristine sample, with an intensity ratio $I_G/I_{2D} = 0.6$. The width of the 2D-peak is also recovered to $w_{2D,\,rel} = 1.03$ relative to the original 2D-peak width. Both observations combined show that, the quality of the graphene film has improved again, and the defect density is reduced; in other words, the graphene sample has recovered much of its original properties.

Further heating of the sample at 300°C for 21 h leads to further reduction of the intensity ratio $I_D/I_G = 0.5$. However, the 2D-peak width is slightly increasing ($w_{2D,\,rel} = 1.05$). In a final, third step, the sample was heated for 20 h at 500°C. During this process, most of the graphene film was destroyed, and the remaining parts had an increased ratio $I_D/I_G = 0.83$, with increased D-peak intensity. It is therefore clear that with our heating setup, graphene is severely damaged at 500°C.

---

[13]P. Wiesen: 'Commissioning of a graphene-loading stage and conductivity measurements during first tritium exposure'. Bachelor's thesis. Karlsruhe: Karlsruhe Institute of Technology, 2023
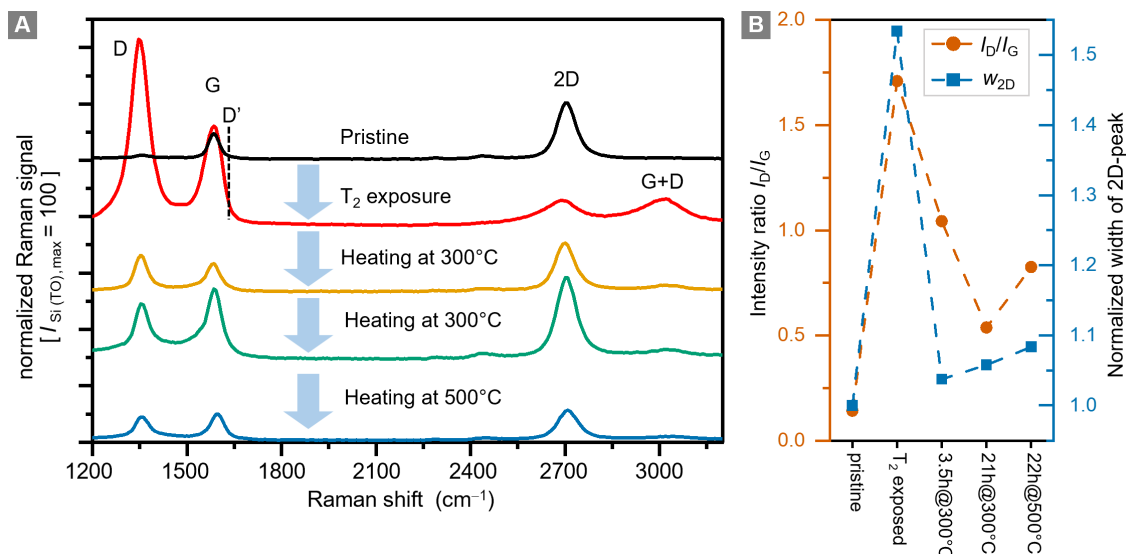
Figure 7.14.: Raman spectra after heating. A - Stacked Raman spectra of pristine, tritium-exposed, and heated graphene; B - Extracted peak parameters from the Raman spectra, namely the intensity I_D/I_G and the 2D-peak width w_{2D}. All measurements are conducted with **Sample A**. Details can be found within the text. Image adapted from [Zel23].

Total activity determination

The results from the LSC measurements are summarized in Table 7.3. The *primary* sample (**Sample A**) released several MBq of activity during each of the three thermal annealing periods. In addition, one of the *secondary* samples (**Sample B**) was placed individually in the annealing oven. The overriding goal of this sample heating was to determine the total activity of the sample. Therefore, the sample was heated in laboratory air at 1400°C for 5 h. At 1400°C any tritium adsorbed in the substrate and on the graphene layer should be completely released. The total activity was determined to be $(1.90 \pm 0.38) \times 10^7$ Bq.

However, it should be noted that, it is not clear from this measurement how much of the tritium activity was retained in the substrate itself compared to the amount of tritium on the graphene layer; this is because characterizing of the tritium retention properties of the substrate was beyond the scope of this work.

The total activity released from the *primary* sample (**Sample A**) during three consecutive heating steps is consistent with the total activity released from the *secondary* sample (**Sample B**) during heating at 1400°C. This latter procedure needs to be considered to be a 'destructive heating' as the surface is likely (irreversibly) oxidized. Based on these findings, it can be concluded that during the three successive heating steps of **Sample A**, most of the activity was released.

Table 7.3.: Activity release of tritium-exposed samples during heating.

Medium	Temperature (°C)	Duration (h)	Released activity (MBq)
*Primary sample (**Sample A** - contacted in-situ)*			
Ar + H$_2$O	300	3.5	(8.0 ± 1.6)
Ar + H$_2$O	300	21	(5.0 ± 1.0)
Ar + H$_2$O	500	22	(6.5 ± 1.3)
			$\sum = (19.5 \pm 3.9)$
*Secondary sample (**Sample B** - not contacted)*			
Air	1400	5	(19.0 ± 4.0)

7.6. Comparison to literature data from hydrogenation experiments

There are numerous studies on the hydrogenation of graphene; however, most do not report or conduct all the necessary measurements and details that would allow drawing conclusive comparisons. For example, even though Ref. [Gui14] extensively studies the effects of hydrogenation on the electronic transport properties, only a two point resistance measurement is used. Therefore, the absolute values of the sheet resistance measurement cannot be compared directly to this work with tritium with a four-point resistance measurement. Overall, the selection of suitable literature for comparison is rather limited.

Ref. [Son16] is one of the few scientific articles that fulfills all requirements. Therein, Son *et al.* demonstrated reversible hydrogenation using XPS, sheet resistance, and Raman measurements, and they reported all relevant details. Using their results, it is possible to soft-of cross-calibrate the XPS $\leftrightarrow$ sheet resistance results, and the XPS $\leftrightarrow$ Raman spectra. Their pristine graphene ('as prepared') samples have a sheet resistance of $R_\square = 631.3\,\Omega/\square$. After hydrogenation for different durations, they use XPS to quantify the hydrogen coverage η_H, and measure the sheet resistance of the samples:

$$\eta_H = 12\,\% \iff R_\square = 107.8 \times 10^3\,\Omega/\square \text{ and} \tag{7.17}$$

$$\eta_H = 25\,\% \iff R_\square = 423.1 \times 10^6\,\Omega/\square. \tag{7.18}$$

Since Son *et al.* did not use *in-situ* sheet-resistance monitoring during hydrogenation, the shape of the $\eta_H(R_\square)$ loading curve is unknown. Using (i) a linear growth model and (ii) a logistic growth model as two possible scenarios, the plateau sheet-resistance value in Figure 7.8 corresponds to

$$R_\square^\infty = 129 \times 10^3\,\Omega/\square \implies \eta_{\text{defects}} = 13 - 20\,\%. \tag{7.19}$$

It should be noted that this is an estimate of the total defect density η_{defects}, which is defined as $\eta_{\text{defects}} = \eta_{\text{vacancy}} + \eta_{\text{H or T}}$. In the work of Son *et al.*, the hydrogenation is completely reversible, as demonstrated by XPS, and thus $\eta_{\text{vacancy}} = 0 \implies \eta_{\text{defects}} = \eta_H$.

Based on their Raman spectra[14], they report the I_D/I_G ratio for six different hydrogen coverage values - $\eta_H = 0$, 12, 15, 18, 23 and 25 %. Comparing those to the $I_D/I_G = 1.7$ ratio observed after tritium exposure in this work (see Figure 7.14), this corresponds to

$$\eta_{\text{defects}} = 12 - 14\,\% \tag{7.20}$$

for the tritium-exposed samples. As shown in Figure 7.14, the intensity ratio is reduced to $I_D/I_G = 0.5$ after heating the sample for 3.5 h at 300°C. Assuming that the adsorption of tritium is reversible, while vacancy-type defects are not completely reversible, this leads to

$$\eta_T \approx 7.4 - 8.7\,\% \tag{7.21}$$

and

$$\eta_{\text{vacancy}} \approx 4.6 - 5.3\,\%. \tag{7.22}$$

However, from discussions in the literature, it is not clear if this assumption is valid. Chen et al. [Che13] have demonstrated 'self-healing' of graphene by thermal annealing, after initial Ar^+-ion bombardment. In their study, the reduction of the I_D/I_G ratio is even more pronounced, with a minimal value of about $I_D/I_G = 0.25$, after annealing at 800°C. However, the relative width of the 2D-peak is increasing significantly (factor > 2) when the annealing temperature exceeds 300°C. This indicates a graphene layer whose quality has worsened.

At similar intensity ratios in comparison to those of Chen et al. [Che13], namely $I_D/I_G \approx 0.5$, here only an increase of the 2D-peak width by a factor of about 5 %, after thermal annealing, for a total of 24 h at 300°C (Figure 7.14). Thus, the quality of the graphene layer is better after the combination of 'tritium exposure + thermal annealing' compared to 'Ar^+-ion bombardment + thermal annealing'.

The above estimate ($\eta_T \approx 7.4 - 8.7\,\%$), obtained under the assumption that vacany-type defects are not reversible, is therefore not accurate and likely overestimates the tritium coverage. Nevertheless, these observations indicate that the change in the Raman spectra seen after thermal annealing exceed the expected effects if self-healing were the only mechanism in play and show that there is a significant tritium coverage of a few percent.

7.7. Concluding remarks

A loading chamber for the exposure of graphene samples to tritium gas was set up, commissioned, and used in a first graphene-loading experiment. For this proof-of-concept experiment, the self-radiolysis of tritium is taken advantage of. In the loading chamber, a graphene sample can be contacted with spring-loaded contacts for *in-situ* sheet resistance monitoring. This is crucial for graphene-loading experiments with tritium because this is the first time these experiments are conducted. Therefore, critical experimental parameters, like the timescale of the loading process, were unknown prior to this work. It was observed that the sheet-resistance reaches a plateau after 55 h of tritium exposure at 400 mbar. In the future, these parameters can be used as an input for tritium↔graphene simulations and for the planning of follow-up experiments.

During the commissioning of the loading chamber, it was found that the setup is not suitable for *in-situ* high-temperature thermal annealing for desorption measurements. Systematic investigations suggest that the thermal movement of the spring-loaded contacts causes severe damage to the graphene layer. The electrical connection of the contacts with

---

[14]It is not known whether their Raman system was calibrated for spectral intensities.

graphene is broken, and sheet-resistance measurements are not possible any longer. The temperature of the heating element had to be limited to 110°C to minimize the damage and the occurrence of this problem. As a consequence, the thermal annealing had to be done *ex-situ*, without *in-situ* sheet resistance measurement, in a tritium compatible oven.

The second generation of the loading chamber has to be improved in this regard - some suggestions were already made by P. Wiesen[15]. In short, the movement of the graphene samples and the spring-loaded contact needs to be limited. Additionally, the graphene layer needs to be protected from damage by the spring-loaded contacts, which could be achieved by bonding gold contact areas in the corner of the graphene samples. Lastly, the insertion and extraction of the graphene sample needs to be improved and made simpler to facilitate even easier handling in a glove box.

After tritium-exposure, the graphene samples were characterized with the CRM described in Section 4.2 (key points of its commissioning can be found in Chapter 6). By analysis of the changes in the Raman spectra of tritiated graphene, in comparison to a pristine graphene sample, the characteristic spectral changes were identified. The spectral changes agree with changes observed in experiments of hydrogen-loading, reported by other groups. Using the CRM, the spectral changes after *ex-situ* thermal annealing of the tritium exposed graphene samples were studied; it was found that the spectral changes are partially reversible, consistent with hydrogenation experiments.

Combining the sheet-resistance measurements, the Raman spectra, and thermal annealing, the results could be compared to hydrogen loading experiments from other groups (for the latter hydrogen coverage was quantified by XPS). From this, it was concluded that the exposure of graphene to tritium leads to a significant tritiation (formation of sp^3-type C-T bonds) with at least 2-3 % tritium coverage. These results are summarized in a journal manuscript, which is under review; a pre-print is available in Ref. [Zel23].

---

[15]P. Wiesen: 'Commissioning of a graphene-loading stage and conductivity measurements during first tritium exposure'. Bachelor's thesis. Karlsruhe: Karlsruhe Institute of Technology, 2023

8. Summary and Outlook

8.1. Summary

Neutrinos are fermions which - as described in the Standard Model of particle physics (SM) - only interact via the weak force. In the SM neutrinos are described as massless. However, since the discovery of neutrino flavor oscillations, it is known that a distinct pattern of non-zero neutrino masses exists. Furthermore, their masses are important parameters in the formation of structure in the early universe. Yet, the masses of neutrinos are so small that they have still to be measured experimentally.

The Karlsruhe Tritium Neutrino (KATRIN) experiment is designed to probe the effective electron neutrino mass $m(\nu_e)$ with previously unattained precision. In the experiment, electrons emitted from the β-decay of tritium are observed, and the end-point spectrum of these electrons is analyzed, to determine the neutrino mass. The current best upper limit of

$$m(\nu_e) \leq 0.8\,\text{eV}$$

was achieved by the KATRIN collaboration based on an initial data set [Ake22b; PDG22]. It is planned to operate KATRIN in its current configuration until 2025 with the aim to reach a final sensitivity of better than $0.3\,\text{eV}$ (90 % C.L.), after a total measurement time of 1000 days [Mer23; Rod23; Lok23].

A central ingredient of KATRIN is tritium, a hydrogen isotope which undergoes β-decay. Handling tritium poses significant challenges due to (i) its radioactivity and (ii) the need for extreme purity and stability in the experimental setup. Any unaccounted changes in the molecular tritium source gas composition can have significant effects on the neutrino mass measurements. Thus, the monitoring and management of tritium are pivotal to KATRIN's success. For this purpose, Raman spectroscopy, a powerful method for molecular analysis, is employed at KATRIN in the form of an in-line Laser Raman (LARA) system. This system provides detailed information about the composition of the tritium gas injected into in the WGTS. Within the framework of this thesis, significant contributions have been made to the gas monitoring by addressing questions regarding the long-term metrological performance of the LARA system within KATRIN requirements.

Beyond the state-of-the-art KATRIN molecular tritium source (the Windowless Gaseous Tritium Source (WGTS)), atomic tritium sources are a subject of increasing scientific interest [Mon15; Pro22; Mer23]. In addition to gaseous atomic tritium sources, tritium

chemically bound to graphene is suggested as a (quasi)-atomic solid-state tritium source and target [Bet13; Bet19b]. This presents a potential application for Raman spectroscopy: It can be used to characterize the tritium-graphene interaction with a Raman system that is suitable for the chemical analysis of tritiated samples. Within the framework of this thesis, a CONFOCAL RAMAN MICROSCOPE (CRM) was designed, set up, and characterized in collaboration with partners from the UNIVERSIDAD AUTÓNOMA DE MADRID (UAM). The CRM was used for first quantitative studies of tritiated graphene samples in order to demonstrate the suitability of such a system for the envisaged applications.

Raman spectroscopy for the monitoring of continuous tritium gas flows

For the KATRIN experiment to reach its goal, the composition of the gas injected into the WGTS needs to be monitored continuously. An ideal source would contain only pure tritium; however, for technical reasons all six hydrogen isotopologues (T_2, DT, D_2, HT, HD and H_2) are present in the source in different and varying molar fractions. Most important for the KATRIN experiment are the tritium purity ϵ_T and the HT/DT-ratio κ because the three tritium-containing molecules T_2, DT, and HT, can all undergo β-decay and contribute to the measured signal. A number of systematic uncertainties depend on the mass of the decaying molecule, which necessitates the monitoring of the composition parameters, ϵ_T and κ, throughout the neutrino mass measurements. From the total systematic uncertainty budget of the KATRIN experiment requirements on the precision and trueness of the monitoring arise, namely a precision of $\leq 0.1\,\%$ on ϵ_T, and a trueness of $\leq 3\,\%$ on ϵ_T and of $\leq 10\,\%$ on κ, respectively.

In KATRIN, a LARA system is employed for this purpose. This system, which evolved over many years at the TLK, can monitor all six hydrogen isotopologues simultaneously and continuously with a precision of $\leq 0.1\,\%$ within 60 seconds of acquisition time per Raman spectrum [Stu10b; Stu10a; Fis11; Fis14]. From these Raman spectra the species concentrations are extracted. In order to do this quantitatively and to fulfill the trueness requirements, two calibration entities are required. For one, the molecule-specific theoretical intensities are needed [Roy11; Sch14; Nie21a; Nie21b]. Second, from the experimental side, calibration of the LARA system is required. This is achieved using the reference standard SRM 2242 provided by NIST to determine the wavelength-dependent spectral sensitivity of the system [Rup12; Sch14; Sch15b; Zel17].

Remaining questions to verify that the LARA system meets KATRIN requirements were addressed within the framework of these studies, namely:

- It was shown that the LARA system can reach the necessary precision even for very low tritium purity ($\epsilon_T \leq 1\,\%$) by combining the Raman-spectroscopic results with the activity monitoring from the FORWARD BEAM MONITOR (FBM). This was used to facilitate the analysis of β-spectra from the 'VERY FIRST TRITIUM' (VFT) and 'FIRST TRITIUM' (FT) campaigns in 2018.

- The hardware and software of the LARA system can be operated for months at a time with minimal unplanned downtime of only about $0.5\,\%$. There was no significant deterioration of the hardware components; over the more than five years of operation only the CCD detector was exchanged preemptively, and the internal mechanical shutter of the spectrometer had to be disabled.

- The SRM 2242 standard material can be used for the intensity calibration of the LARA system, even though its certification expired at the end of 2018. This is an important insight because only one year after the expiration of the certification, the new SRM 2242a was released by NIST in 2019; therefore for this timespan,

no certified reference material was available. Further complicating this subject, the SRM 2242a was released with a new form factor, making it incompatible to use with the existing hardware of the calibration cell. Furthermore, the SRM 2242a certificate is going to expire on 31 December 2024, one year before the end of the KATRIN operation with the current configuration, with no clear future prospects as to when and if a newly certified SRM will be released. Once the SRM 2242a became available, it was used to recalibrate the older SRM 2242. It was found that the spectral sensitivity of the overall system changed only insignificantly in three years of operation at KATRIN, without changes to the system.

By addressing these remaining questions, the LARA system could be operated over the more than five years of the KNM1-11 campaigns within the bounds of the KATRIN requirements. On average, the achieved metrological performance was

$$\frac{\Delta\epsilon_{\mathrm{T}}}{\bar{\epsilon}_{\mathrm{T}}} \leq 1.7 \times 10^{-4} \quad \text{(precision)},$$

$$\frac{\Delta\epsilon_{\mathrm{T}}}{\bar{\epsilon}_{\mathrm{T}}} \leq 8.3 \times 10^{-4} \quad \text{(trueness), and}$$

$$\frac{\Delta\kappa}{\bar{\kappa}} \leq 6.0 \times 10^{-2} \quad \text{(trueness)},$$

with

$$\bar{\epsilon}_{\mathrm{T}} = (98.41 \pm 0.45)\,\% \quad \text{and} \quad \bar{\kappa} = 2.54 \pm 1.10,$$

thus surpassing the KATRIN requirements by at least a factor of 1.5. The excellent stability of the optical assembly, the optics employed and the used hardware components results in a stable operation, as indicated by the quality of the spectra, and a stable spectral sensitivity over many years. This demonstrates that the LARA system is set to fulfill all requirements in the upcoming measurement campaigns.

Raman spectroscopy for tritium-graphene interactions

As stated earlier, tritium bound on graphene was suggested as a possible solid-state (quasi)atomic tritium source / target. The interest in atomic tritium sources arises from the fundamental limitations on the neutrino mass measurement that are associated with the use of molecular tritium as a source of β-electrons. After the β-decay of the tritium in the molecule, the daughter molecule is left in a manifold of excited ro-vibrational states. The relative population of these energy states is known as the FSD, and can be calculated *a priori* [Sae00]. The molecular FSD of the ground-state rotational and vibrational manifold of the daughter molecule has a standard deviation $\sigma_{\mathrm{FSD}} \approx 0.4\,\mathrm{eV}$ [Sae00; Bod15], thus limiting the sensitivity of the neutrino mass measurement. Even with an unprecedented 1 % theoretical uncertainty on the molecular tritium FSD, a molecular source still would limit the sensitivity to about 0.1 eV [Pro22; Hey23].

A (quasi-) atomic tritium source would avoid these limitations. Although theoretical calculations suggest that the improvement with tritiated graphene is less than initially envisioned [App22; Nus22], the study of tritiated graphene is still a first building block for more complex systems with, *e.g.*, carbon nanotubes or nanoporous graphene. In this context, the exploration of tritium-graphene interactions extends beyond current neutrino experiments and the current experimental setup of the KATRIN experiment, opening a new R&D field within KATRIN.

In this work, the versatility and analytical power of Raman spectroscopy is used to study tritium-graphene interactions for the first time. For this purpose, the CRM was used in

combination with complementary methods, namely sheet resistance monitoring and thermal annealing, to gain a first, qualitative understanding of the tritium-graphene interaction.

In a first controlled exposure of graphene to tritium in a dedicated loading system, *in-situ* sheet resistance measurements via the VAN DER PAUW method were used to monitor the tritium-graphene interaction [Pau58]. In these studies, it was found that the sheet resistance reaches a plateau in a chemical equilibrium, after about 55 h of exposure to about 400 mbar of tritium. When deriving the TEMPERATURE COEFFICIENT OF RESISTANCE (TCR) of the graphene samples prior to tritium exposure, and after tritium exposure, it was found that the graphene changes from a metal-like behavior to an insulator-like behavior. Thereafter, the tritium-exposed graphene samples were characterized *ex-situ*. The main results from these measurements are:

- Graphene on a Si/SiO_2 substrate can withstand the bombardment with ions and electrons in the cold-tritium plasma that is created by the self-radiolysis of a tritium gas mixture. The graphene lattice remains intact, without any large scale ($\geq 7\,\mu m$) disintegration and destruction of graphene.

- On the one hand, tritium exposure leads to a rather homogenous (maximum variation of 2-5 %) increase in the defect density across the whole $1\,cm^2$ graphene sample. On the other hand, microscopically, the increase in the defect density turned out to be significant, with a defect coverage of 12-14 %.

- By alternating the CRM scans with thermal annealing of the samples, the nature of the defects could be identified. It was found that at least 2-3 % of the defects are adsorbed tritium atoms, with the remaining defects consisting of vacany-type defects (missing carbon atoms).

In summary, it was demonstrated that the CRM in its current configuration is well suited for first, qualitative experiments with graphene and tritium. The system is fully characterized and well understood, enabling comparison with literature results from other groups. The CRM was used for several measurements and studies on graphene and RW samples, some of which were published in Ref. [Dia22].

By using graphene as a first tritiation sample, it has now been successfully demonstrated that Raman spectroscopy in the form of the CRM can be used for the investigation of radioactive (tritiated) samples at a total sample activity of up to $1 \times 10^{10}\,Bq$. These results are summarized in a journal manuscript, which is under review; a pre-print is available in Ref. [Zel23].

8.2. Outlook

Monitoring of continuous tritium gas flows

The long-term ($\geq$ five years) operation, and intensity calibration performed over the time span of this work, has provided answers to some still-open questions regarding the KATRIN LARA system. With these insights, the KATRIN LARA system is deemed to operate within specifications for at least until the end of the KATRIN data taking in the current experimental configuration. It is anticipated that the LARA system will continue to be used beyond that phase.

Once the TRISTAN detector is installed after 2025 [TRI21; Mer23], β-spectroscopy measurements will continue to initially be carried out with molecular tritium, and therefore the monitoring of the gas composition will still be necessary to reduce systematic uncertainties. The LARA system is also well-equipped for that new task, and will be able to operate within the requirements.

Study of tritium-graphene samples / interactions

With the achieved results within this work, the CRM was established as a new system for the study of tritium-graphene interactions at the TLK. Going forward, there are two main opportunities for improving the system and the method.

First, in the near future, the spectrometer of the CRM will be equipped with a higher-resolution grating. This will enable to determine the nature of the graphene defects directly from the high-spectral resolution Raman spectra without the need for *ex-situ* annealing of the samples.

Second, as the CRM was designed with high flexibility and adaptability in mind, in the more distant future, the CRM or a system based on the CRM can be modified to either (i) be set up in a glove box so that the tritiated samples no longer need to be exposed to the laboratory atmosphere and can have a higher activity; or (ii) allow for *in-situ* Raman microscopy on the graphene sample during exposure. The latter would allow for monitoring the evolution of the different defect types on the graphene surface live with near-real time resolution of 5-20 s. This would open up not only possibilities to better understand the tritium-graphene interaction, but also the cold tritium plasma itself.

The tritiated graphene samples that were produced as part of this work are currently being analyzed with regard to the stability of the tritium-graphene bond, using the CRM and outgassing measurements. If they prove to be sufficiently stable to not permanently contaminate every system they are installed in, they will be used in the near future to measure the β-electron spectrum of decaying tritium bound to graphene using suitable detectors.

Appendices

A. Uncertainty propagation

In general, the combined uncertainty on a function $f(x_i)$ can be calculated by 'Gaussian' uncertainty propagation, which is given by (see *e.g.* Ref. [BIP08; Sch15c]:

$$\Delta f(x_i) = \sqrt{\sum_i c_i \cdot \Delta x_i} = \sqrt{\sum_i \left(\frac{\partial f}{\partial x_i} \cdot \Delta x_i \right)^2} \tag{A.1}$$

with

$$\Delta f(x_i) : \text{Combined uncertainy of } f(x_i) \tag{A.2}$$

$$\Delta x_i : \text{Uncertainty of the input quantity } x_i \tag{A.3}$$

$$c_i = \frac{\partial f}{\partial x_i} : \text{Sensitivity coefficient of of the input quantity } x_i \tag{A.4}$$

HT/DT-ratio κ

For the HT/DT-ratio $\kappa \frac{N_{\mathrm{HT}}}{N_{\mathrm{DT}}}$, this results in:

$$\Delta \kappa = \sqrt{\left(\frac{\partial \kappa}{\partial N_{\mathrm{HT}}} \Delta N_{\mathrm{HT}} \right)^2 + \left(\frac{\partial \kappa}{\partial N_{\mathrm{DT}}} \Delta N_{\mathrm{DT}} \right)^2} \tag{A.5}$$

$$= \sqrt{\left(\frac{1}{N_{\mathrm{DT}}} \Delta N_{\mathrm{HT}} \right)^2 + \left(\frac{-N_{\mathrm{HT}}}{N_{\mathrm{DT}}^2} \Delta N_{\mathrm{DT}} \right)^2}. \tag{A.6}$$

This equation can be futher simplified, when caluclating the relative uncertainty:

$$\delta \kappa = \frac{\Delta \kappa}{\kappa} = \sqrt{\left(\frac{\Delta N_{\mathrm{HT}}}{N_{\mathrm{HT}}} \right)^2 + \left(\frac{\Delta N_{\mathrm{DT}}}{N_{\mathrm{DT}}} \right)^2} = \sqrt{\delta N_{\mathrm{HT}}^2 + \delta N_{\mathrm{DT}}^2}. \tag{A.7}$$

Thus, the relative uncertainty $\delta \kappa$ is only dependent on the relative uncertainties $\delta N_{\mathrm{HT, \, DT}}$.

Tritium purity ϵ_T

For the tritium purity ϵ_T,

$$\epsilon_\mathrm{T} = \frac{N_{\mathrm{T}_2} + \frac{1}{2}(N_\mathrm{DT} + N_\mathrm{HT})}{N_{\mathrm{T}_2} + N_\mathrm{DT} + N_\mathrm{HT} + N_{\mathrm{D}_2} + N_\mathrm{HD} + N_{\mathrm{H}_2}} \equiv \frac{N_{\mathrm{T}_2} + \frac{1}{2}(N_\mathrm{DT} + N_\mathrm{HT})}{\sum_i N_i}, \tag{A.8}$$

this results in:

$$\Delta\epsilon_\mathrm{T}^2 \approx \left(\frac{\partial\epsilon_\mathrm{T}}{\partial N_{\mathrm{T}_2}}\right)^2 \Delta N_{\mathrm{T}_2}^2 + \left(\frac{\partial\epsilon_\mathrm{T}}{\partial N_\mathrm{DT}}\right)^2 \Delta N_\mathrm{DT}^2 + \left(\frac{\partial\epsilon_\mathrm{T}}{\partial N_\mathrm{HT}}\right)^2 \Delta N_\mathrm{HT}^2 \tag{A.9}$$

$$+ \left(\frac{\partial\epsilon_\mathrm{T}}{\partial N_{\mathrm{D}_2}}\right)^2 \Delta N_{\mathrm{D}_2}^2 + \left(\frac{\partial\epsilon_\mathrm{T}}{\partial N_\mathrm{HD}}\right)^2 \Delta N_\mathrm{HD}^2 + \left(\frac{\partial\epsilon_\mathrm{T}}{\partial N_{\mathrm{H}_2}}\right)^2 \Delta N_{\mathrm{H}_2}^2. \tag{A.10}$$

Looking at symmerty in Eq. A.8, one finds that the sensitivity coefficients can be summarized as

$$a := \frac{\partial\epsilon_\mathrm{T}}{\partial N_{\mathrm{T}_2}}, \tag{A.11}$$

$$b := \frac{\partial\epsilon_\mathrm{T}}{\partial N_\mathrm{DT}} = \frac{\partial\epsilon_\mathrm{T}}{\partial N_\mathrm{HT}} \text{ and} \tag{A.12}$$

$$c := \frac{\partial\epsilon_\mathrm{T}}{\partial N_{\mathrm{D}_2}} = \frac{\partial\epsilon_\mathrm{T}}{\partial N_\mathrm{HD}} = \frac{\partial\epsilon_\mathrm{T}}{\partial N_{\mathrm{H}_2}}, \tag{A.13}$$

and thus

$$\Delta\epsilon_\mathrm{T}^2 = a^2 \cdot \Delta N_{\mathrm{T}_2}^2 + b^2 \cdot (\Delta N_\mathrm{DT}^2 + \Delta N_\mathrm{HT}^2) \tag{A.14}$$

$$+ c^2 \cdot (\Delta N_{\mathrm{D}_2}^2 + \Delta N_\mathrm{HD}^2 + \Delta N_{\mathrm{H}_2}^2). \tag{A.15}$$

The sensitivity cooefficients are

$$a = \frac{1}{\sum_i N_i} - \frac{N_{\mathrm{T}_2} + \frac{1}{2}(N_\mathrm{DT} + N_\mathrm{HT})}{(\sum_i N_i)^2} \tag{A.16}$$

$$= \frac{\frac{1}{2}(N_\mathrm{DT} + N_\mathrm{HT}) + N_{\mathrm{D}_2} + N_\mathrm{HD} + N_{\mathrm{H}_2}}{(\sum_i N_i)^2}, \tag{A.17}$$

$$b = \frac{1}{2(\sum_i N_i)} - \frac{N_{\mathrm{T}_2} + \frac{1}{2}(N_\mathrm{DT} + N_\mathrm{HT})}{(\sum_i N_i)^2}, \text{ and} \tag{A.18}$$

$$= \frac{-(N_{\mathrm{T}_2} - N_{\mathrm{D}_2} - N_\mathrm{HD} - N_{\mathrm{H}_2})}{2(\sum_i N_i)^2} \tag{A.19}$$

$$c = \frac{-(N_{\mathrm{T}_2} - \frac{1}{2}N_\mathrm{DT} - \frac{1}{2}N_\mathrm{HT})}{(\sum_i N_i)^2}. \tag{A.20}$$

Here, even the relative uncertainty $\delta\epsilon_\mathrm{T}$ is dependent on the value of ϵ_T.

B. MATLAB code for generating Raman images

This section contains the `MATLAB` scripts used for the creation of the Raman maps shown in this work, *e.g.* Figure 7.11. Note that the scripts have not been revised for readability and other purposes, and are shared '*as-is*' as part of good scientific practice for reproducibility of the results. The Raman data sets can be requested and will be shared upon reasonable request. The necessary software packages are summarized in Table B.1.

Table B.1.: Overview of MATLAB software, functions, and scripts.

Software	Comment
MATLAB*	Version R2022a
Image Processing Toolbox Hyperspectral Imaging Library*	version 22.1.0
Image Processing Toolbox*	version 11.5
Parallel Computing Toolbox*	version 7.6
function to load and prepare data	loadData.m
function to fit Lorentzian to data	From Ref. [Wel23]
full script (minimal working example)	HeatmapScript.m

(*) Mathworks Inc., Natick, Massachusetts, United States

loadData.m

```matlab
function [data, ramanImage, ramanCube, xCoordinate, ...
    yCoordiante, backgroundArray] = ...
    loadData(dataDir, d, nFiles, Wavenumbers, pixelCutOff, ...
        correctBackground, normalizeData)
    xCoordinate = zeros(1,numel(nFiles));
    yCoordiante = zeros(1,numel(nFiles));
    data=cell(1,nFiles);
    cd(dataDir)
    parfor i=1:nFiles
        data{i} = readmatrix(d(i).name);   % read each file
        data{i}=data{i}(pixelCutOff:end);
        cood_string = strsplit(d(i).name,'_');
        cood_string = str2double(cood_string);
        xCoordinate(i) = double(cood_string(1))/1000;
        yCoordiante(i) = double(cood_string(2))/1000;
        backgroundArray(i) = mean(background);
    end
    data=cell2mat(data);
    if normalizeData == true; data = normalize(data,'norm');
        end
    ramanImage = data;
    for i=1:size(ramanImage,1)
        ramanImage2(1,:,i) = ramanImage(i,:);
    end
    ramanImage = ramanImage2;
    ramanCube = hypercube(ramanImage,Wavenumbers);
    clearvars ramanImage2
    data=[Wavenumbers,data];
    toc
end
```

HeatmapScript.m

```matlab
%% Init
mfilePath = mfilename('fullpath');
if contains(mfilePath,'LiveEditorEvaluationHelper')
    mfilePath = matlab.desktop.editor.getActiveFilename;
end
[mfilePath, fName, fExt] = fileparts(mfilePath);
disp(mfilePath);

pixel = 1; %Select a pixel to check different effects
nFiles = 0; % 0 = all
comparePixel =[2 5];
nPreviewFiles = 5000;

wavelengthPath = ⟨path to wavelength calibration file⟩;
waveNumberCutOff = 300; %in cm-1
wavenumbers = readWavenumbers(wavelengthPath);
pixelCutOff = interpolateArray(wavenumbers, waveNumberCutOff);
wavenumbers = wavenumbers(pixelCutOff:end);
clearvars peakRanges;
peakNames = ["Si" "D" "G" "2D"];
waveNumbers2Crop = [[500 650];[1200 1500]; [1550 1800]; [2600
    2800]]; %in cm-1
for i=1:size(waveNumbers2Crop,1)
    peakRanges(i,:) = {interpolateArray(wavenumbers,
        waveNumbers2Crop(i,1)) : ...
    interpolateArray(wavenumbers, waveNumbers2Crop(i,2))};
end

readData = true;
correctBackground = false;
normalizeData = false;

dataDir = ⟨path to data⟩;
outputDir = ⟨path to output folder⟩;
mkdir(outputDir);
d = dir(dataDir + "\*_*_*.csv");
nFiles = useAllFiles(nFiles,d);
nPreviewFiles = setMaxPreviewFiles(nPreviewFiles, nFiles);
%% Read data
if readData == true, [data, ramanImage, ramanCube, xCoordinate
    , yCoordinate, backgroundArray] = ...
    loadData(dataDir, d , nFiles, wavenumbers, pixelCutOff,
        correctBackground, normalizeData);end
cd(mfilePath)
RawSpectraMatrix = data(1:end, 2:end)';




%%
```

```matlab
48  % Preview first n Plots
49  figure('Name',sprintf('Preview of first %0.f spectra',
        nPreviewFiles),'NumberTitle','off');hold on;
50  for n=1:nPreviewFiles
51      plot((wavenumbers), RawSpectraMatrix(n,:),'linewidth',
            1.5);
52  end
53  xlabel("Raman shift in cm^{-1}")
54  ylabel("Intensity in arb. units")
55  hold off;
56
57  RawSpectraMatrix=data(1:end, 2:end)';
58  RawSpectraMatrix=RawSpectraMatrix';
59  %%
60  hold on;
61  for i=comparePixel
62      plot((wavenumbers), RawSpectraMatrix(:,i),'linewidth',
            2.5);
63  end
64  for i=1:size(peakRanges,1)
65      plot(wavenumbers(peakRanges{i}), RawSpectraMatrix(
            peakRanges{i},pixel),'linewidth', 2.5);
66  end
67  ylim([min(RawSpectraMatrix(:,pixel)) max(RawSpectraMatrix(:,
        pixel))])
68  xlim([min(wavenumbers) max(wavenumbers)])
69  xlabel("Raman shift in cm^{-1}")
70  ylabel("Intensity in arb. units")
71  for j=1:size(peakRanges,1)
72      [LFit, fitResults]= lorentzfit(wavenumbers(peakRanges{j}),
            ...
73          RawSpectraMatrix(peakRanges{j},pixel), [], [], '3c',
                optimset('Display','off'));
74      position = fitResults(2);
75      fwhm = sqrt(fitResults(3));
76      offset = fitResults(4);
77      area = sum(LFit-offset);
78      plot(wavenumbers(peakRanges{j}), LFit ,'-x', Color='black'
            )
79  end
80  exportgraphics(gcf,outputDir+"\"+sprintf("Spektrum-%d.png",
        pixel),'Resolution','600');
81  saveas(gcf,outputDir+"\"+sprintf("Spektrum-%d.fig",pixel))
82  %%
83  %Init empty zero-arrays
84  peakArea     = zeros(numel(peakRanges),numel(xCoordinate));
85  peakPosition= zeros(numel(peakRanges),numel(xCoordinate));
86  peakWidth    = zeros(numel(peakRanges),numel(xCoordinate));
87  peakOffset   = zeros(numel(peakRanges),numel(xCoordinate));
88  pixels       = 1:length(xCoordinate);
89
90  %%Analyse data
```

```matlab
 91  tic
 92  for jPeak=1:size(peakRanges,1)
 93      x = wavenumbers(peakRanges{jPeak});
 94      y = RawSpectraMatrix(peakRanges{jPeak} , : );
 95      parfor iFile=1:nFiles
 96          [LFit, fitResults] = lorentzfit(x , y(:,iFile) , [],
                  [], '3c', optimset('Display','off'));
 97          peakPosition(jPeak,iFile) = fitResults(2);
 98          peakWidth(jPeak,iFile) = sqrt(fitResults(3));
 99          peakOffset(jPeak,iFile) = fitResults(4);
100          peakArea(jPeak,iFile) = sum(LFit-fitResults(4));
101          if mod(iFile, 500) == 0; disp(iFile); end
102      end
103  end
104  toc
105
106  %%Plot data
107  peakParameter = peakArea;
108  for i=1:size(peakRanges,1)
109      figure('Renderer', 'painters', 'Position', [10 200 900
                  700], 'Name',sprintf('Heatmaps %s', peakNames(i)),'
                  NumberTitle','off');
110      fig = scatter(xCoordinate',yCoordinate,25,peakParameter(i
                  ,:),"filled",'s');
111      xlim([quantile(xCoordinate,0.01) , quantile(xCoordinate
                  ,0.99)]);
112      ylim([quantile(yCoordinate,0.01) , quantile(yCoordinate
                  ,0.99)]);
113
114      xlabel({'position (in steps)'})
115      ylabel({'position (in steps)'})
116      set ( gca, 'xdir', 'reverse' )
117      c = colorbar;
118      c.Label.String = sprintf("%s-peak intensity (arb. units)",
                  peakNames(i));
119      colormap jet
120      clim([quantile(peakParameter(i,:),0.05) , quantile(
                  peakParameter(i,:),0.95)])
121
122      exportgraphics(gcf,outputDir+"\"+sprintf("Heatmaps-%s.tiff
                  ",peakNames(i)),'Colorspace','gray');
123      exportgraphics(gcf,outputDir+"\"+sprintf("Heatmaps-%s.png
                  ",peakNames(i)),'Resolution','600');
124
125  end
126
127  %% Helper functions %%%%
128  function wavenumbers = readWavenumbers(wavelengthPath)
129      wavelength = readmatrix(wavelengthPath);
130      wavenumbers = 1e7*(1/532 - 1./wavelength);
131  end
132
```

```
133  function [nFiles]=useAllFiles(nFiles, allFiles)
134      if nFiles == 0
135          nFiles = length(allFiles);
136      end
137  end
138
139  function [nPreviewFiles]=setMaxPreviewFiles(nPreviewFiles,
         nFiles)
140      if nPreviewFiles > nFiles
141          nPreviewFiles = nFiles;
142      end
143  end
144  function [xIndex] = interpolateArray(array, yValue)
145      xIndex = fix(interp1(array,find(array),yValue));
146  end
```

C. Matchbox laser manufacturer test report

Integrated Optics, UAB
Company code: 302833442
VAT No: LT100007179012
https://integratedoptics.com
info@integratedoptics.com

PART NUMBER   0532L-15B-NI-PT-NF

ITEM NAME   532 NM LASER (DPSS; PM FIBER)

LASER TEST REPORT
S/N 913532

Spectrum and Polarization

Center wavelength	Spectral width	Polarization extinction ratio
532.08 nm	<0.025 nm	21 dB

NOTE! The resolution of HighFinesse LSA Standard is 20 pm (400 to 600 nm) and 30 pm (600 to 1100 nm). Indicated spectral width is based on internal calculation algorithm of the spectrum analyzer, which can't calculate beyond 5 pm. Dynamic range of the OSA is about 20 dB.

OSA measurement:
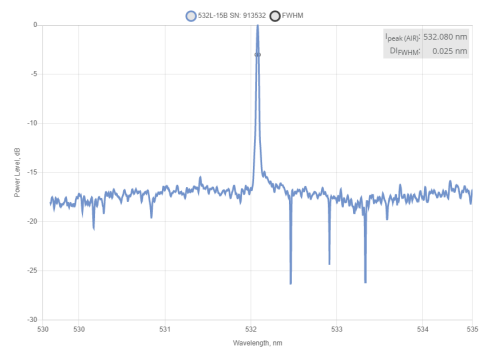
Power Stability

Set Optical Power	Power DAC value	Noise 20Hz - 20MHz	8 Hour Test			
			RMS	Peak-to-peak	Std. deviation	Mean power
102.0 mW	4030	0.81%	0.89 %	5.35%	0.951 mW	107.01 mW

Long Term Power Stability Graph:
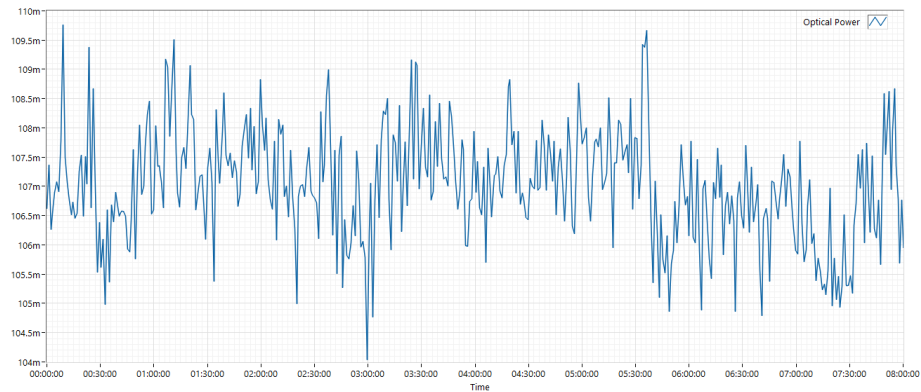
Special notes related to the laser:

144

D. Raster scans of graphene sheets and GFET sensing devices

D.1. Pristine graphene on a Si/SiO$_2$-substrate

In Figure D.1, representative Raman maps of a pristine **graphene-on-Si/SiO$_2$** sample from *Graphenea* are shown [Gra23a]. The raster scan is performed with the same step-width as the tritiated sample that is shown in Figure 7.11 in Chapter 7, namely $\Delta S = 6.25\,\mu m$. Note that this is not the same sample as shown in Figure 7.11 because the sample shown here was destroyed during the commissioning of the tritium loading chamber, as described in Section 7.3. However, the pristine samples from *Graphenea* all look homogenous with the current spatial resolution of the CRM.

For the generation of these maps, the Raman peaks of graphene (2D-, G-, and D-peak) are fitted with a Lorentzian and normalized to the intensity of the TO-peak of Si(O$_2$). The `Matlab` code used for the generation of these maps is given in Appendix B.
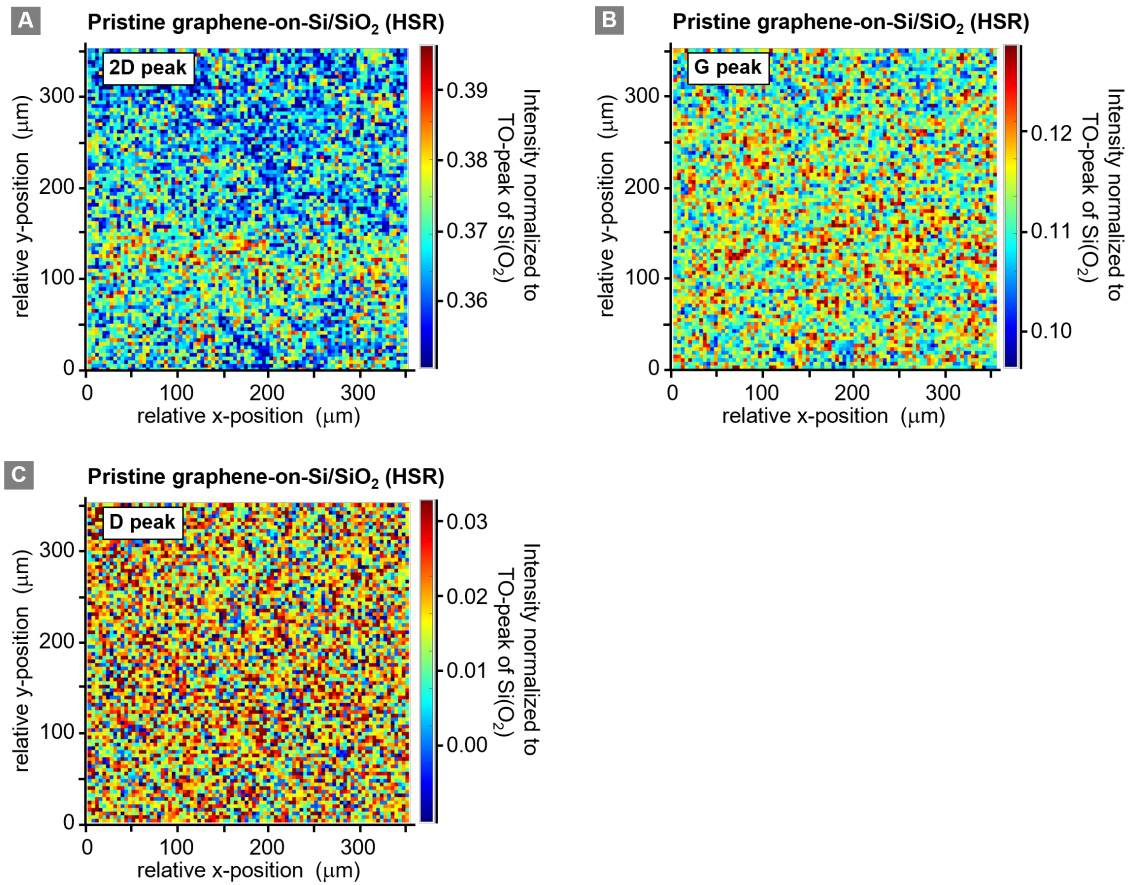
Figure D.1.: Raman maps (with step size $\Delta S = 6.25\,\mu m$) of a pristine graphene-on-Si/SiO$_2$ sample. (a) 2D-peak; (b) G-peak; and (c) D-peak of graphene. The peak intensities are normalized to the TO-peak of Si(O$_2$).

D.2. GFET device with different spatial step-increments

In order to demonstrate the effects of under- and over-sampling on the Raman maps, the Raman maps from raster-scans of a **GFET-sample** are shown in Figure D.2. The sequence displays the same area segment of the device – indicated in panel (a) of the figure – with a series of different step widths, namely $\Delta S = 7\,\text{steps} \equiv 8.75\,\mu\text{m}$, $\Delta S = 4\,\text{steps} \equiv 5.0\,\mu\text{m}$ and $\Delta S = 2\,\text{steps} \equiv 2.5\,\mu\text{m}$. The raster maps shown here are for spectral slices for the three main graphene peaks.

All spectral raster maps clearly reveal the "edges" between the graphene chip and the Si/SiO$_2$ substrate (or metal contacts), regardless of spatial step-increment; these are different in data panels (b) to (d), equal in data panels (d) to (f)). In addition, the spectral image maps shown in panels (d) to (f) for the different graphene peaks stem from the same raster-scan and thus are directly correlated, in contrast to the sequence shown in panels (b) to (d).

With the spatial step increment $\Delta S = 2\,\text{steps} \equiv 2.5\,\mu\text{m}$ (substantially smaller than the laser spot with FDB$\approx 7.3\,\mu\text{m}$) some 'structural features' can be identified as being common to all three spectral images, (d)-(f).
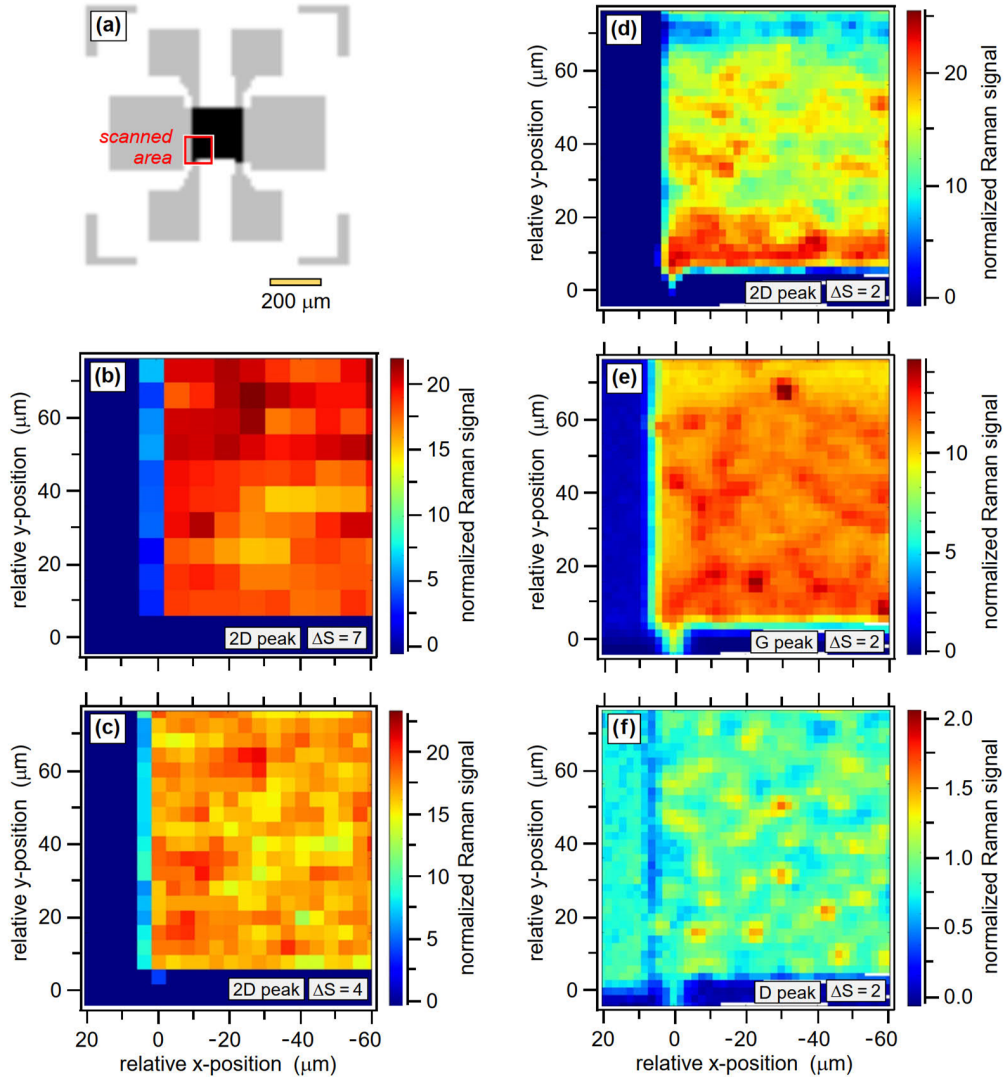
Figure D.2.: CRM Under- and Over-sampling. Images adapted from [Dia22]; details can be found in the text.

E. Exposure of a gold-coated rear-wall (RW) sample to tritiated methane

In a series of test measurements, attempts were made, using CRM raster scanning, to explore whether deposits on the REAR WALL (RW) of KATRIN's rear section could be analyzed, in principle (see Section 2.2.3 for the reasoning as to why such an analysis is desirable).

For this, a number of samples – resembling in their makeup the RW material – were investigated. As the RW itself, these were of layered structure, namely of V4A stainless steel (substrate bulk) with a top coating of $1\,\mu$m of gold. Their size is approximately $0.8\,$mm $\times\ 0.6\,$mm (see Figure E.3a). Samples were characterized using the CRM system; a representative Raman spectrum of a cleaned RW sample is shown in Figure E.3b, which is compared to the spectrum from pure gold (taken from a measurement of a GFET-sample, as shown in Figure 6.1). As can be seen, the RW spectrum is largely dominated by the fluorescence background from gold. In addition, a few small Raman features can be observed; however, these were not analyzed in detail. It is thought that the (small) feature at $2900\,$cm^{-1} is probably associated with the -CH$_3$ stretching mode, originating from residues from the cleaning process with acetone prior to the loading experiment.

A small area of $0.63\,$cm$\times 0.05\,$cm in the upper-left corner of the sample (see top in Figure E.4), that was later used in the tritiated-methane exposure experiment, was scanned with high-spatial resolution ($\Delta S = 6.25\,\mu$m), using a laser power of $100\,$mW and an acquisition time of $t_{\text{acq}} = 5\,$s per spectrum. The related Raman map is shown Figure E.4; the signal is strongest at the locations of scratches in the surface. This is not overly surprising, since any residues are likely to accumulate in the vicinity of these surface-roughness locations.

In order to evaluate the feasibility of detecting minute amounts of deposits (in the discussion in Section 2.2.3 one hypothesis pointed at tritiated amorphous carbon (aC:T)) some of the RW-type samples were exposed to a tritium-substituted methane gas mixture in a rudimentary proof-of-concept loading chamber.

Said proof-of-concept loading chamber consists of a stainless-steel connector element with DN40CF flanges, mounted in vertical orientation and closed on both ends with blind flanges;

(a)   (b)
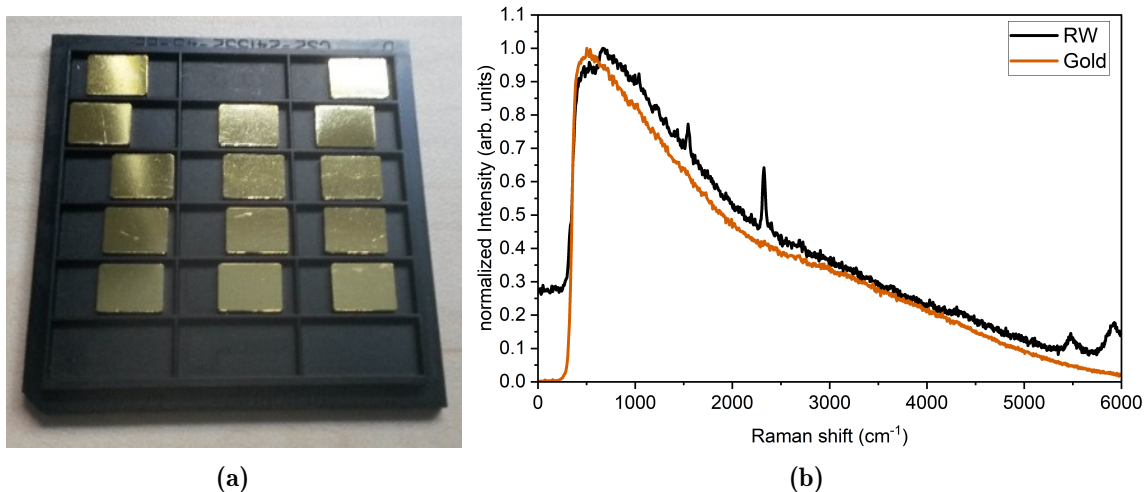
Figure E.3.: Image and Raman spectrum of REAR WALL (RW) samples. (a) Image of RW-samples. (b) Representative RW Raman spectrum (black trace), in comparison to a Raman spectrum of gold (orange trace).
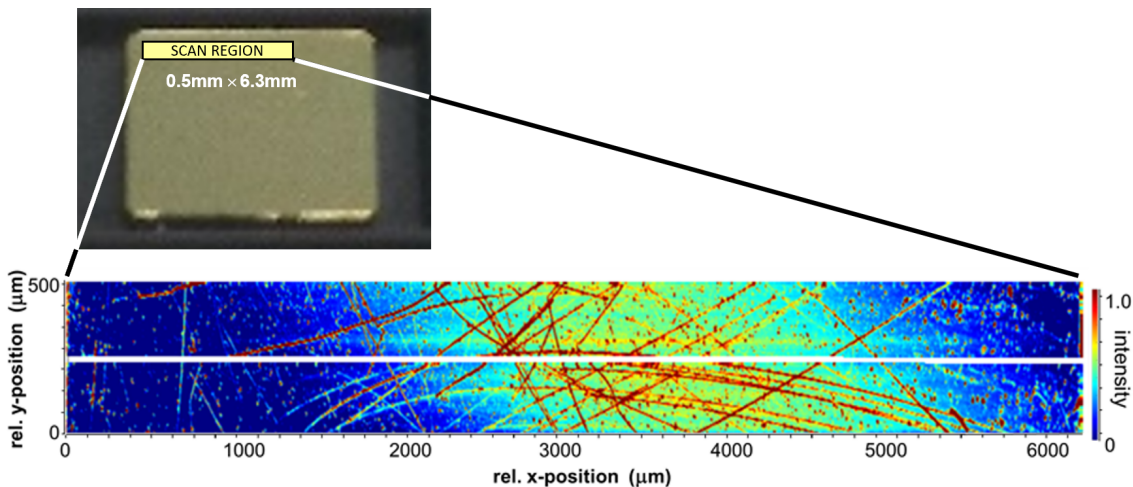
Figure E.4.: REAR WALL (RW) sample scan before the loading experiment, i.e., exposure to tritiated methane (the scanned area is indicated in the image of the sample). For the generation of the map, the Raman peak at $\sim 2900\,\mathrm{cm}^{-1}$ is fitted with a Lorentzian curve; its normalized intensity is shown. The white-stripe area corresponds to an error in the data saving during the two-week-long scan. For further details, see text.

the lower blind flange has four milled recesses, into which the samples are placed. Two VCR access ports are mounted on the sides, facilitating filling and emptying of the chamber.

The loading chamber was connected to the sampling port II of the TRITIUM-HYDROGEN-DEUTERIUM (TRIHYDE) facility via one of the VCR ports. During commissioning, a pressure rise test on the connected system is used to demonstrate a leak rate of less than $1 \times 10^{-9}\,\mathrm{mbar\,L\,s^{-1}}$. The tritiated methane mixture was prepared by D. Díaz Barrero and T. L. Le in the CAPRICE PERMCAT (CAPER)[Bor05] facility at the TLK [Día23].

After exposure for several days, the loading chamber was evacuated for two additional days. Before the tritium-exposed RW sample can be placed in the CRM, the total activity had to be measured to demonstrate that the activity is below the legal limit of $1 \times 10^{10}\,\mathrm{Bq}$. The activity measurement was carried out in two steps.

First, a so-called wipe test was performed on the RW sample. For the wipe test, a styrofoam strip is wiped across the surface of the sample, which is then dissolved in scintillation liquid. The activity of the liquid is measured via LSC. However, these results were not conclusive due to the large uncertainty associated with this method. It should be noted that, it is possible that a significant amount of deposited and/or adsorbed of tritiated methane on the RW surface was removed during the wiping. Second, the sample was placed in a bomb-calorimeter for seven days. Using this measurement, it was confirmed that the activity on the RW sample is below $1 \times 10^{10}\,\mathrm{Bq}$. However, the absolute value could not be determined since the lower limit of detection of the bomb calorimeter is around $1 \times 10^{10}\,\mathrm{Bq}$.

A Raman scan was repeated for an area close to the originally scanned area (indicated in Figure E.4), with an acquisition time of $t_{\mathrm{acq}} = 30\,\mathrm{s}$ per spectrum. However, since the RW sample has no 'land-mark' optical features, which could be used for exact alignment, the scanned regions are not the same, or even necessarily overlapping.

The Raman scans of the exposed RW sample reveal four characteristic types of spectral features, as shown in Figure E.5b:

1. A broad fluorescence signal from the gold surface; this is present as a background signal in all spectra. A representative Raman spectrum of gold (Au) is included in the figure (orange trace).

2. A single (or series of) Raman peak(s) at around $2900\,\text{cm}^{-1}$. In the literature, this is associated with the C-CH$_3$ or C-H stretching modes [Šeb13]. The presence of this peak indicates the presence of some organic material on the gold surface.

3. Broad spectral features above the expected background level from the gold surface.

4. At some locations within the scan area, Raman feature-rich spectra are observed (see the spectrum of "component 3", blue trace).

For the analysis of this data set, PRINCIPAL COMPONENT ANALYSIS (PCA) was used to identify the principal components and their respective spectra; these spectra (see Figure E.5a) are then used as input for a multicomponent analysis. The false-color maps for each component are combined to obtain the full component map (Figure E.5b).

Using a reference measurement of the styrofoam used for the wipe test, *Component 2* and *Component 3* can be identified as being, most likely, remains of the styrofoam material (see Figure E.6 for a comparison of Styrofoam and RW sample spectra). *Component 1* could not be identified, since the one strong peak could not be matched to any specific organic molecule. In conclusion, even though no tritiated methane depositions could be identified, these results established that spatially-resolved, chemical-specific Raman maps can be generated from samples akin to the RW-material used in the KATRIN experiment.

(a) Component Raman spectra   **(b)** Component map
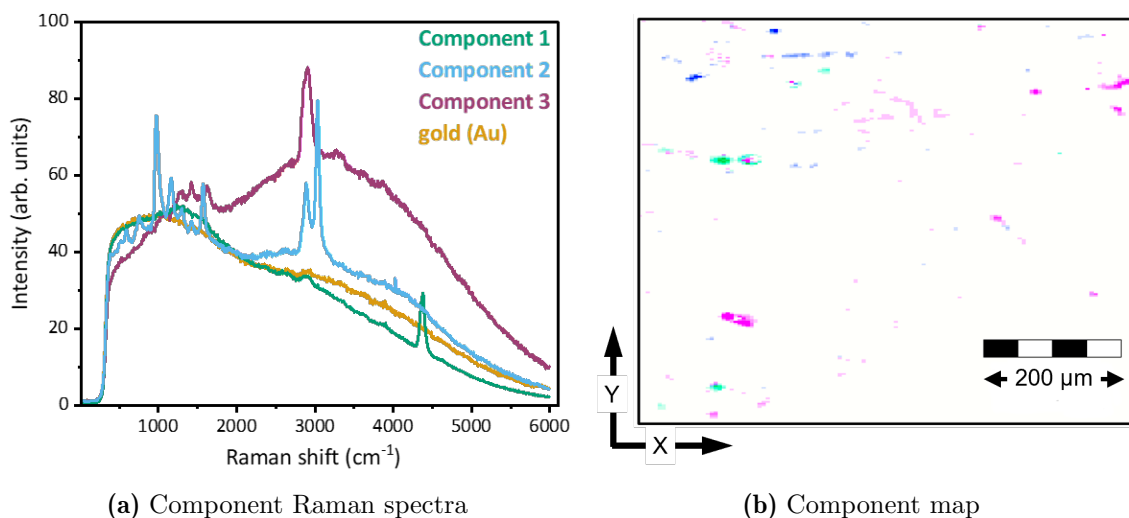
Figure E.5.: Raman image scan of the RW sample after exposure to tritiated methane. (a) Representative Raman spectra of the different "chemical" components on the gold surface. (b) False-color component map; for easier visualization and better contrast, the gold signal areas are displayed in white.
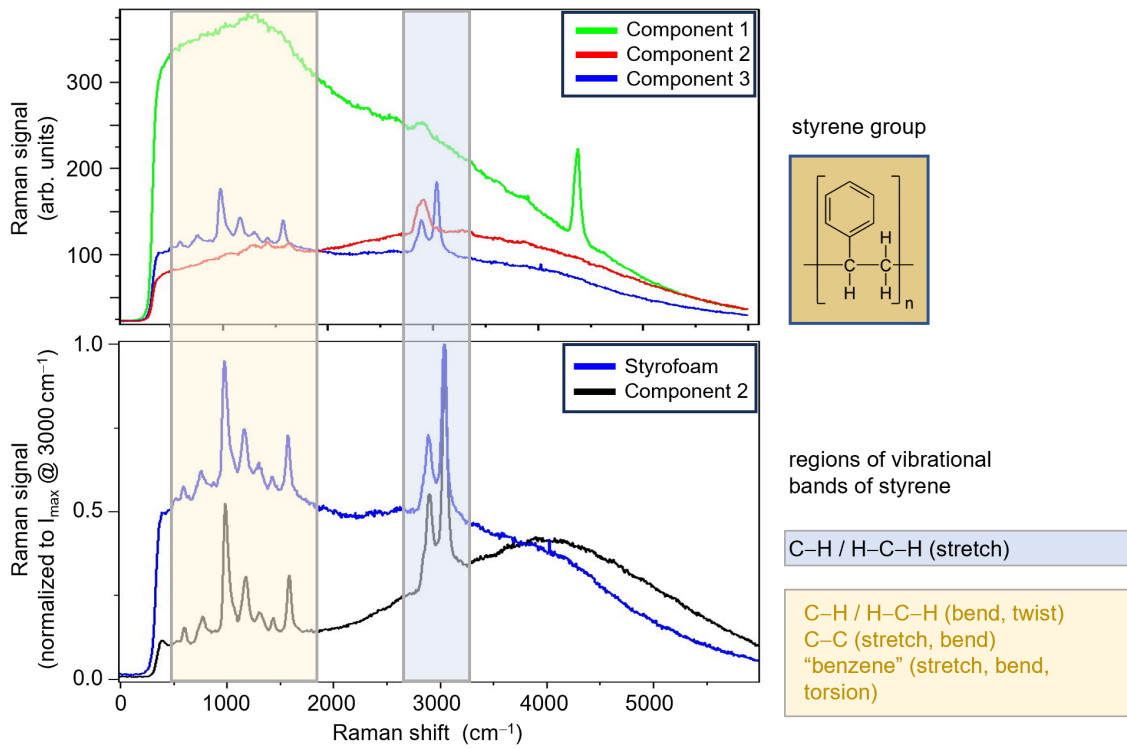
Figure E.6.: Comparison of the observed spectra from the RW sample exposed to tritiated methane with a reference spectrum of a Styrofoam sample. The regions of Raman bands expected for the styrene group (see e.g. Ref [Nod00]) are indicated.

Glossary

RCF Rolling Circle Filter 46

RS Rear Section 14, 17

RS Run Summary 49

RW Rear Wall x, 17, 106, 107, 112, 134, 147–149

SCARF Savitzky–Golay Coupled Advanced Rolling Circle Filter 46, 65, 70

SDS Source and Detection Section 14

SEM Scanning Electron Microscopy 89, 103, 105, 106

SLG Single-layer graphene 40, 102, 103

SM Standard Model of particle physics viii, 1, 4–9, 131

SRM Standard Reference Material 2, 21, 68, 69, 80, 82, 89, 98, 132, 133

STS Source and Transport Section 14

TCR Temperature Coefficient of Resistance 116, 117, 119, 120, 126, 134

TLG Trilayer graphene 102, 103

TLK Tritium Laboratory Karlsruhe 3, 14, 15, 22, 25, 46, 47, 49, 60, 81, 82, 89, 118, 132, 135, 148

TriHyDe Tritium-Hydrogen-Deuterium 49, 81, 118, 148

TSS Tritium Separation System 69, 118

UAM Universidad Autónoma de Madrid 3, 43, 62, 132

Van der Pauw Van der Pauw 108, 110, 113, 115, 119, 123, 134

VFT 'Very First Tritium' 68, 76, 80, 132

WGTS Windowless Gaseous Tritium Source viii, 1, 14–17, 19–21, 44, 69, 70, 76, 80, 88, 131, 132

XPS X-ray Photoelectron Spectroscopy 109, 128, 130

Bibliography

[Agh20]   N. AGHANIM et al.: Planck 2018 results. In *Astronomy & Astrophysics* (2020), volume 641:A6. DOI: 10.1051/0004-6361/201833910.

[Ake19]   M. AKER et al.: Improved Upper Limit on the Neutrino Mass from a Direct Kinematic Method by KATRIN. In *Phys. Rev. Lett.* (2019), volume 123(22):221802. DOI: 10.1103/PhysRevLett.123.221802.

[Ake20a]   M. AKER et al.: First operation of the KATRIN experiment with tritium. In *Eur. Phys. J. C* (2020), volume 80(3):264. DOI: 10.1140/epjc/s10052-020-7718-z.

[Ake20b]   M. AKER et al.: Quantitative Long-Term Monitoring of the Circulating Gases in the KATRIN Experiment Using Raman Spectroscopy. In *Sensors* (2020), volume 20(17):4827. DOI: 10.3390/s20174827.

[Ake22a]   M. AKER et al.: KATRIN: status and prospects for the neutrino mass and beyond. In *Journal of Physics G: Nuclear and Particle Physics* (2022), volume 49(10):100501. DOI: 10.1088/1361-6471/ac834e.

[Ake22b]   M. AKER et al.: Direct neutrino-mass measurement with sub-electronvolt sensitivity. In *Nat. Phys.* (2022), volume 18(2):160–166. DOI: 10.1038/s41567-021-01463-1.

[Ake23a]   M. AKER et al.: Search for keV-scale sterile neutrinos with the first KATRIN data. In *Eur. Phys. J. C* (2023), volume 83(8):763. DOI: 10.1140/epjc/s10052-023-11818-y.

[Ake23b]   M. AKER et al., *In Situ Tritium Decontamination of the KATRIN Rear Wall Using an Ultraviolet/Ozone Treatment*, In Fusion Sci. Technol., published online: 12/07/23, 2023, DOI: 10.1080/15361055.2023.2214695.

[ALE06]   ALEPH COLLABORATION, DELPHI COLLABORATION, L3 COLLABORATION, OPAL COLLABORATION, SLD COLLABORATION, LEP ELECTROWEAK WORKING GROUP, SLD ELECTROWEAK, and HEAVY FLAVOUR GROUPS: Precision electroweak measurements on the Z resonance. In *Phys. Rep.* (2006), volume 427(5-6):257–454. DOI: 10.1016/j.physrep.2005.12.006.

[Ams15]   J. F. AMSBAUGH et al.: Focal-plane detector system for the KATRIN experiment. In *Nucl. Instrum. Methods Phys. Res. A: Accel. Spectrom. Detect. Assoc. Equip.* (2015), volume 778:40–60. DOI: 10.1016/j.nima.2014.12.116.

[App22]   A. Apponi et al.: Heisenberg's uncertainty principle in the PTOLEMY project: A theory update. In *Phys. Rev. D* (2022), volume 106(5):053002. DOI: 10.1103/PhysRevD.106.053002.

[Ara09]   M. A. C. de Araújo, R. Silva, E. de Lima, D. P. Pereira, and P. C. de Oliveira: Measurement of Gaussian laser beam radius using the knife-edge technique: improvement on data analysis. In *Appl. Opt.* (2009), volume 48(2):393–396. DOI: 10.1364/AO.48.000393.

[Ase11]   V. N. Aseev et al.: Upper limit on the electron antineutrino mass from the Troitsk experiment. In *Phys. Rev. D* (2011), volume 84(11):112003. DOI: 10.1103/PhysRevD.84.112003.

[Asp83]   D. E. Aspnes and A. A. Studna: Dielectric functions and optical parameters of Si, Ge, GaP, GaAs, GaSb, InP, InAs, and InSb from 1.5 to 6.0 eV. In *Phys. Rev. B* (1983), volume 27(2):985–1009. DOI: 10.1103/PhysRevB.27.985.

[AST14]   ASTM International. 2014. *ASTM E2529–06 Standard Guide for Testing the Resolution of a Raman Spectrometer*. West Conshohocken, Pennsylvania, USA.

[Bab12]   M. Babutzka et al.: Monitoring of the operating parameters of the KATRIN Windowless Gaseous Tritium Source. In *New J. Phys.* (2012), volume 14(10):103046. DOI: 10.1088/1367-2630/14/10/103046.

[Bal11]   A. A. Balandin: Thermal properties of graphene and nanostructured carbon materials. In *Nat. Mater* (2011), volume 10(8):569–581. DOI: 10.1038/nmat3064.

[Bea08]   Beate Bornschein: Determination of Neutrino Mass from Tritium Beta Decay. In *Fusion Sci. Technol.* (2008), volume 54:59–66. DOI: 10.13182/FST54-59.

[Beg22]   A. Beglarian et al.: Forward Beam Monitor for the KATRIN experiment. In *J. Instrum.* (2022), volume 17(03):T03002. DOI: 10.1088/1748-0221/17/03/T03002.

[Bet04]   H. F. Bettinger: Carbon Nanotubes—Basic Concepts and Physical Properties. By S. Reich, C. Thomsen, J. Maultzsch. In *ChemPhysChem* (2004), volume 5(12):1914–1915. DOI: 10.1002/cphc.200400387.

[Bet13]   S. Betts et al., *Development of a Relic Neutrino Detection Experiment at PTOLEMY: Princeton Tritium Observatory for Light, Early-Universe, Massive-Neutrino Yield*, 2013, URL: https://arxiv.org/pdf/1307.4738.

[Bet19a]   M. G. Betti et al.: A design for an electromagnetic filter for precision energy measurements at the tritium endpoint. In *Prog. Part. Nucl. Phys.* (2019), volume 106:120–131. DOI: 10.1016/j.ppnp.2019.02.004.

[Bet19b]   M. G. Betti et al.: Neutrino physics with the PTOLEMY project: active neutrino properties and the light sterile case. In *J. Cosmol. Astropart. Phys.* (2019), volume 2019(07):047. DOI: 10.1088/1475-7516/2019/07/047.

[Bia20]   Z. Bian et al.: Autofocusing technologies for whole slide imaging and automated microscopy. In *J. Biophotonics* (2020), volume 13:e202000227. DOI: 10.1002/jbio.202000227.

[Bil15]   S. M. Bilenky and C. Giunti: Neutrinoless double-beta decay: A probe of physics beyond the Standard Model. In *Int. J. Mod. Phys. A* (2015), volume 30(04n05). DOI: 10.1142/S0217751X1530001X.

[BIP08]   BIPM, IEC, IFCC, ILAC, ISO, IUPAC, IUPAP, and OIML, *Evaluation of measurement data — Guide to the expression of uncertainty in measurement*, Joint Committee for Guides in Metrology, JCGM 100:2008, 2008, URL: https://www.bipm.org/documents/20126/2071204/JCGM_100_2008_E.pdf (Last accessed: 16.12.2023).

[Bod15]   L. I. Bodine, D. S. Parno, and R. G. H. Robertson: Assessment of molecular effects on neutrino mass measurements from tritium β-decay. In *Phys. Rev. C* (2015), volume 91(3):035505. DOI: 10.1103/PhysRevC.91.035505.

[Bor05]   B. Bornschein, M. Glugla, K. Günther, T. L. Le, K. H. Simon, and S. Welte: Successful Experimental Verification of the Tokamak Exhaust Processing Concept of ITER with the CAPER Facility. In *Fusion Sci. Technol.* (2005), volume 48(1):11–16. DOI: 10.13182/FST05-A870.

[Bur11]   J. S. Burgess, B. R. Matis, J. T. Robinson, F. A. Bulat, F. Keith Perkins, B. H. Houston, and J. W. Baldwin: Tuning the electronic properties of graphene by hydrogenation in a plasma enhanced chemical vapor deposition reactor. In *Carbon* (2011), volume 49(13):4420–4426. DOI: 10.1016/j.carbon.2011.06.034.

[Can11]   L. G. Cançado et al.: Quantifying defects in graphene via Raman spectroscopy at different excitation energies. In *Nano Lett.* (2011), volume 11(8):3190–3196. DOI: 10.1021/nl201432g.

[Cas09]   C. Casiraghi et al.: Raman spectroscopy of graphene edges. In *Nano Lett.* (2009), volume 9(4):1433–1441. DOI: 10.1021/nl8032697.

[Cha22]   J. Cha, H. Choi, and J. Hong: Damage-free hydrogenation of graphene via ion energy control in plasma. In *Appl. Phys. Express* (2022), volume 15(1):015002. DOI: 10.35848/1882-0786/ac4204.

[Che13]   J. Chen, T. Shi, T. Cai, T. Xu, L. Sun, X. Wu, and D. Yu: Self healing of defected graphene. In *Appl. Phys. Lett.* (2013), volume 102(10):103107. DOI: 10.1063/1.4795292.

[Che21]   Y. Cheipesh, V. Cheianov, and A. Boyarsky: Navigating the pitfalls of relic neutrino detection. In *Phys. Rev. D* (2021), volume 104:116004. DOI: 10.1103/PhysRevD.104.116004.

[Chi10a]   I. Childres, L. A. Jauregui, M. Foxe, J. Tian, R. Jalilian, I. Jovanovic, and Y. P. Chen: Effect of electron-beam irradiation on graphene field effect devices. In *Appl. Phys. Lett.* (2010), volume 97(17):173109. DOI: 10.1063/1.3502610.

[Chi10b] S. Chilingaryan, A. Beglarian, A. Kopmann, and S. Vöcking: Advanced data extraction infrastructure: Web based system for management of time series data. In *J. Phys. Conf. Ser.* (2010), volume 219(4):042034. DOI: 10.1088/1742-6596/219/4/042034.

[Cho16] J. H. Choi, J. Lee, S. M. Moon, Y.-T. Kim, H. Park, and C. Y. Lee: A Low-Energy Electron Beam Does Not Damage Single-Walled Carbon Nanotubes and Graphene. In *J. Phys. Chem. Lett.* (2016), volume 7(22):4739–4743. DOI: 10.1021/acs.jpclett.6b02185.

[Cow56] C. L. Cowan, F. Reines, F. B. Harrison, H. W. Kruse, and A. D. McGuire: Detection of the Free Neutrino: a Confirmation. In *Science* (1956), volume 124(3212):103–104. DOI: 10.1126/science.124.3212.103.

[CUO22] CUORE Collaboration, D. Q.Adams et al.: Search for Majorana neutrinos exploiting millikelvin cryogenics with CUORE. In *Nature* (2022), volume 604(7904):53–58. DOI: 10.1038/s41586-022-04497-4.

[Dab92] T. Dabbs and M. Glass: Single-mode fibers used as confocal microscope pinholes. In *Appl. Opt.* (1992), volume 31(6):705–706. DOI: 10.1364/AO.31.000705.

[Dan62] G. Danby, J.-M. Gaillard, K. Goulianos, L. M. Lederman, N. Mistry, M. Schwartz, and J. Steinberger: Observation of High-Energy Neutrino Reactions and the Existence of Two Kinds of Neutrinos. In *Phys. Rev. Lett.* (1962), volume 9(1):36–44. DOI: 10.1103/PhysRevLett.9.36.

[Das14] G. N. Dash, S. R. Pattanaik, and S. Behera: Graphene for Electron Devices: The Panorama of a Decade. In *IEEE J. Electron Devices Soc.* (2014), volume 2(5):77–104. DOI: 10.1109/JEDS.2014.2328032.

[Dav64] R. Davis: Solar Neutrinos. II. Experimental. In *Phys. Rev. Lett.* (1964), volume 12(11):303–305. DOI: 10.1103/PhysRevLett.12.303.

[Dem08] W. Demtröder. 2008. *Laser spectroscopy*. 4. ed. Berlin: Springer,

[Des09] T. Deschaines, J. Hodkiewicz, and P. Henson, *Characterization of Amorphous and Microcrystalline Silicon using Raman Spectroscopy*, Thermo Fisher Scientific, Madison (WI), USA. Application Note 51735, 2009, URL: https://assets.thermofisher.com/TFS-Assets/CAD/Application-Notes/D16998~.pdf (Last accessed: 26.11.2023).

[DES22] DES Collaboration, T. M. C. Abbott et al.: Dark Energy Survey Year 3 results: Cosmological constraints from galaxy clustering and weak lensing. In *Phys. Rev. D* (2022), volume 105:023520. DOI: 10.1103/PhysRevD.105.023520.

[Dia22] D. Diaz Barrero, G. Zeller, M. Schlösser, B. Bornschein, and H. H. Telle: Versatile Confocal Raman Imaging Microscope Built from Off-the-Shelf Opto-Mechanical Components. In *Sensors* (2022), volume 22(24):10013. DOI: 10.3390/s222410013.

[Día23]   D. Díaz Barrero, T. L. Le, S. Niemes, S. Welte, M. Schlösser, B. Born-schein, and H. H. Telle, *Generation and Analysis of Tritium-Substituted Methane*, In Fusion Sci. Technol., published online: 25/05/23, 2023, 1–10, DOI: 10.1080/15361055.2023.2194235.

[DON01]   DONUT Collaboration: Observation of tau neutrino interactions. In *Phys. Lett. B* (2001), volume 504(3):218–224. DOI: 10.1016/S0370-2693(01)00307-0.

[Don09]   Donald Perkins. 2009. *Particle Astrophysics*. 2nd ed., Oxford University Press,

[Dor13]   V. E. Dorgan, A. Behnam, H. J. Conley, K. I. Bolotin, and E. Pop: High-field electrical and thermal transport in suspended graphene. In *Nano Lett.* (2013), volume 13(10):4581–4586. DOI: 10.1021/nl400197w.

[Dos06]   N. Doss, J. Tennyson, A. Saenz, and S. Jonsell: Molecular effects in investigations of tritium molecule β-decay endpoint experiments. In *Phys. Rev. C* (2006), volume 73(2):025502. DOI: 10.1103/PhysRevC.73.025502.

[Dre13]   G. Drexlin, V. Hannen, S. Mertens, and C. Weinheimer: Current Direct Neutrino Mass Experiments. In *Adv. High Energy Phys.* (2013), volume 2013:1–39. DOI: 10.1155/2013/293986.

[Eck12]   A. Eckmann, A. Felten, A. Mishchenko, L. Britnell, R. Krupke, K. S. Novoselov, and C. Casiraghi: Probing the nature of defects in graphene by Raman spectroscopy. In *Nano Lett.* (2012), volume 12(8):3925–3930. DOI: 10.1021/nl300901a.

[Eck13]   A. Eckmann, A. Felten, I. Verzhbitskiy, R. Davey, and C. Casiraghi: Raman study on defective graphene: Effect of the excitation energy, type, and amount of defects. In *Phys. Rev. B* (2013), volume 88(3):035426. DOI: 10.1103/PhysRevB.88.035426.

[Eil03]   P. H. C. Eilers: A perfect smoother. In *Anal. Chem.* (2003), volume 75(14):3631–3636. DOI: 10.1021/ac034173t.

[Eli09]   D. C. Elias et al.: Control of graphene's properties by reversible hydrogenation: evidence for graphane. In *Science* (2009), volume 323(5914):610–613. DOI: 10.1126/science.1167130.

[Fer13]   A. C. Ferrari and D. M. Basko: Raman spectroscopy as a versatile tool for studying the properties of graphene. In *Nat. Nanotechnol.* (2013), volume 8(4):235–246. DOI: 10.1038/nnano.2013.46.

[Fer34]   E. Fermi: Versuch einer Theorie der β-Strahlen. I. In *Z. Physik* (1934), volume 88(3-4):161–177. DOI: 10.1007/BF01351864.

[Fey58]   R. P. Feynman and M. Gell-Mann: Theory of the Fermi Interaction. In *Phys. Rev.* (1958), volume 109(1):193–198. DOI: 10.1103/PhysRev.109.193.

[Fie92]   A. Fiege. 1992. *Tritium*. Forschungsbericht KfK 5055, Karlsruhe: Kernforschungs-zentrum, DOI: 10.5445/IR/270032500.

[Fis11]   S. FISCHER, M. STURM, M. SCHLÖSSER, B. BORNSCHEIN, G. DREXLIN, F. PRIESTER, R. J. LEWIS, and H. H. TELLE: Monitoring of Tritium Purity During Long-Term Circulation in the KATRIN Test Experiment LOOPINO Using Laser Raman Spectroscopy. In *Fusion Sci. Technol.* (2011), volume 60(3):925–930. DOI: `10.13182/FST11-A12567`.

[Fis14]   S. FISCHER: Commissioning of the KATRIN Raman system and durability studies of optical coatings in glove box and tritium atmospheres. Dissertation. Karlsruhe: Karlsruher Institut für Technologie (KIT), 2014. DOI: `10.5445/IR/1000043697`.

[For21]   J. A. FORMAGGIO, A. L. C. DE GOUVÊA, and R. H. ROBERTSON: Direct measurements of neutrino mass. In *Phys. Rep.* (2021), volume 914:1–54. DOI: `10.1016/j.physrep.2021.02.002`.

[Giu12]   A. GIULIANI and A. POVES: Neutrinoless Double-Beta Decay. In *Adv. High Energy Phys.* (2012), volume 2012:1–38. DOI: `10.1155/2012/857016`.

[Gol58]   M. GOLDHABER, L. GRODZINS, and A. W. SUNYAR: Helicity of Neutrinos. In *Phys. Rev.* (1958), volume 109(3):1015–1017. DOI: `10.1103/PhysRev.109.1015`.

[Gra23a] GRAPHENEA, *Monolayer Graphene on 90 nm SiO_2/Si*, 2023, URL: `https://www.graphenea.com/collections/buy-graphene-films/products/monolayer-graphene-on-sio-si-90-nm` (Last accessed: 13.11.2023).

[Gra23b] GRAPHENEA, *Multilayer Graphene on 90 nm SiO_2/Si*, 2023, URL: `https://www.graphenea.com/collections/buy-graphene-films/products/bilayer-graphene-on-sio2-si-10-mm-x-10-mm` (Last accessed: 28.11.2023).

[Gre95]   M. A. GREEN and M. J. KEEVERS: Optical properties of intrinsic silicon at 300 K. In *Prog. Photovolt.: Res. Appl.* (1995), volume 3(3):189–192. DOI: `10.1002/pip.4670030303`.

[Gu91]   M. GU, C. J. R. SHEPPARD, and X. GAN: Image formation in a fiber-optical confocal scanning microscope. In *J. Opt. Soc. Am. A* (1991), volume 8(11):1755. DOI: `10.1364/JOSAA.8.001755`.

[Gui14]   GUILLEMETTE, JONATHAN: Electronic Transport in Hydrogenated Graphene. Dissertation. Montreal, Canada: McGill University, 2014.

[Hak06]   H. HAKEN and H. C. WOLF. 2006. *Molekülphysik und Quantenchemie*. Springer Berlin Heidelberg, DOI: `10.1007/3-540-30315-4_9`.

[Hea03]   M. HEANEY, "Electrical Conductivity and Resistivity", *Electrical measurement, signal processing, and displays*, ed. by J. G. WEBSTER, Principles and applications in engineering series, Boca Raton: CRC Press, 2003, 7–1, DOI: `10.1201/b15664`.

[Hen70]   P. J. HENDRA and C. J. VEAR: Laser Raman spectroscopy. A review. In *Analyst* (1970), volume 95(1129):321. DOI: `10.1039/an9709500321`.

[Her63]   G. Herzberg. 1963. *Molecular Spectra and Molecular Structure: I. Spectra of Diatomic Molecules*. 2. Auflage, D. Van Nostrand Company, Inc., Princeton, New Jeresy,

[Hey23]   S. M. Heyns, *Neutrino Mass Sensitivity Studies Towards Potential Enhancements of the KATRIN Experiment with a High-Resolution Detector and an Atomic Tritium Source*, Master thesis, Karlsruhe, 2023.

[Hig64]   P. W. Higgs: Broken Symmetries and the Masses of Gauge Bosons. In *Phys. Rev. Lett.* (1964), volume 13(16):508–509. DOI: 10.1103/PhysRevLett.13.508.

[Hot36]   H. Hotelling: Relations Between Two Sets of Variates. In *Biometrika* (1936), volume 28(3/4):321. DOI: 10.2307/2333955.

[Hou20]   T. Houdy et al.: Hunting keV sterile neutrinos with KATRIN: building the first TRISTAN module. In *J. Phys. Conf. Ser.* (2020), volume 1468(1):012177. DOI: 10.1088/1742-6596/1468/1/012177.

[Hua11]   M. Huang, T. A. Pascal, H. Kim, W. A. Goddard, and J. R. Greer: Electronic–mechanical coupling in graphene from in situ nanoindentation experiments and multiscale atomistic simulations. In *Nano Lett.* (2011), volume 11(3):1241–1246. DOI: 10.1021/nl104227t.

[INP21]   INP - The IUPAP Neutrino Panel, *IUPAP Neutrino Panel White Paper*, 2021, DOI: 10.5281/ZENODO.5930310.

[ISO23]   ISO Central Secretary, *Accuracy (trueness and precision) of measurement methods and results*, Standard, Geneva, CH: International Organization for Standardization, 2023, URL: https://www.iso.org/obp/ui/#iso:std:iso:5725:-1:ed-2:v1:en (Last accessed: 21.12.2023).

[Ito20]   N. Itoh and N. Hanari: Reliable Evaluation of the Lateral Resolution of a Confocal Raman Microscope by Using the Tungsten-dot Array Certified Reference Material. In *Anal. Sci.* (2020), volume 36(8):1009–1013. DOI: 10.2116/analsci.20P046.

[Jam13]   T. M. James, M. Schlösser, R. J. Lewis, S. Fischer, B. Bornschein, and H. H. Telle: Automated quantitative spectroscopic analysis combining background subtraction, cosmic ray removal, and peak fitting. In *Appl. Spectrosc.* (2013), volume 67(8):949–959. DOI: 10.1366/12-06766.

[Jor11]   A. Jorio, R. Saito, G. Dresselhaus, and M. S. Dresselhaus. 2011. *Raman Spectroscopy in Graphene Related Systems*. Wiley, DOI: 10.1002/9783527632695.

[Kam23]   KamLAND-Zen Collaboration, S. Abe et al.: Search for the Majorana Nature of Neutrinos in the Inverted Mass Ordering Region with KamLAND-Zen. In *Phys. Rev. Lett.* (2023), volume 130(5):051801. DOI: 10.1103/PhysRevLett.130.051801.

[Kas13]   F. Kassel: Weiterentwicklung der laser-Ramanspektroskopie an gasförmigen Wasserstoffisotopologen zur Prozessüberwachung von Tritiumexperimenten. Diploma thesis. Karlsruhe: Karlsruhe Institute of Technology, 2013.

[KAT05]   KATRIN COLLABORATION: KATRIN design report 2004. In *Wissenschaftliche Berichte. FZKA* (2005), volume 7090. DOI: 10.5445/IR/270060419.

[KAT21]   KATRIN COLLABORATION, M. AKER et al.: The design, construction, and commissioning of the KATRIN experiment. In *J. Instrum.* (2021), volume 16(08):T08015. DOI: 10.1088/1748-0221/16/08/T08015.

[Kaz08]   O. KAZACHENKO, B. BORNSCHEIN, N. KERNERT, L. DOERR, M. GLUGLA, V. WEBER, and D. STERN: Tritium Processing Loop for KATRIN Experiment. In *Fusion Sci. Technol.* (2008), volume 54(1):67–70. DOI: 10.13182/FST08-A1766.

[Kei16]   KEITHLEY INSTRUMENTS INC., *Low Level Measurements Handbook: Precision DC Current, Voltage, and Resistance Measurements*, ed. by KEITHLEY INSTRUMENTS, Cleveland, 2016, URL: https://download.tek.com/document/LowLevelHandbook_7Ed.pdf (Last accessed: 2.12.2023).

[Kes02]   N. KESHAVA and J. F. MUSTARD: Spectral unmixing. In *IEEE Signal. Proc. Mag.* (2002), volume 19(1):44–57. DOI: 10.1109/79.974727.

[Kib67]   T. W. B. KIBBLE: Symmetry Breaking in Non-Abelian Gauge Theories. In *Phys. Rev.* (1967), volume 155(5):1554–1561. DOI: 10.1103/PhysRev.155.1554.

[Kin14]   S. KING, *Neutrino Mass Models*, International Neutrino Summer School, St. Andrews, Scotland, 10-22 August, 2014, URL: https://indico.cern.ch/event/300715/contributions/686783/attachments/566733/780664/king_lecture2.pdf (Last accessed: 2.12.2023).

[Kit18]   C. KITTEL. 2018. *Introduction to solid state physics*. Global edition, [9th edition]. Hoboken, NJ: Wiley,

[Kle19a]   M. KLEESIEK et al.: -Decay spectrum, response function and statistical model for neutrino mass measurements with the KATRIN experiment. In *Eur. Phys. J. C.* (2019), volume 79(3). DOI: 10.1140/epjc/s10052-019-6686-7.

[Kle19b]   M. KLEIN: Tritium ions in KATRIN: blocking, removal and detection. Dissertation. Germany: Karlsruhe Insitute of Technology, 2019. DOI: 10.5445/IR/1000093526.

[Kon47]   E. J. KONOPINSKI: H^3 and the Mass of the Neutrino. In *Phys. Rev.* (1947), volume 72:518–519. DOI: 10.1103/PhysRev.72.518.2.

[Kra05]   C. KRAUS et al.: Final results from phase II of the Mainz neutrino mass search in tritium β-decay. In *Eur. Phys. J. C.* (2005), volume 40(4):447–468. DOI: 10.1140/epjc/s2005-02139-7.

[Lei22]   S. LEI, N. SU, and M. LI: Thermal-Resistance Effect of Graphene at High Temperatures in Nanoelectromechanical Temperature Sensors. In *Micromachines* (2022), volume 13(12):2078. DOI: 10.3390/mi13122078.

[Lew08]   R. J. LEWIS, H. H. TELLE, B. BORNSCHEIN, O. KAZACHENKO, N. KERNERT, and M. STURM: Dynamic Raman spectroscopy of hydrogen isotopomer mixtures

in-line at TILO. In *Laser Phys. Lett.* (2008), volume 5(7):522–531. DOI: 10.1002/lapl.200810026.

[Liu12]   C. LIU and R. W. BERG: Determining the Spectral Resolution of a Charge-Coupled Device (CCD) Raman Instrument. In *Appl. Spectrosc.* (2012), volume 66(9):1034–1043. DOI: 10.1366/11-06508.

[Lok22]   A. LOKHOV et al.: Background reduction at the KATRIN experiment by the shifted analysing plane configuration. In *Eur. Phys. J. C.* (2022), volume 82(3):258. DOI: 10.1140/epjc/s10052-022-10220-4.

[Lok23]   A. LOKHOV, *Probing the neutrino mass scale with the KATRIN experiment*, XVIII International Conference on Topics in Astoparticle and Underground Physics (TAUP), 2023, URL: https://indico.cern.ch/event/1199289/contributions/5447195/attachments/2705052/4695809/Lokhov_KATRIN_TAUP2023_short.pdf (Last accessed: 24.11.2023).

[Lon02]   D. A. LONG. 2002. *The Raman Effect: A Unified Treatment of the Theory of Raman Scattering by Molecules*. Chichester, West Sussex, England: John Wiley & Sons Ltd, DOI: 10.1002/0470845767.

[Lóp09]   V. LÓPEZ, R. S. SUNDARAM, C. GÓMEZ-NAVARRO, D. OLEA, M. BURGHARD, J. GÓMEZ-HERRERO, F. ZAMORA, and K. KERN: Chemical Vapor Deposition Repair of Graphene Oxide: A Route to Highly-Conductive Graphene Monolayers. In *Adv. Mater.* (2009), volume 21(46):4683–4686. DOI: 10.1002/adma.200901582.

[Lor02]   T. J. LOREDO and D. Q. LAMB: Bayesian analysis of neutrinos observed from supernova SN 1987A. In *Phys. Rev. D* (2002), volume 65(6):063002. DOI: 10.1103/PhysRevD.65.063002.

[Luc10]   M. M. LUCCHESE, F. STAVALE, E. M. FERREIRA, C. VILANI, M. MOUTINHO, R. B. CAPAZ, C. A. ACHETE, and A. JORIO: Quantifying ion-induced defects and Raman relaxation length in graphene. In *Carbon* (2010), volume 48(5):1592–1597. DOI: 10.1016/j.carbon.2009.12.057.

[Mak62]   Z. MAKI, M. NAKAGAWA, and S. SAKATA: Remarks on the Unified Model of Elementary Particles. In *Prog. Theor. Phys.* (1962), volume 28(5):870–880. DOI: 10.1143/PTP.28.870.

[Mal09]   L. M. MALARD, M. A. PIMENTA, G. DRESSELHAUS, and M. S. DRESSELHAUS: Raman spectroscopy in graphene. In *Phys. Rep.* (2009), volume 473(5-6):51–87. DOI: 10.1016/j.physrep.2009.02.003.

[McC06]   R. L. MCCREERY, "Handbook of Vibrational Spectroscopy", *Handbook of Vibrational Spectroscopy*, ed. by JOHN M. CHALMERS and PETER R. GRIFFITHS, John Wiley & Sons, Ltd, 2006, DOI: 10.1002/0470027320.s0706.

[Mer23]   S. MERTENS, *Direct neutrino mass measurements – review*, Presentation, XVIII International Conference on Topics in Astoparticle and Underground Physics (TAUP), 2023, URL: https://indico.cern.ch/event/1199289/contributions/5262782/attachments/2704343/4694393/Mertens_TAUP.pdf (Last accessed: 23.11.2023).

[Mon15]   B. MONREAL: The Project 8 Radiofrequency Tritium Neutrino Experiment. In *Phys. Procedia* (2015), volume 61:274–277. DOI: `10.1016/j.phpro.2014.12.044`.

[Muc14]   B. MUCHHARLA, T. N. NARAYANAN, K. BALAKRISHNAN, P. M. AJAYAN, and S. TALAPATRA: Temperature dependent electrical transport of disordered reduced graphene oxide. In *2D Mater.* (2014), volume 1(1):011008. DOI: `10.1088/2053-1583/1/1/011008`.

[Neu18]   C. NEUMANN and C. STAMPFER, "Characterization of Graphene by Confocal Raman Spectroscopy", *Confocal Raman Microscopy*, ed. by J. TOPORSKI, T. DIEING, and O. HOLLRICHER, Cham: Springer International Publishing, 2018, 177–194, DOI: `10.1007/978-3-319-75380-5_8`.

[Nie21a] S. NIEMES: Calibration of a Laser-Raman-System using gas samples of all hydrogen isotopologues for KATRIN. Dissertation. Karlsruher Institut für Technologie (KIT): 2021. DOI: `10.5445/IR/1000128966`.

[Nie21b] S. NIEMES et al.: Accurate Reference Gas Mixtures Containing Tritiated Molecules: Their Production and Raman-Based Analysis. In *Sensors* (2021), volume 21(18):6170. DOI: `10.3390/s21186170`.

[NIS08]   NIST. 2008. *Certificate of Analysis (Standard Ref. Mat. 2242).* Gaithersburg, MD, USA.

[NIS19]   NIST. 2019. *Certificate of Analysis (Standard Ref. Mat. 2242a).* Gaithersburg, MD, USA.

[No18]   Y.-S. NO, H. K. CHOI, J.-S. KIM, H. KIM, Y.-J. YU, C.-G. CHOI, and J. S. CHOI: Layer number identification of CVD-grown multilayer graphene using Si peak analysis. In *Sci. Rep.* (2018), volume 8(1):571. DOI: `10.1038/s41598-017-19084-1`.

[Nod00]   L. NODA and O. SALA: A resonance Raman investigation on the interaction of styrene and 4-methyl styrene oligomers on sulphated titanium oxide. In *Spectrochim. Acta A Mol. Biomol. Spectrosc.* (2000), volume 56(1):145–155. DOI: `https://doi.org/10.1016/S1386-1425(99)00128-6`.

[Nov04]   K. S. NOVOSELOV, A. K. GEIM, S. V. MOROZOV, D. JIANG, Y. ZHANG, S. V. DUBONOS, I. V. GRIGORIEVA, and A. A. FIRSOV: Electric field effect in atomically thin carbon films. In *Science* (2004), volume 306(5696):666–669. DOI: `10.1126/science.1102896`.

[Nus22]   S. NUSSINOV and Z. NUSSINOV: Quantum induced broadening: A challenge for cosmic neutrino background discovery. In *Phys. Rev. D* (2022), volume 105(4):043502. DOI: `10.1103/PhysRevD.105.043502`.

[Ott08]   E. W. OTTEN and C. WEINHEIMER: Neutrino mass limit from tritium β-decay. In *Rep. Prog. Phys.* (2008), volume 71(8):086201. DOI: `10.1088/0034-4885/71/8/086201`.

[Pap20]   G. S. PAPANAI, I. SHARMA, and B. K. GUPTA: Probing number of layers and quality assessment of mechanically exfoliated graphene via Raman fingerprint. In *Mater. Today Commun.* (2020), volume 22:100795. DOI: 10.1016/j.mtcomm.2019.100795.

[Pau27]   W. PAULI: Zur Quantenmechanik des magnetischen Elektrons. In *Z. Phys.* (1927), volume 43(9-10):601–623. DOI: 10.1007/BF01397326.

[Pau30]   W. PAULI, *Offener Brief an die Gruppe der Radioaktiven bei der Gauvereins-Tagung zu Tübingen*, 1930, URL: https://cds.cern.ch/record/83282/files/meitner_0393.pdf (Last accessed: 2.12.2023).

[Pau58]   L. J. VAN DER PAUW: A Method of measuring specific resistivity and hall effect of discs of arbitrary shape. In *Philips Res. Rep.* (1958), volume 13(13):1–9. DOI: 10.1142/9789814503464_0017.

[Pau85]   W. PAULI, A. HERMANN, K. V. MEYENN, and V. F. WEISSKOPF. 1985. *Wissenschaftlicher Briefwechsel mit Bohr, Einstein, Heisenberg u.a. Band II: 1930-1939*. Editor Springer-Verlag Berlin Heidelberg,

[PDG22]   PDG (PARTICLE DATA GROUP), R. L. WORKMAN et al.: Review of Particle Physics. In *Prog. Theor. Exp. Phys.* (2022), volume 2022(8):083C01. DOI: 10.1093/ptep/ptac097.

[Pea01]   K. PEARSON: LIII. On lines and planes of closest fit to systems of points in space. In *Lond. Edinb. Dublin philos. mag. j. sci.* (1901), volume 2(11):559–572. DOI: 10.1080/14786440109462720.

[Pla14]   PLANCK COLLABORATION, P. A. R. ADE et al.: Planck 2013 results. I. Overview of products and scientific results. In *Astron. Astrophys.* (2014), volume 571:A1. DOI: 10.1051/0004-6361/201321529.

[Pon08]   P. PONCHARAL, A. AYARI, T. MICHEL, and J.-L. SAUVAJOL: Raman spectra of misoriented bilayer graphene. In *Phys. Rev. B* (2008), volume 78(11):113407. DOI: 10.1103/PhysRevB.78.113407.

[Pon09]   P. PONCHARAL, A. AYARI, T. MICHEL, and J.-L. SAUVAJOL: Effect of rotational stacking faults on the Raman spectra of folded graphene. In *Phys. Rev. B* (2009), volume 79(19):195417. DOI: 10.1103/PhysRevB.79.195417.

[Pon57]   B. PONTECORVO: Mesonium and anti-mesonium. In *Sov. Phys. JETP* (1957), volume 6:429.

[Pov15]   B. POVH, K. RITH, C. SCHOLZ, F. ZETSCHE, and W. RODEJOHANN. 2015. *Particles and nuclei: An introduction to the physical concepts*. 7. ed. Heidelberg et al.: Springer, DOI: 10.1007/978-3-662-46321-5.

[Pri15]   F. PRIESTER, M. STURM, and B. BORNSCHEIN: Commissioning and detailed results of KATRIN inner loop tritium processing system at Tritium Laboratory Karlsruhe. In *Vacuum* (2015), volume 116:42–47. DOI: 10.1016/j.vacuum.2015.02.030.

[Pri22]   F. PRIESTER, A. MARSTELLER, S. NIEMES, N. TUCHSCHERER, and S. WELTE: μRA - New Compact Easy-to-Use Raman System for All Hydrogen Isotopologues. In *Sensors* (2022), volume 22(10):3952. DOI: 10.3390/s22103952.

[Pro22]   PROJECT 8 COLLABORATION, A. ASHTARI ESFAHANI, et al., *The Project 8 Neutrino Mass Experiment*, 2022, DOI: 10.48550/arXiv.2203.07349.

[Ram28]   C. V. RAMAN: A new radiation. In *Indian J. Phys.* (1928), volume 2:387–398.

[Ric59]   F. J. RICHARDS: A Flexible Growth Function for Empirical Use. In *J. Exp. Bot.* (1959), volume 10(2):290–301. DOI: 10.1093/jxb/10.2.290.

[Rob91]   R. G. ROBERTSON, T. J. BOWLES, G. J. STEPHENSON, D. L. WARK, J. F. WILKERSON, and DA KNAPP: Limit on nu -bare mass from observation of the beta decay of molecular tritium. In *Phys. Rev. Lett.* (1991), volume 67(8):957–960. DOI: 10.1103/PhysRevLett.67.957.

[Rod23]   C. RODENBECK, *Direct neutrino mass measurement: With material from the KATRIN, ECHo, HOLMES, Project 8, PTOLEMY and QTNM Collaborations*, Presentation, 42nd International Symposium on Physics in Collision, 2023, URL: https://indico.cern.ch/event/1190468/contributions/5553372/attachments/2733930/4753381/DirectNuMassMeasurement_Rodenbeck_PIC2023.pdf (Last accessed: 23.11.2023).

[Roy11]   R. J. LE ROY. 2011. *Recalculation of Raman transition matrix elements of all hydrogen isotopologues for 532nm laser excitation*. Private communication,

[Rup12]   S. RUPP, *Proof of concept of a calibration method for the laser Raman system for KATRIN based on the determination of the system's spectral sensitivity*, Diploma thesis, 2012, URL: https://www.katrin.kit.edu/publikationen/1dth-SimoneRupp-2012.pdf (Last accessed: 28.08.2023).

[Rup16]   S. RUPP: Development of a highly sensitive hollow waveguide based Raman system for the compositional analysis of the KATRIN tritium source gas. Dissertation: 2016. DOI: 10.5445/IR/1000059079.

[Sac21]   A. SACCO, C. PORTESI, A. M. GIOVANNOZZI, and A. M. ROSSI: Graphene edge method for three–dimensional probing of Raman microscopes focal volumes. In *J. Raman Spectrosc.* (2021), volume 52(10):1671–1684. DOI: 10.1002/jrs.6187.

[Sae00]   A. SAENZ, S. JONSELL, and P. FROELICH: Improved Molecular Final-State Distribution of HeT^+ for the β-Decay Process of T_2. In *Phys. Rev. Lett.* (2000), volume 84(2):242–245. DOI: 10.1103/PhysRevLett.84.242.

[Sah15]   H. SAHIN, O. LEENAERTS, S. K. SINGH, and F. M. PEETERS: Graphane. In *WIREs Comput. Mol. Sci.* (2015), volume 5(3):255–272. DOI: 10.1002/wcms.1216.

[Sai98]   R. SAITO, G. DRESSELHAUS, and M. S. DRESSELHAUS. 1998. *Physical Properties of Carbon Nanotubes*. Published By Imperial College Press And Distributed By World Scientific Publishing Co, DOI: 10.1142/p080.

[Sch06]   D. K. SCHRODER. 2006. *Semiconductor material and device characterization*. Third edition. Hoboken, N.J and Piscataway, NJ: Wiley-Interscience and IEEE Press, DOI: 10.1002/0471749095.

[Sch09]   M. SCHLÖSSER, *First Laser Raman measurements with tritium for KATRIN and studies of systematic effects of the LARA-setup*, Diploma thesis, 2009, URL: http://www.katrin.kit.edu/publikationen/091216_MS_diploma_thesis_with_Cover.pdf (Last accessed: 2.12.2023).

[Sch13a]   M. SCHLÖSSER, S. RUPP, H. SEITZ, S. FISCHER, B. BORNSCHEIN, T. M. JAMES, and H. H. TELLE: Accurate calibration of the laser Raman system for the Karlsruhe Tritium Neutrino Experiment. In *J. Mol. Struct.e* (2013), volume 1044:61–66. DOI: 10.1016/j.molstruc.2012.11.022.

[Sch13b]   M. SCHLÖSSER, H. SEITZ, S. RUPP, P. HERWIG, C. G. ALECU, M. STURM, and B. BORNSCHEIN: In-line calibration of Raman systems for analysis of gas mixtures of hydrogen isotopologues with sub-percent accuracy. In *Anal. Chem.* (2013), volume 85(5):2739–2745. DOI: 10.1021/ac3032433.

[Sch14]   M. SCHLOSSER. 2014. *Accurate calibration of Raman systems*. Cham, Switzerland: Springer International Publishing, DOI: 10.1007/978-3-319-06221-1.

[Sch15a]   M. SCHLOESSER, O. PAKARI, S. RUPP, S. MIRZ, and S. FISCHER: How to make Raman-inactive helium visible in Raman spectra of tritium-helium gas mixtures. In *Fusion Sci. Technol.* (2015), volume 67(3):559–562. DOI: 10.13182/FST14-T79.

[Sch15b]   M. SCHLÖSSER, S. RUPP, T. BRUNST, and T. M. JAMES: Relative Intensity Correction of Raman Systems with National Institute of Standards and Technology Standard Reference Material 2242 in 90°-Scattering Geometry. In *Appl. Spectrosc.* (2015), volume 69(5):597–607. DOI: 10.1366/14-07748.

[Sch15c]   W. SCHMID, S. MIEKE, and M. HOXHA, *Main steps to the determination of measurement uncertainty according to GUM*, 2015, URL: https://www.ptb.de/cms/fileadmin/_migrated/user_upload/2_Mieke_GUM_Method_Summer_School_2015.pdf (Last accessed: 16.12.2023).

[Sch22]   R. W. SCHMIDT, S. WOUTERSEN, and F. ARIESE: RamanLIGHT—a graphical user-friendly tool for pre-processing and unmixing hyperspectral Raman spectroscopy images. In *J. Opt.* (2022), volume 24(6):064011. DOI: 10.1088/2040-8986/ac6883.

[Sch87]   C. SCHWARTZ and R. J. LE ROY: Nonadiabatic eigenvalues and adiabatic matrix elements for all isotopes of diatomic hydrogen. In *J. Mol. Spectrosc.* (1987), volume 121(2):420–439. DOI: 10.1016/0022-2852(87)90059-2.

[Šeb13]   J. ŠEBEK, R. KNAANIE, B. ALBEE, E. O. POTMA, and R. B. GERBER: Spectroscopy of the C-H stretching vibrational band in selected organic molecules. In *J. Phys. Chem. A* (2013), volume 117(32):7442–7452. DOI: 10.1021/jp4014674.

[Sgi21]   R. SGIER, C. LORENZ, A. REFREGIER, J. FLURI, D. ZÜRCHER, and F. TARSI-TANO, *Combined* 13×2-*point analysis of the Cosmic Microwave Background*

and Large-Scale Structure: implications for the S_8-tension and neutrino mass constraints, 2021, DOI: 10.48550/arXiv.2110.03815.

[Sim15]   SIMONE RUPP, TIMOTHY M. JAMES, HELMUT H. TELLE, MAGNUS SCHLÖSSER, and BEATE BORNSCHEIN: Enhanced Sensitivity of Raman Spectroscopy for Tritium Gas Analysis Using a Metal-Lined Hollow Glass Fiber. In *Fusion Sci. Technol.* (2015), volume 67(3):547–550. DOI: 10.13182/FST14-T76.

[Sme23]   A. SMEKAL: Zur Quantentheorie der Dispersion. In *Naturwissenschaften* (1923), volume 11(43):873–875. DOI: 10.1007/BF01576902.

[SNO01]   SNO COLLABORATION: Measurement of the Rate of $\nu_e + d \to p + p + e^-$ Interactions Produced by ^8B Solar Neutrinos at the Sudbury Neutrino Observatory. In *Phys. Rev. Lett.* (2001), volume 87(7):071301. DOI: 10.1103/PhysRevLett.87.071301.

[Sof07]   J. O. SOFO, A. S. CHAUDHARI, and G. D. BARBER: Graphane: A two-dimensional hydrocarbon. In *Phys. Rev. B* (2007), volume 75(15):153401. DOI: 10.1103/PhysRevB.75.153401.

[Son16]   J. SON et al.: Hydrogenated monolayer graphene with reversible and tunable wide band gap and its field-effect transistor. In *Nat. Commun.* (2016), volume 7:13261. DOI: 10.1038/ncomms13261.

[Spe07]   G. SPERANZA, L. MINATI, and M. ANDERLE: The C1s core line in irradiated graphite. In *J. Appl. Phys.* (2007), volume 102(4):043504. DOI: 10.1063/1.2769332.

[Stu10a] M. STURM, M. SCHLÖSSER, R. J. LEWIS, B. BORNSCHEIN, G. DREXLIN, and H. H. TELLE: Monitoring of all hydrogen isotopologues at tritium laboratory Karlsruhe using Raman spectroscopy. In *Laser Phys.* (2010), volume 20(2):493–507. DOI: 10.1134/S1054660X10030163.

[Stu10b] M. STURM: Aufbau und Test des Inner-Loop-Systems der Tritiumquelle von KATRIN. Dissertation: Karlsruher Institut für Technologie, 2010. DOI: 10.5445/IR/1000019355.

[Stu21]   M. STURM et al.: Kilogram scale throughput performance of the KATRIN tritium handling system. In *Fusion Eng. Des.* (2021), volume 170:112507. DOI: 10.1016/j.fusengdes.2021.112507.

[Sud58]   E. C. G. SUDARSHAN and R. E. MARSHAK: Chirality Invariance and the Universal Fermi Interaction. In *Phys. Rev.* (1958), volume 109:1860–1862. DOI: 10.1103/PhysRev.109.1860.2.

[Sup98]   SUPER-KAMIOKANDE COLLABORATION: Measurements of the Solar Neutrino Flux from Super-Kamiokande's First 300 Days. In *Phys. Rev. Lett.* (1998), volume 81(6):1158–1162. DOI: 10.1103/PhysRevLett.81.1158.

[Tab00]   T. TABATA and T. SHIRAI: Analytic cross sections for collisions of H^+, H_2^+, H_3^+, H, H_2 and H^- with hydrogen molecules. In *At. Data Nucl. Data Tables* (2000), volume 76(1):1–25. DOI: 10.1006/adnd.2000.0835.

[Tan22]   I. TANSERI, S. HAGSTOTZ, S. VAGNOZZI, E. GIUSARMA, and K. FREESE: Updated neutrino mass constraints from galaxy clustering and CMB lensing-galaxy cross-correlation measurements. In *J. High Energy Astrophys.* (2022), volume 36:1–26. DOI: 10.1016/j.jheap.2022.07.002.

[Tay01]   D. J. TAYLOR, M. GLUGLA, and R.-D. PENZHORN: Enhanced Raman sensitivity using an actively stabilized external resonator. In *Review of Scientific Instruments* (2001), volume 72(4):1970–1976. DOI: 10.1063/1.1353190.

[Tel18]   H. H. TELLE and Á. GONZÁLEZ UREÑA. 2018. *Laser spectroscopy and laser imaging*. Boca Roton, London, and New York: CRC Press, DOI: 10.1201/9781315156989.

[Top18]   J. TOPORSKI, T. DIEING, and O. HOLLRICHER. 2018. *Confocal Raman Microscopy*. Cham, Switzerland: Springer International Publishing, DOI: 10.1007/978-3-319-75380-5.

[Trä15]   J. TRÄGÅRDH, K. MACRAE, C. TRAVIS, R. AMOR, G. NORRIS, S. H. WILSON, G.-L. OPPO, and G. MCCONNELL: A simple but precise method for quantitative measurement of the quality of the laser focus in a scanning optical microscope. In *J. Microsc.* (2015), volume 259(1):66–73. DOI: 10.1111/jmi.12249.

[TRI21]   TRISTAN GROUP, *Conceptual Design Report: KATRIN with TRISTAN modules*, 2021, URL: https://www.katrin.kit.edu/downloads/TRISTAN_ _Technical_Design_Report%20(10).pdf (Last accessed: 13.11.2023).

[Tui70]   F. TUINSTRA and J. L. KOENIG: Raman Spectrum of Graphite. In *J. Chem. Phys.* (1970), volume 53(3):1126–1130. DOI: 10.1063/1.1674108.

[Val22]   E. D. VALENTINO and A. MELCHIORRI: Neutrino Mass Bounds in the Era of Tension Cosmology. In *Astrophys. J. Lett.* (2022), volume 931(2):L18. DOI: 10.3847/2041-8213/ac6ef5.

[Ven11]   P. VENEZUELA, M. LAZZERI, and F. MAURI: Theory of double-resonant Raman spectra in graphene: Intensity and line shape of defect-induced and two-phonon bands. In *Phys. Rev. B* (2011), volume 84(3):035433. DOI: 10.1103/PhysRevB.84.035433.

[Wel17]   S. WELTE, E. FANGHÄNEL, S. FISCHER, F. KRAMER, T. L. LE, M. STURM, and N. TUCHSCHERER: Experimental Performance Test of Key Components of the KATRIN Outer Tritium Loop. In *Fusion Sci. Technol.* (2017), volume 71(3):316–320. DOI: 10.1080/15361055.2017.1291233.

[Wel23]   J. WELLS, *lorentzfit(x,y,varargin)*, MATLAB Central File Exchange, 2023, URL: https://www.mathworks.com/matlabcentral/fileexchange/33775-lorentzfit-x-y-varargin (Last accessed: 16.12.2023).

[Whi18]   K. E. WHITENER: Review Article: Hydrogenated graphene: A user's guide. In *J. Vac. Sci. Technol. A* (2018), volume 36(5):05G401. DOI: 10.1116/1.5034433.

[Wu22]   E. WU, C. SCHNEIDER, R. WALZ, and J. PARK: Adsorption of hydrogen isotopes on graphene. In *Nucl. Eng. Technol.* (2022), volume 54(11):4022–4029. DOI: `10.1016/j.net.2022.06.014`.

[Yan11]   X.-Z. YAN and C. S. TING: Compressibility of interacting electrons in bilayer graphene. In *Phys. Rev. B* (2011), volume 84(3):035457. DOI: `10.1103/PhysRevB.84.035457`.

[Yu10]   P. Y. YU and M. CARDONA. 2010. *Fundamentals of semiconductors: Physics and materials properties*. Fourth edition. Heidelberg and Dordrecht and London and New York: Springer, DOI: `10.1007/978-3-642-00710-1`.

[Zel17]   G. ZELLER, *Development of a calibration procedure and calculation of the uncertainty budget for the KATRIN laser Raman system*, Master thesis, Karlsruhe, 2017, URL: `https://www.katrin.kit.edu/publikationen/mth-Zeller.pdf` (Last accessed: 28.02.2023).

[Zel23]   G. ZELLER et al., *First observation of tritium adsorption on graphene*, Submitted to Nanoscale Advances, 2023, DOI: `10.48550/arXiv.2310.16645`, (Last accessed: 2.12.2023).

[Zha07]   J. ZHAO, H. LUI, D. I. MCLEAN, and H. ZENG: Automated autofluorescence background subtraction algorithm for biomedical Raman spectroscopy. In *Appl. Spectrosc.* (2007), volume 61(11):1225–1232. DOI: `10.1366/000370207782597003`.

[Zha17]   X. ZHANG, S. CHEN, Z. LING, X. ZHOU, D.-Y. DING, Y. S. KIM, and F. XU: Method for Removing Spectral Contaminants to Improve Analysis of Raman Imaging Data. In *Sci. Rep.* (2017), volume 7(1):39891. DOI: `10.1038/srep39891`.

[Zub20]   K. ZUBER. 2020. *Neutrino Physics*. Boca Raton, FL: CRC Press, DOI: `10.1201/9781315195612`.

Danksagung

Diese Arbeit wäre ohne die Unterstützung und Hilfe vieler Menschen unmöglich gewesen. Ich möchte daher diese Seiten nutzen, um ein paar dankende Worte festzuhalten.

Zunächst möchte ich mich herzlich bei Prof. Dr. Kathrin Valerius bedanken, die die Betreuung dieser – in mancher Hinsicht, untypischen – Arbeit übernommen hat. Mit einem offenen Ohr hat sie sich immer Zeit für meine Fragen genommen. Damit hat sie mir immer sowohl den notwendigen Freiraum als auch den Rückhalt bei dieser Arbeit gegeben.

Ein herzlicher Dank gilt ebenso Prof. Dr. Helmut H. Telle, der mich wiederholt ermutigte, das Projekt *Promotion* anzugehen. Mit seiner Offenheit und Begeisterung hat es mir ermöglicht mich zu entfalten, und auch einen Blick über den Tellerrand zu werfen.

Weiterhin bedanke ich mich herzlich bei Dr. Beate Bornschein – ohne ihre Unterstützung und ausgezeichnete Arbeit am TLK, wäre mein wissenschaftlicher Werdegang mit großer Wahrscheinlichkeit bereits nach der Masterarbeit beendet gewesen.

Ähnliches gilt für Dr. Magnus Schlösser, der mir immer das Gefühl gegeben hat, ein wichtiger Teil der Arbeitsgruppe zu sein und sein volles Vertrauen schenkte. Sein Enthusiasmus für die wissenschaftliche Arbeit ist ansteckend und motivierend. Herzlichen Dank dafür.

Besonderer Dank geht auch an Dr. Bennet Krasch und Dr. Simon Niemes, meine langjährigen Mitstreiter der (inoffiziellen) LARA-Gruppe. Von beiden konnte ich viel lernen und insbesondere in den ersten Jahren am TLK haben sie für mich eine Mentor-ähnliche Rolle eingenommen, und standen immer mit Rat und Tat zur Seite. Auch jetzt schätze ich den Austausch mit euch in besonderem Maße.

Bei meinen ehemaligen Bürokollegen Max Aker und Dominic Batzler bedanke ich mich für den regen (wissenschaftlichen) Austausch, die angenehme Zeit, und allzeitige Bereitschaft für Diskussionen. I thank my new office colleague Deseada Díaz Barrero for the great teamwork during her summers at TLK, and the warm and welcoming reception during my research stay in Madrid.

For their work in the reprogramming of LARAsoft, I would like to thank András Bükki-Deme and Julian Sandrock. Without their work, the day-to-day work would have been associated with many annoyances and the further development of LARAsoft would hardly have been possible. In diesem Sinne auch ein Dank an Felix Schwarz, der seinen Beitrag zur Weiterentwicklung von LARAsoft leistet und dabei hilft, die Software für die Zukunft besser zu machen.

Danke, ebenfalls an die Bachelorstudenten Jannik Demand und Paul Wiesen, die auf ihre jeweils eigene Art und Weise und zu ganz verschiedenen Zeiten meiner Arbeit, jeweils zu Beginn und zum Ende, einen entscheidenden Beitrag geleistet haben. In diesem Kontext auch vielen Dank an Christian Goffing, der im Endspurt immer bereit war, beim Aufbau der Beladungskammer und dem Betrieb von TriHyDe zu helfen.